In memoriam

George Herrmann

GEORGE HERRMANN: IN APPRECIATION

TERRY J. DELPH AND DEWEY H. HODGES

This issue of the *Journal of the Mechanics of Materials and Structures* is dedicated to the memory of George Herrmann, who, among his many other activities, played a not insignificant role in its founding. It contains a selection of papers on a wide range of topics in mechanics written by a number of his numerous colleagues, associates, and students. We, the editors of this issue, are privileged to have been in the last category.

George Herrmann played a major role in the mechanics community in the latter half of the twentieth century, and his influence persists to the present day. Born in Moscow in 1921, he was brought to Switzerland in 1933 and was educated there, receiving his doctorate from ETH in 1949. After a short stint at the École Polytechnique in Montreal, he moved to Columbia University in 1951, where he stayed until 1962. He then moved to Northwestern University, and finally, in 1970, to Stanford University. At Stanford, he served as Chair of the Department of Applied Mechanics and then, when the Department merged with the Department of Mechanical Engineering in 1975, as Chair of the Division of Applied Mechanics. He held this post until his retirement from Stanford in 1984.

His research interests were broad, and touched on many of the major themes in mechanics over the last 60 years: plate and shell theory, stability theory, vibrations of elastic bodies, wave propagation, and fracture mechanics. He remained active in research following his retirement from Stanford, and, in later years, developed an interest in the mechanics of solids as viewed from an Eshelbean standpoint. This he pursued vigorously with longtime collaborator Reinhold Kienzler up to his death in 2007. His work brought him wide recognition and a number of awards from various professional societies. Among these were election to the National Academy of Engineering, the Centennial Medal of the American Society of Mechanical Engineers, the von Karman medal of the American Society of Civil Engineers, and the Eringen medal of the Society of Engineering Science.

His service to the mechanics community was equally important. He served on innumerable boards and committees, and was quite influential in the Applied Mechanics Division of the American Society of Mechanical Engineers. In an era in which important Soviet work in mechanics was largely unknown in the West, he began the English translation of *Prikladnaya Matematika i Mekhanika*, the premier Russian language mechanics journal and served for many years as its translation editor. Perhaps most significantly, he founded the *International Journal of Solids and Structures* in 1965 and served as its Editor until his retirement from Stanford, building it into one of the most reputable journals in the field.

On a personal level, George Herrmann was a man of great warmth and charm. Those of us who were his students will recall his kindness and consideration, even on those occasions on which we tried his patience. Particularly impressive was his uncanny ability to find the best line of attack on a given research problem, where he was often able to obtain significant results with only a minimum of tools. His lectures were clear, focused, and well-organized, and his courses were always popular with the students. He was an accomplished linguist, and constantly amazed those of us around him by his ability to converse

with the seminar speaker of the day in the speaker's native language. While at Stanford, he organized frequent outings, excursions, and dinners for the students and faculty that did much to build a strong sense of camaraderie within the Department, and later the Division, of Applied Mechanics.

We think that we can speak for the contributors to this issue, and certainly for ourselves, in saying that it was a privilege to have known him.

TERRY J. DELPH: `tjd1@lehigh.edu`
Lehigh University, Mechanical Engineering and Mechanics, 19 Memorial Drive West, Bethlehem, PA 18015, United States

DEWEY H. HODGES: `dhodges@gatech.edu`
Georgia Institute of Technology, Daniel Guggenheim School of Aerospace Engineering, 270 Ferst Drive, Atlanta, GA 30332-0150, United States

EXISTENCE OF ONE-COMPONENT RAYLEIGH WAVES, STONELEY WAVES, LOVE WAVES, SLIP WAVES AND ONE-COMPONENT WAVES IN A PLATE OR LAYERED PLATE

THOMAS C. T. TING

It is known that one-component surface (Rayleigh) waves exist in an anisotropic elastic half-space. Since the solution shows that the displacement normal to the free surface vanishes everywhere, a one-component surface wave is also a one-component slip wave in the half-space if the boundary of the half-space is a slippery surface. We show that no other one-component slip waves exist for the half-space. As to steady waves in a bimaterial that consists of two dissimilar anisotropic elastic materials, one-component slip waves can be constructed from two one-component surface waves. There are no other one-component slip waves for a bimaterial. By imposing the continuity of the displacement at the interface on the one-component slip wave, a one-component Stoneley wave is obtained. Although one-component waves for the half-space can also propagate in a homogeneous plate, we present new one-component waves in a plate for which the Stroh eigenvalue p is real. By superposition of the one-component waves in the layer and in the half-space, one-component Love waves can be constructed. Finally, we show that one-component waves can propagate in a layered plate.

1. Introduction

Surface (Rayleigh) waves in an anisotropic elastic half-space in general consist of two or three components. Even for an isotropic elastic material, surface waves consist of two components. It was first pointed out by Barnett et al. [1991] that one-component surface waves exist for certain special anisotropic elastic materials. Further study on one-component surface waves was done by Barnett and Chadwick [1991], Chadwick [1992], Norris [1992], Ting [1992], and Wang and Gundersen [1993]. The question of whether one-component steady waves exist in a bimaterial when the interface is in sliding contact or perfectly bonded remains open. Also open is the question of whether one-component waves exist in Love waves and in layered plates. The purpose of this paper is to address these questions.

   The basic equations for steady waves in an anisotropic elastic medium based on the Stroh formalism [Stroh 1962; Barnett and Lothe 1973; Chadwick and Smith 1977; Ting 1996a] are outlined in Section 2. A modified version [Ting 2000] that is more suitable for steady waves is presented in Section 3. This version is employed to find one-component surface waves. The solution shows that the displacement normal to the free surface vanishes everywhere. Hence one-component Rayleigh waves are also one-component slip waves in the half-space when the boundary of the half-space is a slippery surface. We proved in Section 4 that there are no other one-component slip waves in the half-space. Steady state waves propagating in a bimaterial of dissimilar anisotropic materials are studied in Section 5. If the interface is in sliding

contact, one can simply take two one-component surface waves for the two half-spaces that automatically satisfy the sliding contact conditions. Again we show that there are no other one-component slip waves for the bimaterial. As for the Stoneley waves for which the interface is perfectly bonded, one-component Stoneley waves can be obtained from the one-component slip waves in the bimaterial by choosing the material constants such that the displacement is continuous at the interface. This is presented in Section 6. Thus we obtain a one-component Stoneley wave that is also a one-component slip wave. The question of whether there are other one-component Stoneley waves is still open. The one-component waves obtained here are valid if the strain energy density is positive and nonzero. This means that the 5×5 matrix of the reduced elastic compliance $s'_{\alpha\beta}$ must be positive definite. In Section 7 we present conditions for positive definiteness of $s'_{\alpha\beta}$ for which one-component Rayleigh waves can propagate. Section 8 studies the existence of one-component waves in a homogeneous plate. Although one-component waves in the half-space can also propagate in the plate, we present new solutions in which the Stroh eigenvalue p is real. By superposition of one-component waves in a plate and in the half-space, one-component Love waves can be obtained. This is presented in Section 9. Finally, in Section 10, we show how to construct one-component waves in a layered plate. The interface between the layers can be perfectly bonded or in sliding contact.

2. Basic equations

In a fixed rectangular coordinate system $x_i\,(i = 1, 2, 3)$, the equation of motion is

$$\sigma_{ij,j} = \rho \ddot{u}_i, \tag{2.1}$$

where σ_{ij} is the stress, u_i is the displacement, ρ is mass density, the dot denotes differentiation with respect to time t and a comma denotes differentiation with respect to x_i. The stress-strain relation is

$$\sigma_{ij} = C_{ijks} u_{k,s}, \tag{2.2}$$

$$C_{ijks} = C_{jiks} = C_{ksij} = C_{ijsk}, \tag{2.3}$$

in which C_{ijks} is the elastic stiffness. The C_{ijks} is positive definite and possesses the full symmetry shown in Equation (2.3). The third equality in (2.3) is redundant because the first two imply the third [Ting 1996a].

For two-dimensional steady state motion in the x_1-direction with a constant wave speed $v > 0$, a general solution for the displacement $\mathbf{u}$ in (2.1) and (2.2) is

$$\mathbf{u} = \mathbf{a}e^{ikz}, \qquad z = x_1 + px_2 - vt, \tag{2.4}$$

where $k > 0$ is the real wave number, t is the time, and p and $\mathbf{a}$ satisfy the equation

$$[\mathbf{Q} - X\mathbf{I} + p(\mathbf{R} + \mathbf{R}^T) + p^2\mathbf{T}]\,\mathbf{a} = \mathbf{0}, \qquad X = \rho v^2. \tag{2.5}$$

In the above, the superscript T denotes the transpose, $\mathbf{I}$ is the identity matrix and

$$Q_{ik} = C_{i1k1}, \qquad R_{ik} = C_{i1k2}, \qquad T_{ik} = C_{i2k2}. \tag{2.6}$$

Introducing the vector

$$\mathbf{b} = (\mathbf{R}^T + p\mathbf{T})\mathbf{a} = -p^{-1}(\mathbf{Q} - X\mathbf{I} + p\mathbf{R})\mathbf{a}, \tag{2.7}$$

where the second equality follows from (2.5), the stress computed from (2.2) and (2.4) can be written as

$$\sigma_{i1} = X u_{i,1} - \phi_{i,2}, \qquad \sigma_{i2} = \phi_{i,1}, \tag{2.8}$$

where the vector

$$\boldsymbol{\phi} = \mathbf{b} e^{ikz} \tag{2.9}$$

is the stress function. The two equations in (2.7) can be written as

$$\mathbf{N}\boldsymbol{\xi} = p\boldsymbol{\xi}, \tag{2.10}$$

where [Ingebrigtsen and Tonning 1969]

$$\mathbf{N} = \begin{bmatrix} \mathbf{N}_1 & \mathbf{N}_2 \\ \mathbf{N}_3 + X\mathbf{I} & \mathbf{N}_1^T \end{bmatrix}, \qquad \boldsymbol{\xi} = \begin{bmatrix} \mathbf{a} \\ \mathbf{b} \end{bmatrix}, \tag{2.11}$$

and

$$\mathbf{N}_1 = -\mathbf{T}^{-1}\mathbf{R}^T, \qquad \mathbf{N}_2 = \mathbf{T}^{-1}, \qquad \mathbf{N}_3 = \mathbf{R}\mathbf{T}^{-1}\mathbf{R}^T - \mathbf{Q}. \tag{2.12}$$

The matrix $\mathbf{N}_2$ is symmetric and positive definite while $-\mathbf{N}_3$ is symmetric and positive semidefinite [Ting 1988; 1996a].

There are six eigenvalues p and six associated eigenvectors $\boldsymbol{\xi} = (\mathbf{a}, \mathbf{b})$. For a steady wave propagating in the half-space $x_2 \geq 0$, p must be complex with a positive imaginary part so that the displacement $\mathbf{u}$ computed from (2.4) vanishes at $x_2 = \infty$. If the six eigenvalues p are all complex, they consist of three pairs of complex conjugates. Let p_1, p_2, p_3 be the eigenvalues with a positive imaginary part. The general solution for the displacement $\mathbf{u}$ and the stress function $\boldsymbol{\phi}$ obtained from a superposition of (2.4) and (2.9) associated with p_1, p_2, p_3 is

$$\mathbf{u} = \sum_{m=1}^{3} q_m \mathbf{a}_m e^{ikz_m}, \qquad \boldsymbol{\phi} = \sum_{m=1}^{3} q_m \mathbf{b}_m e^{ikz_m}, \tag{2.13}$$

$$z_m = x_1 + p_m x_2 - vt, \tag{2.14}$$

where $(\mathbf{a}_m, \mathbf{b}_m)$ $(m = 1, 2, 3)$ are the eigenvectors associated with the eigenvalues p_m $(m = 1, 2, 3)$, and q_m are arbitrary constants. The q_m can be chosen such that the boundary condition at $x_2 = 0$ is satisfied.

If the boundary $x_2 = 0$ is a traction-free surface, the boundary condition is

$$\boldsymbol{\phi} = \mathbf{0} \qquad \text{at } x_2 = 0. \tag{2.15}$$

Equation (2.13) then gives

$$\sum_{m=1}^{3} q_m \mathbf{b}_m = \mathbf{0}. \tag{2.16}$$

In general, all three q_m (m=1,2,3) are needed to satisfy (2.16). We then have three-component surface waves. For certain anisotropic elastic materials of which isotropic materials are special cases, only two q_m are needed. We have two-component surface waves. Barnett et al. [1991] were the first ones to point out that there are anisotropic elastic materials for which one-component surface waves can propagate in the half-space. This is presented briefly in the next section.

3. One-component surface waves

The explicit expression of $\mathbf{N}_1$, $\mathbf{N}_2$, $\mathbf{N}_3$ in (2.12) was given in [Ting 1988] in terms of the elastic compliance $s_{\alpha\beta}$, and in [Barnett and Chadwick 1991] in terms of the elastic stiffness $C_{\alpha\beta}$. The $C_{\alpha\beta}$ is the contracted notation of C_{ijks}. $\mathbf{N}_1$, $\mathbf{N}_2$, $\mathbf{N}_3$ have a complicated expression in terms of $s_{\alpha\beta}$ or $C_{\alpha\beta}$. For the problems we will study here, an alternate equation to (2.10) is more convenient. It is shown in [Ting 2000] that (2.10) can be written in the form

$$
\begin{bmatrix}
Xs'_{61} - p & -1 & Xs'_{65} & s'_{66} - ps'_{61} & s'_{62} & s'_{64} - ps'_{65} \\
Xs'_{21} & -p & Xs'_{25} & s'_{26} - ps'_{21} & s'_{22} & s'_{24} - ps'_{25} \\
Xs'_{41} & 0 & Xs'_{45} - p & s'_{46} - ps'_{41} & s'_{42} & s'_{44} - ps'_{45} \\
Xs'_{11} - 1 & 0 & Xs'_{15} & s'_{16} - ps'_{11} & s'_{12} & s'_{14} - ps'_{15} \\
0 & X & 0 & -1 & -p & 0 \\
Xs'_{51} & 0 & Xs'_{55} - 1 & s'_{56} - ps'_{51} & s'_{52} & s'_{54} - ps'_{55}
\end{bmatrix}
\begin{bmatrix}
a_1 \\ a_2 \\ a_3 \\ b_1 \\ b_2 \\ b_3
\end{bmatrix} = \mathbf{0},
\tag{3.1}
$$

where

$$
s'_{\alpha\beta} = s_{\alpha\beta} - \frac{s_{a3}s_{3\beta}}{s_{33}}
\tag{3.2}
$$

is the *reduced elastic compliance*.

For a one-component free surface wave,

$$
\sigma_{21} = \sigma_{22} = \sigma_{23} = 0,
\tag{3.3}
$$

at $x_2 = 0$. This means that, from (2.8) and (2.9), $\mathbf{b} = \mathbf{0}$ or

$$
b_1 = b_2 = b_3 = 0.
\tag{3.4}
$$

Equation (3.1) reduces to

$$
\begin{bmatrix}
Xs'_{61} - p & -1 & Xs'_{65} \\
Xs'_{21} & -p & Xs'_{25} \\
Xs'_{41} & 0 & Xs'_{45} - p
\end{bmatrix}
\begin{bmatrix}
a_1 \\ a_2 \\ a_3
\end{bmatrix} = \mathbf{0},
\tag{3.5a}
$$

and

$$
\begin{bmatrix}
Xs'_{11} - 1 & 0 & Xs'_{15} \\
0 & -X & 0 \\
Xs'_{51} & 0 & Xs'_{55} - 1
\end{bmatrix}
\begin{bmatrix}
a_1 \\ a_2 \\ a_3
\end{bmatrix} = \mathbf{0}.
\tag{3.5b}
$$

The second of the three scalar equations implicit in Equation (3.5b) demands that

$$
a_2 = 0.
\tag{3.6}
$$

Since $\operatorname{Im} p > 0$ (otherwise $\mathbf{u}$ does not vanish at $x_2 = 8$) Equation $(3.5a)_{1,3}$ tells us that a_1 and a_3 are nonzero and that the ratio of a_1 to a_3 cannot be real. It follows from $(3.5a)_2$ and $(3.5b)_{1,3}$ that

$$
Xs'_{11} = 1 = Xs'_{55}, \qquad s'_{12} = s'_{15} = s'_{25} = 0.
\tag{3.7}
$$

Equation (3.5a) reduces to

$$
\begin{bmatrix}
Xs'_{16} - p & Xs'_{56} \\
Xs'_{14} & Xs'_{45} - p
\end{bmatrix}
\begin{bmatrix}
a_1 \\ a_3
\end{bmatrix} = \mathbf{0}.
\tag{3.8}
$$

For a nontrivial solution for a_1 and a_3 we must have

$$(Xs'_{16} - p)(Xs'_{45} - p) - X^2 s'_{14} s'_{56} = 0, \tag{3.9}$$

or

$$p = \tfrac{1}{2} X \left(\varepsilon + i\sqrt{-\kappa} \right), \tag{3.10a}$$

where

$$\varepsilon = s'_{45} + s'_{16}, \qquad \kappa = (s'_{45} - s'_{16})^2 + 4 s'_{14} s'_{56}. \tag{3.10b}$$

The p must be complex so that

$$\kappa = (s'_{45} - s'_{16})^2 + 4 s'_{14} s'_{56} < 0. \tag{3.11}$$

This means that s'_{14} and s'_{56} cannot vanish and must have the opposite signs. Thus a one-component surface wave cannot propagate in monoclinic materials with the symmetry plane at $x_2 = 0$ or $x_3 = 0$ because s'_{14} and s'_{56} vanish for these materials [Barnett et al. 1991; Chadwick 1992].

The fact that $\mathbf{b} = \mathbf{0}$, that is, $\boldsymbol{\phi} = \mathbf{0}$, does not mean that all stresses vanish. Only σ_{i2} ($i=1,2,3$) vanish. σ_{11} and σ_{31} can be computed from $(2.8)_1$ while σ_{33} is from

$$0 = s_{31}\sigma_{11} + s_{33}\sigma_{33} + s_{35}\sigma_{31}, \tag{3.12}$$

which is the vanishing of the strain ε_{33}. Thus both the displacement and the stress are polarized on the plane $x_2 = 0$. It can be shown [Ting 1992] that the vectors (a_1, a_3) and $(\sigma_{11}, \sigma_{31})$ are orthogonal to each other.

The existence of Rayleigh waves in a general anisotropic elastic half-space has been studied by Barnett and Lothe [1978; 1987; 1989].

4. One-component slip waves in the half-space

If the boundary of the half-space is a slippery surface, we must have

$$u_2 = \sigma_{21} = \sigma_{23} = 0. \tag{4.1}$$

This means that

$$a_2 = b_1 = b_3 = 0. \tag{4.2}$$

Equation (4.2) is implied by (3.4) and (3.6). Hence the one-component surface waves presented in the previous section can also propagate in the half-space with a slippery surface.

Equations (3.4) and (3.6) have the restriction $b_2 = 0$ which is not required in (4.2). One may ask if there are other one-component slip waves in the half-space for which $b_2 \neq 0$. The answer is negative. The proof is very simple. Equation (3.1) consists of six scalar equations of which the fifth equation is

$$Xa_2 = b_1 + pb_2. \tag{4.3}$$

When (4.2) holds, (4.3) demands that $b_2 = 0$. Thus there are no one-component slip waves for the half-space for which $b_2 \neq 0$.

5. One-component slip waves in a bimaterial

Let the half-space $x_2 \geq 0$ be occupied by an anisotropic elastic material and the half-space $x_2 \leq 0$ be occupied by a different anisotropic elastic material. For a one-component wave, the solution for the material in $x_2 \geq 0$ is given in (2.4) and (2.9). The same solution applies for the material in $x_2 \leq 0$ and is written as

$$\hat{\mathbf{u}} = \hat{\mathbf{a}}e^{ik\hat{z}}, \qquad \hat{\boldsymbol{\phi}} = \hat{\mathbf{b}}e^{ik\hat{z}}, \tag{5.1}$$

where we have used the *hat* to distinguish the solution for the material in $x_2 \leq 0$ from the solution for the material in $x_2 \geq 0$. In Equation (5.1),

$$\hat{z} = x_1 + \hat{p}x_2 - vt, \qquad \operatorname{Im}\hat{p} < 0. \tag{5.2}$$

The imaginary part of $\hat{p}$ must be negative so that the displacement and the stress function vanish at $x_2 = -\infty$.

In this section we consider the case in which the interface $x_2 = 0$ is in sliding contact. This means that

$$b_1 = b_3 = 0, \qquad \hat{b}_1 = \hat{b}_3 = 0, \tag{5.3a}$$

$$b_2 = \hat{b}_2, \qquad a_2 = \hat{a}_2. \tag{5.3b}$$

Equation (4.3) gives, using (5.3a),

$$b_2 = p^{-1}Xa_2, \qquad \hat{b}_2 = \hat{p}^{-1}\hat{X}\hat{a}_2, \tag{5.4}$$

or, by (5.3b),

$$(p^{-1}X - \hat{p}^{-1}\hat{X})a_2 = 0. \tag{5.5}$$

But X and $\hat{X}$ are real, positive and nonzero while $\operatorname{Im}p > 0$ and $\operatorname{Im}\hat{p} < 0$. Hence $p^{-1}X - \hat{p}^{-1}\hat{X}$ cannot vanish. Thus Equation (5.5), and hence (5.4) and (5.3b) tells us that

$$a_2 = b_2 = \hat{a}_2 = \hat{b}_2 = 0. \tag{5.6}$$

The result is that a one-component slip wave in the bimaterial consists of two one-component Rayleigh waves in the two half-spaces. There are no other one-component slip waves.

In conclusion, a one-component slip wave exists in a bimaterial if the reduced elastic compliance of the material in $x_2 \geq 0$ satisfies the conditions given in (3.7) and (3.11). The eigenvalue p is given by (3.10). The reduced elastic compliance of the material in $x_2 \leq 0$ satisfies the same conditions given in (3.7) and (3.11). The eigenvalue $\hat{p}$ is given by

$$\hat{p} = \frac{\hat{X}}{2}\left(\hat{\varepsilon} - i\sqrt{-\hat{\kappa}}\right),$$

where the imaginary part is negative and

$$\hat{\varepsilon} = \hat{s}'_{45} + \hat{s}'_{16}, \qquad \hat{\kappa} = (\hat{s}'_{45} - \hat{s}'_{16})^2 + 4\hat{s}'_{14}\hat{s}'_{56} < 0.$$

Slip waves in a bimaterial that consists of two general anisotropic elastic half-spaces have been studied by Barnett et al. [1988].

6. One-component Stoneley waves

We study in this section the case in which the interface $x_2 = 0$ is perfectly bonded. This means that

$$\hat{a}_i = a_i, \quad \hat{b}_i = b_i, \qquad i = 1, 2, 3. \tag{6.1}$$

The one-component slip waves in a bimaterial presented in the previous section satisfy the interface conditions (6.1) except

$$\hat{a}_1 = a_1, \qquad \hat{a}_3 = a_3. \tag{6.2}$$

If we can choose the elastic constants of the bimaterial such that (6.2) holds, we have a one-component Stoneley wave, albeit a rather strange one, because it is also a slip wave. It suffices to consider the condition

$$\frac{\hat{a}_3}{\hat{a}_1} = \frac{a_3}{a_1}. \tag{6.3}$$

From $(3.8)_1$ we have

$$\frac{a_3}{a_1} = \frac{p - X s'_{16}}{X s'_{56}} = \frac{p s'_{11} - s'_{16}}{s'_{56}}, \tag{6.4}$$

where the second equality follows from (3.7). Substitution of p from (3.10) yields

$$\frac{a_3}{a_1} = \frac{(s'_{45} - s'_{16}) + i\sqrt{-(s'_{45} - s'_{16})^2 - 4 s'_{14} s'_{56}}}{2 s'_{56}}. \tag{6.5}$$

For the material in $x_2 \leq 0$, $\operatorname{Im} \hat{p} < 0$ so that

$$\frac{\hat{a}_3}{\hat{a}_1} = \frac{(\hat{s}'_{45} - \hat{s}'_{16}) - i\sqrt{-(\hat{s}'_{45} - \hat{s}'_{16})^2 - 4 \hat{s}'_{14} \hat{s}'_{56}}}{2 \hat{s}'_{56}}. \tag{6.6}$$

Equation (6.3) holds if

$$\hat{s}'_{56} s'_{56} < 0 \qquad \text{and} \qquad \frac{\hat{s}'_{45} - \hat{s}'_{16}}{\hat{s}'_{56}} = \frac{s'_{45} - s'_{16}}{s'_{56}}, \qquad \frac{\hat{s}'_{14}}{\hat{s}'_{56}} = \frac{s'_{14}}{s'_{56}}. \tag{6.7}$$

In particular, the equations in (6.7) hold when

$$\hat{s}'_{56} = -s'_{56}, \qquad \hat{s}'_{45} = -s'_{45}, \qquad \hat{s}'_{16} = -s'_{16}, \qquad \hat{s}'_{14} = -s'_{14}. \tag{6.8}$$

The wave speed v obtained from $(2.5)_2$ and (3.7) is

$$v^2 = (\rho s'_{11})^{-1}. \tag{6.9}$$

This must be the same for the half-space $x_2 \leq 0$ so that we must have

$$\hat{\rho} \hat{s}'_{11} = \rho s'_{11}. \tag{6.10}$$

Equation (6.10) is the additional condition that is required for a one-component Stoneley wave to propagate in the bimaterial. It is also a slip wave.

To see if there is one-component Stoneley wave that is not a slip wave, we have to solve (3.1) for p, **a** and **b** in terms of X. The same solutions apply to the material in $x_2 \leq 0$, with $\operatorname{Im} \hat{p} < 0$. Imposing the

conditions that $\hat{\mathbf{a}} = \mathbf{a}$, $\hat{\mathbf{b}} = \mathbf{b}$ and $\hat{X}/\hat{\rho} = X/\rho$, one obtains restrictions imposed on the reduced elastic compliances $s'_{\alpha\beta}$ and $\hat{s}'_{\alpha\beta}$. This is easier said than done because the algebra would be too complicated. Hence the question is open if there exist one-component Stoneley waves that are not slip waves.

The existence of Stoneley waves in a general anisotropic elastic bimaterial was studied by Barnett et al. [1985] and Chadwick and Currie [1974].

It should be noted that the application of (4.3) for the materials in $x_2 \geq 0$ and $x_2 \leq 0$ leads to, using (6.1),

$$Xa_2 = b_1 + pb_2, \qquad \hat{X}a_2 = b_1 + \hat{p}b_2. \tag{6.11}$$

The following are obvious:

(i) If $a_2 = 0$, we must have $b_1 = b_2 = 0$.

(ii) If $b_1 = 0$, following the discussion in (5.5) and (5.6) we must have $a_2 = b_2 = 0$.

(iii) If $b_2 = 0$, we must have either $X = \hat{X}$ (which means $\rho = \hat{\rho}$) or $a_2 = b_1 = 0$.

Thus, the vanishing of any one of a_2, b_1, b_2 implies the vanishing of the remaining two with the exception of when $b_2 = 0$ and $X = \hat{X}$.

7. Positive definiteness of strain energy density

The above solutions for one-component waves are valid if, under the restrictions imposed on the elastic constants, the strain energy density is positive and nonzero. The strain energy density is positive and nonzero if the 6×6 symmetric matrix of the elastic stiffness $C_{\alpha\beta}$ or the 6×6 symmetric matrix of the elastic compliance $s_{\alpha\beta}$ is positive definite. For the one-component Rayleigh waves, Barnett et al. 1991 provide a numerical example of a 6×6 symmetric matrix $s_{\alpha\beta}$ that is positive definite subject to the conditions (3.7) and (3.11). We will present here a set of general conditions for which the strain energy density is positive definite under the restrictions (3.7) and (3.11).

The matrices $C_{\alpha\beta}$ and $s_{\alpha\beta}$ are the inverse of each other. For two-dimensional deformations of an anisotropic elastic body, the elements of the third column, and hence the third row, of $C_{\alpha\beta}$ do not appear in the analysis. Let $C^o_{\alpha\beta}$ be the 5×5 matrix obtained from $C_{\alpha\beta}$ by deleting the third row and the third column. It can be shown that $C^o_{\alpha\beta}$ and the 5×5 matrix of the reduced elastic compliance $s'_{\alpha\beta}$ are the inverse of each other [Ting 1996a; 1996b]. Both $C^o_{\alpha\beta}$ and $s'_{\alpha\beta}$ must be positive definite. When a positive definite $s'_{\alpha\beta}$ is obtained, taking the inverse of $s'_{\alpha\beta}$ gives a positive definite $C^o_{\alpha\beta}$. By inserting $C_{3\beta}$ ($\beta = 1, 2, \ldots, 6$) in the third row and $C_{\alpha3}$ ($\alpha = 1, 2, \ldots, 6$) in the third column we obtain $C_{\alpha\beta}$. One can choose C_{33} large enough (see below) to obtain a positive definite $C_{\alpha\beta}$. The inverse of $C_{\alpha\beta}$ provides a positive definite $s_{\alpha\beta}$. Hence it suffices to consider the positive definiteness of the 5×5 matrix $s'_{\alpha\beta}$.

A matrix is positive definite if and only if the leading principal minors of the matrix are positive and nonzero [Hohn 1965]. For the 5×5 matrix of the reduced elastic compliance $s'_{\alpha\beta}$ that provides one-component Rayleigh waves in the half-space, we have, from (3.7),

$$s'_{\alpha\beta} = \begin{bmatrix} s'_{11} & 0 & s'_{14} & 0 & s'_{16} \\ & s'_{22} & s'_{24} & 0 & s'_{26} \\ & & s'_{44} & s'_{45} & s'_{46} \\ & & & s'_{11} & s'_{56} \\ & & & & s'_{66} \end{bmatrix}. \tag{7.1}$$

Only the upper triangle of the matrix is shown because the matrix is symmetric. To study the conditions for the matrix to be positive definite, we will move the fourth column to the second column and the fourth row to the second row. Thus the new matrix is

$$s^*_{\alpha\beta} = \begin{bmatrix} s'_{11} & 0 & 0 & s'_{14} & s'_{16} \\ & s'_{11} & 0 & s'_{54} & s'_{56} \\ & & s'_{22} & s'_{24} & s'_{26} \\ & & & s'_{44} & s'_{46} \\ & & & & s'_{66} \end{bmatrix}. \tag{7.2}$$

If the matrix $s'_{\alpha\beta}$ in (7.1) is positive definite, so is the matrix $s^*_{\alpha\beta}$ in (7.2) and vice versa. We can prescribe the off-diagonal elements of $s^*_{\alpha\beta}$ arbitrarily subject to condition (3.11). We can then choose, as shown below, the diagonal elements s'_{11}, s'_{22}, s'_{44} and s'_{66}, in that order, such that all leading principal minors of $s^*_{\alpha\beta}$ are positive and nonzero.

Let Δ_1, Δ_2, ..., be the first, second, ..., principal minors of $s^*_{\alpha\beta}$. We have

$$\Delta_1 = s'_{11}, \quad \Delta_2 = (s'_{11})^2, \quad \Delta_3 = s'_{22}(s'_{11})^2, \quad \Delta_4 = \begin{vmatrix} s'_{11} & 0 & 0 & s'_{14} \\ & s'_{11} & 0 & s'_{54} \\ & & s'_{22} & s'_{24} \\ & & & s'_{44} \end{vmatrix}, \quad \Delta_5 = |s^*_{\sigma\beta}|. \tag{7.3}$$

The matrix $s^*_{\alpha\beta}$ is positive definite if Δ_α ($\alpha = 1, 2, \ldots, 5$) are all positive and nonzero. The first three equations in (7.3) tell us that we must have

$$s'_{11} > 0, \qquad s'_{22} > 0. \tag{7.4}$$

We show below that we can always choose s'_{44} and s'_{55} such that $\Delta_4 > 0$ and $\Delta_5 > 0$.

Let $\mathbf{U}$ be a symmetric square matrix that is divided as

$$\mathbf{U} = \begin{bmatrix} \mathbf{E} & \mathbf{G} \\ \mathbf{G}^T & \mathbf{F} \end{bmatrix}, \tag{7.5}$$

where $\mathbf{E}$ and $\mathbf{F}$ are symmetric square matrices. If $\mathbf{U}$ is positive definite, so are $\mathbf{E}$ and $\mathbf{F}$, and the inverse of $\mathbf{E}$ exists. From

$$\mathbf{U} = \begin{bmatrix} \mathbf{E} & \mathbf{G} \\ \mathbf{G}^T & \mathbf{F} \end{bmatrix} = \begin{bmatrix} \mathbf{E} & 0 \\ \mathbf{G}^T & \mathbf{I} \end{bmatrix} \begin{bmatrix} \mathbf{I} & \mathbf{E}^{-1}\mathbf{G} \\ 0 & \mathbf{F} - \mathbf{G}^T\mathbf{E}^{-1}\mathbf{G} \end{bmatrix}, \tag{7.6}$$

we have

$$|\mathbf{U}| = |\mathbf{E}| \cdot |\mathbf{F} - \mathbf{G}^T\mathbf{E}^{-1}\mathbf{G}|. \tag{7.7}$$

The determinant of a larger matrix is replaced by a product of the determinants of smaller matrices. We pay the price because we must compute the inverse of E [Ting 1996b].

In computing Δ_4 in Equation (7.3), we choose

$$\mathbf{E} = \begin{bmatrix} s'_{11} & 0 & 0 \\ & s'_{11} & 0 \\ & & s'_{22} \end{bmatrix}, \qquad \mathbf{G} = \begin{bmatrix} s'_{14} \\ s'_{54} \\ s'_{24} \end{bmatrix}, \qquad \mathbf{F} = s'_{44}. \tag{7.8}$$

We then have

$$\Delta_4 = \Delta_3[s'_{44} - (s'^2_{14} + s'^2_{54})(s'_{11})^{-1} - s'^2_{24}(s'_{22})^{-1}]. \tag{7.9}$$

Hence $\Delta_4 > 0$ if

$$s'_{44} > (s'^2_{14} + s'^2_{54})(s'_{11})^{-1} + s'^2_{24}(s'_{22})^{-1}. \tag{7.10}$$

For Δ_5 we choose

$$\mathbf{E} = \begin{bmatrix} s'_{11} & 0 & 0 & s'_{14} \\ & s'_{11} & 0 & s'_{54} \\ & & s'_{22} & s'_{24} \\ & & & s'_{44} \end{bmatrix}, \qquad \mathbf{G} = \begin{bmatrix} s'_{16} \\ s'_{56} \\ s'_{26} \\ s'_{46} \end{bmatrix}, \qquad \mathbf{F} = s'_{66}. \tag{7.11}$$

Hence $\Delta_5 > 0$ if we choose s'_{66} such that

$$s'_{66} > \mathbf{G}^T\mathbf{E}^{-1}\mathbf{G}, \tag{7.12}$$

where

$$\mathbf{E}^{-1} =$$
$$\frac{1}{\Delta_4} \begin{bmatrix} s'_{11}(s'_{22}s'_{44} - s'^2_{24}) - s'_{22}s'^2_{45} & -s'_{14}s'_{22}s'_{45} & -s'_{11}s'_{14}s'_{24} & s'_{11}s'_{22}s'_{14} \\ & s'_{11}(s'_{22}s'_{44} - s'^2_{24}) - s'_{22}s'^2_{14} & -s'_{11}s'_{24}s'_{45} & -s'_{11}s'_{22}s'_{45} \\ & & s'_{11}(s'_{11}s'_{44} - s'^2_{14} - s'^2_{45}) & s'_{11}s'^2_{24} \\ & & & s'^2_{11}s'_{22} \end{bmatrix}$$

Thus one-component Rayleigh waves presented earlier are valid if the conditions (7.4), (7.10) and (7.12) are satisfied.

The above illustration shows that, after the off-diagonal elements of the matrix are specified, one can always choose the diagonal elements of the matrix in succession, so that the Δ_i are positive and nonzero. The same procedure can be employed to find a positive definite matrix $s'_{\alpha\beta}$ for materials for which other one-component steady waves can propagate.

8. One-component waves in a plate

Consider a plate of uniform thickness h whose mid-plane is parallel to the plane $x_2 = 0$. Let the surfaces of the plate be traction-free or a slippery surface. The one-component Rayleigh waves presented in (3.5)–(3.11) apply here. We have

$$\mathbf{u} = \mathbf{a}e^{ikz}, \qquad z = x_1 + px_2 - vt. \tag{8.1}$$

The imaginary part of p need not be positive. Hence (3.1) and (6.5) are replaced by

$$p^{\pm} = \tfrac{1}{2}X\left(\varepsilon \pm i\sqrt{-\kappa}\right), \tag{8.2}$$

$$\left(\frac{a_3}{a_1}\right)^{\pm} = \frac{(s'_{45} - s'_{16}) \pm i\sqrt{-(s'_{45} - s'_{16})^2 - 4s'_{14}s'_{56}}}{2s'_{56}}. \tag{8.3}$$

However, these two are not the only solutions because the Stroh eigenvalue p need not be complex for a plate of finite thickness. Below, we will present new solutions associated with a real p.

When p is real, (3.11) is replaced by

$$\kappa = (s'_{45} - s'_{16})^2 + 4s'_{14}s'_{56} \geq 0. \tag{8.4}$$

From Equation (3.5b) we have $a_2 = 0$ so that (3.6) remains valid. Since p is real, (3.5a) suggests that a_1 and a_3 are also real. For a nontrivial solution of a_1, a_3 from (3.5b) we must have

$$(Xs'_{11} - 1)(Xs'_{55} - 1) - (Xs'_{15})^2 = 0. \tag{8.5}$$

It gives two solutions

$$X^{\pm} = \frac{(s'_{55} + s'_{11}) \pm \sqrt{(s'_{55} - s'_{11})^2 + (2s'_{15})^2}}{2(s'_{11}s'_{55} - s'_{15}s'_{15})} > 0. \tag{8.6}$$

They are both real and positive. Equation (3.5b) also gives

$$\frac{a_3}{a_1} = \frac{1 - Xs'_{11}}{Xs'_{15}}. \tag{8.7}$$

Use of Equation (8.6) leads to

$$\frac{a_3}{a_1} = \frac{(s'_{55} - s'_{11}) \mp \sqrt{(s'_{55} - s'_{11})^2 + (2s'_{15})^2}}{2s'_{15}} = \tan\theta^{\pm}, \tag{8.8}$$

say, for $X = X^{\pm}$. The displacement (u_1, u_3) is polarized along a straight line on a plane parallel to $x_2 = 0$. The line makes an angle θ^+ (or θ^-) with the x_1-axis when $X = X^+$ (or X^-). It is known that the polarization vectors a associated with two different X are orthogonal to each other. Indeed, one can show that

$$(\tan\theta^+)(\tan\theta^-) = -1, \tag{8.9}$$

so that θ^+ and θ^- differ by ninety degrees.

With $a_2 = 0$, Equation (3.5a)$_2$ gives

$$\frac{a_3}{a_1} = \frac{-s'_{12}}{s'_{25}}. \tag{8.10}$$

Equation (3.5a)$_{1,3}$ reduces to (3.8). It has a nontrivial solution for a_1, a_3 if (3.9) holds,

$$p^{\pm} = \frac{X}{2}\left\{(s'_{45} + s'_{16}) \pm \sqrt{(s'_{45} - s'_{16})^2 + 4s'_{14}s'_{56}}\right\}. \tag{8.11}$$

The two roots are real in view of (8.4). The a_1, a_3 obtained from (3.8)$_1$ is

$$\frac{a_3}{a_1} = \frac{p - Xs'_{16}}{Xs'_{56}}, \tag{8.12}$$

or, using (8.11),

$$\frac{a_3}{a_1} = \frac{(s'_{45} - s'_{16}) \pm \sqrt{(s'_{45} - s'_{16})^2 + 4s'_{14}s'_{56}}}{2s'_{56}}, \tag{8.13}$$

for $p = p^{\pm}$. We therefore have four sets of solutions associated with (X^+, p^+), (X^+, p^-), (X^-, p^+) and (X^-, p^-). Equations (8.8), (8.10) and (8.13) should be compatible. Hence the conditions for the

one-component waves are

$$\frac{(s'_{55} - s'_{11}) \mp \sqrt{(s'_{55} - s'_{11})^2 + (2s'_{15})^2}}{2s'_{15}} = \frac{-s'_{12}}{s'_{25}}, \tag{8.14}$$

for $X = X^{\pm}$ and

$$\frac{(s'_{45} - s'_{16}) \pm \sqrt{(s'_{45} - s'_{16})^2 + 4s'_{14}s'_{56}}}{2s'_{56}} = \frac{-s'_{12}}{s'_{25}}, \tag{8.15}$$

for $p = p^{\pm}$. These are in addition to (8.4).

The one-component waves in plates with real p are the exceptional bulk waves studied by Alshits and Lothe [1979]. They employed a different derivation. The derivation presented above provides explicit expression of the solution for X and p, and the restrictions (8.14), (8.15) and (8.4) on $s'_{\alpha\beta}$ so that one-component waves with real p can propagate in a plate.

The existence of one-component waves in plates with real p is not guaranteed unless the 5×5 matrix $s'_{\alpha\beta}$ is positive definite, subject to (8.14), (8.15) and (8.4). Since the diagonal elements s'_{11} and s'_{55} appear in (8.14), we will rearrange the 5×5 matrix $s'_{\alpha\beta}$ and consider

$$s^*_{\alpha\beta} = \begin{bmatrix} s'_{11} & s'_{15} & s'_{12} & s'_{14} & s'_{16} \\ & s'_{55} & s'_{52} & s'_{54} & s'_{56} \\ & & s'_{22} & s'_{24} & s'_{26} \\ & & & s'_{44} & s'_{46} \\ & & & & s'_{66} \end{bmatrix}. \tag{8.16}$$

The first two principal minors are

$$\Delta_1 = s'_{11}, \qquad \Delta_2 = s'_{11}s'_{55} - (s'_{15})^2. \tag{8.17}$$

We can choose s'_{11}, s'_{15} and s'_{55} such that

$$s'_{11} > 0, \qquad s'_{55} > (s'_{15})^2/s'_{11}. \tag{8.18}$$

We next choose the remaining off-diagonal elements such that (8.4), (8.14) and (8.15) are satisfied. Following the procedure illustrated in Section 7, we can choose s'_{22}, s'_{44} and s'_{66} in that order such that Δ_3, Δ_4 and Δ_5 are positive and nonzero.

As a special case, let

$$s'_{11} = s'_{55}, \qquad s'_{14}s'_{56} = 0. \tag{8.19}$$

Equations (8.6) and (8.8) reduce to

$$X^{\pm} = (s'_{11} \mp s'_{15})^{-1}, \qquad a_3 = \mp a_1, \tag{8.20}$$

and (8.11) simplifies to

$$p^+ = Xs'_{45}, \qquad p^- = Xs'_{16}. \tag{8.21}$$

For $X = (s'_{11} - s'_{15})^{-1}$ and $p = Xs'_{45}$, we have $a_3 = -a_1$ and (3.5a) is satisfied if

$$s'_{14} = s'_{12} - s'_{25} = s'_{16} - s'_{45} - s'_{56} = 0. \tag{8.22}$$

For $X = (s'_{11} - s'_{15})^{-1}$ and $p = Xs'_{16}$, we have $a_3 = -a_1$ and (3.5a) is satisfied if

$$s'_{56} = s'_{12} - s'_{25} = s'_{16} - s'_{45} + s'_{14} = 0. \tag{8.23}$$

For $X = (s'_{11} + s'_{15})^{-1}$ and $p = Xs'_{45}$, we have $a_3 = a_1$ and (3.5a) is satisfied if

$$s'_{14} = s'_{12} + s'_{25} = s'_{16} - s'_{45} + s'_{56} = 0. \tag{8.24}$$

For $X = (s'_{11} + s'_{15})^{-1}$ and $p = Xs'_{16}$, we have $a_3 = a_1$ and (3.5a) is satisfied if

$$s'_{56} = s'_{12} + s'_{25} = s'_{16} - s'_{45} - s'_{14} = 0. \tag{8.25}$$

If the material is isotropic, there are two solutions, $X = 1/s'_{11}$ and $X = 1/s'_{55}$, while $p = 0$. We have

$$(a_1, a_3) = (1, 0), \qquad s'_{12} = 0, \qquad \text{for } X = 1/s'_{11} = 2\mu, \tag{8.26}$$

where μ is the shear modulus and

$$(a_1, a_3) = (0, 1), \qquad \text{for } X = 1/s'_{55} = \mu. \tag{8.27}$$

The solution in (8.26) is a longitudinal wave that leaves $\sigma_{22} = 0$. s'_{12} must vanish. Otherwise σ_{22} does not vanish. The solution in (8.27) is a horizontally polarized shear wave.

Unlike the one-component waves associated with a complex p, the materials for which one-component waves associated with a real p can propagate can be any anisotropic elastic material, including the isotropic materials.

Steady waves in a plate of general anisotropy have been extensively studied in the literature. The readers may consult the references listed in the more recent studies by Shuvalov [2000; 2004] and Ting [2008].

9. One-component Love waves

Let an anisotropic elastic layer of thickness $\hat{h}$ occupy the region $0 \geq x_2 \geq -\hat{h}$. It is attached to the half-space $x_2 \geq 0$ of different anisotropic elastic material. The surface $x_2 = -\hat{h}$ of the layer can be traction-free or a slippery surface.

If the interface $x_2 = 0$ between the layer and the half-space is in sliding contact, the solution for one-component Rayleigh waves obtained in Section 4 applies for the half-space while the solutions for a homogeneous plate given in Section 8 apply to the layer here. As shown in Section 8, there are two possible solutions for the layer when p is complex and four possible solutions when p is real.

If the interface between the layer and the half-space is perfectly bonded, we have to impose the continuity of the displacement at the interface between the layer and the half-space at $x_2 = 0$ and demand that the wave speed v be the same in the layer and the half-space. The wave speed is the same if (6.10) holds, where the hat refers to materials in the layer. The displacement is continuous if

$$\frac{a_3}{a_1} = \frac{\hat{a}_3}{\hat{a}_1}. \tag{9.1}$$

(a_3/a_1) for the half-space is given in (6.5), which is complex. $(\hat{a}_3/\hat{a}_1)$ for the layer can be either one of the two solutions associated with a complex $\hat{p}$ presented in (8.3). The imaginary part of $\hat{p}$ can be

positive or negative. We cannot employ the solutions associated with a real $\hat{p}$ for the layer because the displacement would not be complex.

Love waves for which the layer and the half-space are general anisotropic elastic materials have been studied by Shuvalov and Every [2002]. Ting [2009] considered the case in which the interface can be either perfectly bonded or in a sliding contact.

10. One-component waves in a layered plate

Consider first a plate that consists of two layers. One layer has thickness h and occupies the region $0 \leq x_2 \leq h$. The solution is given by

$$\mathbf{u} = \mathbf{a}\, e^{ikz}, \tag{10.1}$$

where

$$z = x_1 + p x_2 - vt. \tag{10.2}$$

The other layer has the thickness $\hat{h}$ and occupies the region $-\hat{h} \leq x_2 \leq 0$. The solution is given by

$$\hat{\mathbf{u}} = \hat{\mathbf{a}}\, e^{ik\hat{z}}, \tag{10.3}$$

where

$$\hat{z} = x_1 + \hat{p} x_2 - vt. \tag{10.4}$$

The surfaces at $x_2 = h$ and $x_2 = -\hat{h}$ of the plate can be traction-free or slippery surfaces.

If the interface at $x_2 = 0$ is in sliding contact, any one of the solutions for a homogeneous plate given in Section 8 applies to each layer. There are two possible solutions when p is complex and four possible solutions when p is real for the layer. Thus there are six possible solutions for each layer in the plate.

If the interface between the layer and the half-space is perfectly bonded, we have to impose the continuity of the displacement at the interface $x_2 = 0$ and demand that the wave speed v be the same in the two layers. The wave speed is the same if

$$X/\rho = \hat{X}/\hat{\rho}. \tag{10.5}$$

The displacement is continuous if Equation (9.1) holds. For (9.1) to hold, it is necessary that the p in both layers be either complex or real.

For a plate that consists of n layers, the problem is simple if all interfaces between the layers are in sliding contact. In this case, each layer can have any one of the six one-component waves (two associated with a complex p and four associated with a real p) presented in Section 8. The solution in each layer is independent of the solutions in other layers.

If some of the interfaces are perfectly bonded, we have to impose the continuity of the displacement across the perfectly bonded interfaces. Let $h_1, h_2,\ldots, h_n$ be the thicknesses of the layers that occupy the regions

$$h_1 \geq x_2 \geq 0,$$
$$h_1 + h_2 \geq x_2 \geq h_1,$$
$$\ldots \tag{10.6}$$
$$h_1 + h_2 + \ldots + h_n \geq x_2 \geq h_1 + h_2 + \ldots + h_{n-1},$$

respectively. Let the interface between the m-th and $(m+1)$-th layers be perfectly bonded. The solution for the one-component wave shown in (2.4) can have a more general expression. For the m-th layer, we let

$$\mathbf{u}^{(m)} = \mathbf{a}^{(m)} e^{ikz^{(m)}}, \qquad m = 1, 2, \ldots, n, \tag{10.7}$$

where

$$z^{(m)} = x_1 + p^{(m)}(x_2 - \alpha_m) + \beta_m - vt. \tag{10.8}$$

The α_m and β_m are constants to be determined. The solution for the $(m+1)$-th layer is obtained by replacing m by $(m+1)$ in (10.7) and (10.8). At the interface between the m-th and $(m+1)$-th layers,

$$x_2 = \sum_{i=1}^{m} h_i, \tag{10.9}$$

so that (10.8) gives

$$z^{(m)} = x_1 + p^{(m)} \sum_{i=1}^{m} h_i - p^{(m)} \alpha_m + \beta_m - vt,$$
$$z^{(m+1)} = x_1 + p^{(m+1)} \sum_{i=1}^{m} h_i - p^{(m+1)} \alpha_{m+1} + \beta_{m+1} - vt. \tag{10.10}$$

To enforce the continuity of the displacement at the interface, $z^{(m)}$ and $z^{(m+1)}$ in (10.10) must be identical. They are identical if we set

$$\alpha_m = \sum_{i=1}^{m-1} h_i, \qquad \beta_m = \sum_{i=1}^{m-1} p^{(i)} h_i. \tag{10.11}$$

Equation (10.10) then gives

$$z^{(m)} = x_1 + \beta_{m+1} - vt = z^{(m+1)}. \tag{10.12}$$

The continuity of the displacement at the interface is

$$\frac{a_3^{(m)}}{a_1^{(m)}} = \frac{a_3^{(m+1)}}{a_1^{(m+1)}}. \tag{10.13}$$

The Stroh eigenvalues $p^{(m)}$ and $p^{(m+1)}$ must be either complex or real. If they are complex, there are two possible solutions as shown in Section 8 for each of the two layers. If they are real, there are four possible solutions for each of the two layers. The wave speed v must be the same for the two layers. This means that

$$\frac{X^{(m)}}{\rho^{(m)}} = \frac{X^{(m+1)}}{\rho^{(m+1)}}. \tag{10.14}$$

Equations (10.13) and (10.14) must be satisfied for the two layers whose interface is perfectly bonded.

Thus, it is not difficult to see that one-component waves can propagate in a special layered plate in which the interfaces can be in sliding contact or perfectly bonded. The dispersion equations for a general anisotropic elastic layered plate can be found in [Alshits et al. 2003] and [Ting 2008].

Remarks

We have shown that one-component steady waves can propagate in the half-space in which the boundary surface can be traction-free or a slippery surface. We have also shown that one-component steady waves can propagate in a bimaterial for which the interface can be in sliding contact or perfectly bonded. The basic solution common to all one-component steady waves is the one-component surface wave. It has the characteristic that the stress σ_{i2} ($i = 1, 2, 3$) and the displacement u_2 vanish everywhere. Thus any plane that is parallel to $x_2 = 0$ is a free surface and also a slippery surface. Because of this, the half-space need not be infinite in extent. We could have a plate of finite thickness h whose surfaces are either traction-free or slippery surfaces. One-component steady waves can propagate in the plate and the wave is *not* dispersive. Likewise, the bimaterial need not be infinite in extent. If one of the two half-spaces is finite we have one-component Love waves. If both half-spaces are finite, we have a plate that consists of two layers. Again one-component steady waves can propagate in the two-layered plate and the wave is not dispersive. For the plate of finite thickness, the Stroh eigenvalue need not be complex. We present new one-component waves that can propagate in a plate and a layered plate that consists of any number of layers. These waves are not dispersive.

Acknowledgements

References

[Alshits and Lothe 1979] V. I. Alshits and J. Lothe, "Elastic waves in triclinic crystals, III: the problem of existence of exceptional waves and some of their general properties", *Sov. Phys. Crystallogr.* **24** (1979), 644–648.

[Alshits et al. 2003] V. I. Alshits, M. Deschamps, and G. A. Maugin, "Elastic waves in anisotropic plates: short-wavelength asymptotics of the dispersion branches v_n, (k", *Wave Motion* **37**:3 (2003), 273–292.

[Barnett and Chadwick 1991] D. M. Barnett and P. Chadwick, "The existence of one-component surface waves and exceptional subsequent transonic states of types 2, 4, and E1 in anisotropic elastic media", pp. 199–214 in *Modern theory of anisotropic elasticity and applications*, edited by J. J. Wu et al., SIAM Proceedings, SIAM, Philadelphia, 1991.

[Barnett and Lothe 1973] D. M. Barnett and J. Lothe, "Synthesis of the sextic and the integral formalism for dislocations, Greens function and surface waves in anisotropic elastic solids", *Phys. Norv.* **7** (1973), 13–19.

[Barnett and Lothe 1978] D. M. Barnett and J. Lothe, "The existence of Rayleigh (surface) waves solutions in anisotropic elastic half-spaces", pp. 445–457 in *Modern problems in elastic wave propagation*, edited by J. Miklowitz and J. Achenbach, Wiley, New York, 1978.

[Barnett and Lothe 1987] D. M. Barnett and J. Lothe, "On the existence of type-6 transonic states in linear elastic media of cubic symmetry", *P. Roy. Soc. Lond. A Mat.* **411**:1840 (1987), 251–263.

[Barnett and Lothe 1989] D. M. Barnett and J. Lothe, "Surface wave existence theory for the case of zero curvature transonic state", pp. 33–38 in *Elastic wave propagation*, edited by M. F. McCarthy and M. A. Hayes, North-Holland, Amsterdam, 1989.

[Barnett et al. 1985] D. M. Barnett, J. Lothe, S. D. Gavazza, and M. J. P. Musgrave, "Considerations of the existence interfacial (Stoneley) waves in bonded anisotropic elastic half-spaces", *P. Roy. Soc. Lond. A Mat.* **402**:1822 (1985), 153–166.

[Barnett et al. 1988] D. M. Barnett, S. D. Gavazza, and J. Lothe, "Slip waves along the interface between two anisotropic elastic half-spaces in sliding contact", *P. Roy. Soc. Lond. A Mat.* **415**:1849 (1988), 389–419.

[Barnett et al. 1991] D. M. Barnett, P. Chadwick, and J. Lothe, "The behaviour of elastic surface waves polarized in a plane of materials symmetry, I: addendum", *P. Roy. Soc. Lond. A Mat.* **433**:1889 (1991), 699–710.

[Chadwick 1992] P. Chadwick, "Some remarks on the existence of one-component surface waves in elastic materials with symmetry", *Phys. Scripta* **44** (1992), 94–97. The Jens Lothe Symposium Volume.

[Chadwick and Currie 1974] P. Chadwick and P. K. Currie, "Stoneley waves at an interface between elastic crystals", *Q. J. Mech. Appl. Math.* **27**:4 (1974), 497–503.

[Chadwick and Smith 1977] P. Chadwick and G. D. Smith, "Foundations of the theory of surface waves in anisotropic elastic materials", *Adv. Appl. Mech.* **17** (1977), 303–376.

[Hohn 1965] F. E. Hohn, *Elementary matrix algebra*, Macmillan, New York, 1965.

[Ingebrigtsen and Tonning 1969] K. A. Ingebrigtsen and A. Tonning, "Elastic surface waves in crystal", *Phys. Rev.* **184**:3 (1969), 942–951.

[Norris 1992] A. N. Norris, "One-component surface waves in materials with symmetry", *J. Mech. Phys. Solids* **40**:7 (1992), 1569–1582. The P. Chadwick Symposium Volume.

[Shuvalov 2000] A. L. Shuvalov, "On the theory of wave propagation in anisotropic plates", *P. Roy. Soc. Lond. A Mat.* **456**:2001 (2000), 2197–2222.

[Shuvalov 2004] A. L. Shuvalov, "General relationship for guided acoustic waves in anisotropic plates", *P. Roy. Soc. Lond. A Mat.* **460**:2049 (2004), 2671–2679.

[Shuvalov and Every 2002] A. L. Shuvalov and A. G. Every, "Some properties of surface acoustic waves in anisotropic-coated solids, studied by the impedance method", *Wave Motion* **36**:3 (2002), 257–273.

[Stroh 1962] A. N. Stroh, "Steady state problems in anisotropic elasticity", *J. Math. Phys.* **41** (1962), 77–103.

[Ting 1988] T. C. T. Ting, "Some identities and the structure of N_i in the Stroh formalism of anisotropic elasticity", *Q. J. Appl. Math. Mech.* **46** (1988), 109–120.

[Ting 1992] T. C. T. Ting, "The motion of one-component surface waves", *J. Mech. Phys. Solids* **40**:7 (1992), 1637–1650. The P. Chadwick Symposium Volume.

[Ting 1996a] T. C. T. Ting, *Anisotropic elasticity: theory and applications*, Oxford University Press, New York, 1996.

[Ting 1996b] T. C. T. Ting, "Positive definiteness of anisotropic elastic constants", *Math. Mech. Solids* **1**:3 (1996), 301–314.

[Ting 2000] T. C. T. Ting, "A new modified Lekhnitskii formalism *à la* Stroh for steady-state waves in anisotropic elastic materials", *Wave Motion* **32**:2 (2000), 125–140.

[Ting 2008] T. C. T. Ting, "Dispersion equations for steady waves in an anisotropic elastic plate or a layered plate", *P. Roy. Soc. Lond. A Mat.* **464**:2091 (2008), 613–629.

[Ting 2009] T. C. T. Ting, "Steady waves in an anisotropic elastic layer attached to a half-space or between two half-spaces — a generalization of Love waves and Stoneley waves", *Math. Mech. Solids* **14**:1-2 (2009), 52–71.

[Wang and Gundersen 1993] L. Wang and S. A. Gundersen, "Existence of one component surface waves in anisotropic elastic media", *Phys. Scripta* **47**:3 (1993), 394–404.

THOMAS C. T. TING: tting@uic.edu
Division of Mechanics and Computation, Stanford University, Durand 262, Stanford, CA 94305, United States

ACOUSTIC EMISSION FROM A SURFACE-BREAKING CRACK IN A LAYER UNDER CYCLIC LOADING

JAN D. ACHENBACH

An isotropic, homogeneous, elastic layer is subjected to a time-harmonic tensile stress of constant amplitude parallel to the free surfaces. The cyclic stresses are assumed to generate a surface-breaking crack of length $l(t)$ which propagates normally to the top surface of the layer. The unloading of the crack faces generates acoustic emission, which is composed of Lamb waves. The elastodynamic reciprocity theorem for time-harmonic waves is used to determine the amplitudes of the radiated system of time-harmonic Lamb waves.

1. Introduction

One way of detecting a surface-breaking crack is by measuring the acoustic emission that is generated by nucleation and growth of the crack. To understand the acoustic emission requires the assistance of a suitable measurement model, for a proper interpretation of measured data. In this paper we provide such a model for nucleation, growth, and opening and closing of a surface-breaking crack in a layer which is subjected to cyclic loading.

The geometry is shown in Figure 1. The layer is homogeneous, isotropic, and linearly elastic. A two-dimensional geometry of plane strain is considered. Prior to crack nucleation the layer is in a state of stress defined by

$$\tau_{11} = \Delta\tau \sin(\omega\tau). \tag{1}$$

A standard way of calculating the acoustic emission from a crack in a stress-field defined by Equation (1) is to consider a crack whose faces are subjected to a compressive stress just equal and opposite to the stress given by Equation (1):

$$x_1 = 0^{\pm}, \quad -h \le z \le -h + l(t): \quad \tau_{11} = -\Delta\tau \sin(\omega t), \tag{2a}$$
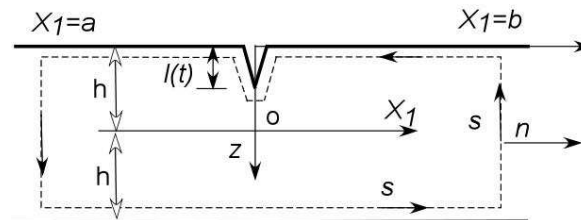
$$\tau_{1z} = 0. \tag{2b}$$

Figure 1. Surface-breaking crack in an elastic layer.

If the two stress fields, Equations (1) and (2), are superimposed, the crack faces are rendered free of tractions. It then follows that the crack-face loading defined by Equations (2a), (2b) can be considered as the excitation that generates the acoustic emission due to the presence of traction-free crack faces. It should be noted that the crack length $l(t)$ is a function of time due to growth of the crack, but the effect of this time dependence is assumed to be of a quasistatic nature.

A loading of the form defined by Equations (2a), (2b) generates time-harmonic wave modes in a layer, known as Lamb waves. For a given frequency, ω, the dimensionless wave number kh, where h is the thickness of the layer, can be obtained from the Rayleigh–Lamb frequency equation. For a given frequency, this frequency equation has real-valued, imaginary and complex roots [Achenbach 1973], which define specific modes of wave motion. In this paper, we only consider the real-valued roots, since they define wave modes that are not attenuated, and that thus can be detected at some distance from their point of excitation.

There are two kinds of wave modes in a layer: modes whose displacements are either symmetric or antisymmetric with respect to the mid-plane of the layer. For the case at hand both symmetric and antisymmetric modes are generated. These modes propagate away from the plane of the crack in both the positive and negative x_1 direction.

2. Time-harmonic waves in an elastic layer

In a two-dimensional geometry, relative to the $x_1 z$ coordinate system of Figure 1, and for the case of plane strain, the modes of symmetric motion, propagating away from the plane of the crack in a homogeneous, isotropic, linearly elastic layer may be represented by (see [Achenbach 2003, p. 150])

$$u_1^n = \pm i A_n^S V_S^n(z) e^{\pm i k_n x_1}, \tag{3}$$

$$u_z^n = A_n^S W_S^n(z) e^{\pm i k_n x_1}. \tag{4}$$

In these expressions, $\exp(-i\omega t)$ has been omitted. The index n defines the n-th mode, and k_n is the wave number of that mode. The plus or minus sign applies to propagation in the positive or negative x_1-direction, respectively. The mode shapes for the *symmetric* modes are

$$V_S^n(z) = s_1 \cos(pz) + s_2 \cos(qz), \tag{5}$$

$$W_S^n(z) = s_3 \sin(pz) + s_4 \sin(qz), \tag{6}$$

with

$$s_1 = 2\cos(qh), \qquad\qquad s_2 = -\big[(k_n^2 - q^2)/k_n^2\big]\cos(ph), \tag{7}$$

$$s_3 = -2(p/k_n)\cos(qh), \qquad s_4 = -\big[(k_n^2 - q^2)/qk_n\big]\cos(ph), \tag{8}$$

where

$$p^2 = \frac{\omega^2}{c_L^2} - k_n^2 \quad \text{and} \quad q^2 = \frac{\omega^2}{c_T^2} - k_n^2. \tag{9}$$

Equation (9) shows the dependence of p and q on n. For simplicity of notation, this dependence will not be explicitly indicated until the next section, when we replace p and q by

$$p_n^2 = \frac{\omega^2}{c_L^2} - k_n^2 \quad \text{and} \quad q_n^2 = \frac{\omega^2}{c_T^2} - k_n^2.$$

The relevant corresponding stresses are (see [Achenbach 1973, p. 150])

$$\tau_{1z}^n = \pm i A_n^S T_{1z}^{Sn}(z)e^{\pm ik_n x_1}, \tag{10}$$

$$\tau_{zz}^n = A_n^S T_{zz}^{Sn}(z)e^{\pm ik_n x_1}, \tag{11}$$

$$\tau_{11}^n = A_n^S T_{11}^{Sn}(z)e^{\pm ik_n x_1}. \tag{12}$$

In these expressions

$$T_{1z}^{Sn}(z) = \mu[s_5 \sin(pz) + s_6 \sin(qz)], \tag{13}$$

$$T_{zz}^{Sn}(z) = \mu[s_7 \cos(pz) + s_8 \cos(qz)], \tag{14}$$

$$T_{11}^{Sn}(z) = \mu[s_9 \cos(pz) + s_{10} \cos(qz)], \tag{15}$$

where

$$s_5 = 4p \cos(qh), \qquad\qquad s_6 = [(k_n^2 - q^2)^2/qk_n^2] \cos(ph), \tag{16}$$

$$s_7 = [2(k_n^2 - q^2)/k_n] \cos(qh), \qquad s_8 = -[2(k_n^2 - q^2)/k_n] \cos(ph), \tag{17}$$

$$s_9 = [2(2p^2 - k_n^2 - q^2)/k_n] \cos(qh), \quad s_{10} = [2(k_n^2 - q^2)/k_n] \cos(ph). \tag{18}$$

The condition that the faces of the layer are free of surface tractions yields the well-known Rayleigh–Lamb frequency equation for symmetric modes

$$\frac{\tan(qh)}{\tan(ph)} = -\frac{4pqk^2}{(q^2 - k^2)^2}, \tag{19}$$

which relates k_n and ω.

Similarly, for the *antisymmetric* modes we have

$$u_1^n = \pm i A_n^A V_A^n(z)e^{\pm ik_n x_1}, \tag{20}$$

$$u_z^n = A_n^A W_A^n(z)e^{\pm ik_n x_1}, \tag{21}$$

$$\tau_{1z}^n = \pm i A_n^A T_{1z}^{An}(z)e^{\pm ik_n x_1}, \tag{22}$$

$$\tau_{zz}^n = A_n^A T_{zz}^{An}(z)e^{\pm ik_n x_1}, \tag{23}$$

$$\tau_{11}^n = A_n^A T_{11}^{An}(z)e^{\pm ik_n x_1}. \tag{24}$$

The displacement mode shapes are

$$V_A^n(z) = a_1 \sin(pz) + a_2 \sin(qz), \tag{25}$$

$$W_A^n(z) = a_3 \cos(pz) + a_4 \cos(qz), \tag{26}$$

where

$$a_1 = 2\sin(qh), \qquad a_2 = -[(k_n^2 - q^2)/k_n^2]\sin(ph), \qquad (27)$$

$$a_3 = 2(p/k_n)\sin(qh), \qquad a_4 = [(k_n^2 - q^2)/qk_n]\sin(ph); \qquad (28)$$

also

$$T_{1z}^{An}(z) = \mu[a_5\cos(pz) + a_6\cos(qz)], \qquad (29)$$

$$T_{zz}^{An}(z) = \mu[a_7\sin(pz) + a_8\sin(qz)], \qquad (30)$$

$$T_{11}^{An}(z) = \mu[a_9\sin(pz) + a_{10}\sin(qz)]. \qquad (31)$$

In these expressions

$$a_5 = -4p\sin(qh), \qquad a_6 = -[(k_n^2 - q^2)^2/qk_n^2]\sin(ph), \qquad (32)$$

$$a_7 = [2(k_n^2 - q^2)/k_n]\sin(qh), \qquad a_8 = -[2(k_n^2 - q^2)/k_n]\sin(ph), \qquad (33)$$

$$a_9 = [2(2p^2 - k_n^2 - q^2)/k_n]\sin(qh), \qquad a_{10} = [2(k_n^2 - q^2)/k_n]\sin(ph). \qquad (34)$$

For the antisymmetric modes the Rayleigh–Lamb frequency equation is

$$\frac{\tan(qh)}{\tan(ph)} = -\frac{(q^2 - k^2)^2}{4pqk^2}. \qquad (35)$$

It was shown in [Achenbach 2003, p. 152] that the following orthogonality relation holds for the symmetric modes

$$I_{mn}^S = 0 \quad \text{for} \quad m \neq n, \qquad (36)$$

where

$$I_{mn}^S = \int_{-h}^{h} \left[T_{11}^{Sm}(z)V_S^n(z) - T_{1z}^{Sn}(z)W_S^m(z) \right] dz. \qquad (37)$$

Similarly, for the antisymmetric modes we have

$$I_{mn}^A = 0 \quad \text{for} \quad m \neq n, \qquad (38)$$

where

$$I_{mn}^A = \int_{-h}^{h} \left[T_{11}^{Am}(z)V_A^n(z) - T_{1z}^{An}(z)W_A^m(z) \right] dz. \qquad (39)$$

3. Acoustic emission from a surface-breaking crack

In this section, we will consider the steady part of the response generated by Equation (2). We will consider a crack-face loading of the form

$$\tau_{11} = \Delta\tau e^{-i\omega t}, \qquad (40)$$

$$\tau_{1z} = 0, \qquad (41)$$

with the understanding that the imaginary part of the solution applies. The loading defined by Equations (40)–(41) will generate a system of symmetric and antisymmetric modes. By virtue of the general forms discussed in the previous section this system of wave modes may be represented by

$$u_1^A(x_1, z) = \pm i \left\{ \sum_{m=0}^{\infty} A_m^S V_S^m(z) e^{\pm i k_m^S x_1} + \sum_{m=0}^{\infty} A_m^A V_A^m(z) e^{\pm i k_m^A x_1} \right\}, \tag{42}$$

$$u_z^A(x_1, z) = \left\{ \sum_{m=0}^{\infty} A_m^S W_S^m(z) e^{\pm i k_m^S x_1} + \sum_{m=0}^{\infty} A_m^A W_A^m(z) e^{\pm i k_m^A x_1} \right\}, \tag{43}$$

where the plus and minus signs are for propagation in the positive and negative x_1-directions, that is, for $x_1 > 0$ and $x_1 < 0$, respectively. The relevant corresponding stresses are

$$\tau_{11}^A(x_1, z) = \left\{ \sum_{m=0}^{\infty} A_m^S T_{11}^{Sm}(z) e^{\pm i k_m^S x_1} + \sum_{m=0}^{\infty} A_m^A T_{11}^{Am}(z) e^{\pm i k_m^A x_1} \right\}, \tag{44}$$

$$\tau_{1z}^A(x_1, z) = \pm i \left\{ \sum_{m=0}^{\infty} A_m^S T_{1z}^{Sm}(z) e^{\pm i k_m^S x_1} + \sum_{m=0}^{\infty} A_m^A T_{1z}^{Am}(z) e^{\pm i k_m^A x_1} \right\}. \tag{45}$$

In these expressions the terms p and q are redefined as

$$p_m^2 = \frac{\omega^2}{c_L^2} - k_m^2 \quad \text{and} \quad q_m^2 = \frac{\omega^2}{c_T^2} - k_m^2. \tag{46}$$

4. Application of the reciprocity theorem

Following a method developed in [Achenbach 2003], the Lamb waves generated by acoustic emission from a surface breaking crack will be obtained by an application of the elastodynamic reciprocity theorem for time-harmonic wave motion. For a body of region V and surface S this reciprocity theorem (see [Achenbach 2003, p. 92]) may be written as

$$\int_V (f_j^A u_j^B - f_j^B u_j^A) dV = \int_S (\tau_{ij}^B u_j^A - \tau_{ij}^A u_j^B) n_i \, dS, \tag{47}$$

where n_i are the components of the outward normal to S, and f_j, u_j, and τ_{ij} are the components of body forces, displacements, and stresses. In Equation (47), the superscripts denote two elastodynamic solutions for the same body, State A and State B, where in the present application State A is the desired solution of the acoustic emission problem and State B is an auxiliary solution, or in our terminology, a virtual wave.

The coefficients A_m^S and A_m^A will be determined by application of the reciprocity theorem. For this application the contour S, shown in Figure 1 has a loop Σ around the crack. State A is the solution of the acoustic emission problem defined by Equations (42)–(45). For state B, the virtual wave, we select

the n-th symmetric mode propagating in the positive x_1-direction

$$u_1^B(x_1, z) = i B_n^S V_S^n(z) e^{i k_n^S x_1},$$ (48)

$$u_z^B(x_1, z) = B_n^S W_S^n(z) e^{i k_n^S x_1},$$ (49)

$$\tau_{11}^B(x_1, z) = B_n^S T_{11}^{Sn}(z) e^{i k_n^S x_1},$$ (50)

$$\tau_{1z}^B(x_1, z) = i B_n^S T_{1z}^{Sn}(z) e^{i k_n^S x_1}.$$ (51)

Since there are no body forces in this application of the reciprocity theorem, Equation (47) reduces to

$$\int_S (\tau_{ij}^B u_j^A - \tau_{ij}^A u_j^B) n_i \, dS = 0.$$ (52)

For the contour shown in Figure 1, there are possible contributions from the line $x_1 = a$, $-h \leq z \leq h$, which we call J_1, from $x_1 = b$, $-h \leq z \leq h$, called J_2, and from σ, the contour around the crack, called J_3. There are no contributions from the free surfaces at $z = \pm h$.

First let us consider the contribution from $x_1 = a$. Along $x_1 = a$ we have

$$J_1 = -\int_{-h}^{h} F_{AB}(x_1, z)\big|_{x_1=a} dz,$$ (53)

where

$$F_{AB} = \tau_{11}^B u_1^A + \tau_{1z}^B u_z^A - \tau_{11}^A u_1^B - \tau_{1z}^A u_z^B.$$ (54)

Substitution of the summations given by Equations (42)–(45) for State A, and the n-th virtual mode given by Equations (48)–(51) for State B, in Equation (53) yields after some manipulation

$$J_1 = \sum_{m=0}^{\infty} i A_m^S B_n^S \big[I_{mn}^S + I_{nm}^S \big] e^{i(k_m - k_n)a} + \sum_{m=0}^{\infty} i A_m^A B_n^S \big[I_{mn}^{AS} + I_{nm}^{AS} \big] e^{i(k_m - k_n)a},$$ (55)

where I_{mn}^S and I_{nm}^S are defined by Equation (37), and I_{mn}^{AS} is given by

$$I_{mn}^{AS} = \int_{-h}^{h} \big[T_{11}^{Am}(z) V_S^n(z) - T_{1z}^{An}(z) W_S^n(z) \big] dz,$$ (56)

with an analogous definition for I_{nm}^{AS}. Inspection of Equations (31), (5), (29), (6) shows that the terms in Equation (56) are

$$\mu \big[a_9 \sin(p_m z) + a_{10} \sin(q_m z) \big] \big[s_1 \cos(p_n z) + s_2 \cos(q_n z) \big]$$ (57)

and

$$\mu \big[a_5 \cos(p_n z) + a_6 \cos(q_n z) \big] \big[s_3 \sin(p_m z) + s_4 \sin(q_m z) \big].$$ (58)

These terms are of the general forms

$$\sin(\alpha z) \cos(\beta z) = \tfrac{1}{2} \big[\sin(\alpha + \beta)z + \sin(\alpha - \beta)z \big].$$

Such terms when integrated over z from $z = -h$ to $z = h$ yield zero. Hence the second summation in Equation (55) vanishes. In addition, by virtue of the results given by Equation (36), the first summation

in Equation (55) only produces a nonzero result when $n = m$. Consequently we find

$$J_1 = 2i A_m^S B_m^S I_{mm}^S. \tag{59}$$

A computation of the contribution from $x_1 = b$ leads to

$$J_2 = 0. \tag{60}$$

This is in agreement with the observation made in [Achenbach 2003, p. 101] that contributions are obtained only when States A and B are counterpropagating. Across $x_1 = b$ the two states both propagate in the positive x_1 direction.

Next we consider the contribution from the integration along Σ. Here it should be understood that the virtual wave defined as State B is for a layer without a surface-breaking crack. State B applies to a cracked layer if the faces of the crack are subjected to tractions equal to the ones that would exist in the uncracked layer for State B. This implies that for State B the displacements and the stresses are continuous across the crack faces.

In terms of the coordinate s, which increases in the counterclockwise direction, the contributions from the two line elements that make up Σ require careful consideration. Along $x_1 = 0^+$, $-h \le z \le -h + l$, where l is the length of the crack, the integration is similar to the one along $x_1 = a$, $-h \le z < h$. We obtain

$$J_3^+ = - \int_{-h}^{-h+l} F_{AB}(x_1, z)\big|_{x_1=0^+} dz. \tag{61}$$

However, along $x_1 = 0^-$, $-h \le z \le -h + l$, some more care must be exercised. We find

$$J_3^- = \int_{-h}^{-h+l} F_{AB}(x_1, z)\big|_{x_1=0^-} dz, \tag{62}$$

and thus

$$J_3 = \int_{-h}^{-h+l} \left\{ F_{AB}(x_1, z)_{x_1=0^-} - F_{AB}(x_1, z)\big|_{x_1=0^+} \right\} dz. \tag{63}$$

From the definition of $F_{AB}(x_1, z)$ it follows that the integral of Equation (63) is composed of differences of equivalent quantities on the two crack faces. It can also be noted that the crack opens up symmetrically and thus $u_1^{A+} = -u_1^{A-}$ and $u_z^{A+} = u_z^{A-}$. Also $u_1^{B+} = u_1^{B-}$ and $u_z^{B+} = u_z^{B-}$. In addition $\tau_{11}^{B+} = \tau_{11}^{B-}$, $\tau_{1z}^{B+} = \tau_{1z}^{B-}$, $\tau_{11}^{A+} = \tau_{11}^{A-}$ and $\tau_{1z}^{A-} = \tau_{1z}^{A+} = 0$. As a consequence, only the first terms in F_{AB} on both sides remain, and Equation (63) reduces to

$$J_3 = - \int_{-h}^{-h+l} \tau_{11}^B(0, z) \Delta u_1(0, z) dz, \tag{64}$$

where

$$\Delta u_1(0, z) = u_1^A(0^+, z) - u_1^A(0^-, z) = 2u_1^A(0^+, z). \tag{65}$$

The quantity Δu_1 is called the crack opening displacement (COD).

The expression for J_3 can be further simplified by substitution of $\tau_{11}^B(0, z)$ from Equation (50). The result is

$$J_3 = -B_m^S \int_{-h}^{-h+l} T_{11}^{Sm}(z) \Delta u_1(0, z) dz. \tag{66}$$

From the condition that the total contour integral must vanish, the quantity A_m^S can then by solved from $J_1 + J_2 + J_3 = 0$ and Equations (59) and (66) as

$$A_m^S = \frac{-i}{2I_{mm}^S} \int_{-h}^{-h+l} T_{11}^{Sm}(z) \Delta u_1(0, z) dz. \tag{67}$$

In Equation (65) $u_1^A(0^+, z)$ is the normal displacement on the crack faces. It should be noted that the crack-opening displacement $\Delta u_1(x_1, z)$ is, as yet, unknown.

By selecting the n-th antisymmetric mode as the virtual wave we obtain in a totally analogous manner

$$A_m^A = \frac{-i}{2I_{mm}^A} \int_{-h}^{-h+l} T_{11}^{AM}(z) \Delta u_1(0_1 z) dz. \tag{68}$$

5. Crack-opening displacement

The crack-opening displacement, Equation (65), due to loading of the crack faces by a uniform pressure, can be calculated numerically by using, for example, the boundary element method. A quasistatic approximation to the COD can, however, be computed by using a simple idea from fracture mechanics based on energy considerations.

The propagation of a crack requires a certain amount of energy, which can be calculated provided that the stress-intensity factor is known. For a surface-breaking crack of length l in a layer of thickness $2h$, uniformly loaded by uniform pressure $\Delta \tau$ on its crack faces, the stress-intensity factor is of the general form

$$K_I = \Delta \tau (\pi l)^{1/2} F(l/h). \tag{69}$$

The energy required to form this crack can be looked up in a book on fracture mechanics, for example [Kanninen and Popelar 1985], as

$$G = \int_0^l \frac{1 - v^2}{E} K_I^2 \, dl. \tag{70}$$

The energy that was provided to open the crack is

$$U = \tfrac{1}{2} \Delta \tau \int_{-h}^{-h+l} \Delta u_1(0, z) dz = \frac{1}{2} \Delta \tau \, \overline{\Delta u_1} \, l, \tag{71}$$

where

$$\overline{\Delta u_1} = \frac{1}{l} \int_{-h}^{-h+l} \Delta u_1(0, z) dz. \tag{72}$$

The integral in Equation (71) is the crack opening volume (COV). The equality of U and G yields an expression for $\overline{\Delta u_1}$ as

$$\overline{\Delta u_1} = \frac{G}{\frac{1}{2} \Delta \tau l}. \tag{73}$$

By the use of Equation (73) the expressions for A_m^S and A_m^A can now be written as

$$A_m^S = -i \frac{\overline{\Delta u}}{2I_{mm}^S} \int_{-h}^{-h+l} T_{11}^{Sm}(z)\,dz, \tag{74}$$

$$A_m^A = -i \frac{\overline{\Delta u}}{2I_{mm}^A} \int_{-h}^{-h+l} T_{11}^{Am}(z)\,dz. \tag{75}$$

Substitution in Equations (42)–(45) yields expressions whose imaginary parts are the radiated fields of acoustic emission.

6. Conclusions

The steady state solutions as given by Equations (42)–(45) are indeed obtained in a very simple manner. They represent propagating waves which appear as superpositions on the quasistatic displacement generated by the externally applied stress field.

The analogous problem for a surface-breaking crack in a half-space under cyclic loading is discussed in [Achenbach 2008].

References

[Achenbach 1973] J. D. Achenbach, *Wave propagation in elastic solids*, vol. 16, North-Holland Series in Applied Mathematics and Mechanics, North-Holland, Amsterdam, 1973.

[Achenbach 2003] J. D. Achenbach, *Reciprocity in elastodynamics*, Cambridge monographs on mechanics, Cambridge University Press, Cambridge, UK, 2003.

[Achenbach 2008] J. D. Achenbach, "Acoustic emission from a surface-breaking crack under cyclic loading", *Acta Mech.* **195**:1-4 (2008), 61–68.

[Kanninen and Popelar 1985] M. F. Kanninen and C. H. Popelar, *Advanced fracture mechanics*, vol. 15, Oxford engineering science series, Oxford University Press, New York, 1985.

JAN D. ACHENBACH: achenbach@northwestern.edu
Center for Quality Engineering and Failure Prevention, Northwestern University, 2137 N. Tech Drive, Evanston, IL 60208, United States
http://www.mech.northwestern.edu/web/people/faculty/achenbach.php

TRANSVERSE AND TORSIONAL SHEAR STRESSES IN PRISMATIC BODIES HAVING INHOMOGENEOUS MATERIAL PROPERTIES USING A NEW 2D STRESS FUNCTION

LAMPROS C. KOURTIS, HANEESH KESARI, DENNIS R. CARTER AND GARY S. BEAUPRÉ

We introduce a new formulation to concurrently calculate torsional and transverse shear stresses in prismatic beams with homogeneous or inhomogeneous material properties. This new formulation is generated using kinematic assumptions for the torsion problem and using a new stress function for the transverse shear problem that accounts for Poisson effects. The effect of gradients in material properties is captured explicitly as body forces. The results using this new formulation are compared to full three-dimensional solutions and show good agreement (l^2 error metric in the order of 10^{-4}), while both modeling and computational costs are significantly lower. The numerical implementation of this new formulation can be used to analyze stresses in arbitrary cross sections ranging from structural members (civil) to long bones (biomechanics) with either homogeneous or inhomogeneous material properties.

1. Introduction

The problem of out-of-plane shear stress calculation in cross sections of prismatic beams presents significant interest in a variety of applications ranging from structural engineering to biomechanics. Out-of-plane shear stresses are created by either torsional or transverse loads. In most cases, the two problems of torsional shear and transverse shear have been addressed separately.

In cases of simple cross sectional geometries, elementary mechanics of materials approaches to the transverse shear problem [Young and Budynas 2002; Goodier 1962] yield approximations of the stress distribution and of the maximum stress values. Depending on the application however, these approximations might underestimate the actual stresses present: for example, for a square cross section, the maximum shear stress value may be underestimated by up to 18% (for $\nu = 0.5$) while for a circular cross section the maximum shear stress value may be underestimated by up to 12% (for $\nu = 0$) [Barber 1992]. For more detailed analysis, the exact two-dimensional elasticity solution that describes the complete out-of-plane shear stress distribution is developed and applied to analytically described cross sections (such as the ellipse or the rectangle) in many classical elasticity textbooks [Barber 1992; Timoshenko and Goodier 1984; Sokolnikoff 1956].

The torsional shear problem is addressed more frequently in the literature. Many textbooks [Timoshenko and Goodier 1984; Sokolnikoff 1956] present the generalized problem under the Saint-Venant assumption and solve it for specific analytically described cross sections (such as the ellipse, rectangle). Structural engineering elements (such as I-beams) under torsion may be studied by expanding the solution of the rectangle (primitive) to each of the discrete subregions of the cross section with special considerations at the junctions where primitives meet [Goodier 1962]. Thin-walled closed sections (such

as cellular shapes) are usually studied using Bredt's formulas by adding an analogue of Kirchhoff's law for shells [Gjelsvik 1981; Timoshenko and Goodier 1984; Schulz and Filippou 1998]. Sokolnikoff [1956] discusses the inhomogeneous beam problem, for a finite number of components having different elastic properties, where additional boundary conditions are imposed at their interfaces.

The finite element method has been used to address the problem of torsion of cross sections of arbitrary shape using a two-dimensional formulation. Herrmann [1965] presented a solution to the torsion problem of homogeneous beams based on the Saint-Venant assumption and a numerical formulation using the Ritz technique. A computer implementation using the Galerkin formulation, called VA-TWIST, to analyze homogeneous, prismatic beams subjected to torsional loading was developed by [Levenston et al. 1994]. Mason and Herrmann [1968] proposed a finite element formulation to the transverse shear problem by minimizing the total potential energy of an unknown warping function across the section. An alternative formulation [Gruttmann et al. 1999] introduces a warping function for torsion and two new functions for transverse shear — one for the pure transverse shear contribution and one for the effect of Poisson's ratio due to flexure, all solved numerically using the finite element method. Reissner [1979; 1983; 1993] used the principle of minimum complementary energy to derive seven differential equations of equilibrium to determine stresses in the complex problem of axial, bending, transverse and torsional loads. However, these formulations are sometimes difficult to implement in a numerical solution [Gruttmann et al. 1999]. They also regard bodies as homogeneous, failing thus to capture inhomogeneity contributions, an important factor in biomechanics [Kourtis et al. 2008] or composite materials studies. Muskhelishvili [1963] derived the governing equations to calculate torsional stresses in beams containing different reinforcing materials; the equations can lead to closed-form or series solutions for simple geometries.

The goal of this paper is to present a new method to determine shear stresses caused by torsional and transverse shear loads on an arbitrarily-shaped prismatic body having inhomogeneous material properties. This new formulation is obtained by superimposing two relatively simple solutions, one for torsion (derived from an assumed displacement field) and one for transverse shear (derived from an assumed strain field).

Routinely, elasticity problems are reformulated by introducing stress functions. For example, in the Airy stress function formulation in plane elasticity, stresses are constructed as derivatives of an unknown function in a manner such that the equilibrium conditions are automatically satisfied; the problem then only requires solving the compatibility equations subject to the boundary conditions. The stress function itself has no obvious physical interpretation in this case. The problem can also be reformulated such that compatibility is automatically satisfied; the problem then only requires solving the equilibrium equations subject to the boundary conditions. An example of this approach is the Love strain function in the axisymmetric elasticity problem [Barber 1992]. The elasticity formulation presented in this work follows this second approach.

2. Materials and methods

A prismatic body is subjected to far-field transverse and torsional loads (Figure 1); Ω represents the cross section interior, Γ denotes the boundary of the section such that $\Omega \cap \Gamma = 0$. The x and y axes lie in-plane; the z axis defines the out-of-plane direction. At the section under examination, there exist an angular twist θ (or alternatively torsion T in cases where the center of shear coincides with the centroid) and
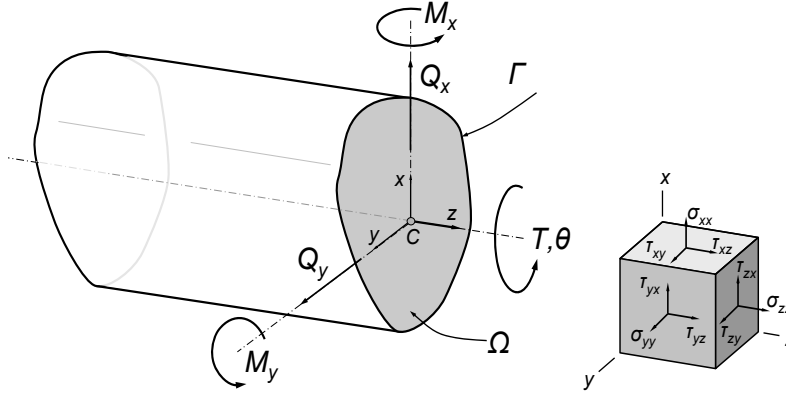
Figure 1. A prismatic beam with Cartesian coordinate system. Bending moments M_x, M_y transverse shear forces Q_x, Q_y and angular twist θ and torque T are shown at a representative cross section. Transverse shear and torsional loads create shear stresses τ_{zx} and τ_{zy}.

transverse forces Q_x and Q_y (obtained easily using the method of sections) as well as bending moments M_x and M_y.

Since the cross section has inhomogeneous material properties, the effective centroid $C : (C_x^*, C_y^*)$ is defined in both integral and finite element form as in [Carpenter et al. 2005]:

$$(C_x^*, C_y^*) = \left(\frac{\int x E(x,y) dA}{\int E(x,y) dA}, \; \frac{\int y E(x,y) dA}{\int E(x,y) dA} \right) = \left(\frac{\sum x_i A_i E_i}{\sum A_i E_i}, \; \frac{\sum y_i A_i E_i}{\sum A_i E_i} \right), \tag{1}$$

where i enumerates the elements, x_i, y_i are the element's centroid coordinates, A_i is its area and E_i its elastic modulus.

For convenience, we shift the coordinate system so the effective centroid (C_x^*, C_y^*) is at the origin:

$$(C_x^*, C_y^*) = (0, 0). \tag{2}$$

The flexural rigidities I_{xx}^*, I_{yy}^* about the axes, the generalized moment of inertia I_{xy}^* and the axial stiffness are calculated using inhomogeneous beam theory [Carpenter et al. 2005]:

$$I_{xx}^* = \int y^2 E(x,y) \, dA = \sum ((I_{xx}^e E)_i + y_i^2 A_i E_i), \tag{3}$$

$$I_{yy}^* = \int x^2 E(x,y) \, dA = \sum ((I_{yy}^e E)_i + x_i^2 A_i E_i), \tag{4}$$

$$I_{xy}^* = \int xy E(x,y) \, dA = \sum ((I_{xy}^e E)_i + x_i y_i A_i E_i), \tag{5}$$

$$A^* = \int E(x,y) \, dA = \sum A_i E_i, \tag{6}$$

where the sum runs over all elements and I_{xx}^e, I_{yy}^e, I_{xy}^e denote each element's moment of inertias about its centroid.

Transverse forces Q_x, Q_y applied to the body at a distance z from the cross section under examination cause bending stresses. Ignoring any axial forces and assuming small strains, the normal stresses in the longitudinal direction σ_{zz} are given as in [Bartel et al. 2006]:

$$\sigma_{zz} = \left(\frac{Q_x I_{xx}^* - Q_y I_{xy}^*}{I_{xx}^* I_{yy}^* - I_{xy}^{*\,2}} E_i x_i + \frac{Q_y I_{yy}^* - Q_x I_{xy}^*}{I_{xx}^* I_{yy}^* - I_{xy}^{*\,2}} E_i y_i \right) \cdot z. \tag{7}$$

The prismatic bar with the given cross section and properties under torsional and/or transverse loads is examined away from the points of load application to avoid stress concentrations. Although transverse shear and torsion can be solved separately and the stresses can then be superimposed, we developed a single formulation to address transverse shear and torsion simultaneously.

Transverse shear. Euler-Bernoulli beam theory assumes that the out-of-plane normal stress varies linearly with the distance z, but the theory neglects Poisson effects. In this section we use classical elasticity to derive the transverse shear stress distribution due to bending in a prismatic beam of arbitrary cross section and inhomogeneous material properties. For this analysis, we make the following assumptions:

- $\sigma_{xx} = \sigma_{yy} = \tau_{xy} = 0$.

- τ_{zx} , τ_{zy} are independent of z.

- The normal stress σ_{zz} varies as described in (7).

- The Poisson's ratio ν is constant across Ω.

- G, E are arbitrary spatial functions of x, y, at least piecewise continuous across Ω.

For notational convenience, we introduce

$$\alpha = \frac{Q_x I_{xx}^* - Q_y I_{xy}^*}{I_{xx}^* I_{yy}^* - I_{xy}^{*\,2}} \qquad \text{and} \qquad \beta = \frac{Q_y I_{yy}^* - Q_x I_{xy}^*}{I_{xx}^* I_{yy}^* - I_{xy}^{*\,2}}, \tag{8}$$

so (7) becomes

$$\sigma_{zz} = [\alpha \cdot x \cdot E(x,y) + \beta \cdot y \cdot E(x,y)] \cdot z. \tag{9}$$

The assumptions above on stress imply the following constraints on strain from linear elasticity:

$$\varepsilon_{xx} = -\frac{\nu}{E(x,y)} \sigma_{zz}, \quad \varepsilon_{yy} = -\frac{\nu}{E(x,y)} \sigma_{zz}, \quad \varepsilon_{zz} = -\frac{1}{E(x,y)} \sigma_{zz}, \quad \gamma_{xy} = 0. \tag{10}$$

The form of γ_{zx} and γ_{zy} is still unknown. However from the assumptions we know that γ_{zx} and γ_{zy} are not functions of z. Therefore:

$$\gamma_{zx} = \frac{\tau_{zx}}{G(x,y)} \qquad \text{and} \qquad \gamma_{zy} = \frac{\tau_{zy}}{G(x,y)}. \tag{11}$$

Further information about the form of γ_{zx} and γ_{zy} can be found using the compatibility conditions. We therefore assume the following form for γ_{zx} and γ_{zy} that satisfies compatibility:

$$\gamma_{zx} = \phi_{,x} - 2\beta\nu xy, \quad \gamma_{zy} = \phi_{,y} - 2\alpha\nu xy, \tag{12}$$

where a subscript variable after a comma indicates partial differentiation with respect to that variable. The unknown function $\phi = \phi(x,y)$ is C^2 continuous in Ω.

It is easy to see that the six compatibility relations (13) are satisfied either identically (left column and first equality on second column), or due to the definition of shear strain in (12):

$$\varepsilon_{xx,yy} + \varepsilon_{yy,xx} = \gamma_{xy,xy}, \qquad 2\varepsilon_{zz,xy} = \gamma_{yz,xz} + \gamma_{xz,yz} - \gamma_{xy,zz},$$
$$\varepsilon_{yy,zz} + \varepsilon_{zz,yy} = \gamma_{yz,yz}, \qquad 2\varepsilon_{xx,yz} = -\gamma_{yz,xx} + \gamma_{xz,xy} + \gamma_{xy,xz}, \qquad (13)$$
$$\varepsilon_{xx,zz} + \varepsilon_{zz,xx} = \gamma_{xz,xz}, \qquad 2\varepsilon_{yy,xz} = \gamma_{yz,xy} - \gamma_{xz,yy} + \gamma_{xy,yz}.$$

From (11) and (12) we obtain the following form for transverse shear stresses due to bending:

$$\tau_{zx} = G(x, y)(\phi_{,x} - 2\beta v x y), \qquad \tau_{zy} = G(x, y)(\phi_{,y} - 2a v x y). \qquad (14)$$

Equation (14) will be used later in the development of the strong form of the problem. Having provided a form for the transverse shear using a stress function, we proceed to find a form for the torsional shear using kinematic assumptions. We then superimpose the two to satisfy equilibrium.

Torsional shear. In this section we derive the torsional shear stress distribution in a beam of arbitrary cross section and inhomogeneous material properties due to torsion based on kinematic relations (Saint-Venant) for a presumed displacement field and for small deformations.

For this analysis, the following assumptions are made:

- $\sigma_{xx} = \sigma_{yy} = \sigma_{zz} = \tau_{xy} = 0$.

- τ_{zx}, τ_{zy} are independent of z.

- G is an arbitrary spatial function of x, y, at least piecewise continuous across Ω.

Using similar notation as in the previous section, the in-plane torsional displacements u_x, u_y vary linearly with the distance from the centroid of the cross section (C_x^*, C_y^*) and are given by:

$$u_x = -\theta \cdot y \cdot z, \qquad u_y = \theta \cdot x \cdot z, \qquad (15)$$

where θ is the linear angle of twist.

Torsion is assumed to occur around the effective centroid of the cross section; the same relations hold for off-centroid torsion cases by replacing (C_x^*, C_y^*) with the center of rotation (C_x, C_y).

A function ψ, called the warping function, is chosen such that the out-of-plane displacements u_z caused by torsion are given by

$$u_z = \theta \cdot \psi(x, y). \qquad (16)$$

Since we assume a displacement field, the compatibility equations are automatically satisfied. From (16) we derive a relation for the torsional shear strains:

$$\gamma_{xz} = u_{z,x} + u_{x,z}, \qquad \gamma_{yz} = u_{z,y} + u_{y,z}. \qquad (17)$$

Assuming linear isotropic or transverse isotropic elastic material properties, substituting (15) and (16) in (17), and employing the constitutive relations we obtain

$$\tau_{xz} = G(x, y)\theta(\psi_{,x} - y), \qquad \tau_{yz} = G(x, y)\theta(\psi_{,y} + x). \qquad (18)$$

Governing relations and boundary conditions. The equations for equilibrium can be written in compact notation as $\sigma_{ij,j} = 0$. The two equilibrium relations in x and y directions are identically satisfied due to the nature of the assumptions. The third equilibrium equation yields

$$\sigma_{zz,z} + \tau_{zx,x} + \tau_{zy,y} = 0. \tag{19}$$

Invoking linear superposition we combine expressions (18) and (14), for the stresses arising respectively from torsion and transverse shear, with (19), obtaining

$$E(\alpha x + \beta y) + (G(\theta \psi_{,x} - \theta y + \phi_{,x} - 2\beta \nu xy))_{,x} + (G(\theta \psi_{,y} + \theta x + \phi_{,y} - 2\alpha \nu xy)) = 0, \tag{20}$$

where G, E are given functions of x, y. It is useful to combine the two unknown functions ψ, ϕ by setting

$$\Xi \overset{\text{def}}{=} \theta \psi + \phi. \tag{21}$$

The scalar function ψ, due to the nature of the kinematic assumptions, can be interpreted as a measure of the out of plane deformations (u_z), and is called the warping function; the scalar function φ, however, lends itself to no such physical interpretation.

Simplifying the preceding expression yields the governing equation for the combined transverse shear and torsional shear problem:

$$(G\Xi_{,x})_{,x} + (G\Xi_{,y})_{,y} = 2\nu xy(\beta G_{,x} + \alpha G_{,y}) - (E - 2G\nu)(\alpha x + \beta y) + \theta(G_{,x}y - G_{,y}x) = f(x, y). \tag{22}$$

Note that for an isotropic elastic solid, E can be replaced by

$$E = 2(1 + \nu)G. \tag{23}$$

The boundary conditions are obtained by imposing zero traction at the boundaries Γ:

$$\tau_{zx} \cdot n_x + \tau_{zy} \cdot n_y = 0 \quad \text{on } \Gamma, \tag{24}$$

where $\boldsymbol{n}$ is the normal vector to the boundary Γ. Combining the stresses arising from the torsion (18) and the transverse shear (14) in (24), and recalling (21), we obtain

$$G(\Xi_{,i}n_i) = G\big((\theta y + 2\beta \nu xy)n_x - (\theta x - 2\alpha \nu xy)n_y\big) \quad \text{on } \Gamma. \tag{25}$$

Using (22) and (25), the strong form of the shear problem becomes:

Given α, β, θ and functions $G(x, y)$ and $E(x, y)$, find $\Xi \in C^2$ such that

$$\begin{aligned} (G\Xi_{,i})_{,i} &= f(x, y) \text{ on } \Omega, \\ G\Xi_{,i}n_i &= Gt_in_i \quad \text{on } \Gamma, \end{aligned} \tag{26}$$

where

$$f(x, y) = 2\nu xy(\beta G_{,x} + \alpha G_{,y}) - (E - 2G\nu)(\alpha x + \beta y) + \theta(G_{,x}y - G_{,y}x), \quad \boldsymbol{t} = \begin{bmatrix} \theta y + 2\beta \nu xy \\ -\theta x + 2\alpha \nu xy \end{bmatrix}. \tag{27}$$

The function $f(x, y)$ can be thought of as body force and $\boldsymbol{t}$ can be thought of as a traction vector. The importance of the material property gradient terms $G_{,x}$ and $G_{,y}$ in the expression of $f(x, y)$ will be discussed later.

Finite element approximation. Based on the strong form definition of the problem just given, we introduce the trial function space

$$\Upsilon = \{w \mid w \in \mathcal{H}^1 \text{ on } \Omega\},$$

which provides the weak form as

$$\int_\Omega w\big(G\Xi_{,ii} + G_{,i}\Xi_{,i} - f(x,y)\big)\, d\Omega = 0 \quad \text{for all } (x,y) \in \Omega, \tag{28}$$

$$\int_\Omega w(G\Xi_{,i})_i\, d\Omega = \int_\Omega w f(x,y)\, d\Omega. \tag{29}$$

Integrating by parts and using the divergence theorem we get

$$\int_\Gamma (wG\Xi_{,i})n_i\, d\Gamma - \int_\Omega w_{,i}G\Xi_i\, d\Omega = \int_\Omega w f(x,y)\, d\Omega. \tag{30}$$

After incorporating the boundary conditions we obtain the weak form of the problem:

Given a, β, θ and functions $G(x,y)$ and $E(x,y)$, find $\Xi \in \Upsilon$ such that

$$\int_\Omega w_{,i}G\Xi_{,i}\, d\Omega = \int_\Gamma wGt_i n_i\, d\Gamma - \int_\Omega w f(x,y)\, d\Omega, \tag{31}$$

where $f(x,y)$ and $\mathbf{t}$ are as in (27).

Introducing the finite element function space and element shape functions [Hughes 2000] we have

$$k_{ab}^e = \int_{\Omega^e} N_{a,i}^e G^e N_{b,i}^e\, d\Omega^e, \tag{32}$$

where a and b range over the nodes and superscript e refers to the element space; G^e is the shear modulus assigned to the element. Moreover

$$f_a^e = (f_a^f)^e + (f_a^g)^e, \qquad \text{with} \quad (f_a^f)^e = -\int_{\Omega^e} N_a^e f(x,y)\, d\Omega^e, \quad (f_a^g)^e = \int_{\Gamma^e} N_a^e G t_i n_i\, d\Gamma^e.$$

Note that $(f_a^f)^e$ can be easily computed using Gauss quadrature. The gradients of the shear modulus can be calculated using the shape function derivatives:

$$G_{,x} = \int N_{a,x} G_a\, d\Omega, \qquad G_{,y} = \int N_{a,y} G_a\, d\Omega^e, \tag{33}$$

where G_a, the shear modulus for node a, can be taken as the average of the shear modulus values G^e of the elements sharing that node.

The shear stresses are calculated from (14), (18) and (21) as

$$\tau_{zx} = G(x,y)(\Xi_{,x} - 2\beta v x y - \theta y), \qquad \tau_{zy} = G(x,y)(\Xi_{,y} - 2\alpha v x y + \theta x). \tag{34}$$

The torque, T, corresponding to the given angular twist θ can be calculated by integrating over the element stress contributions weighted linearly by their distance from the centroid:

$$T = \int_\Omega (x\tau_{zy} - y\tau_{zx})\, d\Omega, \tag{35}$$

or by substituting the stresses from (34) and, since $\phi = 0$ (no transverse shear), by replacing $\Xi = \theta \psi$ from (21):

$$T = \int_\Omega G(x, y)(x \, \Xi_{,y} - y \, \Xi_{,x}) \, d\Omega. \tag{36}$$

The integral term in (35) and (36) is called the torsional rigidity and is denoted by K^*. Note that (36) provides the net torque T supported by the prismatic beam when it is subjected to an angular twist about its effective centroid.

The numerical implementation of this formulation can be downloaded from https://simtk.org/home/va-batts.

3. Results

Validation examples. In the case of torsionless bending of a homogeneous body having an idealized geometry (circle or rectangle), the new formulation in (26)–(27) reduces to the relations provided in [Timoshenko and Goodier 1984], and a numerical comparison has been provided [Kourtis et al. 2008]. Similarly, in the case of pure torsion of a homogeneous body having those geometries, the new formulation reduces to the relations provided in [Barber 1992]. In addition, we numerically compared the solution to several problems of torsionless bending of homogeneous bodies having arbitrary geometries provided in [Gruttmann et al. 1999] to the solutions obtained using the new formulation, obtaining excellent agreement (results not shown).

Several representative cross sectional geometries are presented and analyzed in this section. We provide a verification of the new formulation by comparison to the three-dimensional elasticity solution, for the homogeneous and inhomogeneous material property cases. Comparison of the 2D model using the new formulation to a 3D elasticity model is the only way to validate models having arbitrary cross sections and inhomogeneous material properties; in addition, the 3D model is generated by extruding the 2D mesh conveniently guaranteeing correspondence between node and integration point locations.

Example 1 (Homogeneous elliptic beam). A solid elliptical beam subjected to transverse loads and to torsion was analyzed using the new formulation and the results compared to the three-dimensional solution. The axis lengths were taken as $a = 100$ mm and $b = 60$ mm, and the elastic modulus as 1 MPa. The cross section was meshed using 924 quadrilateral 4-node elements. The predicted shear stresses τ from the new formulation were compared to the three-dimensional solution, τ_{3D} (Figure 2). The three-dimensional solution was found using an extruded model, that was composed of 19,404 elements, analyzed with ABAQUS. The number of element layers in the out-of-plane (extruded) direction was chosen in order to maintain an element aspect ratio of less than 10 to 1. The l^2 error metric

$$l^2 = \sqrt{\frac{(\tau - \tau_{3D})^2}{\tau_{3D}^2}} \tag{37}$$

was found to be 3.25×10^{-4}.

Example 2 (Homogeneous I-beam). A standard structural member, the steel I-beam, was subjected to torsional and transverse shear loads, in the form of an about-the-centroid torsional displacement (angle of twist) and a vertical transverse load. The dimensions of the cross section are given in Figure 3.
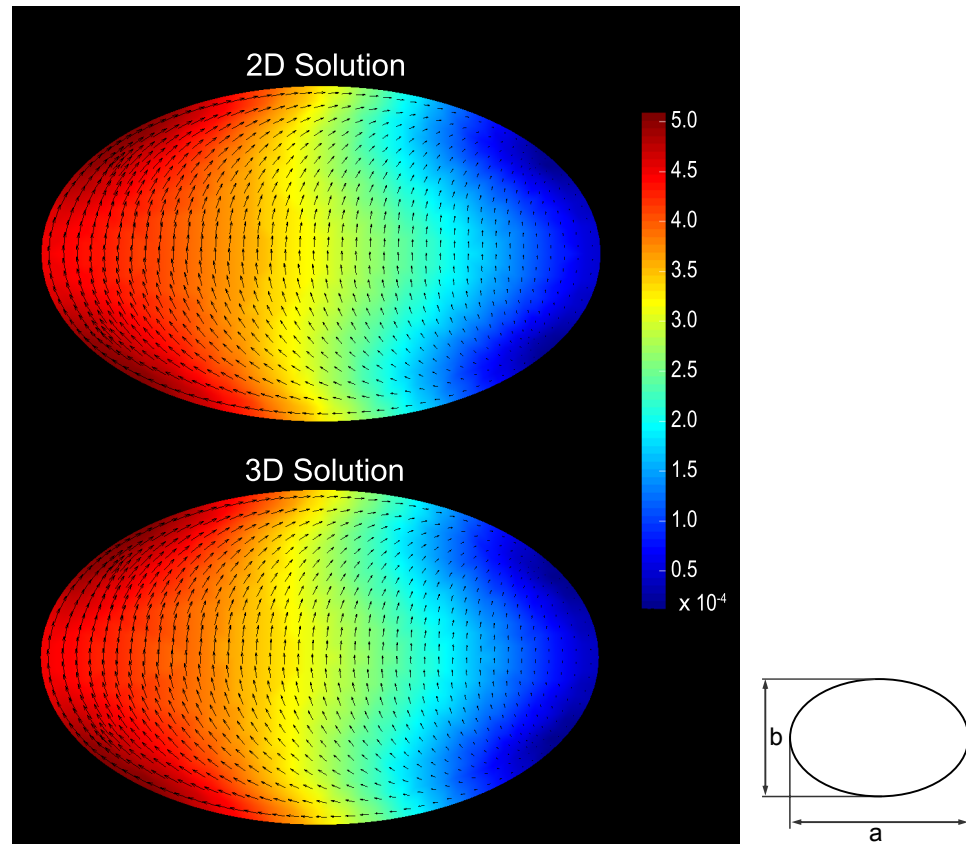
Figure 2. Validation example 1: A homogeneous beam with an elliptic cross section (axis lengths $a = 100$ mm and $b = 60$ mm), with an elastic modulus $E = 1$ MPa, is subjected to a transverse force of 1 N acting in the vertical direction and applied through the centroid, combined with an applied angular twist of 3.5×10^{-7} degree/mm. The resulting shear stresses [MPa] demonstrate minimal stress on the right side and maximum stress on the left side; the transverse shear stresses are either decreased or increased by the torsional shear stresses. Top: solution obtained with the new two-dimensional implementation (1,954 DOF). Bottom: representative cross section of the solution obtained with a full, three-dimensional finite element analysis (61,551 DOF). The l^2 error metric is 3.25×10^{-4}.

Since analytical solutions for this cross section are only approximations of the elasticity solution, a full three-dimensional model was created and analyzed. The cross section was meshed using 946 linear quadrilateral 4-node elements and stresses were calculated using the proposed formulation. The same two-dimensional mesh was extruded, yielding 23 element layers to produce a three-dimensional prismatic beam composed of 21,758 linear 8-node hex elements, 2.5 times longer than the height of the I-beam. As in Example 1, the number of element layers in the out-of-plane direction was chosen in order to maintain an element aspect ratio of less than 10 to 1. The boundary conditions were applied to the prism by fully
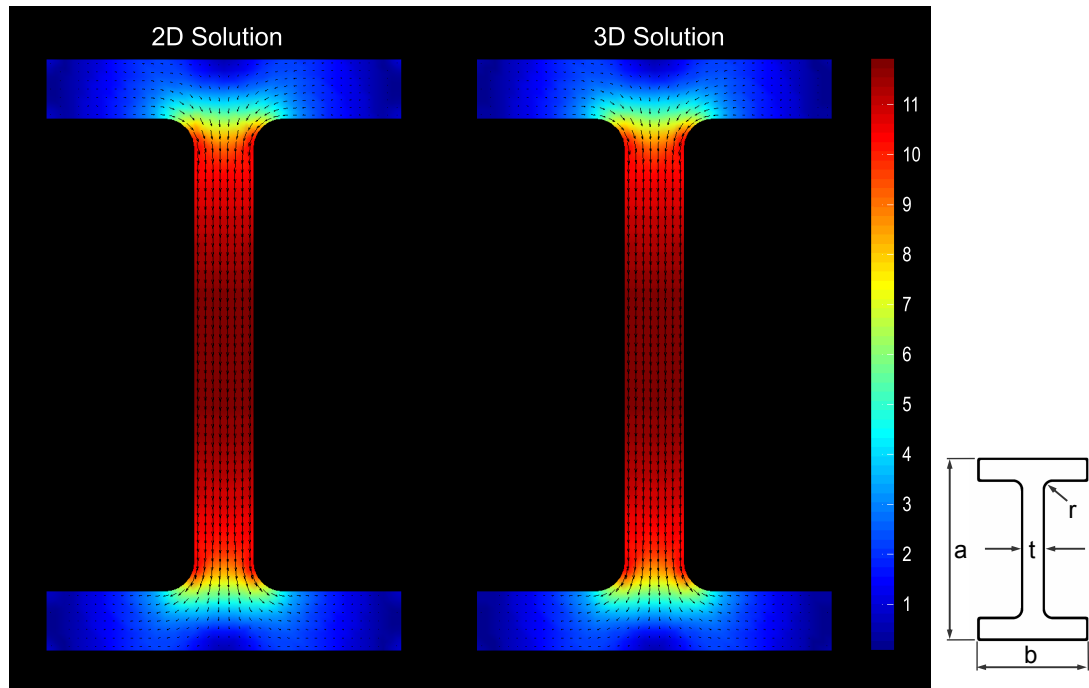
Figure 3. Validation example 2: A homogeneous I-beam ($a = 100$ mm, $b = 60$ mm, $t = 10$ mm, $r = 5$ mm) with elastic modulus 100 MPa is subjected to a transverse force of 100 N acting in the vertical direction and applied through the centroid. No torsion or twist is applied. The resulting shear stresses (MPa) are shown for the new two-dimensional implementation (left; 2,166 DOF) and for the full, three-dimensional finite element analysis (right; 74,727 DOF). l^2 error metric: 7.72×10^{-4}.

constraining the nodes of one end and by tying [ABAQUS 2002] the nodes of the other end to a reference point, which was then subjected to the transverse force and the angular twist. Stresses calculated using the two-dimensional model were compared to the three-dimensional solution (Figure 3). The location for comparison within the three-dimensional model was chosen so as not to be influenced by any stress concentrations associated with the imposed boundary conditions. In this case, the l^2 error metric was found to be 7.72×10^{-4}. One source of error using the proposed two-dimensional formulation is the poor definition of the normals at the corner elements, which causes artifacts.

Example 3 (Inhomogeneous rectangle: steel reinforced concrete beam). A solid rectangular beam, subjected to a transverse force and to a torsional twist around its centroid, was analyzed using the new formulation. The results were then compared to the three-dimensional solution. The dimensions of the beam and the rebar elements and the magnitudes of the applied loads are given in Figure 4. Steel was modeled to be 7 times stiffer than concrete [Hendy and Johnson 2006]. No-slip conditions were assumed between the steel rebar and the concrete. The cross section was meshed using 2,507 linear quadrilateral 4-node elements. As in the I-beam example, the two-dimensional mesh was extruded to produce a three-dimensional prismatic beam composed of 67,689 linear 8-node hex elements and the boundary conditions
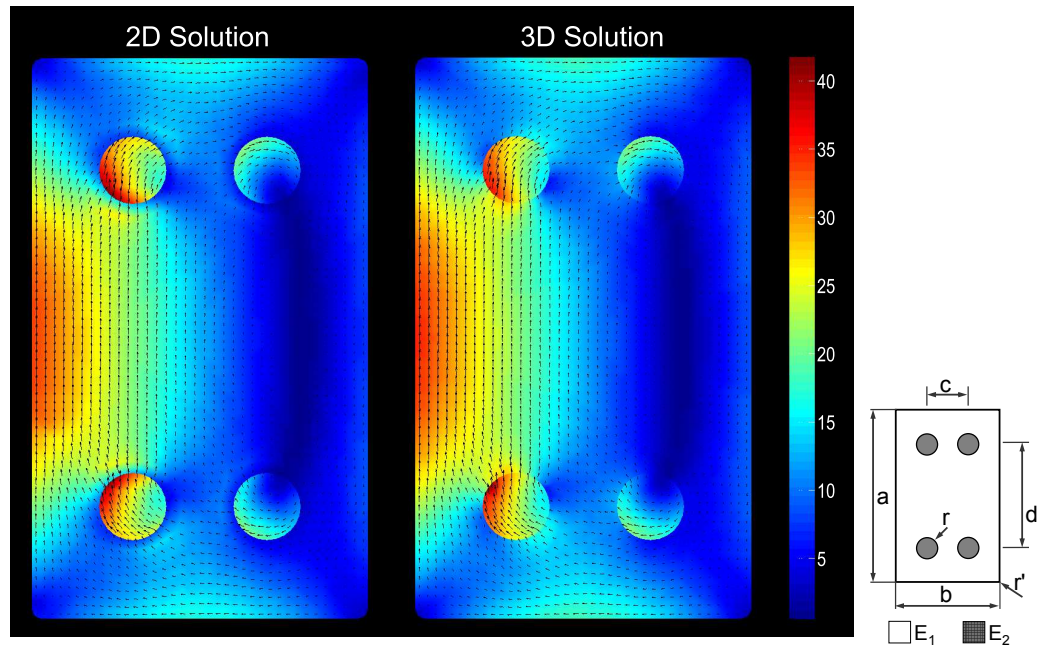
Figure 4. Validation example 3: A rectangular beam made of concrete containing rebar (the four circles), with dimensions $a = 100$ mm, $b = 60$ mm, $c = 30$ mm, $d = 50$ mm, $r = 6$ mm, $r' = 1$ mm, is subjected to 50 kN of transverse force applied in the vertical direction through the centroid along with 3.5×10^{-7} degree/mm of angular twist about its centroid. The rebar material ($E_2 = 200{,}000$ MPa) is approximately seven times stiffer than the concrete material ($E_1 = 29{,}000$ MPa). The plot shows the shear stresses in the two materials, along with the shear stress direction. The resulting shear stresses [MPa] are shown both for the new two-dimensional implementation (left; 5,220 DOF) and for the full, three-dimensional finite element analysis (right; 211,410 DOF). l^2 error metric: 8.31×10^{-3}.

were applied respectively. The stress calculated using the proposed formulation is in good agreement with that derived from the three-dimensional model (Figure 4), with an l^2 error metric of 8.31×10^{-3}.

Application example: Inhomogeneous cross section of a bone instrumented with a cemented prosthesis. We next considered an example involving a complex biomechanical application: a hip replacement in which a metallic stem is inserted into the intramedullary canal of the femur and orthopaedic cement fills the remaining space. Bone is by nature a highly inhomogeneous material; its density and its elastic modulus vary from site to site. Using well established methods, tomographic X-ray images can provide information on the local bone density and hence the elastic modulus at each location within the cross section. After creating the finite element mesh to represent the bone cross section, each element was assigned an individual set of material properties corresponding to the local (element) image properties [Kourtis et al. 2008]. The longitudinal elastic modulus, $E(x, y)$, was found to range from 2,000 MPa to 17,500 MPa throughout the cross section. The shear modulus of the bone was then calculated according to
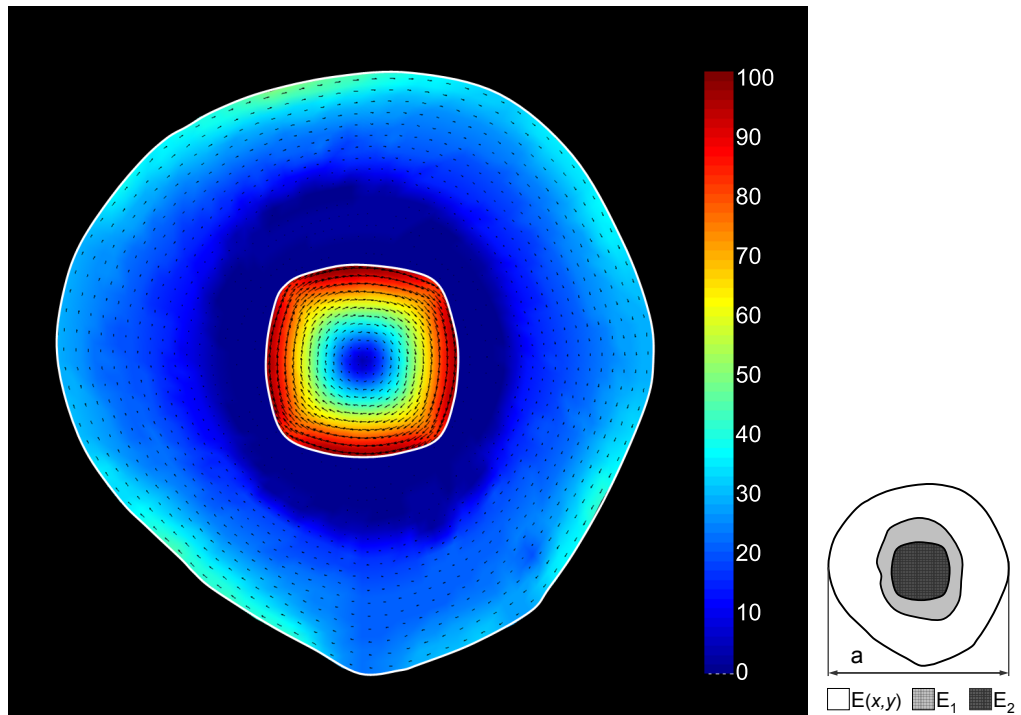
Figure 5. Stresses (MPa) are shown for a model consisting of the shaft of the femur ($a \sim 23$ mm) with a titanium alloy prosthesis cemented within the intramedullary cavity. The applied torsional and transverse shear loads were estimated for stair ascent. The maximum shear stress within the bone was 52.64 MPa whereas the maximum shear stress within the implant was 98.23 MPa. The highest PMMA cement shear stress close to the metal implant was 2.17 MPa.

the relation $G = 0.19E$ introduced in [Reilly and Burstein 1975]. An implant made of titanium Ti6Al4V alloy (elastic modulus $E_2 = 114{,}000$ MPa) was assumed to be inserted in the intramedullary canal, and orthopedic cement (PMMA) with elastic modulus $E_1 = 2{,}350$ MPa [Williams and Johnson 1989] fills the remaining space between the bone and the implant. The model was subjected to torsional and peak transverse loads ($F_{\text{M}-\text{L}} = 0.59$ BW, $F_{\text{A}-\text{P}} = 0.61$ BW, $T_z = 2.24$ BW m, where BW $= 80$ kg is the body weight), corresponding to a stair climbing load case obtained from biomechanical studies [Bergmann et al. 2001]. The problem was then solved using the new two-dimensional formulation (Figure 5). Since this is a closed section that is approximately axisymmetric, we made the assumption that the center of shear coincides with the effective centroid of the cross section [Tapley and Poston 1990]. The analysis showed that the maximum shear stress within the bone was 52.64 MPa, while the maximum shear stress within the implant was 98.23 MPa. Stresses in the PMMA cement were significantly lower, and went up to 2.17 MPa near the metal implant interface. Studies have shown that the metal-cement interface shear stress limit depends on the surface treatment (roughness) of the implant; for a grit-blasted metal surface the interface shear stress limit is reported in the order of 7.8–8.61 MPa [Müller and Schürmann 1999].

4. Discussion

The mathematical method presented in this article provides a straightforward means of accurately calculating torsional and transverse shear stresses of a prismatic beam having inhomogeneous material properties, and at low computational cost since no three-dimensional solution is needed. As seen from the results, comparison to the "gold standard" three-dimensional solutions, shows extremely low l^2 error metrics. Depending on the needs, the new formulation can be either used to calculate pure torsional shear, or pure transverse shear or combination thereof. The new formulation can also be used to analyze beams with either homogeneous or inhomogeneous material properties.

Amongst other features, this formulation provides a chance to explore "torqueless" twisting during which a beam will twist even though it is only subjected to transverse loads. This may occur because of the geometry and/or inhomogeneity of the beam as well as the direction and location of the applied transverse load. Torqueless twisting will occur if transverse forces are not applied through the center of shear. In addition, a beam only subjected to an angular twist about an axis other than the center of shear will undergo bending as if it were loaded by a transverse load. However, in closed solid sections, such as the ones examined in this study, the center of shear is very close to the effective centroid [Tapley and Poston 1990], therefore the assumption made in the torque calculation section that they coincide.

It is interesting to take a closer look at the terms in the strong form of the problem, Equations (26)–(27), and quantify their contribution to the overall result. The function $f(x, y)$ right-hand side of the domain equation has three terms: the first and last represent the effects of the gradients of material properties on the calculation of shear stresses created by the transverse load and the angular displacement, respectively. In the transverse shear case, this gradient term is "activated" as a result of a Poisson effect. The Poisson effect is also responsible for the second term in the boundary condition equation; without this, the transverse shear stress distribution would vary in one direction only. In order to quantify the importance of these terms we examined the case of an inhomogeneous square beam containing an insert that is one-third as stiff as the rest of the beam. We calculated stresses using (26)–(27) and then recalculated stresses after omitting the material property gradient terms (Figure 6). A qualitative inspection of the plots indicates that both the absolute values of the stress as well as the stress distribution are affected by the presence of these terms. More specifically, the highest stress for the torsion problem differed by -7.7% while for the transverse shear problem the difference was -4.1%. These differences are expected to be even larger for larger mismatches between the various properties of the beam; for example, if the shear moduli of the two materials in this example had a tenfold difference, the maximum stresses would differ by -10.5% and -5.9% for the torsion and the transverse shear problems, respectively.

One of the limitations of the new formulation is that unlike the elastic and shear moduli (E, G) that are spatial functions across the domain Ω, Poisson's ratio remains constant. Still, using this formulation, one could vary Poisson's ratio for each element according to some spatial function and obtain approximate results; however (26) does not include terms that correspond to the spatial gradient of the Poisson's ratio. Another limitation of the formulation is that it can only be used with isotropic or transverse isotropic materials; anisotropic and orthotropic material models inherently cannot be described by this two-dimensional approach.

The new formulation offers an easier and faster method to determine shear stresses compared with a full, three-dimensional approach. In terms of computational cost, in order to maintain the same element
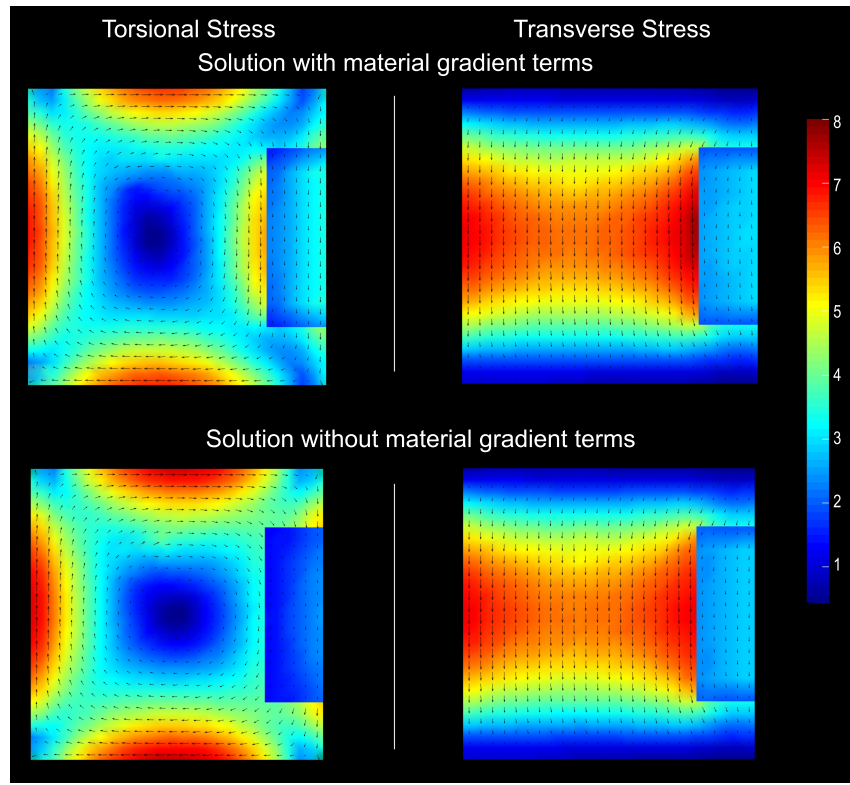
Figure 6. Importance of the material property gradient terms in Equations (26)–(27). A square beam with an insert (right), one-third as stiff. Left: torsional stresses [MPa]. The absolute stress values are different and the overall distribution changes with the incorporation of the material property gradient terms. Right: transverse stresses [MPa]. Here there is less difference between the solutions with and without the shear modulus spatial gradient terms, but the latter solution underestimates shear stresses.

aspect ratio, it can be shown that the number of three-dimensional elements must increase as the number of two-dimensional elements raised to the 1.5 power. In addition, the three-dimensional elements would have an extra degree of freedom for each node, again rendering the two-dimensional solution more attractive (see comparison of degrees of freedom for the 2D and 3D cases in captions of Figures 1–3). Especially in cases where multiple analysis are needed, such as in plasticity or fatigue studies, the computational cost benefit of the two-dimensional approach can be substantial. Second, a three-dimensional model requires an extrusion meshing step after the original two-dimensional mesh creation, which along with the material properties assignment can prove time consuming. Most commercial software meshing packages do not offer the option of "inheriting" material properties from a two-dimensional parent mesh to its three-dimensional extruded mesh. In addition, coupling the torsion and the transverse shear problems into one, further decreases the computational requirements. Also, the application of boundary conditions in a three-dimensional model is not always trivial, as for example at least one end may need to be constrained relative to a reference point to which the actual displacements or loads are applied.

Acknowledgments

References

[ABAQUS 2002] *ABAQUS theory manual*, Hibbitt, Karlsson and Sorensen, Inc., Providence, RI, 2002.

[Barber 1992] J. R. Barber, *Elasticity*, Kluwer, Dordrecht, 1992.

[Bartel et al. 2006] D. L. Bartel, D. T. Davy, and T. M. Keaveny, *Orthopaedic biomechanics: mechanics and design in musculoskeletal systems*, 1st ed., Pearson/Prentice Hall, Upper Saddle River, NJ, 2006.

[Bergmann et al. 2001] G. Bergmann, G. Deuretzbacher, M. Heller, F. Graichen, A. Rohlmann, J. Strauss, and G. N. Duda, "Hip contact forces and gait patterns from routine activities", *J. Biomech.* **34**:7 (2001), 859–871.

[Carpenter et al. 2005] R. D. Carpenter, G. S. Beaupré, T. F. Lang, E. S. Orwoll, and D. R. Carter, "New QCT analysis approach shows the importance of fall orientation on femoral neck strength", *J. Bone Miner. Res.* **20**:9 (2005), 1533–1542.

[Gjelsvik 1981] A. Gjelsvik, *The theory of thin walled bars*, Wiley, New York, 1981.

[Goodier 1962] J. N. Goodier, "Torsion", pp. 1–27 in *Handbook of engineering mechanics*, edited by W. Flugge, McGraw-Hill, New York, 1962.

[Gruttmann et al. 1999] F. Gruttmann, R. Sauer, and W. Wagner, "Shear stresses in prismatic beams with arbitrary cross-sections", *Int. J. Numer. Methods Eng.* **45**:7 (1999), 865–889.

[Hendy and Johnson 2006] C. R. Hendy and R. P. Johnson, *Designers' guide to EN 1994-2: Eurocode 4: design of composite steel and concrete structures*, Thomas Telford, London, 2006.

[Herrmann 1965] L. R. Herrmann, "Elastic torsional analysis of irregular shapes", *J. Eng. Mech.* (*ASCE*) **91**:6 (1965), 11–19.

[Hughes 2000] T. J. R. Hughes, *The finite element method: linear static and dynamic finite element analysis*, Dover, Mineola, NY, 2000. Pages 60–70.

[Kourtis et al. 2008] L. C. Kourtis, D. R. Carter, H. Kesari, and G. S. Beaupré, "A new software tool (VA-BATTS) to calculate bending, axial, torsional and transverse shear stresses within bone cross sections having inhomogeneous material properties", *Comput. Methods Biomech. Biomed. Engin.* **11**:5 (2008), 463–476.

[Levenston et al. 1994] M. E. Levenston, G. S. Beaupré, and M. C. van der Meulen, "Improved method for analysis of whole bone torsion tests", *J. Bone Miner. Res.* **9**:9 (1994), 1459–1465.

[Mason and Herrmann 1968] W. E. Mason and L. R. Herrmann, "Elastic shear analysis of general prismatic beams", *J. Eng. Mech.* (*ASCE*) **94**:4 (1968), 965–983.

[Müller and Schürmann 1999] R. T. Müller and N. Schürmann, "Shear strength of the cement metal interface: an experimental study", *Arch. Orthop. Trauma Surg.* **119**:3–4 (1999), 133–138.

[Muskhelishvili 1963] N. I. Muskhelishvili, *Some basic problems of the mathematical theory of elasticity: fundamental equations, plane theory of elasticity, torsion, and bending*, Noordhoff, Groningen, 1963.

[Reilly and Burstein 1975] D. T. Reilly and A. H. Burstein, "The elastic and ultimate properties of compact bone tissue", *J. Biomech.* **8**:6 (1975), 393–405.

[Reissner 1979] E. Reissner, "Some considerations on the problem of torsion and flexure of prismatical beams", *Int. J. Solids Struct.* **15**:1 (1979), 41–53.

[Reissner 1983] E. Reissner, "Further considerations on the problem of torsion and flexure of prismatical beams", *Int. J. Solids Struct.* **19**:5 (1983), 385–392.

[Reissner 1993] E. Reissner, "A note on the problem of flexure of prismatical beams", *Int. J. Solids Struct.* **30**:4 (1993), 455–462.

[Schulz and Filippou 1998] M. Schulz and F. C. Filippou, "Generalized warping torsion formulation", *J. Eng. Mech.* (*ASCE*) **124**:3 (1998), 339–347.

[Sokolnikoff 1956] I. S. Sokolnikoff, *Mathematical theory of elasticity*, McGraw-Hill, New York, 1956. Pages 91–248.

[Tapley and Poston 1990] B. D. Tapley and T. R. Poston (editors), *Eshbach's handbook of engineering fundamentals*, 4th ed., Wiley-Interscience, New York, 1990. Pages 4–26.

[Timoshenko and Goodier 1984] S. Timoshenko and J. N. Goodier, *Theory of elasticity*, 3rd ed., McGraw-Hill, New York, 1984. Pages 258–313.

[Williams and Johnson 1989] J. L. Williams and W. J. H. Johnson, "Elastic constants of composites formed from PMMA bone cement and anisotropic bovine tibial cancellous bone", *J. Biomech.* **22**:6–7 (1989), 673–682.

[Young and Budynas 2002] W. C. Young and R. G. Budynas, *Roark's formulas for stress and strain*, 7th ed., McGraw-Hill, New York, 2002. Pages 129 and 401.

LAMPROS C. KOURTIS: kourtis@stanford.edu
Bone and Joint Center of Excellence, VA Palo Alto Health Care System, Palo Alto, CA 94304, United States

and

Biomechanical Engineering Division, 496 Lomita Mall, Room 226, Stanford University, Stanford, CA 94305, United States

HANEESH KESARI: haneesh@stanford.edu
Mechanics and Computation Division, Department of Mechanical Engineering, 496 Lomita Mall, Stanford University, Stanford, CA 94305, United States

DENNIS R. CARTER: dcarter@stanford.edu
Bone and Joint Center of Excellence, VA Palo Alto Health Care System, Palo Alto, CA 94304, United States

and

Biomechanical Engineering Division, 496 Lomita Mall, Room 226, Stanford University, Stanford, CA 94305, United States

GARY S. BEAUPRÉ: beaupre@va51.stanford.edu
Bone and Joint Center of Excellence, VA Palo Alto Health Care System, Palo Alto, CA 94304, United States

and

Biomechanical Engineering Division, 496 Lomita Mall, Room 226, Stanford University, Stanford, CA 94305, United States

VIBRATION CHARACTERISTICS OF CURVED BEAMS

CHONG-SEOK CHANG AND DEWEY H. HODGES

The paper presents a concise framework studying the coupled vibration of curved beams, whether the curvature is built-in or is caused by loading. The governing equations used are both geometrically exact and fully intrinsic, with a maximum degree of nonlinearity equal to two. For beams with initial curvature, the equations of motion are linearized about the reference state. For beams that are curved because of the loading, the equations of motion are linearized about the equilibrium state. A central difference spatial discretization scheme is applied, and the resulting linearized ordinary differential equations are cast as an eigenvalue problem. Numerical examples are presented, including: (1) validation of the analysis for both in-plane and out-of-plane vibration by comparison with published results, and (2) presentation of results for vibration of curved beams with free-free, clamped-clamped, and pinned-pinned boundary conditions. For coupled vibration, the numerical results also exhibit the low-frequency mode transition or veering phenomenon. Substantial differences are also shown between the natural frequencies of curved beams and straight beams, and between initially curved and bent beams with the same geometry.

1. Introduction

For decades, the vibration of curved beams, rings, and arches has been extensively investigated by many researchers. About 400 references, which have covered the in-plane (i.e. in the plane of the undeformed, initially curved beam), out-of-plane (i.e. out of the plane of the undeformed, initially curved beam), coupled, and nonlinear vibrations, are summarized in [Chidamparam and Leissa 1993]. While linear theory is adequate for free-vibration analysis of initially curved beams, when a beam is brought into a state of high curvature by the loads acting on it, one must linearize the equations of nonlinear theory about the static equilibrium state. Thus, the behavior of a beam curved under load will differ substantially from an initially curved beam of identical geometry. The geometrically exact, fully intrinsic theory of curved and twisted beams [Hodges 2003] provides an excellent framework in which to elegantly study the coupled vibration characteristics of curved beams, particularly those curved because they are loaded. This is because of their simplicity. Each term can be intuitively interpreted. There are no displacement or rotation variables (which is what is meant by intrinsic in this context); as a result there are no nonlinearities of degree larger than two. Both finite element and finite difference discretization schemes are easily applied to these equations for numerical computations, and the framework presented herein is much simpler than that of other nonlinear beam theories. Because of these observations, we have revisited the topic and broadened the base of cases studied.

This paper provides details of how to make use of the fully intrinsic equations for calculating natural frequencies for simple engineering problems. One aspect of these calculations that is substantially different from the usual approach involves the proper way to enforce boundary conditions. Published results

for in-plane [Chidamparam and Leissa 1995; Tarnopolskaya et al. 1996; Fung 2004] and out-of-plane vibration [Irie et al. 1982; Howson and Jemah 1999] will be compared with the results from the present work. Results for coupled vibration are also presented as part of an investigation of low-frequency mode transition [Tarnopolskaya et al. 1999], also referred to as veering phenomena [Chen and Ginsberg 1992].

It was shown analytically in [Hodges 1999] that initially curved, isotropic beams possess stretch-bending elastic coupling, that this coupling is proportional to initial curvature when the beam reference line is along the locus of cross-sectional centroids, and that this coupling cannot be ignored for calculation of the equilibrium state of high circular arches. The Variational Asymptotic Beam Sectional (VABS) analysis [Cesnik and Hodges 1997; Yu et al. 2002; Hodges 2006] can be used to numerically calculate this coupling term. Based on results obtained from VABS, it is easy to show that there is another term, which also depends on initial curvature but reflects shear-torsion coupling. This term becomes zero if the beam reference axis is along the locus of sectional shear centers rather than the locus of sectional centroids. The location of the sectional shear center depends on the initial curvature, but an analytical expression for that dependence is unknown. Therefore, without a cross-sectional analysis tool such as VABS, which provides an accurate cross-sectional stiffness matrix as a function of initial curvature, certain aspects of the analysis presented herein would be impossible.

2. Intrinsic beam formulation

The geometrically exact, intrinsic governing equations [Hodges 2003] for the dynamics of an initially curved and twisted, generally anisotropic beam are

$$
\begin{aligned}
F'_B + \widetilde{K}_B F_B + f_B &= \dot{P}_B + \widetilde{\Omega}_B P_B, \\
M'_B + \widetilde{K}_B M_B + (\tilde{e}_1 + \tilde{\gamma}) F_B + m_B &= \dot{H}_B + \widetilde{\Omega}_B H_B + \widetilde{V}_B P_B, \\
V'_B + \widetilde{K}_B V_B + (\tilde{e}_1 + \tilde{\gamma}) \Omega_B &= \dot{\gamma}, \\
\Omega'_B + \widetilde{K}_B \Omega_B &= \dot{\kappa},
\end{aligned}
\tag{1}
$$

where F_B and M_B are the internal force and moment measures, P_B and H_B are the sectional linear and angular momenta, V_B and Ω_B are the velocity and angular velocity measures, γ and κ are the force and moment strain measures, k contains the initial twist and curvature measures of the beam, $K_B = k + \kappa$ contains the total curvature measures, and f_B and m_B are external force and moment measures, where loads such as gravitational, aerodynamic, and mechanical applied loads are taken into account. All quantities are expressed in the basis of the deformed beam cross-sectional frame except k which is in the basis of the undeformed beam cross-sectional frame. The tilde operator as in $\tilde{a}b$ reflects a matrix form of the cross product of vectors $\mathbf{a} \times \mathbf{b}$ when both vectors and their cross product are all expressed in a common basis.

A central difference discretization scheme is applied to the intrinsic governing equations in space to obtain a numerical solution. The scheme satisfies both of the space-time conservation laws derived in [Hodges 2003]. This scheme can be viewed as equivalent to a particular finite element discretization, and the intrinsic governing equations are expressed as element and nodal equations. The n-th element

equations, which are a spatially discretized form of (1), are

$$\frac{\widehat{F}_l^{n+1} - \widehat{F}_r^n}{dl} + (\widetilde{\overline{\kappa}}^n + \widetilde{k}^n)\overline{F}^n + \overline{f}^n - \dot{\overline{P}}^n - \widetilde{\overline{\Omega}}^n \overline{P}^n = 0,$$

$$\frac{\widehat{M}_l^{n+1} - \widehat{M}_r^n}{dl} + (\widetilde{\overline{\kappa}}^n + \widetilde{k}^n)\overline{M}^n + (\widetilde{e}_1 + \widetilde{\overline{\gamma}}^n)\overline{F}^n + \overline{m}^n - \dot{\overline{H}}^n - \widetilde{\overline{\Omega}}^n \overline{H}^n - \widetilde{\overline{V}}^n \overline{P}^n = 0,$$

$$\frac{\widehat{V}_l^{n+1} - \widehat{V}_r^n}{dl} + (\widetilde{\overline{\kappa}}^n + \widetilde{k}^n)\overline{V}^n + (\widetilde{e}_1 + \widetilde{\overline{\gamma}}^n)\overline{\Omega}^n - \dot{\overline{\gamma}}^n = 0,$$

$$\frac{\widehat{\Omega}_l^{n+1} - \widehat{\Omega}_r^n}{dl} + (\widetilde{\overline{\kappa}}^n + \widetilde{k}^n)\overline{\Omega}^n - \dot{\overline{\kappa}}^n = 0,$$

(2)

where dl is the element length. The variables with $\widehat{(\ )}$ are nodal variables, and the superscript indicates the corresponding node where the variable is defined. Nodal variables are defined at both the left and right of nodes, which are indicated by subscript l and r. The variables with $\overline{(\ )}$ are element variables. (The details of discretization are described in [Hodges 2003].)

The equations for node n need to include possible discontinuities caused by a nodal mass, a nodal force, and slope discontinuity, so that

$$\widehat{F}_r^n - \widehat{C}_{lr}^{n^T}\widehat{F}_l^n + \widehat{f}^n - \dot{\widehat{P}}_r^n - \widetilde{\widehat{\Omega}}_r^n \widehat{P}_r^n = 0,$$

$$\widehat{M}_r^n - \widehat{C}_{lr}^{n^T}\widehat{M}_l^n + \widehat{m}^n - \dot{\widehat{H}}_r^n - \widetilde{\widehat{\Omega}}_r^n \widehat{H}_r^n - \widetilde{\widehat{V}}_r^n \widehat{P}_r^n = 0,$$

(3)

where $\widehat{C}_{lr}$ reflects the slope discontinuity, $\widehat{f}^n$ and $\widehat{m}^n$ are external forces and moments applied at n-th node, and

$$\widehat{V}_l^n = \widehat{C}_{lr}^n \widehat{V}_r^n, \qquad \widehat{\Omega}_l^n = \widehat{C}_{lr}^n \widehat{\Omega}_r^n. \tag{4}$$

One may also include gravitational force in the analysis. When this is done, the formulation needs additional gravity equations, details of which may be found in [Patil and Hodges 2006].

3. Boundary conditions

Boundary conditions are needed to complete the formulation. Here, we describe boundary conditions for simple engineering problems, such as pinned-pinned and clamped-clamped conditions. At each end, for the static case, either natural boundary conditions in terms of $\widehat{F}$ and $\widehat{M}$ or geometric boundary conditions in terms of u and C^{iB} may be prescribed. Here u is a column matrix of displacement measures u_i in the cross-sectional frame of the undeformed beam. Although these geometric boundary conditions are in terms of displacement and rotation variables, they are easily expressed in terms of other variables such as κ, γ, etc., given in (13), keeping the formulation intrinsic.

If displacement and rotation variables appear in the boundary conditions for the free-vibration case, a numerical Jacobian would become necessary since determination of an analytical expression for it is intractable. Fortunately, when calculating free-vibration frequencies, one may for convenience replace boundary conditions on displacement and rotation variables with boundary conditions in terms of generalized velocities $\widehat{V}$ and $\widehat{\Omega}$. With the use of velocity boundary conditions, however, rigid-body modes will not be eliminated from the results.

3.1. *Pinned-pinned boundary conditions.* A total of 12 boundary conditions is necessary to calculate free-vibration frequencies, given by

$$\widehat{V}_l^1 = \widehat{M}_l^1 = 0, \tag{5}$$

$$\widehat{V}_r^{N+1} = 0 \quad \text{or} \quad \begin{cases} e_1^T C^{iB^{N+1}} \widehat{F}_r^{N+1} = 0, \\ e_2^T \widehat{V}_r^{N+1} = 0, \\ e_3^T C^{iB^{N+1}} \widehat{V}_r^{N+1} = 0, \end{cases} \tag{6}$$

$$\widehat{M}_r^{N+1} = 0, \tag{7}$$

where $C^{iB^{N+1}}$ is the rotation matrix of the beam cross-section at the right end. Equation (5) fixes the left boundary in space but leaves it free to rotate about all three axes. One can apply a geometric boundary condition of zero displacement at the left end. One may take advantage of the intrinsic formulation through applying the velocity boundary condition given in (5). The right boundary condition of (6) allows free movement in the axial direction while holding velocity components in the transverse directions to zero, as shown in the right part of Figure 1. When there are no applied loads, one can simply make use of trivial values as the state about which the equations are linearized.
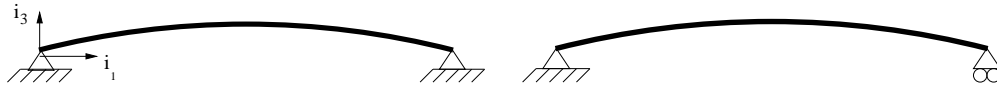
Figure 1. Schematics of initially curved beams with pinned-pinned boundary conditions.

For a loaded case, however, the state about which the equations are linearized should be the static equilibrium state. To determine the static equilibrium, six boundary conditions are necessary. (For static equilibrium, the equations for V and Ω, namely $(2)_3$ and $(2)_4$, become trivial. That reduces the number of boundary conditions to 6 from 12.) They are given by $\widehat{M}_l^1 = 0$ and

$$u_1^{N+1} = 0 \quad \text{or} \quad e_1^T C^{iB^{N+1}} \widehat{F}_r^{N+1} = 0, \tag{8}$$
$$u_2^{N+1} = u_3^{N+1} = 0.$$

The right end can be chosen either free to move in the axial direction or to be fixed in space, which is described in (8). For static equilibrium, one must apply displacement boundary conditions, which appear in (8).

3.2. *Clamped-clamped boundary conditions.* The boundary conditions are

$$\widehat{V}_l^1 = \widehat{\Omega}_l^1 = 0 \tag{9}$$

Figure 2. Initially curved beam with clamped-clamped boundary condition.

and

$$\widehat{V}_r^{N+1} = \widehat{\Omega}_r^{N+1} = 0 \tag{10}$$

Equations (9) and (10) are for boundaries that are fixed in space and which constrain the rotation about all three axes to be zero.

Like the pinned-pinned boundary condition, for a loaded case, the boundary conditions for a static equilibrium are

$$u_{\text{def}}^{N+1} = 0, \tag{11}$$

$$\widehat{C}_{\text{undef}}^{i B^{N+1}{}^T} \widehat{C}_{\text{def}}^{i B^{N+1}} = \Delta, \tag{12}$$

where u_{def} is the column matrix of displacement measures at the right end of the beam, and $\widehat{C}_{\text{def}}^{i B^{N+1}}$, $\widehat{C}_{\text{undef}}^{i B^{N+1}}$ are the rotation matrices of the beam cross-section at the right end after deformation and in the undeformed state, respectively.

The geometric boundary conditions for static equilibrium can be described by the generalized strain-displacement equations from [Hodges 2003], namely

$$(r + u)' = C^{iB}(\gamma + e_1), \qquad C^{Bi'} = -(\widetilde{\kappa} + \widetilde{k})C^{Bi}, \tag{13}$$

where r is the column matrix of position vector measures and u is the column matrix of displacement measures, both in the undeformed beam cross-sectional basis, and C^{Bi} is the rotation matrix of the beam cross-sectional reference frame in the deformed configuration. Equations (13) can be discretized as

$$r^{n+1} + u^{n+1} = r^n + u^n + \overline{C}^{i B^n}(\overline{\gamma}^n + e_1)dl$$
$$\widehat{C}^{Bi^{n+1}} = \left(\frac{\Delta}{dl} + \frac{\widetilde{\overline{\kappa}} + \widetilde{k}^n}{2}\right)^{-1}\left(\frac{\Delta}{dl} - \frac{\widetilde{\overline{\kappa}} + \widetilde{k}^n}{2}\right)\widehat{C}^{Bi^n} \tag{14}$$

4. Linearization

The governing equations in the previous section are linearized about a static equilibrium so that they reduce to an eigenvalue problem to calculate the vibration frequencies. First,

$$X = X_{\text{eq}} + X^*(t) \tag{15}$$

where X is a state, X_{eq} is a value of the state at a static equilibrium, and X^* is a small perturbation about the static value of the state. The linearized element equations from the intrinsic beam formulation are then

$$\frac{\widehat{F}_l^{*n+1} - \widehat{F}_r^{*n}}{dl} + (\widetilde{\overline{\kappa}}_{\text{eq}}^n + \widetilde{k}^n)\overline{F}^{*n} + \widetilde{\overline{\kappa}}^{*n}\overline{F}_{\text{eq}}^n + \mu^n \overline{g}^{*n} = \dot{\overline{P}}^{*n},$$

$$\frac{\widehat{M}_l^{*n+1} - \widehat{M}_r^{*n}}{dl} + (\widetilde{\overline{\kappa}}_{\text{eq}}^n + \widetilde{k}^n)\overline{M}^{*n} + \widetilde{\overline{\kappa}}^{*n}\overline{M}_{\text{eq}}^n + (\widetilde{e}_1 + \widetilde{\overline{\gamma}}_{\text{eq}}^n)\overline{F}^{*n} + \widetilde{\overline{\gamma}}^{*n}\overline{F}_{\text{eq}}^n + \mu^n \widetilde{\xi}^n \overline{g}^{*n} = \dot{\overline{H}}^{*n},$$

$$\frac{\widehat{V}_l^{*n+1} - \widehat{V}_r^{*n}}{dl} + (\widetilde{\overline{\kappa}}_{\text{eq}}^n + \widetilde{k}^n)\overline{V}^{*n} + (\widetilde{e}_1 + \widetilde{\overline{\gamma}}_{\text{eq}}^n)\overline{\Omega}^{*n} = \dot{\overline{\gamma}}^{*n},$$

$$\frac{\widehat{\Omega}_l^{*n+1} - \widehat{\Omega}_r^{*n}}{dl} + (\widetilde{\overline{\kappa}}_{\text{eq}}^n + \widetilde{k}^n)\overline{\Omega}^{*n} = \dot{\overline{\kappa}}^{*n}. \tag{16}$$

The linearized nodal equations are

$$\widehat{F}_r^{*n} - \widehat{C}_{lr}^{n^T} \widehat{F}_l^{*n} + \widehat{\mu}^n \widehat{g}_r^{*n} - \dot{\widehat{P}}_r^{*n} = 0, \qquad \widehat{M}_r^{*n} - \widehat{C}_{lr}^{n^T} \widehat{M}_l^{*n} + \widehat{\mu}^n \widetilde{\widehat{\xi}}^n \widehat{g}_r^{*n} - \dot{\widehat{H}}_r^{*n} = 0. \qquad (17)$$

These linearized equations of motion can be expressed in matrix form as $A\dot{\widehat{X}} = B\widehat{X}$, which is a system of first-order equations. When $\widehat{X} = \check{X} \exp(\lambda t)$ is assumed, the system is easily cast as a generalized eigenvalue problem of the form

$$B\check{X} = A\lambda\check{X}. \qquad (18)$$

When B^{-1} exists, the equation can be rearranged into a standard eigenvalue problem, such that

$$\frac{1}{\lambda}\check{X} = B^{-1}A\check{X}, \qquad A^*\check{X} = \lambda^*\check{X}. \qquad (19)$$

When the eigenvalues are pure imaginary, the motion is of simple harmonic type.

5. Validation

A typical cross-sectional model has the form

$$\begin{Bmatrix} \gamma_{11} \\ 2\gamma_{12} \\ 2\gamma_{13} \\ \kappa_1 \\ \kappa_2 \\ \kappa_3 \end{Bmatrix} = \begin{bmatrix} R_{11} & R_{12} & R_{13} & S_{11} & S_{12} & S_{13} \\ R_{12} & R_{22} & R_{23} & S_{21} & S_{22} & S_{23} \\ R_{13} & R_{23} & R_{33} & S_{31} & S_{32} & S_{33} \\ S_{11} & S_{21} & S_{31} & T_{11} & T_{12} & T_{13} \\ S_{12} & S_{22} & S_{32} & T_{12} & T_{22} & T_{23} \\ S_{13} & S_{23} & S_{33} & T_{13} & T_{23} & T_{33} \end{bmatrix} \begin{Bmatrix} F_1 \\ F_2 \\ F_3 \\ M_1 \\ M_2 \\ M_3 \end{Bmatrix}, \qquad \begin{Bmatrix} \gamma \\ \kappa \end{Bmatrix} = \begin{bmatrix} R_{3\times3} & S_{3\times3} \\ S_{3\times3}^T & T_{3\times3} \end{bmatrix} \begin{Bmatrix} F \\ M \end{Bmatrix}, \qquad (20)$$

where the 3×3 submatrices R, S, and T, which make up the cross-sectional flexibility matrix, are computed by VABS [Cesnik and Hodges 1997; Yu et al. 2002; Hodges 2006] for various initial curvatures. Though not essential, to make the shear-torsion elastic couplings $S_{21} = S_{31} = 0$, the stiffness matrix may be recomputed at the cross-sectional shear center.

In-plane and out-of-plane vibrations are separately validated by comparison with results from various published papers. Either in-plane or out-of-plane vibration can be approximated by setting some of the components in the submatrices equal to very small values, which minimally affects the results. For example, for inextensibility, one would simply set R_{11} to a very small value; for shear indeformability one would set R_{22} and R_{33} to very small values. Likewise, one could set certain elements of the flexibility matrix equal to very small values to approximate either in-plane or out-of-plane vibrations. Setting these small numbers equal to zero may result in the problem's becoming ill-conditioned because, for certain boundary conditions, a variable cannot be assumed to be zero unless the associated governing equations and variables are eliminated from the formulation. For the same reason, one should not set certain components too small for a given boundary condition.

Example: in-plane free-vibration of curved beams with different half-angles. The beam investigated has length $\ell = 10$ m and an initial curvature such that $hk_2 = h/R_r = 0.01$ where ℓ is the total length of beam, h is the thickness of the cross-section, $R_r = 1/k_2$ is the radius of the curved beam (or arch), and α is the half-angle of the arch ($\ell = 2R_r\alpha$). For beams of constant length, α is clearly a measure of the initial curvature. Values associated with $\alpha = 10°$ and $30°$ are selectively given in Table 1. For $h/R_r = 0.01$ and

$\ell = 10$ m, the nondimensional frequencies of an arch having a rectangular cross-section are calculated for both pinned-pinned and clamped-clamped boundary conditions. Results obtained are given in Tables 2 and 3. For the pinned-pinned boundary, both ends are fixed in space but free to rotate about an axis perpendicular to the plane of the undeformed beam, which is the left case of Figure 1. The results agree well with those of [Chidamparam and Leissa 1995] for both extensible and inextensible cases.

| | Example 1: in-plane | | | |
| | extensible | | inextensible | |
α	10°	30°	10°	30°
R_{11}	1.7407e-10	1.5667e-09	1.7407e-15	1.5667e-14
R_{22}	5.7624e-15	5.1862e-14	5.7624e-15	5.1862e-14
R_{33}	5.7623e-15	5.1861e-14	5.7623e-15	5.1861e-14
S_{12}	1.4477e-11	3.9088e-10	1.4477e-16	3.9088e-15
S_{21}	1.7517e-19	4.6425e-18	1.7517e-19	4.6425e-18
T_{11}	4.1277e-13	3.3435e-11	4.1277e-13	3.3435e-11
T_{22}	2.5451e-08	2.0616e-06	2.5451e-08	2.0616e-06
T_{33}	2.5451e-13	2.0616e-11	2.5451e-13	2.0616e-11
R_r	28.648	9.5493	28.648	9.5493
$h = b$	2.8648e-01	9.5493e-02	2.8648e-01	9.5493e-02
ξ_3	2.5092e-04	8.3638e-05	2.5092e-04	8.3638e-05

| | Example 2: out-of-plane | | | | | |
| | $\sigma_2 = \sigma_3 = 20$ | | | $\sigma_2 = \sigma_3 = 100$ | | |
α	30°	60°	90°	30°	60°	90°
R_{11}	2.1039e-11	8.4156e-11	1.8935e-10	5.2235e-10	2.0894e-09	4.7012e-09
R_{22}	6.9672e-11	2.7869e-10	6.2705e-10	1.7292e-09	6.9166e-09	1.5563e-08
R_{33}	6.9327e-16	2.7731e-15	6.2394e-15	1.7289e-14	6.9153e-14	1.5560e-13
S_{12}	1.0467e-16	8.3736e-16	2.8260e-15	2.6082e-15	2.0864e-14	7.0451e-14
S_{21}	3.9071e-14	3.1195e-13	1.0694e-12	3.6632e-14	3.2723e-13	−4.2443e-12
T_{11}	5.8829e-10	9.4127e-09	4.7652e-08	3.7136e-07	5.9415e-06	3.0081e-05
T_{22}	3.6587e-15	5.8539e-14	2.9635e-13	2.2905e-12	3.6646e-11	1.8553e-10
T_{33}	3.6465e-10	5.8344e-09	2.9537e-08	2.2902e-07	3.6642e-06	1.8551e-05
R_r	4.7746	2.3873	1.5915	4.7746	2.3873	1.5915
$h = b$	8.2699e-01	4.1349e-01	2.7566e-01	1.6539e-01	8.2699e-02	5.5133e-02
ξ_3	1.2655e-02	6.3274e-03	4.2183e-03	5.0199e-04	2.5100e-04	1.6733e-04

Table 1. Nonzero cross-sectional constants used for validation of in-plane and out-of plane free-vibration results (flexibility submatrices R_{ij}, S_{ij}, T_{ij}, radius of curvature R_r, thickness of cross-section h, width of cross-section b, shear center location ξ_3)

| | extensible case | | | | | | | |
| | [Chidamparam and Leissa 1995] | | | | Current approach | | | |
α	mode 1	mode 2	mode 3	mode 4	mode 1	mode 2	mode 3	mode 4
5°	449.38	1293.4	2916.1	5179.0	448.26	1293.9	2917.8	5185.3
10°	318.10	321.49	736.39	1293.5	317.77	321.60	736.59	1294.7
20°	78.552	167.74	321.48	331.25	78.580	167.91	321.85	331.15
30°	33.623	74.838	141.56	216.39	33.636	74.897	141.72	216.79
40°	17.963	41.425	78.631	122.18	17.969	41.455	78.720	122.40
	inextensible case							
	[Chidamparam and Leissa 1995]				Current approach			
α	mode 1	mode 2	mode 3	mode 4	mode 1	mode 2	mode 3	mode 4
5°	1293.5	2765.6	5181.5	7957.4	1293.9	2766.5	5186.9	7962.1
10°	321.51	690.04	1293.5	1987.9	321.60	690.43	1294.9	1991.1
20°	78.558	171.15	321.53	495.61	78.579	171.26	321.87	496.41
30°	33.626	75.080	141.58	219.26	33.635	75.125	141.73	219.61
40°	17.964	41.467	78.641	122.54	17.969	41.492	78.724	122.74

Table 2. Nondimensional free-vibration frequencies $\lambda = \omega R_r^2 \sqrt{m/EI}$ of pinned-pinned circular arches.

In Table 2, the dominant types of motion are identified for each mode. For $\alpha = 5°$ and $10°$ for the extensible case, the dominant motion in modes 1–4 are first symmetric bending, first antisymmetric bending, second symmetric bending, and second antisymmetric bending motions, respectively. For both the extensible case with $\alpha \geq 20°$ and the inextensible case, the dominant types of motion in modes 1–4 are first antisymmetric bending, second symmetric bending, second antisymmetric bending motions, and third symmetric bending, respectively. Only the extensible cases have unique frequencies of 448.26 and 317.77 for mode 1, which are identified as first symmetric bending modes.

The following discussion explains further about what contributes to the disappearance of the first symmetric bending for both extensible case with $\alpha \geq 20°$ and inextensible case. First, consider the free-vibration frequencies of $\alpha \geq 20°$ for both extensible and inextensible cases. Note that both frequencies are close to each other, especially as α increases. This is because of the low-frequency mode transition. By holding the beam's total length constant, a beam with a larger α has higher initial curvature. Because of this high initial curvature, the frequencies of certain modes change from one value to another while simultaneously the corresponding dominant type of motion for that mode is changing. (The next section has a more detailed explanation for this phenomenon.) Second, the first symmetric bending will be coupled strongly to the stretching mode. This explains why the mode is absent when the beam is inextensible.

The convergence of numerical solutions for a circular arch with $\alpha = 20°$ is tested as the number of elements increases. Figure 3 shows that the four lowest frequencies decrease monotonically as the number of elements increases. The relative difference between the results of $N = 80$ and 160 is less than 1%, and all the results presented here are for $N = 160$ elements.

	extensible case							
	[Chidamparam and Leissa 1995]				Current approach			
α	mode 1	mode 2	mode 3	mode 4	mode 1	mode 2	mode 3	mode 4
5°	788.17	2021.7	3969.3	6226.8	788.34	2022.8	3972.3	6226.5
10°	388.56	503.49	999.44	1636.6	338.60	503.72	1000.3	1638.8
20°	123.96	209.32	338.91	406.99	124.02	209.45	339.03	407.54
30°	53.735	98.426	179.31	250.07	53.760	98.505	179.56	250.47
40°	29.215	55.020	99.680	145.38	29.228	55.066	99.818	145.67
	inextensible case							
	[Chidamparam and Leissa 1995]				Current approach			
α	mode 1	mode 2	mode 3	mode 4	mode 1	mode 2	mode 3	mode 4
5°	2021.9	3641.9	6557.9	9500.9	2022.8	3635.4	6566.8	9466.0
10°	503.54	909.14	1637.2	2373.7	503.76	909.86	1639.4	2378.4
20°	123.97	225.96	407.11	592.01	124.03	226.14	407.65	593.16
30°	53.740	99.458	179.36	262.06	53.762	99.536	179.60	262.57
40°	29.217	55.194	99.705	146.58	29.230	55.238	99.837	146.87

Table 3. Nondimensional free-vibration frequencies $\lambda = \omega R_r^2 \sqrt{m/EI}$ of clamped-clamped circular arches.
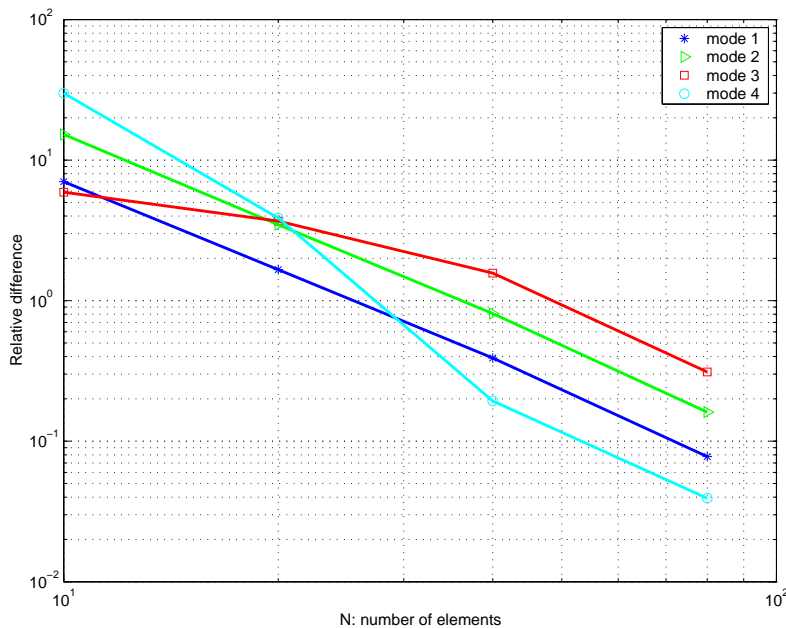
Figure 3. Relative differences of nondimensional free-vibration frequencies $\lambda = \omega R_r^2 \sqrt{m/EI}$ for $N = 10, 20, 40$, and 80 with respect to $N = 160$ of pinned-pinned circular arches with $\alpha = 20°$.

| | $\sigma_2 = \sigma_3 = 20$ | | | | | | | | | | | |
| | [Irie et al. 1982] | | | | [Howson and Jemah 1999] | | | | present | | | |
α	m1	m2	m3	m4	m1	m2	m3	m4	m1	m2	m3	m4
30°	16.74	36.92*	40.45	69.92	16.743	36.921*	40.449	69.618	16.579	36.398	40.232	68.711
60°	4.282	11.69	22.05*	22.38	4.2836	11.768	22.045*	22.379	4.2606	11.644	21.875*	22.329
90°	1.776	4.982	10.13	16.76	1.7764	4.9814	10.133	16.762	1.7687	4.9584	10.111	16.778

| | $\sigma_2 = \sigma_3 = 100$ | | | | | | | | | | | |
| | [Irie et al. 1982] | | | | [Howson and Jemah 1999] | | | | present | | | |
α	m1	m2	m3	m4	m1	m2	m3	m4	m1	m2	m3	m4
30°	19.40	54.03	105.6	172.8	19.401	54.029	105.65	172.77	19.385	54.049	105.88	173.52
60°	4.451	12.83	25.99	43.57	4.4512	12.826	25.988	43.570	4.4444	12.810	25.990	43.630
90°	1.804	5.198	10.92	18.72	1.8042	5.1975	10.917	18.725	1.7998	5.1857	10.905	18.727

Table 4. Nondimensional free-vibration frequencies $\lambda = \omega R_r^2 \sqrt{m/(EI)_3}$ of clamped-clamped circular arches (∗ represents modes in which torsion is dominant; m1 stands for mode 1, etc.)

Example: out-of-plane free-vibration of a curved beam with different half-angles. The out-of-plane free-vibration frequencies of a clamped-clamped arch with square cross-section are shown in Table 4 for two different slenderness ratios ($\sigma_2 = \sigma_3 = 20$ and 100). The slenderness ratio $\sigma_2^2 = AR_r^2/I_2$ is expressed in terms of the cross-sectional area A, the radius of curvature R_r, and the second moment of area I_2; similar relations apply to σ_3. The beam length is 5 m. The out-of-plane free-vibration frequencies are shown in Table 4 with the ones from [Irie et al. 1982; Howson and Jemah 1999] and they are very close to each other. The material properties and cross-sectional constants for each case are listed in Table 1. It should be noted that these results include shear deformation and rotary inertia; particularly for smaller values of σ_2 and σ_3, results are more accurate when these phenomena are included in the calculations. The present results are based on section constants from VABS, values of which may differ slightly from the approximations used in [Irie et al. 1982; Howson and Jemah 1999].

6. Coupled free-vibration frequencies for initially curved beams

In this section the coupled free-vibration characteristics of beams with various values of initial curvature k_2 are examined. No external forces and moments are applied to beams. The free-vibration frequencies of beams with free-free, clamped-clamped, and pinned-pinned boundary conditions are shown in Figure 4 and Table 5 for various values of initial curvature k_2. The length of the beam is 10 m; the width and height are 0.1 m. The material properties are taken to be those of aluminum: $E = 7 \times 10^{10}$ N/m^2, $G = 2.55 \times 10^{10}$ N/m^2, and $\rho = 2700$ kg/m^3.

The eight lowest-frequency modes of beams with various levels of initial curvature are identified, and the frequencies are plotted in Figure 4 and given in Table 5. For the cases of low initial curvatures, modes 1, 2, 3, 4, ..., correspond to the modes for which the dominant motions are first symmetric out-of-plane
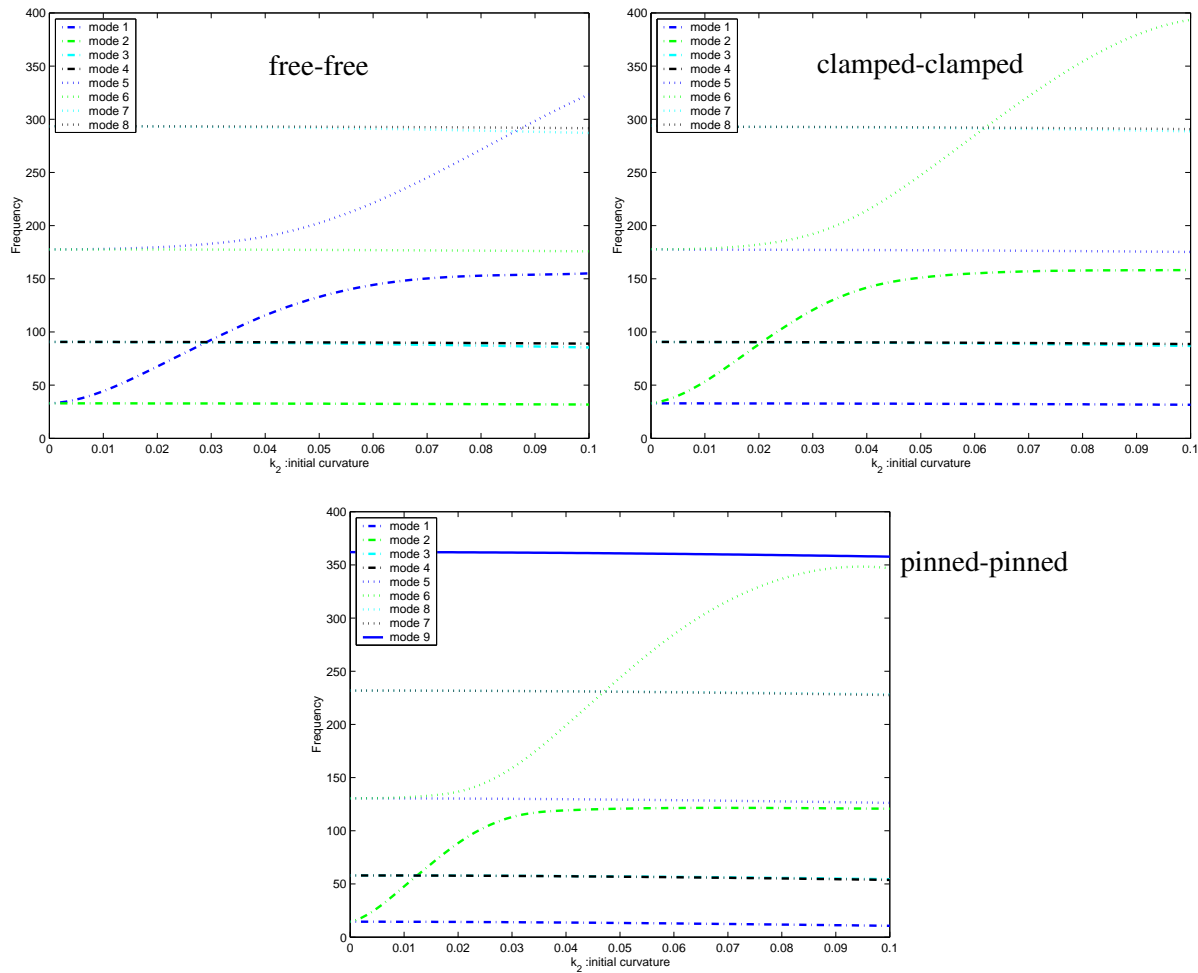
Figure 4. Vibration frequency versus initial curvature k_2 for initially curved beams with different boundary conditions.

bending (1OB), first symmetric in-plane bending (1IB), first antisymmetric out-of-plane bending (1AOB), first antisymmetric in-plane bending (1AIB), etc., respectively. The plots show that for the free-free case, the frequency of mode 1 departs from the one for zero initial curvature and approaches the one for mode 5. The dominant type of motion also changes from 1OB to 2OB as the initial curvature increases. The four lowest mode shapes for a beam with initial curvature $k_2 = 0.10$ are shown in Figure 5. The dominant motion of mode 1 transitions from 1OB to 2OB when the initial curvature becomes larger.

On the other hand, for both clamped-clamped and pinned-pinned boundaries, the frequency of mode 2 changes from the one for zero initial curvature and approaches to the one for mode 6. Its dominant motion changes from 1IB to 2IB. Figure 6 shows the mode transition of mode 2 from dominant 1IB to dominant 2IB as the initial curvature k_2 increases for the pinned-pinned case. This phenomenon, which is often referred to as veering [Chen and Ginsberg 1992] or frequency mode transition [Tarnopolskaya et al. 1996; Tarnopolskaya et al. 1999], results from the nature of the eigenvalues of a general self-adjoint

Free-free boundary condition								
k_2	mode 1	mode 2	mode 3	mode 4	mode 5	mode 6	mode 7	mode 8
0.00	32.885	32.885	90.629	90.629	177.61	177.61	293.45	293.45
0.02	67.530	32.836	90.407	90.564	179.66	177.54	293.18	293.38
0.04	115.64	32.694	89.746	90.368	189.71	177.32	292.37	293.15
0.06	144.23	32.462	88.668	90.042	221.34	176.96	291.06	292.78
0.08	152.93	32.151	87.208	89.591	271.52	176.47	289.29	292.26
0.10	155.13	31.772	85.408	89.018	323.39	175.83	287.11	291.58
Clamped-clamped boundary condition								
k_2	mode 1	mode 2	mode 3	mode 4	mode 5	mode 6	mode 7	mode 8
0.00	32.882	32.882	90.660	90.660	177.81	177.81	294.14	294.14
0.02	32.810	88.424	90.472	90.398	177.31	182.21	292.91	292.82
0.04	32.639	141.65	90.235	89.940	177.05	214.22	292.63	292.29
0.06	32.365	155.10	89.844	89.188	176.62	284.85	292.18	291.41
0.08	32.003	157.82	89.304	88.156	176.01	354.19	291.55	290.20
0.10	31.571	158.24	88.622	86.863	175.25	393.53	290.73	288.68
Pinned-pinned boundary condition								
k_2	mode 1	mode 2	mode 3	mode 4	mode 5	mode 6	mode 7	mode 8
0.00	14.506	14.506	58.011	58.011	130.48	130.48	231.85	231.85
0.02	14.307	57.811	57.865	88.397	130.28	136.74	231.65	231.70
0.04	13.739	57.234	57.428	119.21	129.70	199.11	231.07	231.26
0.06	12.880	56.331	56.712	121.43	128.79	230.16	230.53	284.68
0.08	11.825	55.167	55.732	121.40	127.62	228.99	229.54	336.91
0.10	10.665	53.794	54.509	120.75	126.21	227.58	228.28	346.84

Table 5. Vibration frequencies versus initial curvature k_2 for free-free, clamped-clamped, and pinned-pinned boundary conditions.

system when a certain parameter changes in the system. In the present study, it is the initial curvature k_2 that changes.

7. Coupled vibration of initially curved beams under end moments

Now the vibration characteristics of curved beams are considered, including beams both with curvature that is built-in and curvature that occurs because the beam is loaded with end moments. The section properties vary according to the initial curvature. Sample results are given in Table 6 on page 688. (Material properties are the same as those given in the previous section.) In the general case we consider an beam with various initial curvatures k_2, loaded under various equal and opposite values of applied moments at the ends giving rise to a constant value of bending moment $\overline{M}_2$. To facilitate this parametric study, the total static equilibrium value of curvature $\overline{K}_2$ is divided into two parts: the initial curvature k_2

mode 2 (dominant 1IB: 31.772 rad/sec)

mode 3 (dominant 1AOB: 85.408 rad/sec)

mode 4 (dominant 1AIB: 89.018 rad/sec)

mode 1 (dominant 2OB: 155.13 rad/sec)
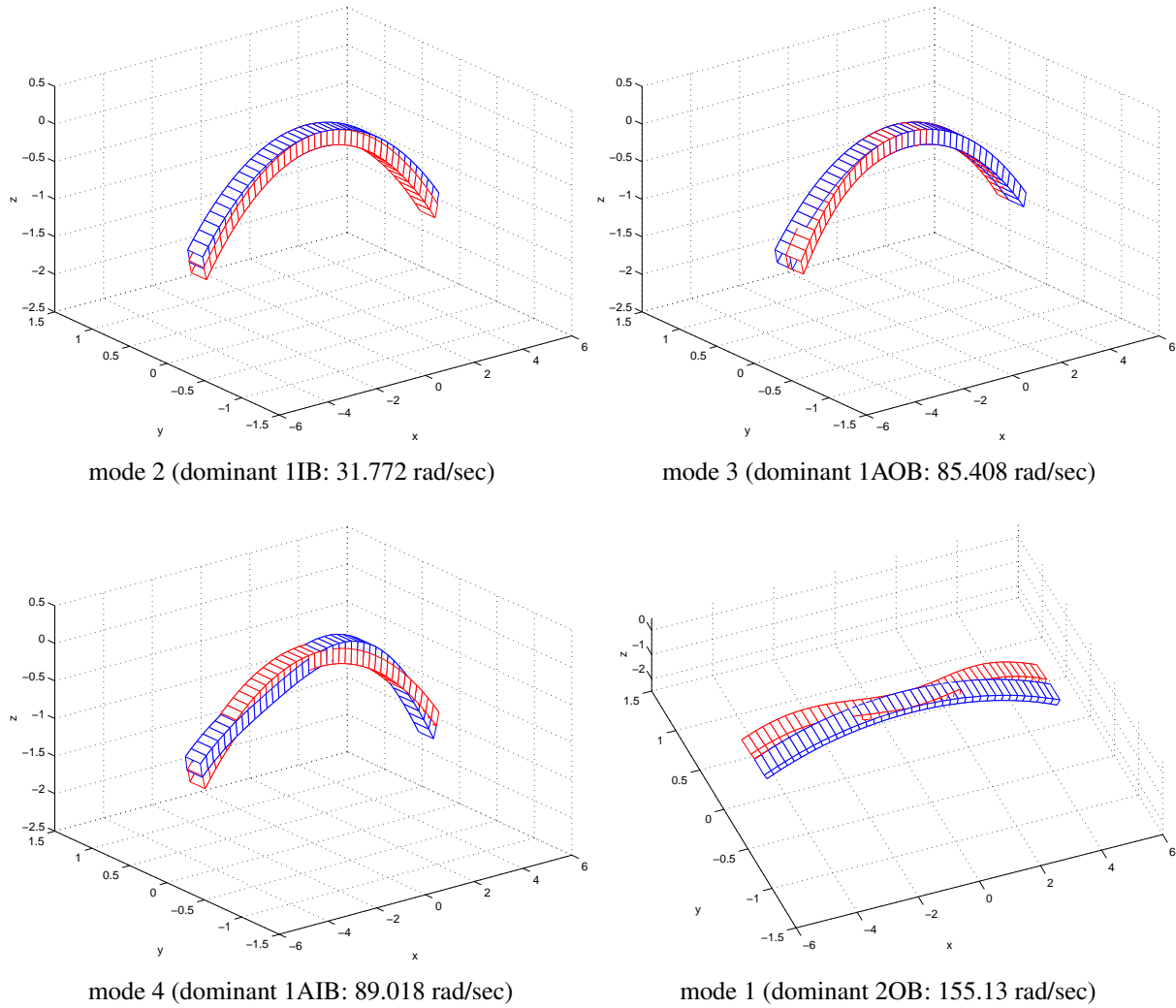
Figure 5. Four lowest modes of an initially curved free-free beam ($k_2 = 0.10$).

and the curvature caused by the applied end moments $\overline{M}_2/EI_2$. The total curvature is then

$$\overline{K}_2 = k_2 + \frac{\overline{M}_2}{EI_2} \tag{21}$$

where EI_2 is the vertical bending stiffness for bending in the plane of the initially curved beam. A nondimensional curvature ratio β is then introduced as the ratio of the initial curvature to the final total curvature and defined as

$$\beta = \frac{k_2}{\overline{K}_2} \qquad (\overline{K}_2 \neq 0) \tag{22}$$

For example, if $\beta = 0$, the beam has a zero initial curvature. If $\beta = 1$, the beam's initial curvature is the total curvature, which means that no end moments will be applied. If $\beta = -1$, the beam has an opposite initial curvature to the final configuration. Figure 7 shows initial configurations of beam with

$k_2 = 0.01$ $k_2 = 0.02$

$k_2 = 0.03$ $k_2 = 0.10$
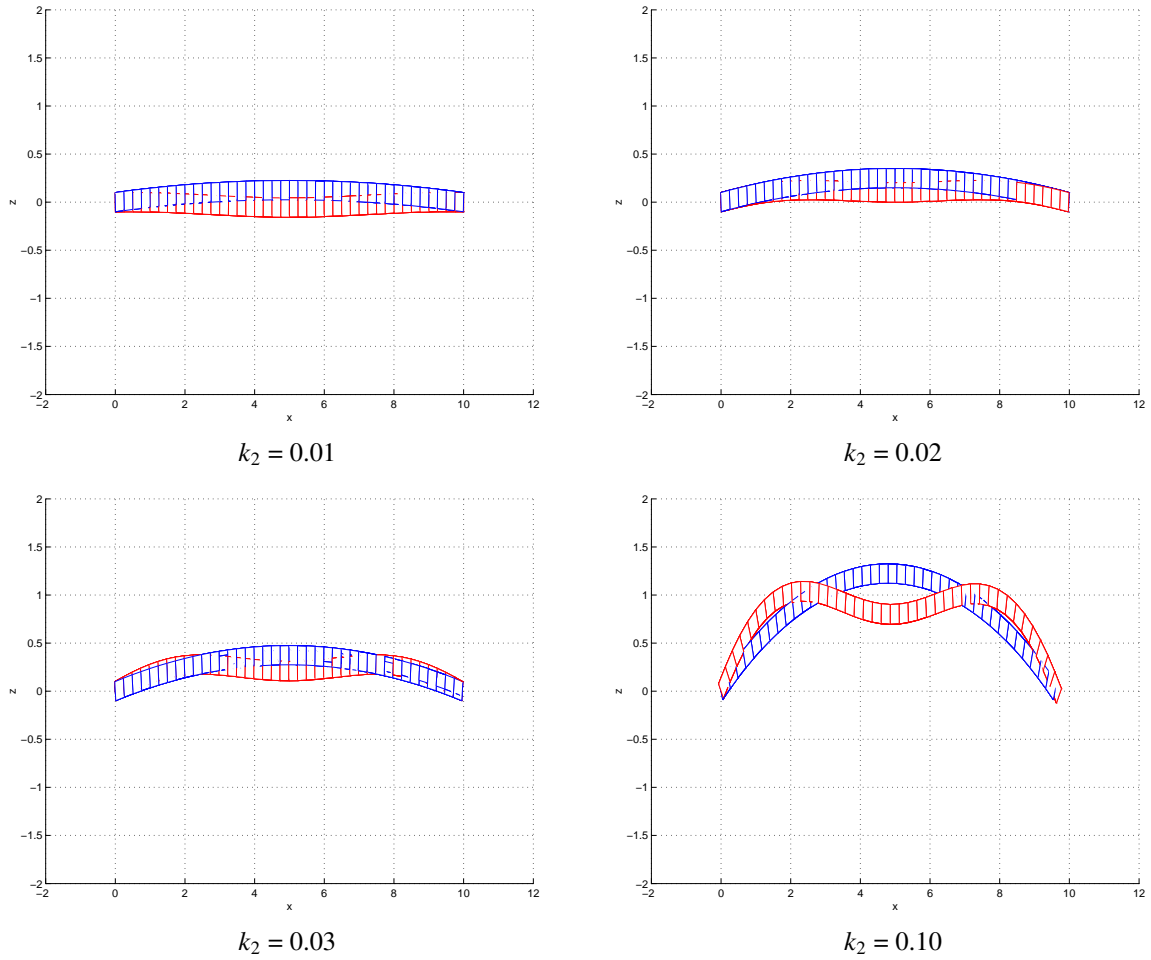
Figure 6. Mode transition of initially curved pinned-pinned beams (mode 2).

R_r	1/0.1	1/0.07	1/0.04	1/0.01
R_{11}	1.4286e-09	1.4286e-09	1.4286e-09	1.4286e-09
R_{22}	4.7292e-09	4.7291e-09	4.7291e-09	4.7291e-09
R_{33}	4.7291e-09	4.7291e-09	4.7291e-09	4.7291e-09
S_{12}	3.4133e-10	2.3790e-10	1.3619e-10	3.4476e-11
S_{21}	−1.1431e-12	8.6327e-13	9.5232e-14	−6.7113e-13
T_{11}	2.7802e-06	2.7803e-06	2.7803e-06	2.7803e-06
T_{22}	1.7143e-06	1.7143e-06	1.7143e-06	1.7143e-06
T_{33}	1.7143e-06	1.7143e-06	1.7143e-06	1.7143e-06
ξ_3	8.7588e-05	6.1310e-05	3.5034e-05	8.7585e-06

Table 6. Nonzero cross-sectional constants used for calculation of coupled free-vibration frequencies for initially curved beams (flexibility submatrices R_{ij}, S_{ij}, T_{ij}, radius of curvature R_r, and shear center location ξ_3).
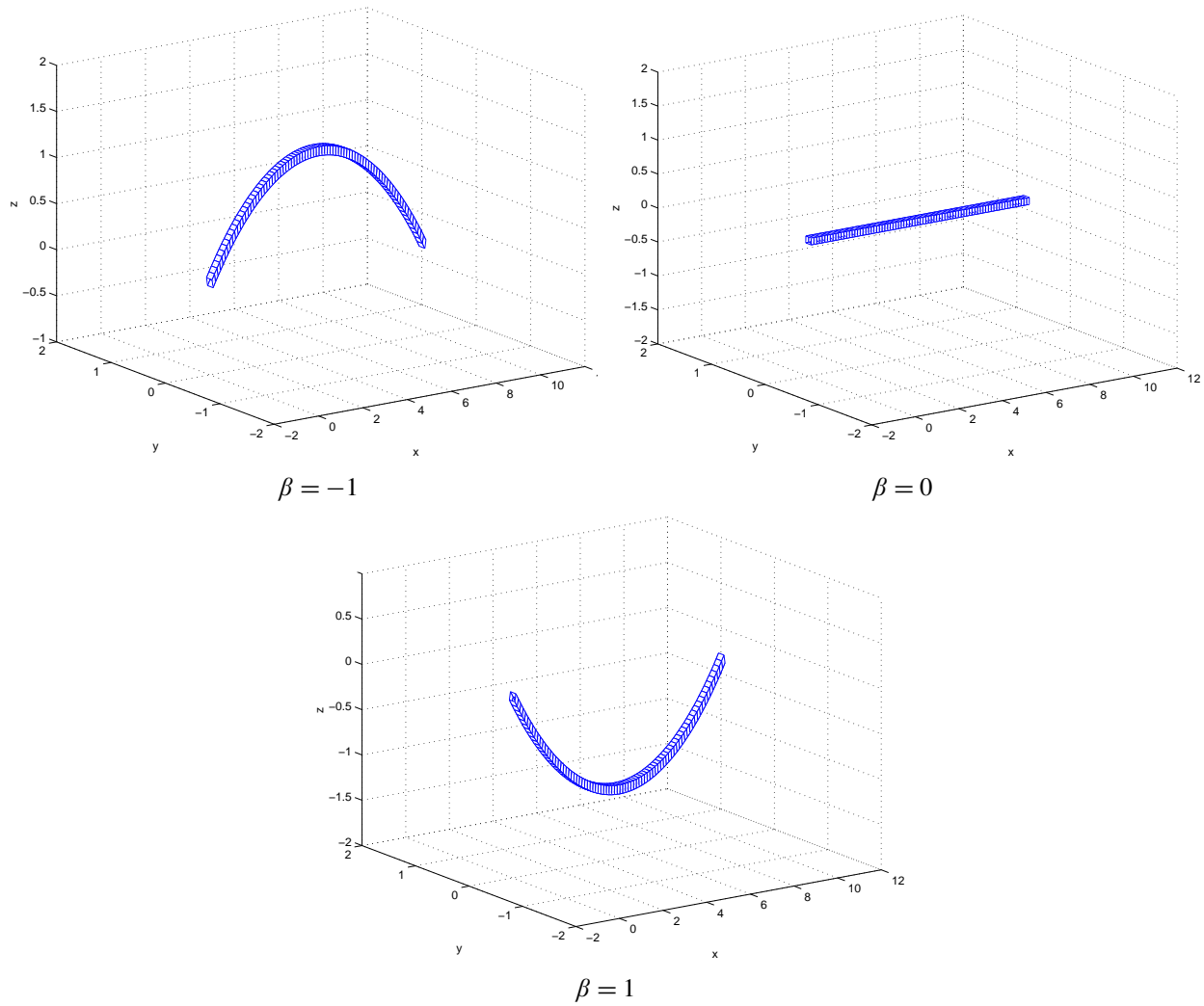
Figure 7. Initial configurations of beams with different β.

β	mode 1	mode 2	mode 3	mode 4	mode 5	mode 6
0	31.842	32.548	89.567	90.630	177.94	179.13
0.1	31.842	96.606	89.567	90.209	177.94	185.45
0.2	31.842	125.16	89.567	89.776	177.94	199.11
0.3	31.842	140.08	89.332	89.568	177.94	211.83
0.4	31.842	147.61	88.878	89.568	177.94	229.92
0.5	31.842	151.58	88.412	89.568	177.95	248.30

Table 7. Vibration frequencies versus curvature ratio β for initially curved free-free beams.
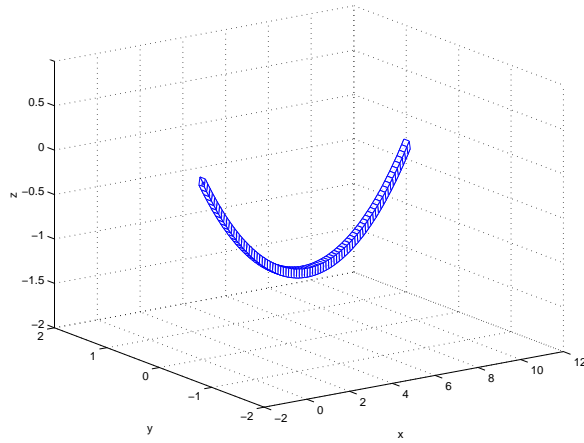
Figure 8. Final deformed configuration ($\overline{K}_2 = -0.10$) with end moments.
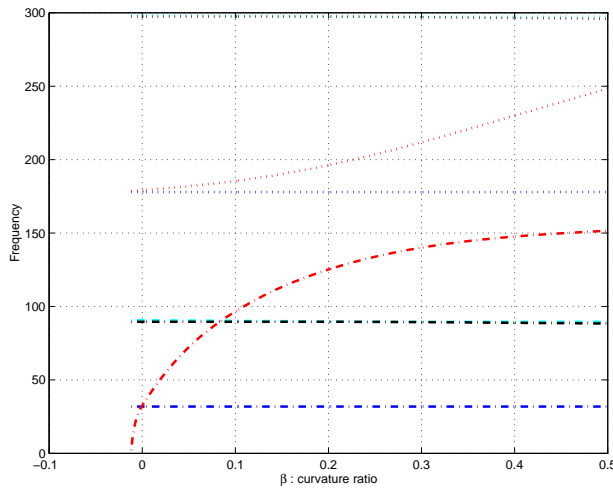
Figure 9. Vibration frequencies versus curvature ratio β for beams under end moments.

$\beta = -1, 0, 1$. (One can picture intermediate configurations of different β.) End moments are applied to deform the beam with various β so that $\overline{K}_2 = -0.10$ as shown in Figure 8. A rectangular cross-section is chosen to determine beam properties. The ratio r of height h to width b can be defined as

$$r = \frac{h}{b} \tag{23}$$

Table 7 on the previous page and Figure 9 show the vibration frequencies for various β. It is noticeable that frequencies for modes 2 and 6 change depending on β, which here indicates the value of initial curvature k_2. The frequency of mode 2, in which the dominant motion is the first out-of-plane bending motion, decreases as β decreases, becoming zero when $\beta = -0.0117$, indicating a lateral-torsional

buckling instability. As the initial curvature approaches close to that of the opposite sign of the final total curvature $\overline{K} = -0.10$ (i.e. β becomes a larger negative value), the larger end moments apply. For β lower than the critical value β_{cr}, the eigenvalues for mode 2 become pure real, which indicates that the mode is unstable.

8. Conclusion

The paper describes numerical procedures used to investigate the coupled free-vibration of curved beams, both initially curved and curved because of loading. Present results agree well with those from published papers. The governing equations of the present approach do not require displacement and rotation variables. Even in cases where displacement and rotation variables appear in the boundary conditions, this does not prohibit the use of the formulation. The reason is that these variables can be easily recovered from the formulation (i.e. they are secondary variables and can be expressed in terms of the primary variables). This feature makes the whole analysis quite concise.

The analysis provides the spectrum of free-vibration frequencies for given arbitrary configurations. The corresponding vibration mode shapes are easily visualized in order to observe which types of motion are dominant and which others are associated with the mode. The numerical examples show that it is necessary to include extensibility for beams with small initial curvature. Otherwise, one cannot observe those modes that are coupled to stretching motion. Note that low-frequency mode transition exists for beams with high initial curvatures.

The coupled free-vibration shows that the behaviors of simple engineering beam free-vibration problems are significantly different when beams are initially curved. The variation depends on the values of initial curvature and the types of boundary conditions. For certain regions of initial curvatures, the frequency and dominant motion of certain modes transition from the ones for zero initial curvature to those for the next higher mode. The shear center and neutral axis locations, as is true for the cross-sectional elastic constants, change as functions of initial curvature.

The case of end-loaded beams is also considered. In particular, when the geometries of an initially curved beam and an end-loaded beam are the same, results obtained demonstrate significant differences in behavior. Loading an initially curved beam affects the vibration characteristics and may lead to lateral-torsional buckling instability. Additional work should be done to address the instabilities of such configurations.

References

[Cesnik and Hodges 1997] C. E. S. Cesnik and D. H. Hodges, "VABS: a new concept for composite rotor blade cross-sectional modeling", *J. Am. Helicopter Soc.* **42**:1 (1997), 27–38.

[Chen and Ginsberg 1992] P.-T. Chen and J. H. Ginsberg, "On the relationship between veering of eigenvalue loci and parameter sensitivity of eigenfunctions", *J. Vib. Acoust.* (*ASME*) **114**:2 (1992), 141–148.

[Chidamparam and Leissa 1993] P. Chidamparam and A. W. Leissa, "Vibrations of planar curved beams, rings and arches", *Appl. Mech. Rev.* **46**:9 (1993), 467–483.

[Chidamparam and Leissa 1995] P. Chidamparam and A. W. Leissa, "Influence of centerline extensibility on the in-plane free vibrations of loaded circular arches", *J. Sound Vib.* **183**:5 (1995), 779–795.

[Fung 2004] T. C. Fung, "Improved approximate formulas for the natural frequencies of simply supported Bernoulli–Euler beams with rotational restrains at the ends", *J. Sound Vib.* **273**:1–2 (2004), 451–455.

[Hodges 1999] D. H. Hodges, "Non-linear inplane deformation and buckling of rings and high arches", *Int. J. Non-Linear Mech.* **34**:4 (1999), 723–737.

[Hodges 2003] D. H. Hodges, "Geometrically exact, intrinsic theory for dynamics of curved and twisted anisotropic beams", *AIAA J.* **41**:6 (2003), 1131–1137.

[Hodges 2006] D. H. Hodges, *Nonlinear composite beam theory*, Progress in Astronautics and Aeronautics **213**, AIAA, Reston, VA, 2006.

[Howson and Jemah 1999] W. Howson and A. Jemah, "Exact out-of-plane natural frequencies of curved Timoshenko beams", *J. Eng. Mech.* (*ASCE*) **125**:1 (1999), 19–25.

[Irie et al. 1982] T. Irie, G. Yamada, and K. Tanaka, "Natural frequencies of out-of-plane vibration of arcs", *J. Appl. Mech.* (*ASME*) **49** (1982), 910–913.

[Patil and Hodges 2006] M. J. Patil and D. H. Hodges, "Flight dynamics of highly flexible flying wings", *J. Aircr.* **43**:6 (2006), 1790–1799.

[Tarnopolskaya et al. 1996] T. Tarnopolskaya, F. de Hoog, N. H. Fletcher, and S. Thwaites, "Asymptotic analysis of the free in-plane vibrations of beams with arbitrarily varying curvature and cross-section", *J. Sound Vib.* **196**:5 (1996), 659–680.

[Tarnopolskaya et al. 1999] T. Tarnopolskaya, F. R. de Hoog, and N. H. Fletcher, "Low-frequency mode transition in the free in-plane vibration of curved beams", *J. Sound Vib.* **228**:1 (1999), 69–90.

[Yu et al. 2002] W. Yu, V. V. Volovoi, D. H. Hodges, and X. Hong, "Validation of the variational asymptotic beam sectional analysis", *AIAA J.* **40**:10 (2002), 2105–2112.

CHONG-SEOK CHANG: `juliera324@hotmail.com`
Georgia Institute of Technology, School of Aerospace Engineering, 270 Ferst Drive, Atlanta, GA 30332-1510, United States

DEWEY H. HODGES: `dhodges@gatech.edu`
Georgia Institute of Technology, School of Aerospace Engineering, 270 Ferst Drive, Atlanta, GA 30332-1510, United States
http://www.ae.gatech.edu/~dhodges/

NONLINEAR DYNAMIC RESPONSE OF AN ACCELERATING COMPOSITE ROTOR BLADE USING PERTURBATIONS

MEHRDAAD GHORASHI AND FRED NITZSCHE

The general nonlinear intrinsic differential equations of a composite beam are solved in order to obtain the elastodynamic response of an accelerating rotating hingeless composite beam. The solution utilizes the results of the linear variational asymptotic method applied to cross-sectional analysis. The integration algorithm implements the finite difference method in order to solve the transient form of the nonlinear intrinsic differential equations. The motion is analyzed since the beam starts rotating from rest, until it reaches the steady state condition. It is shown that the transient solution of the nonlinear dynamic formulation of the accelerating rotating beam converges to the steady state solution obtained by an alternative integration algorithm based on the shooting method. The effects of imposing perturbations on the steady state solution have also been analyzed and the results are shown to be compatible with those of the accelerating beam. Finally, the response of a nonlinear composite beam with embedded anisotropic piezocomposite actuators is illustrated. The effect of activating actuators at various directions on the steady state forces and moments generated in a rotating beam has been analyzed. These results can be used in controlling the nonlinear elastodynamic response of adaptive rotating beams.

A list of symbols can be found starting on page 713.

1. Introduction

The helicopter with its ability to take-off and land vertically is a crucial means of aerial transportation. Expanding the domain of application of helicopters, however, face a few serious constraints. Among them is the relatively poor ride quality due to severe vibration and noise. Vibration can reduce the fatigue life of structural components and hence increase the operating costs. Furthermore, environmental consequences of noise and vibration have limited the range of application and the velocity of helicopters. That is why reducing noise and vibration is a major goal in the design of helicopters.

Analysis of rotating blades can be performed using three-dimensional finite element method (FEM) models. However, modeling initially twisted and curved active helicopter rotor blades using three-dimensional FEM is extremely expensive. Also, for preliminary design and for control synthesis, this approach is quite computationally intensive. As an alternative, and since a helicopter rotor blade is a slender structural member, one may model it as a thin-walled composite beam.

In the past two decades, research has focused on the analysis of anisotropic composite beams using the variational asymptotic method (VAM), an excellent review of which can be found in [Hodges 2006]. VAM, as a powerful method for analyzing thin-walled beams made of composites was first introduced

in [Berdichevskii 1981]. It is computationally more efficient than a complete three-dimensional model and it starts from the elastic energy functional.

For certain simple cases like isotropic beams with relatively simple cross-sectional geometries, the sectional constants can be calculated in closed form. For complex cross-sections made of composites, a two-dimensional FEM discretization has been introduced which implements the VAM cross-sectional analysis. This FEM code is called the *Variational Asymptotic Beam Sectional* Analysis program (VABS). This concept was introduced in [Hodges et al. 1992] and applied to box and I-beams with initial twist and initial curvature.

The results of the VAM cross-sectional analysis have been validated in [Yu et al. 2002b] and [Yu and Hodges 2004]. VABS solutions have been compared with those of the three-dimensional elasticity solution. Identical results were reported for beams with elliptical and rectangular cross-sections. It has been demonstrated that although the application of VABS is restricted to beam problems, it provides a level of accuracy which is comparable to that of standard three-dimensional finite element codes, but with far smaller computing and processing requirements.

The foundations of the Timoshenko model have been developed in [Yu et al. 2002a]. Also, the inclusion of active elements in the analysis was carried out by Cesnik and his coworkers. In [Cesnik and Shin 1998], an asymptotic formulation for analyzing multicell composite helicopter rotor blades with integral anisotropic active plies was presented.

In [Cesnik et al. 2001], the dynamic characteristics of the active twist rotor (ATR) blades were investigated, both analytically and experimentally. The ATR system is intended for vibration and potentially for noise reduction in helicopters through individual blade control (IBC). The numerical results for the beam torsional loads showed an average error of 20% in magnitude and virtually no difference in phase for the blade frequency response.

Not many papers have discussed the method of solution of the one-dimensional intrinsic equations of a beam. In the solutions presented in [Shang and Hodges 1995] and [Cesnik et al. 2001] the solution is performed in two steps. The first step is to calculate the steady state response. Then, the perturbed motion of the blade about the obtained steady state position is obtained by solving the perturbed steady state equations for small perturbations of variables.

This perturbed steady state solution is, of course, valid in the vicinity of the steady state response. If, however, obtaining the whole dynamics of the beam including its start from static equilibrium and acceleration to full speed and even experiencing some perturbations afterwards is the aim, other solution methods should be sought. The purpose of this paper is to present such an alternative solution. In order to verify the results, the results of this alternative method are compared against those of the perturbed steady state method.

In this paper the beam is assumed to accelerate from its state of rest and reach a constant speed of rotation. Both transient and steady state solutions are obtained. The analysis utilizes the results of the cross-sectional analysis and the solution of the nonlinear intrinsic equations of the beam is performed using finite differences, perturbations and the shooting method. To verify the solution, the resulting solutions are compared against those of the perturbed steady state method. The obtained simulation code is a powerful tool for analyzing the nonlinear response of composite rotor blades; and for the ultimate aim of efficient noise and vibration control of helicopters.

This paper is based on [Ghorashi 2009] and its principal features are:

1. Nonlinear dynamic analysis of passive clamped rotating composite beams (transient and steady state solutions) accelerating from zero to full speed.

2. Analyzing the effect of input perturbations on the response of rotating beams which are already at their steady state. This is an extension to [Ghorashi and Nitzsche 2008] where only the steady state response of rotating beams has been discussed.

3. Nonlinear dynamic analysis of a rotating composite beam with embedded actuators and analyzing the sensitivity of the response of the beam to activating the actuators located at various angles.

2. The intrinsic differential equations

The nonlinear one-dimensional analysis along a rotating beam utilizes the results of the cross-sectional analysis. It results in the generalized stress and strain resultants as well as the one-dimensional displacements. For the case of generalized Timoshenko beam, the nonlinear intrinsic equations of motion are [Hodges 2006]

$$F' + \tilde{K}F + f = \dot{P} + \tilde{\Omega}P \quad \text{and} \quad M' + \tilde{K}M + (\tilde{e}_1 + \tilde{\gamma})F + m = \dot{H} + \tilde{\Omega}H + \tilde{V}P, \tag{1}$$

where the total curvature and twist of the beam are the summation of their initial values and the added curvature and twist as a result of elastic deformation, that is,

$$K = k + \kappa. \tag{2}$$

Here, F and M are column vectors of internal forces and moments, respectively. The first element of F is the axial force and the second and third elements are the shear forces, expressed in the deformed beam basis. Similarly, the first element of M is the twisting moment and the second and third elements are bending moments.

The generalized sectional linear and angular momenta P and H are conjugate to motion variables by derivatives of the kinetic energy function $\mathcal{K}$:

$$P = \left(\frac{\partial \mathcal{K}}{\partial V}\right)^T \quad \text{and} \quad H = \left(\frac{\partial \mathcal{K}}{\partial \Omega}\right)^T. \tag{3}$$

The nonlinear intrinsic kinematical equations of a beam that should be solved together with the preceding equations are [Hodges 2006]

$$V' + \tilde{K}V + (\tilde{e}_1 + \tilde{\gamma})\Omega = \dot{\gamma} \quad \text{and} \quad \Omega' + \tilde{K}\Omega = \dot{\kappa}. \tag{4}$$

The momentum-velocity equations are [Hodges 2006]

$$\begin{Bmatrix} P \\ H \end{Bmatrix} = \begin{bmatrix} \mu\Delta & -\mu\tilde{\bar{\xi}} \\ \mu\tilde{\bar{\xi}} & i \end{bmatrix} \begin{Bmatrix} V \\ \Omega \end{Bmatrix}, \tag{5}$$

where $\mu = \langle\langle\rho\rangle\rangle$ (with $\langle\langle u\rangle\rangle$ defined as $\int_A u\,(1 - x_2 k_3 - x_3 k_2)\,dx_2\,dx_3$, see below),

$$\xi = \begin{Bmatrix} 0 \\ x_2 \\ x_3 \end{Bmatrix}, \qquad \tilde{\bar{\xi}} = \begin{bmatrix} 0 & -\bar{x}_3 & \bar{x}_2 \\ \bar{x}_3 & 0 & 0 \\ -\bar{x}_2 & 0 & 0 \end{bmatrix}, \qquad i = \langle\langle\rho(\xi^T\xi\cdot\Delta - \xi\xi^T)\rangle\rangle = \begin{bmatrix} i_2 + i_3 & 0 & 0 \\ 0 & i_2 & i_{23} \\ 0 & i_{23} & i_3 \end{bmatrix}. \tag{6}$$

The quantity $(1 - x_2 k_3 - x_3 k_2)$ appearing in the definition of the averaging operator $\langle\langle \cdot \rangle\rangle$ is the square root of the determinant g of the metric tensor in curvilinear coordinates.

Finally, the two-dimensional analysis results in the warping functions as well as the stiffness matrix used in the constitutive equations

$$\begin{Bmatrix} \gamma \\ \kappa \end{Bmatrix} = \underbrace{\begin{bmatrix} R & Z \\ Z^T & T \end{bmatrix}}_{S^{-1}} \begin{Bmatrix} F \\ M \end{Bmatrix}, \qquad \begin{Bmatrix} F \\ M \end{Bmatrix} = \underbrace{\begin{bmatrix} A & B \\ B^T & D \end{bmatrix}}_{S} \begin{Bmatrix} \gamma \\ \kappa \end{Bmatrix}. \tag{7}$$

Equations (1), (2), (4), (5), and (7)$_1$ form a system of twelve nonlinear partial differential equations and fifteen algebraic equations. They have a total of nine unknown vectors: $F, M, V, \Omega, P, H, \gamma, \kappa$, and K, at every node along the beam and at every instant of time. In what follows, these equations are solved using the perturbation method as well as finite differences in time and space.

3. Derivation of the generic nonlinear term

Figure 1 illustrates a beam discretized by N nodes along its span. The corresponding finite difference space-time grid presentation is seen in Figure 2. For a generic variable $\phi(x, t)$, we use the convention

$$\phi_i = \phi(x, t), \tag{8}$$

where i is the beam node number corresponding to the coordinate x. At the points neighboring (x, t) in Figure 2, the same variable can be expressed as

$$\phi_{i+1} = \phi(x + \Delta x, t), \qquad \phi_i^+ = \phi(x, t + \Delta t), \qquad \phi_{i+1}^+ = \phi(x + \Delta x, t + \Delta t), \tag{9}$$
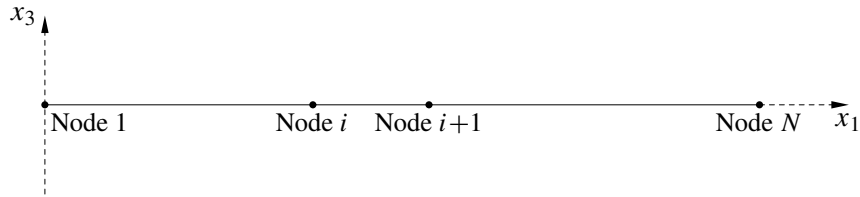
Figure 1. Nodes along the beam and the coordinate system of the undeformed beam.
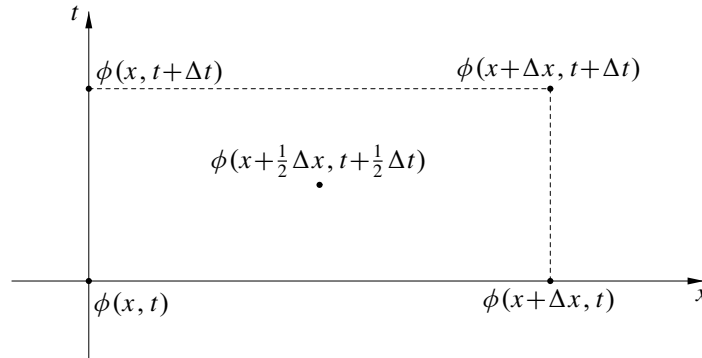
Figure 2. Time-space grid for the numerical solution of a partial differential equation.

where the superscript $+$ refers to the next time step.

Using Taylor series expansions

$$\phi\left(x + \tfrac{1}{2}\Delta x, t + \tfrac{1}{2}\Delta t\right) = \phi\left(x, t + \tfrac{1}{2}\Delta t\right) + \phi'\left(x, t + \tfrac{1}{2}\Delta t\right) \times \tfrac{1}{2}\Delta x, \tag{10}$$

$$\phi\left(x, t + \tfrac{1}{2}\Delta t\right) = \phi(x, t) + \dot{\phi}(x, t) \times \tfrac{1}{2}\Delta t, \tag{11}$$

and the notation given in Equations (8) and (9) one obtains

$$\phi\left(x + \tfrac{1}{2}\Delta x, t + \tfrac{1}{2}\Delta t\right) = \tfrac{1}{4}(\phi^+_{i+1} + \phi^+_i + \phi_{i+1} + \phi_i) + O(\Delta x^2, \Delta t^2), \tag{12}$$

$$\phi'\left(x + \tfrac{1}{2}\Delta x, t + \tfrac{1}{2}\Delta t\right) = \frac{1}{2\Delta x}(\phi^+_{i+1} - \phi^+_i + \phi_{i+1} - \phi_i) + O(\Delta x^2, \Delta t^2), \tag{13}$$

$$\dot{\phi}\left(x + \tfrac{1}{2}\Delta x, t + \tfrac{1}{2}\Delta t\right) = \frac{1}{2\Delta t}(\phi^+_{i+1} - \phi_{i+1} + \phi^+_i - \phi_i) + O(\Delta x^2, \Delta t^2). \tag{14}$$

Equations (12)–(14) provide the second-order approximate finite difference expressions for a variable and its derivatives with respect to time and space. They were used in [Ghorashi 1994] and [Esmailzadeh and Ghorashi 1997] to solve a moving load problem. In what follows, Equations (12)–(14) will be used in order to convert the system of nonlinear partial differential equations (1) and (4) into a set of difference equations.

Consider a generic nonlinear vector term $\tilde{\phi}\lambda$ with scalar components $\phi_m\lambda_n$ ($m = 1:3$, $n = 1:3$). One may use perturbations in time and space in order to express these components in terms of the nodal values of variables ϕ_m and λ_n. For the perturbations in space, $\phi^+_{m,i+1} = \phi^+_{m,i} + \check{\phi}_{m,i+1}$. Similarly, for the perturbations in time, $\phi^+_{m,i} = \phi_{m,i} + \hat{\phi}_{m,i}$. Therefore,

$$\phi_m\lambda_n = \tfrac{1}{16}(3\phi_{m,i} + 2\hat{\phi}_{m,i} + \check{\phi}_{m,i+1} + \phi_{m,i+1})(3\lambda_{n,i} + 2\hat{\lambda}_{n,i} + \check{\lambda}_{n,i+1} + \lambda_{n,i+1}). \tag{15}$$

For small perturbations, (15) reduces to [Ghorashi 2009]

$$\phi_m\lambda_n = \tfrac{1}{16}\left[(\phi^+_{m,i+1} + \phi^+_{m,i})(\lambda_{n,i+1} + 3\lambda_{n,i}) + (\lambda^+_{n,i+1} + \lambda^+_{n,i})(\phi_{m,i+1} + 3\phi_{m,i})\right]$$
$$+ \tfrac{1}{16}(\phi_{m,i+1}\lambda_{n,i+1} + \phi_{m,i+1}\lambda_{n,i} + \phi_{m,i}\lambda_{n,i+1} - 3\phi_{m,i}\lambda_{n,i}). \tag{16}$$

This is the equation for the generic nonlinear term.

4. The finite difference formulation and solution algorithm

Using (16) for all of the nonlinear terms in (1), and (4), one obtains

$$A_i q^+_i + B_i q^+_{i+1} = J_i, \tag{17}$$

where the right-hand side contains the currently known quantities, the column state vector

$$q = \begin{bmatrix} F_1 & F_2 & F_3 & M_1 & M_2 & M_3 & V_1 & V_2 & V_3 & \Omega_1 & \Omega_2 & \Omega_3 & P_1 & P_2 & P_3 & H_1 & H_2 & H_3 & \gamma_{11} & 2\gamma_{12} & 2\gamma_{13} & \kappa_1 & \kappa_2 & \kappa_3 \end{bmatrix}^T \tag{18}$$

has 24 elements, the A_i and B_i are 24×24 matrices and q_i and the J_i are column vectors. The expressions for A_i, B_i, and J_i are given in the Appendix.

Equation (17) is composed of 24 algebraic equations with 48 unknowns and as such it is not solvable on its own. To solve the problem, one should utilize initial and boundary conditions as was done for a similar formulation in [Ghorashi 1994] and [Esmailzadeh and Ghorashi 1997]. Using (17) we have

$$q_1^+ = M_{N-1}^{\text{tot}} \cdot q_N^+ + T_{N-1}^{\text{tot}}, \tag{19}$$

where $M_{N-1}^{\text{tot}} = a_1 a_2 a_3 a_4 \cdots a_{N-1}$ and $T_{N-1}^{\text{tot}} = b_1 + a_1 b_2 + a_1 a_2 b_3 + \cdots + a_1 a_2 a_3 \cdots a_{N-2} b_{N-1}$ with $a_i = -A_i^{-1} B_i$ and $b_i = A_i^{-1} J_i$, respectively.

For a hingeless beam with the root (that is, node 1) on the axis of rotation, the boundary conditions at the root are

$$V = \begin{Bmatrix} 0 \\ 0 \\ 0 \end{Bmatrix}, \qquad \Omega = \begin{Bmatrix} 0 \\ 0 \\ \Omega_3 \end{Bmatrix} \tag{20}$$

and at the tip (node N)

$$F = \begin{Bmatrix} 0 \\ 0 \\ 0 \end{Bmatrix}, \qquad M = \begin{Bmatrix} 0 \\ 0 \\ 0 \end{Bmatrix}. \tag{21}$$

By implementing (20) and (21) in (19), the latter equation can be solved for the remainder of the unknowns at the root and at the tip of the beam. Then, (17) can be used to calculate the state vectors at all intermediate nodes.

5. Case studies

5.1. *The isotropic rectangular solid model.* Figure 3 illustrates a prismatic beam having a solid rectangular section made of a homogeneous isotropic material for which

$$E = 1.792 \times 10^{13} \, \text{N/m}^2, \quad v = 0.3, \quad A = 0.02 \, \text{m}^2, \quad \rho = 1770 \, \text{kg/m}^3. \tag{22}$$
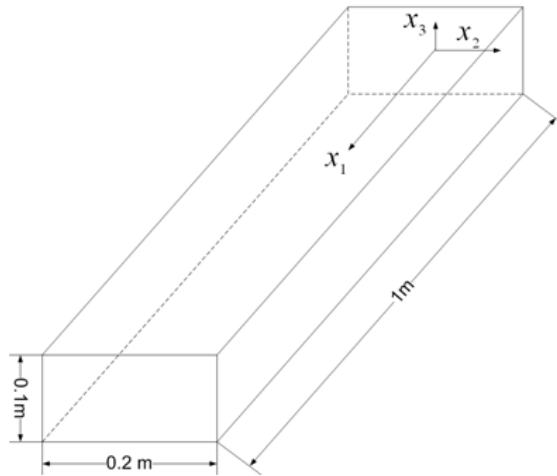
Figure 3. The geometry of the rotating beam and the coordinate system.

Using VABS one obtains

$$i = \begin{bmatrix} 8.333 & 0 & 0 \\ 0 & 1.6667 & 0 \\ 0 & 0 & 6.6667 \end{bmatrix} \times 10^{-5} \times 1770 \tag{23}$$

and

$$S = \begin{bmatrix} 0.358 \times 10^{12} & 0 & 0 & 0 & 0 & 0 \\ 0 & 0.1373 \times 10^{12} & 0 & 0 & 0 & 0 \\ 0 & 0 & 0.1074 \times 10^{12} & 0 & 0 & 0 \\ 0 & 0 & 0 & 0.354 \times 10^9 & 0 & 0 \\ 0 & 0 & 0 & 0 & 0.298 \times 10^9 & 0 \\ 0 & 0 & 0 & 0 & 0 & 0.119 \times 10^{10} \end{bmatrix}. \tag{24}$$

The beam rotates about x_3 with the variable angular velocity shown in Figure 4. The corresponding moment at the root is also plotted in the same figure. It is observed that when the beam reaches its steady state velocity, this moment converges to zero. This observation is expected since no drag force exists in the model.

Since the most significant force generated in the beam is the axial force F_1, it is beneficial to have an alternative expression for this force in order to be used for verification. Using linear elasticity and Newton's second law of motion one obtains

$$F_1 = \tfrac{1}{2}\rho A\Omega_3^2(L^2 - x_1^2). \tag{25}$$
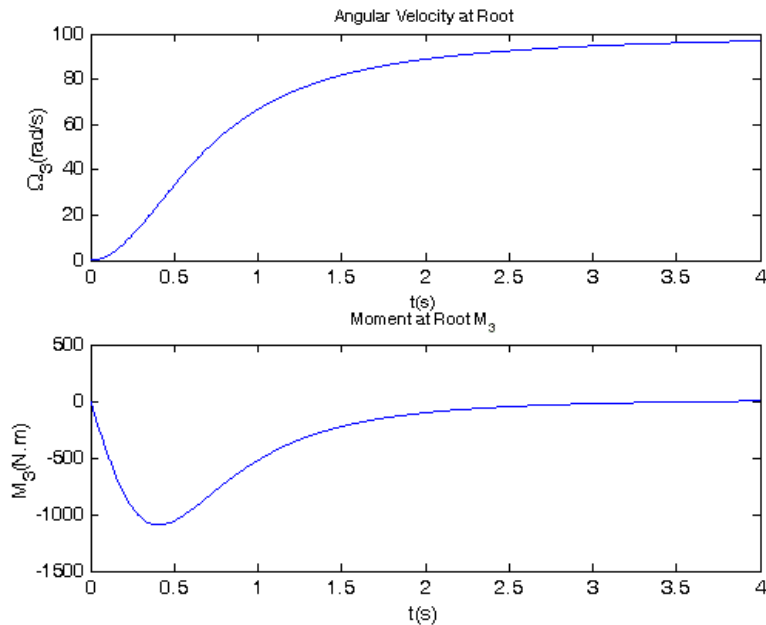
Figure 4. Time history diagram of the angular velocity Ω_3 at the root and the corresponding bending moment at the clamped root.
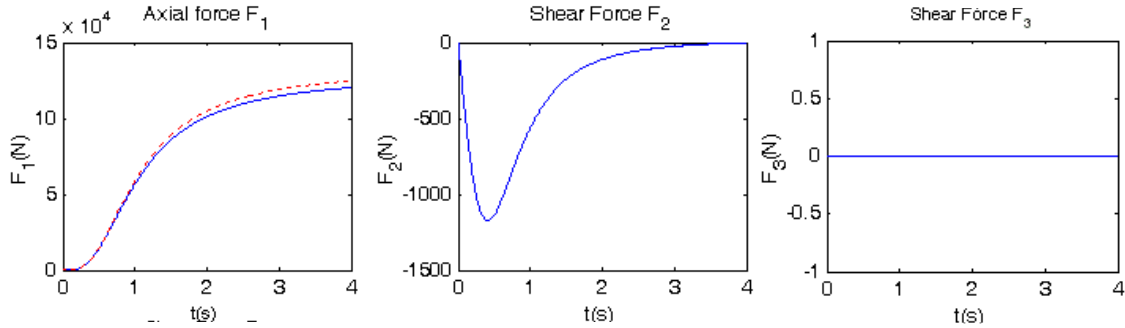
Figure 5. Time history diagram of the internal forces at the midspan (solid lines), and a comparison with the result of (25) (dashed line in left panel).
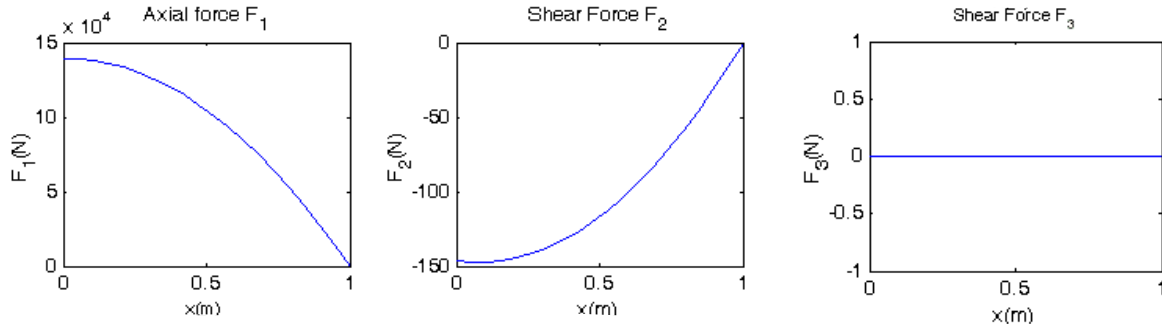

Figure 6. Variation of the internal force components along the beam at $t = 2s$.

Figure 5 illustrates the time history diagram of the induced internal forces at the midspan. It is observed that the measured F_1 is close to that of the approximation of (25). The distributions of the induced internal forces along the span are plotted in Figure 6.

5.2. *The composite box model.* The figure illustrates the cross-section of a composite square box beam with constant properties along the beam span and a cross-section of 2.5 cm between midlines. The upper and lower sides are made of four plies of AS4/3506-1 at 45° with the beam axis, and the lateral sides are made of four plies of a typical anisotropic piezocomposite actuator (APA) at −45°. The thickness of each ply is 0.127 mm and the length of the box is $L = 10$ cm. The cross-section of this model was discussed in [Cesnik and Palacios 2003] and the UM/VABS input file for this case is among the examples provided with the software.
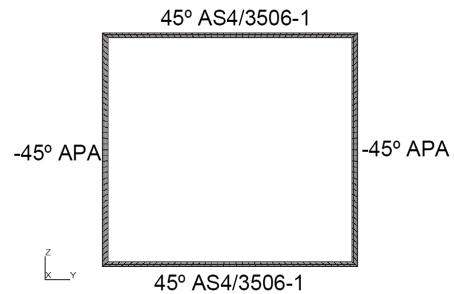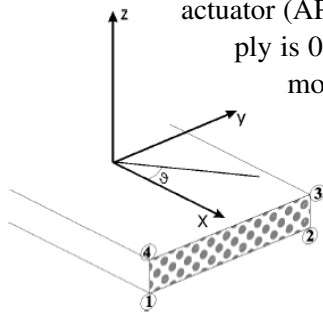
The ply angles mentioned are the angles of fibers with the longitudinal x-axis as shown in the cross-sectional view to the left, which is taken from [Palacios 2005]. The convention for material orientation within the element is also shown.

	E_{11} GPa	E_{22} GPa	G_{12} GPa	G_{23} GPa	ν_{12}	ν_{23}	d_{111} pm/V	d_{112} pm/V	t mm	inter-electrode distance, mm
AS4/3506-1	142	9.8	6.0	4.8	0.3	0.42	—	—	0.127	—
APA	42.2	17.5	5.5	4.4	0.354	0.42	381	−160	0.127	1.143

Table 1. Material properties of active box beam [Cesnik and Palacios 2003].

The material properties are listed in Table 1. It is furthermore assumed that $\rho = 1770\,\text{kg/m}^3$ and $E_{33} = 0.8E_{22}$ and $\nu_{13} = \nu_{23} = \nu_{12}$ [Cesnik and Palacios 2003].

Using these data, the stiffness matrix can be calculated by UM/VABS as

$$S = \begin{bmatrix} 7.977 \times 10^5 & -0.9873 & -0.8575 & -1.5056 \times 10^3 & -7.3017 \times 10^{-3} & 1.348 \times 10^{-3} \\ -0.9873 & 2.5482 \times 10^5 & 4.6845 \times 10^{-3} & -3.897 \times 10^{-3} & 1.962 \times 10^3 & 5.9626 \times 10^{-5} \\ -0.8575 & 4.6845 \times 10^{-3} & 2.296 \times 10^5 & 1.0716 \times 10^{-2} & 9.912 \times 10^{-5} & -2.8055 \times 10^2 \\ -1.5056 \times 10^3 & -3.897 \times 10^{-3} & 1.0716 \times 10^{-2} & 86.95 & 2.1193 \times 10^{-4} & 1.6532 \times 10^{-4} \\ -7.3017 \times 10^{-3} & 1.962 \times 10^3 & 9.912 \times 10^{-5} & 2.1193 \times 10^{-4} & 90.397 & 3.6091 \times 10^{-6} \\ 1.348 \times 10^{-3} & 5.9626 \times 10^{-5} & -2.8055 \times 10^2 & 1.6532 \times 10^{-4} & 3.6091 \times 10^{-6} & 79.4434 \end{bmatrix}. \tag{26}$$

Also

$$i = \begin{bmatrix} 9.9555 & 0 & 0 \\ 0 & 4.9777 & 0 \\ 0 & 0 & 4.9777 \end{bmatrix} \times 10^{-9} \times 1770. \tag{27}$$

The cross-sectional area is $5.08 \times 10^{-5}\,\text{m}^2$ and the model has 50 nodes along its span. The beam accelerates from rest to 100 rad/s. Parts of the transient response of the beam from rest to full speed are illustrated in Figures 7 to 9.

6. Steady state solution using the shooting method

The finite difference solution formulated and implemented in Sections 3 and 4 can provide the response of a rotating beam during acceleration to full speed, its convergence to steady state response and also during any existing disturbance that can drive the system out of the steady state response.

In [Ghorashi and Nitzsche 2008] and [Ghorashi 2009] a method for obtaining the steady state response of rotating hingeless beams using the shooting method has been presented. The mathematical basis for
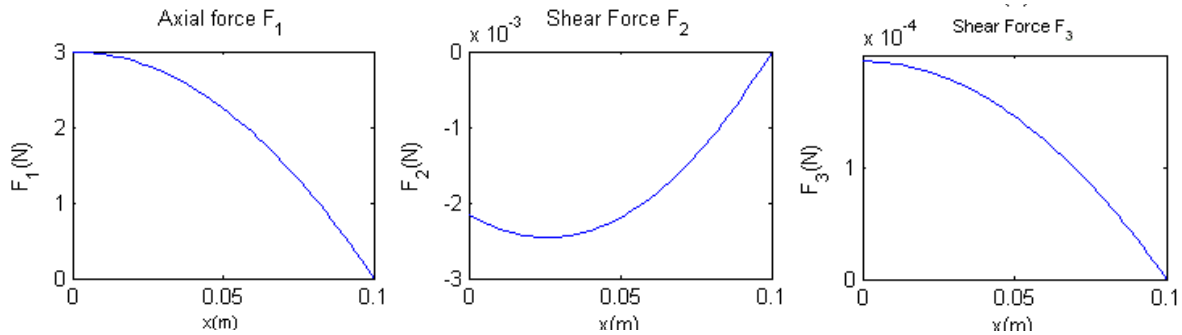
Figure 7. Variation of the internal force components along the beam at $t = 3s$.
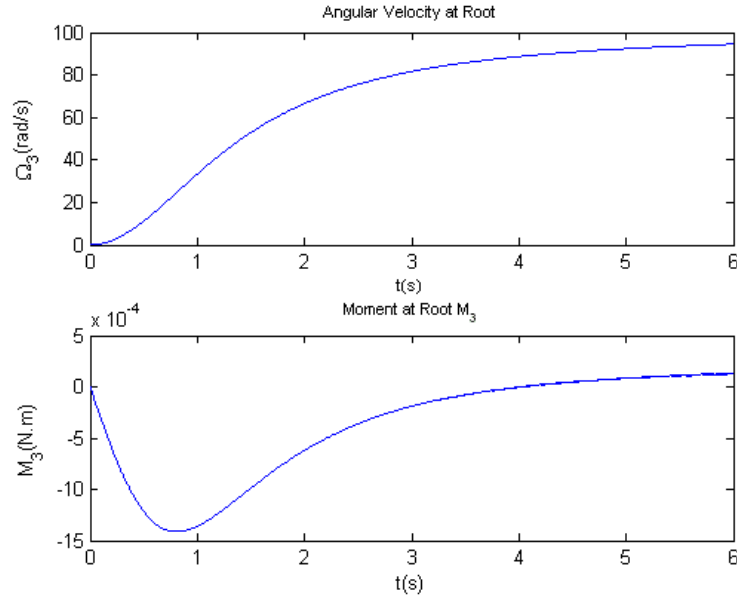
Figure 8. Time history diagram of the angular velocity Ω_3 at the root and the corresponding bending moment at the clamped root.
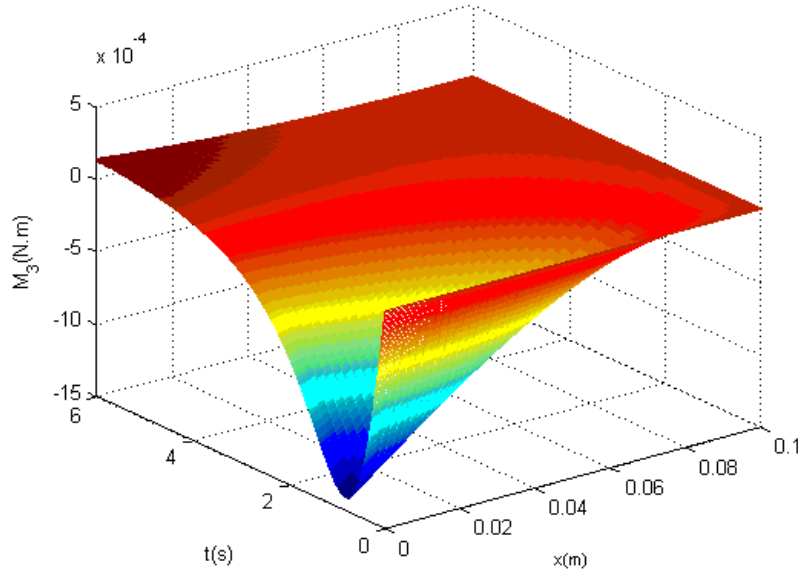
Figure 9. The time-space variation of M_3 at the root.

the method has been discussed in detail in, for example, [Esmailzadeh et al. 1995] and [Zwillinger 1998]. In this section this method is briefly reviewed and in the next section it will be used to provide solutions for the case of perturbed steady state. This perturbed steady state solution has the same logic as the one used in [Shang and Hodges 1995] and [Cesnik et al. 2001] although the mathematical details are different.

The steady state form of the governing equations (1) and (4) are the equations (28), (29), (30), and (31) listed below

$$F_1' = -K_2 F_3 + K_3 F_2 + \Omega_2 P_3 - \Omega_3 P_2 - f_1,$$
$$F_2' = -K_3 F_1 + K_1 F_3 + \Omega_3 P_1 - \Omega_1 P_3 - f_2, \tag{28}$$
$$F_3' = -K_1 F_2 + K_2 F_1 + \Omega_1 P_2 - \Omega_2 P_1 - f_3,$$

$$M_1' = -K_2 M_3 + K_3 M_2 - 2\gamma_{12} F_3 + 2\gamma_{13} F_2 + \Omega_2 H_3 - \Omega_3 H_2 + V_2 P_3 - V_3 P_2 - m_1,$$
$$M_2' = -K_3 M_1 + K_1 M_3 - 2\gamma_{13} F_1 + (1 + \gamma_{11}) F_3 + \Omega_3 H_1 - \Omega_1 H_3 + V_3 P_1 - V_1 P_3 - m_2, \tag{29}$$
$$M_3' = -K_1 M_2 + K_2 M_1 - (1 + \gamma_{11}) F_2 + 2\gamma_{12} F_1 + \Omega_1 H_2 - \Omega_2 H_1 + V_1 P_2 - V_2 P_1 - m_3,$$

$$V_1' = -K_2 V_3 + K_3 V_2 - 2\gamma_{12}\Omega_3 + 2\gamma_{13}\Omega_2,$$
$$V_2' = -K_3 V_1 + K_1 V_3 + (1 + \gamma_{11})\Omega_3 - 2\gamma_{13}\Omega_1, \tag{30}$$
$$V_3' = -K_1 V_2 + K_2 V_1 - (1 + \gamma_{11})\Omega_2 + 2\gamma_{12}\Omega_1,$$

$$\Omega_1' = -K_2\Omega_3 + K_3\Omega_2,$$
$$\Omega_2' = -K_3\Omega_1 + K_1\Omega_3, \tag{31}$$
$$\Omega_3' = -K_1\Omega_2 + K_2\Omega_1.$$

These equations form a system of twelve nonlinear ordinary differential equations in terms of the components of F, M, V and Ω. They should be solved together with the hingeless boundary conditions (20) and (21) at the root and the tip of the beam, respectively. The solution would be the nonlinear steady state response of the rotating composite beam.

To solve this problem, the original nonlninear boundary value problem is converted into an initial value problem, by guessing the unknown values of force and moment components at the root. Next, the Runge–Kutta method is used to solve this initial value problem. If this solution satisfies the force and moment boundary conditions at the tip of the beam, the correct solution to the boundary value problem has been obtained. Otherwise, the assumed initial conditions at the root are in error and should be modified.

The modification is performed iteratively by the use of the Newton–Raphson algorithm. The solution of the initial value problem and the update of the initial conditions are repeated until the correct solution to the problem is obtained.

Denote the known (target) values of the boundary conditions at tip of the beam by β_j, where $j = 1, \ldots, 6$. These conditions are related to physical quantities with current (actual) values g_j. These quantities are used for verifying the implemented initial conditions at the root of the beam.

Also, the unknown initial conditions at the root are shown by α_i, where $i = 1, \ldots, 6$. The guessed values of these variables at the root are denoted by α_{i0}. Each g_j at the free end is a function of the adopted values of the initial conditions. Using those guessed values, a corresponding estimation for β_j at the free end is obtained and denoted by β_{j0}

$$g_j(\alpha_{i0}, L) = \beta_{j0}. \tag{32}$$

The proper initial conditions at the root α_i are those for which g_j becomes equal to the known boundary value β_j. The desired g_j can be related to $g_j(\alpha_{i0}, L)$ using the Taylor series expansion

$$g_j(\alpha_i, L) \approx g_j(\alpha_{i0}, L) + \sum_{i=1}^{6} \frac{\partial g_j}{\partial \alpha_i}(\alpha_{i0}, L) \times \Delta\alpha_i. \tag{33}$$

For ideal initial conditions, the left-hand side of Equation (33) is zero. Expanding the rest

$$0 = \begin{Bmatrix} g_1(\alpha_{i0}, L) \\ g_2(\alpha_{i0}, L) \\ g_3(\alpha_{i0}, L) \\ g_4(\alpha_{i0}, L) \\ g_5(\alpha_{i0}, L) \\ g_6(\alpha_{i0}, L) \end{Bmatrix} + \begin{bmatrix} \partial g_1/\partial\alpha_1 & \partial g_1/\partial\alpha_2 & \partial g_1/\partial\alpha_3 & \partial g_1/\partial\alpha_4 & \partial g_1/\partial\alpha_5 & \partial g_1/\partial\alpha_6 \\ \partial g_2/\partial\alpha_1 & \partial g_2/\partial\alpha_2 & \partial g_2/\partial\alpha_3 & \partial g_2/\partial\alpha_4 & \partial g_2/\partial\alpha_5 & \partial g_2/\partial\alpha_6 \\ \partial g_3/\partial\alpha_1 & \partial g_3/\partial\alpha_2 & \partial g_3/\partial\alpha_3 & \partial g_3/\partial\alpha_4 & \partial g_3/\partial\alpha_5 & \partial g_3/\partial\alpha_6 \\ \partial g_4/\partial\alpha_1 & \partial g_4/\partial\alpha_2 & \partial g_4/\partial\alpha_3 & \partial g_4/\partial\alpha_4 & \partial g_4/\partial\alpha_5 & \partial g_4/\partial\alpha_6 \\ \partial g_5/\partial\alpha_1 & \partial g_5/\partial\alpha_2 & \partial g_5/\partial\alpha_3 & \partial g_5/\partial\alpha_4 & \partial g_5/\partial\alpha_5 & \partial g_5/\partial\alpha_6 \\ \partial g_6/\partial\alpha_1 & \partial g_6/\partial\alpha_2 & \partial g_6/\partial\alpha_3 & \partial g_6/\partial\alpha_4 & \partial g_6/\partial\alpha_5 & \partial g_6/\partial\alpha_6 \end{bmatrix} \begin{Bmatrix} \Delta\alpha_1 \\ \Delta\alpha_2 \\ \Delta\alpha_3 \\ \Delta\alpha_4 \\ \Delta\alpha_5 \\ \Delta\alpha_6 \end{Bmatrix}. \tag{34}$$

The Jacobian matrix in Equation (34) includes the sensitivities of the boundary values at the tip with respect to the assumed initial conditions at the root which are

$$\frac{\partial g_j}{\partial \alpha_2}(\alpha_{i0}, L) = \frac{g_j(\alpha_{10}, \alpha_{20}+\epsilon, \alpha_{30}, \alpha_{40}, \alpha_{50}, \alpha_{60}, L) - g_j(\alpha_{10}, \alpha_{20}-\epsilon, \alpha_{30}, \alpha_{40}, \alpha_{50}, \alpha_{60}, L)}{2\epsilon}. \tag{35}$$

So, the best modifications of the initial conditions are

$$\begin{Bmatrix} \Delta\alpha_1 \\ \Delta\alpha_2 \\ \Delta\alpha_3 \\ \Delta\alpha_4 \\ \Delta\alpha_5 \\ \Delta\alpha_6 \end{Bmatrix} = - \begin{bmatrix} \partial g_1/\partial\alpha_1 & \partial g_1/\partial\alpha_2 & \partial g_1/\partial\alpha_3 & \partial g_1/\partial\alpha_4 & \partial g_1/\partial\alpha_5 & \partial g_1/\partial\alpha_6 \\ \partial g_2/\partial\alpha_1 & \partial g_2/\partial\alpha_2 & \partial g_2/\partial\alpha_3 & \partial g_2/\partial\alpha_4 & \partial g_2/\partial\alpha_5 & \partial g_2/\partial\alpha_6 \\ \partial g_3/\partial\alpha_1 & \partial g_3/\partial\alpha_2 & \partial g_3/\partial\alpha_3 & \partial g_3/\partial\alpha_4 & \partial g_3/\partial\alpha_5 & \partial g_3/\partial\alpha_6 \\ \partial g_4/\partial\alpha_1 & \partial g_4/\partial\alpha_2 & \partial g_4/\partial\alpha_3 & \partial g_4/\partial\alpha_4 & \partial g_4/\partial\alpha_5 & \partial g_4/\partial\alpha_6 \\ \partial g_5/\partial\alpha_1 & \partial g_5/\partial\alpha_2 & \partial g_5/\partial\alpha_3 & \partial g_5/\partial\alpha_4 & \partial g_5/\partial\alpha_5 & \partial g_5/\partial\alpha_6 \\ \partial g_6/\partial\alpha_1 & \partial g_6/\partial\alpha_2 & \partial g_6/\partial\alpha_3 & \partial g_6/\partial\alpha_4 & \partial g_6/\partial\alpha_5 & \partial g_6/\partial\alpha_6 \end{bmatrix}^{-1} \begin{Bmatrix} g_1(\alpha_{i0}, L) \\ g_2(\alpha_{i0}, L) \\ g_3(\alpha_{i0}, L) \\ g_4(\alpha_{i0}, L) \\ g_5(\alpha_{i0}, L) \\ g_6(\alpha_{i0}, L) \end{Bmatrix}. \tag{36}$$

The calculated increments are then used to improve the initial guess values

$$\alpha_i = \alpha_{i0} + \Delta\alpha_i. \tag{37}$$

Now the whole procedure can be repeated using the new set of assumed initial conditions (37). By repeating this algorithm, the unknown initial conditions will gradually improve. The procedure can be terminated when a properly defined convergence criterion like $\sum_{i=1}^{6} |g_j(\alpha_i, L)| < \epsilon$ is satisfied. At this instant, the correct initial conditions and consequently, the correct steady state response of the beam have been obtained with enough accuracy.

6.1. *The isotropic rectangular solid model.* The isotropic rectangular solid model introduced before is considered again. A root angular velocity of $\Omega_3 = 100$ rad/s is applied and the steady state response of the beam is sought.

Figure 10 illustrates the corresponding steady state distribution of the axial force F_1, which is the dominant force, along the beam. To plot this figure, the shooting method and the finite-difference method (FDM), discussed in Sections 3 and 4 were used. It is observed that the transient finite difference solution
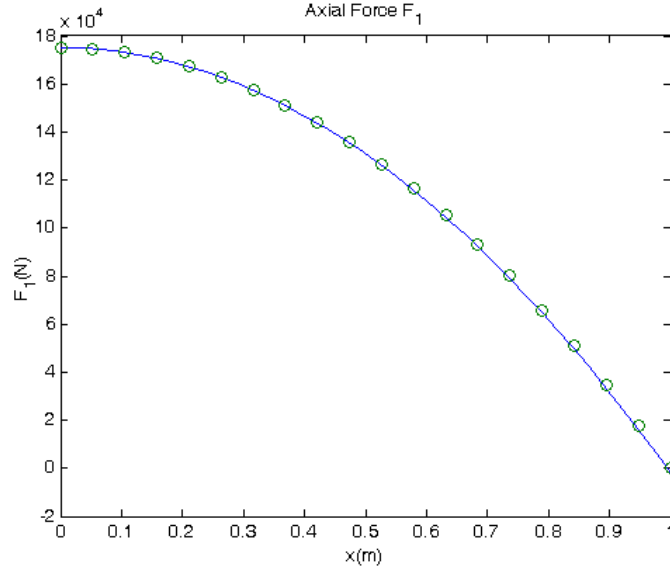
Figure 10. The steady state values of the internal force F_1 along the beam using the shooting method (solid line) the FDM (circles).

has converged to the steady state response obtained by the shooting method and that the two steady state solutions are almost identical.

7. Perturbed steady state analysis

Consider a rotating beam already in its steady state condition. Now the response of this beam to a small input perturbation is of interest. Referring to Figure 2, for every dependent variable one may write

$$\phi\left(x + \tfrac{1}{2}\Delta x, t + \tfrac{1}{2}\Delta t\right) = \phi_{ss}\left(x + \tfrac{1}{2}\Delta x\right) + \phi_p\left(x + \tfrac{1}{2}\Delta x, t + \tfrac{1}{2}\Delta t\right). \tag{38}$$

That is, the whole solution for the variable of interest is the summation of its steady state value and the perturbations about the steady state. Using (38) for the two variables ϕ_m and λ_n, the perturbation part of the generic nonlinear term $\phi_m \lambda_n$ can be written as

$$\left\{\phi_m\left(x + \tfrac{1}{2}\Delta x, t + \tfrac{1}{2}\Delta t\right)\lambda_n\left(x + \tfrac{1}{2}\Delta x, t + \tfrac{1}{2}\Delta t\right)\right\}_p$$
$$= \phi_{m,ss}\left(x + \tfrac{1}{2}\Delta x\right)\lambda_{n,p}\left(x + \tfrac{1}{2}\Delta x, t + \tfrac{1}{2}\Delta t\right) + \phi_{m,p}\left(x + \tfrac{1}{2}\Delta x, t + \tfrac{1}{2}\Delta t\right)\lambda_{n,ss}\left(x + \tfrac{1}{2}\Delta x\right). \tag{39}$$

Or, using (12),

$$\left\{\phi_m\left(x + \tfrac{1}{2}\Delta x, t + \tfrac{1}{2}\Delta t\right)\lambda_n\left(x + \tfrac{1}{2}\Delta x, t + \tfrac{1}{2}\Delta t\right)\right\}_p$$
$$= \tfrac{1}{8}\left[(\phi_{m,ss,i+1} + \phi_{m,ss,i})(\lambda^+_{n,p,i+1} + \lambda^+_{n,p,i} + \lambda_{n,p,i+1} + \lambda_{n,p,i})\right]$$
$$+ \tfrac{1}{8}\left[(\lambda_{n,ss,i+1} + \lambda_{n,ss,i})(\phi^+_{m,p,i+1} + \phi^+_{m,p,i} + \phi_{m,p,i+1} + \phi_{m,p,i})\right]. \tag{40}$$

Implementation of (40) puts the dynamic governing Equations (1), (2), (4), (5) and (7)$_1$ into matrix form:

$$A_{ss,i}q^+_{p,i} + B_{ss,i}q^+_{p,i+1} = J_{ss,i}, \tag{41}$$

where q_p contains the perturbations of the variables given in (18). The rest of the solution is similar to that of Section 4.

It should be pointed out that the present method provides solutions only in the vicinity of the steady state solution. Whereas, the previously mentioned FDM obtains solutions for the whole dynamics of the accelerating beam up to full speed.

7.1. *The isotropic rectangular solid model.* The isotropic rectangular solid model introduced before is considered. The steady state angular velocity is $\Omega_3 = 93.5$ rad/s and a root angular velocity perturbation of

$$\Omega_{3,p,1} = \sin(93.5t) \text{ rad/s} \tag{42}$$

is applied at the root (that is, at node number 1) as shown in Figure 11. The implementation of the above-mentioned method results in the perturbations of all of the dependent variables.

Having calculated the perturbations of all of the dependent variables, one may now use (38) in order to get the complete dynamic response. In Figures 11 to 14, the steady state values are plotted with solid lines until $t = 2.667$ s. At this instant, the angular velocity perturbation given by (42) is applied at the root of the beam. In Figures 12 to 14, the effects of this perturbation on bending moment and force components at the root have been illustrated with solid lines.

Alternatively, one may use the algorithm discussed in Section 4 for an accelerating beam to do the same job. In this case, the beam starts to rotate from rest and at $t = 2.667$ s when the beam has an
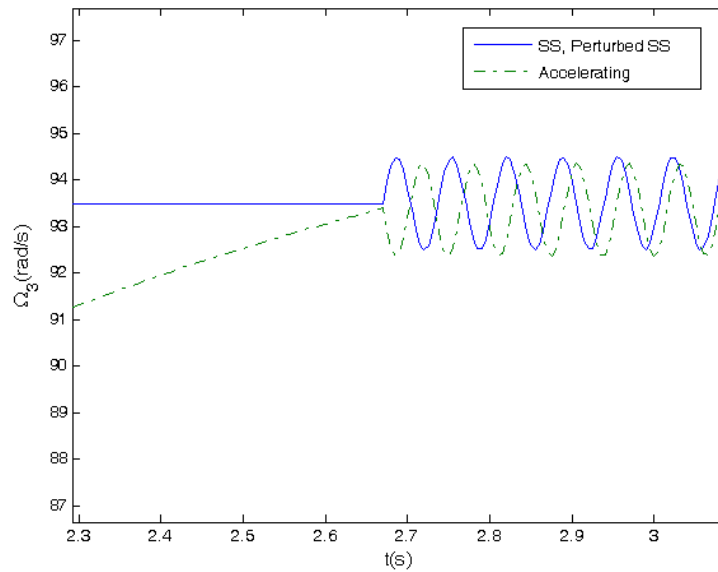
Figure 11. Steady state, accelerating, and perturbed steady state angular velocities at the root.
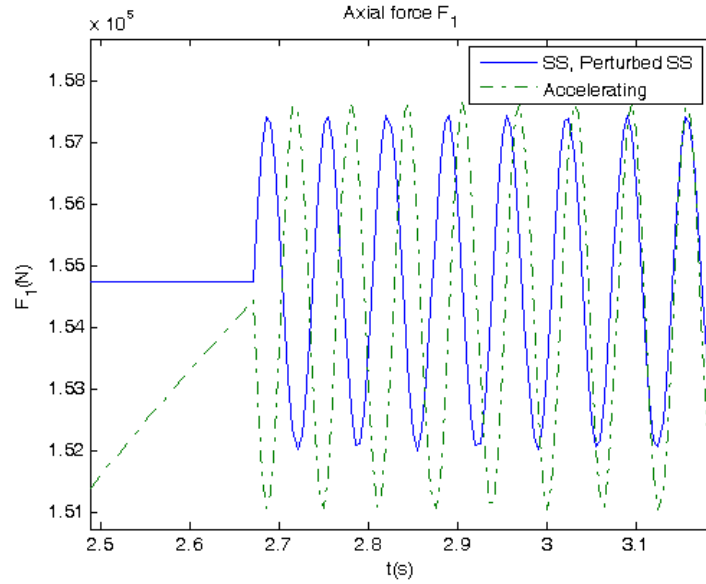
Figure 12. Steady state, accelerating and perturbed axial force at the root.
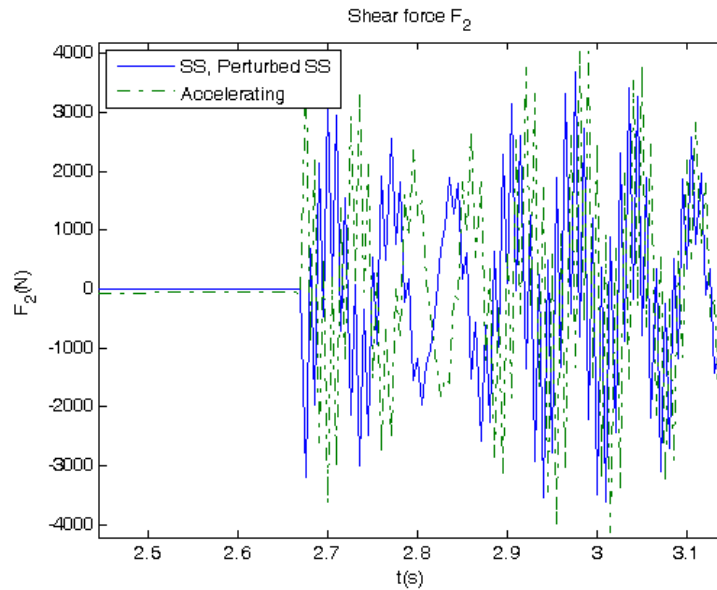
Figure 13. Steady state, accelerating and perturbed shear force at the root.

angular velocity of 93.5 rad/s, the perturbation shown in (42) is applied. In Figures 12 to 14 the results corresponding to this algorithm are plotted with dash-dotted lines.

It can be observed that the predictions of the perturbed steady state method discussed in this section are close to those of the accelerating beam presented in Section 4. The results of such an analysis can
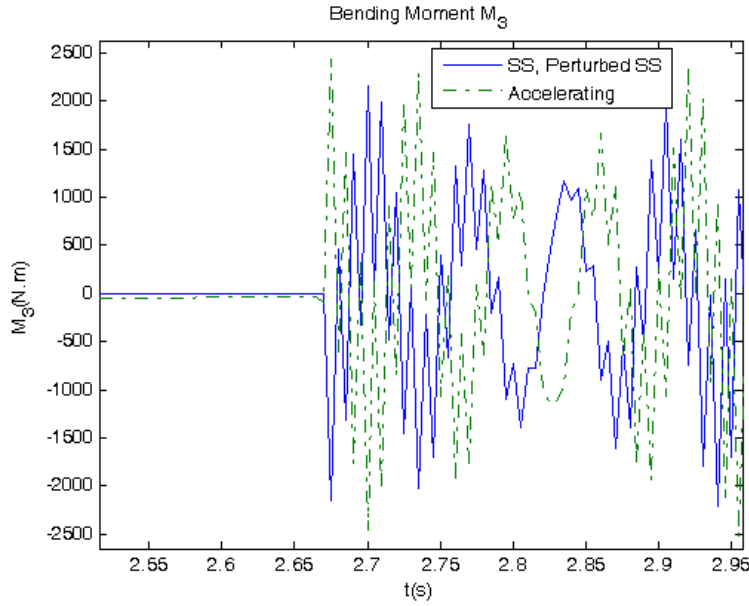
Figure 14. Steady state, accelerating and perturbed bending moment at the root.

therefore be used in order to estimate the degree of sensitivity of each of the output variables to input perturbations.

8. The one-dimensional beam analysis with embedded actuators

For linear piezoelectric materials, the interaction between the electrical and mechanical variables can be described by linear relations. The constitutive equations can be written in matrix form as

$$\{S\} = [s]\{T\} + [d]^t\{E\}, \tag{43}$$

$$\{D\} = [d]\{T\} + [\varepsilon]\{E\}, \tag{44}$$

where S is the strain, D is the electric displacement (charge per unit area), s is the compliance (strain per unit stress), d is the piezoelectric moduli (m/V), and ε is the piezodielectric matrix (F/m). Also, T is the stress vector and E is the electric field intensity (V/m).

With actuators in the structure, the applied force and moment vector per unit length on the structure at every location and every time can be written as the summation of a mechanically applied component and one due to the actuators:

$$\left\{ \begin{matrix} f \\ m \end{matrix} \right\} = \left\{ \begin{matrix} f_M \\ m_M \end{matrix} \right\} + \left\{ \begin{matrix} f_A \\ m_A \end{matrix} \right\}. \tag{45}$$

For a certain actuation scenario, UM/VABS can provide the vector of actuator forces for each active material. Therefore, the whole actuator force is obtained by adding up all of these forces. Substitution

of (45) into (1) gives

$$F' + \tilde{K}F + (f_M + f_A) = \dot{P} + \tilde{\Omega}P \tag{46}$$

$$M' + \tilde{K}M + (\tilde{e}_1 + \tilde{\gamma})F + (m_M + m_A) = \dot{H} + \tilde{\Omega}H + \tilde{V}P. \tag{47}$$

8.1. *Static active composite airfoil.* Consider the case of actuation of piezocomposite actuators embedded in a composite wing similar to what is discussed in [Cesnik et al. 2003]. The UM/VABS input file for this case is among the examples provided with the software. The airfoil is a NACA 4415 airfoil with double cells and has a spar located at 38.6% chord from the leading edge, as shown in Figure 15.

Figure 16 illustrates the ply lay-up definitions and orientation angles on the section. A passive 0° ply is used to enclose the cross-section. The inner layers consist of 90°, +45°, −45° and 0° active plies (that is, [0, +90, +45, −45, 0]). The angles are measured with respect to the axis along the wing span. The spar has no active layers.

The material properties of the applied passive and active materials are shown in Table 2. Each layer has a thickness of 3429 μm and a constant electric potential of +1000 V between the two electrodes at a distance of 1100 μm has been applied to the actuators.
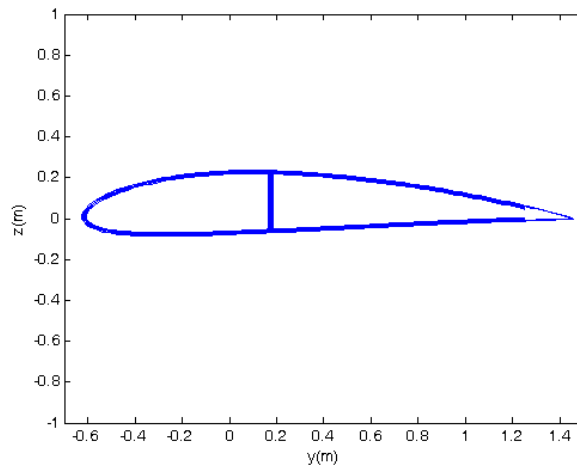
Figure 15. Cross-section of the airfoil.
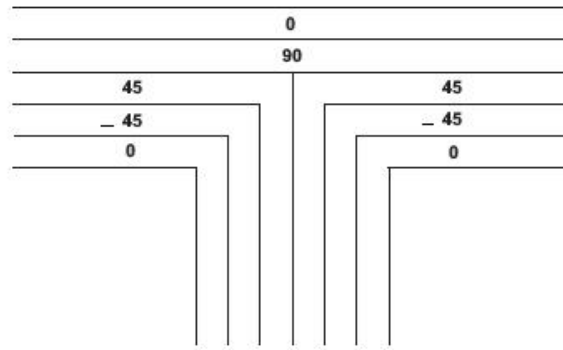
Figure 16. Ply layups and orientation angles of the airfoil cross-section [Cesnik et al. 2003].

	E_{11} GPa	E_{22} GPa	E_{33} GPa	G_{12} GPa	G_{13} GPa	G_{23} GPa	ν_{12}	ν_{13}	ν_{23}	ρ kg/m^3	d_{11} pm/V	d_{12} pm/V	d_{13} pm/V
Passive										1716	—	—	—
Active	19.3	9.8	9.8	5.5	5.5	4.4	0.35	0.35	0.496	4060	310	−130	−130

Table 2. Material properties of active composite airfoil [Cesnik et al. 2003].

Using these data, the stiffness matrix of the cross-section was calculated by UM/VABS as

$$S = \begin{bmatrix}
1.12577 \times 10^9 & 3.615437 \times 10^3 & -1.28217 \times 10^4 & -1.64732 \times 10^5 & -2.168324 \times 10^5 & -5.681057 \times 10^6 \\
3.615437 \times 10^3 & 3.15555 \times 10^8 & -4.04582 \times 10^5 & -1.0509 \times 10^7 & 7.05125 \times 10^4 & 4.33983 \times 10^3 \\
-1.28217 \times 10^4 & -4.04582 \times 10^5 & 2.79485 \times 10^7 & -1.06215 \times 10^7 & 5.81197 \times 10^2 & 1.08681 \times 10^4 \\
-1.64732 \times 10^5 & -1.0509 \times 10^7 & -1.06215 \times 10^7 & 1.75149 \times 10^7 & -2.4470 \times 10^3 & 2.00316 \times 10^3 \\
-2.168324 \times 10^5 & 7.05125 \times 10^4 & 5.81197 \times 10^2 & -2.4470 \times 10^3 & 1.39200 \times 10^7 & 1.16753 \times 10^5 \\
-5.681057 \times 10^6 & 4.33983 \times 10^3 & 1.08681 \times 10^4 & 2.00316 \times 10^3 & 1.16753 \times 10^5 & 3.3672 \times 10^8
\end{bmatrix} \tag{48}$$

Using UM/VABS, forces, moments, and stress components generated as a result of activating plies at various directions were calculated and some of the results are listed in Table 3. As expected, the active spanwise ply actuation generates the maximum axial force F_1. Also, the $\pm 45°$ plies are mainly responsible for twist generation.

Figure 17 illustrates the distribution of various stress components across the cross-section when only the 90° plies are activated by the 1000 V actuation.
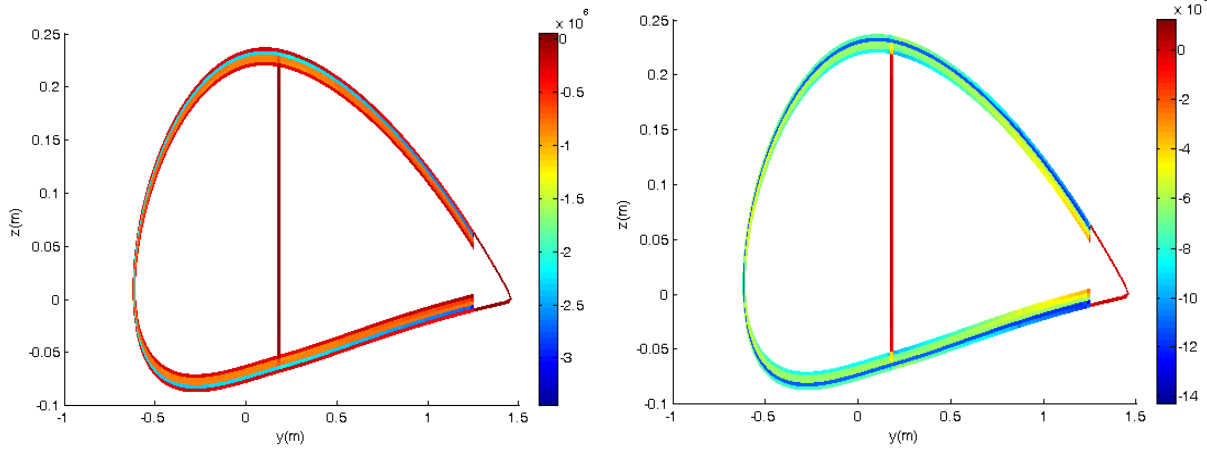
Figure 17. Distribution of the T_{11} (left) and T_{22} (right) stress component due to 1000 V actuation of the 90° plies (distorted image for clarity).

8.2. *Steady state response of rotating active airfoil.* Consider the case of actuation of piezocomposite actuators embedded in the composite airfoil discussed before. This time, however, the 3 m beam is rotating at an angular velocity of 100 rad/s and its steady state response under different actuation scenarios is of interest. To this end the method discussed in Section 6 is utilized. Using $\mu = 248.35$ kg/m, the

	0° ply actuation	90° ply actuation	±45° ply actuation	all together
extension (N/m)	71042	−21653	49705	99095
shear F_2 (N/m)	0.603	5.089	2.658	8.349
shear F_3 (N/m)	1.095	19.705	−16.799	4.002
twist (N.m/m)	−0.288	15.67	−238.13	−222.746
bending M_2 (N.m/m)	−41.44	15.19	−33.03	−59.28
bending M_3 (N.m/m)	454.29	−409.01	575.276	620.557

Table 3. Actuation forces and moments generated by active plies at various directions.

UM/VABS two-dimensional analysis resulted in the inertia matrix

$$i = \begin{bmatrix} 77.255 & 0 & 0 \\ 0 & 3.1362 & -0.20052 \\ 0 & -0.20052 & 74.119 \end{bmatrix}. \tag{49}$$

Considering no activation, the steady state response of the beam was obtained. To analyze the effect of coupling, two cases were considered. First, all of the terms in the stiffness and mass matrices were included in the analysis. Then, off-diagonal terms were ignored. The difference of these two solutions provides an overall estimation of the impact of coupling. The results are plotted in Figure 18.
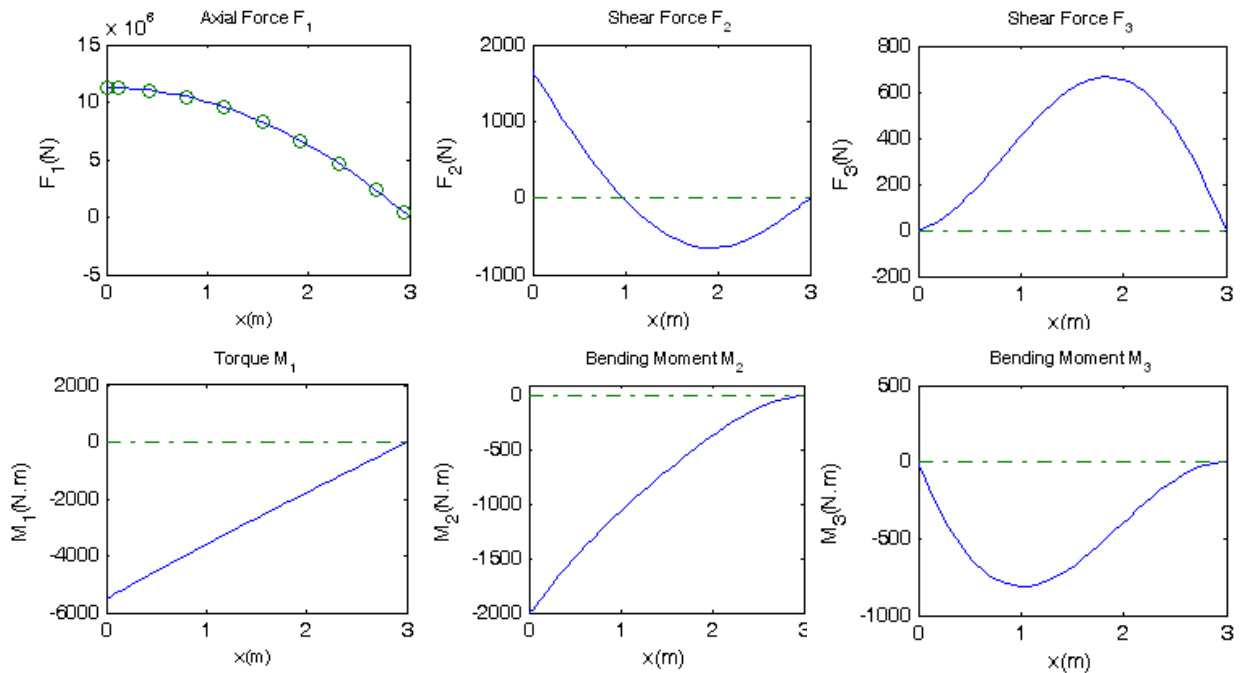
Figure 18. Variation of internal force components (top row) and internal moment components (bottom row) along the beam. The coupled solution is indicated by a solid line, the uncoupled solution by a dashed line or circles.
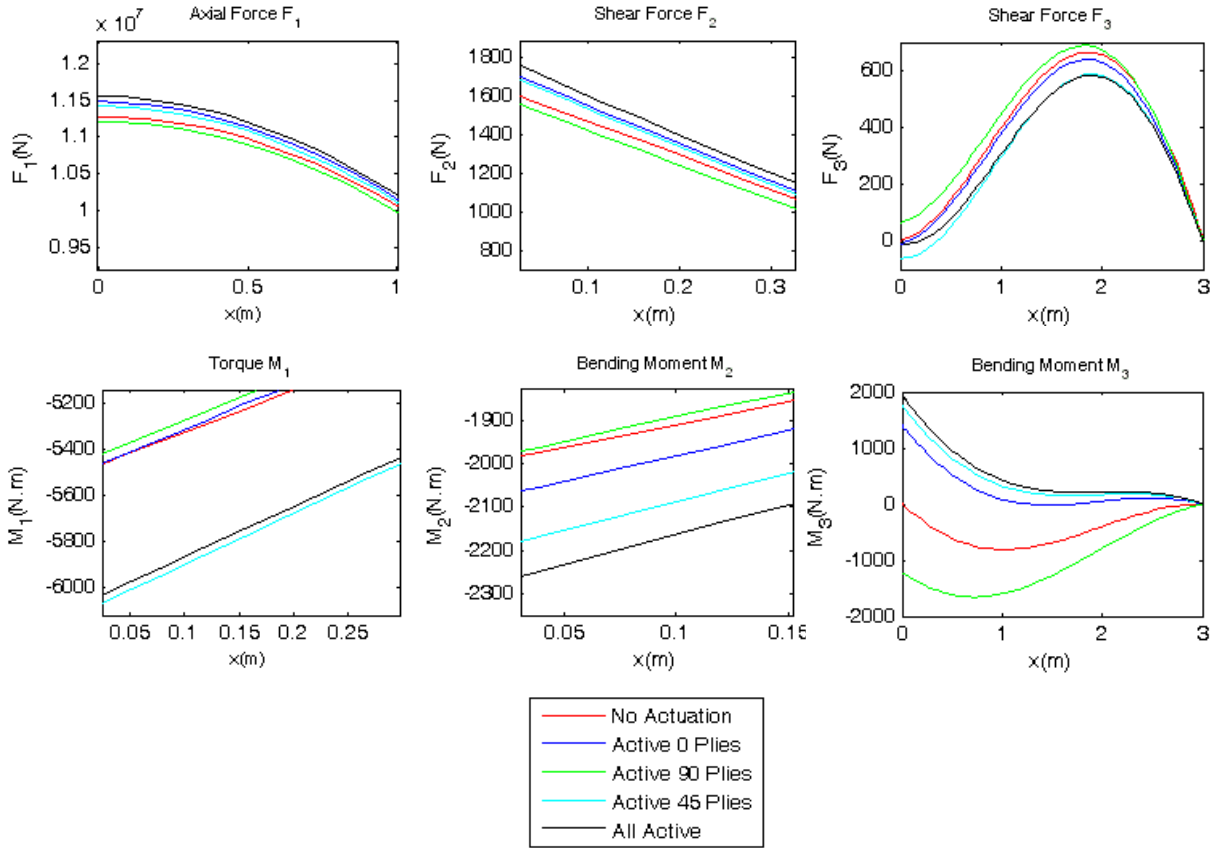
Figure 19. Steady-state variation of internal force components (top row) and internal moment components (bottom row) along the beam, due to various modes of activation of anisotropic piezocomposite actuators (zoomed).

Next, the effect of the activation of each active ply was investigated. To this end, these plies were activated one by one by applying a +1000 V potential to them and the corresponding steady state solutions were obtained. Finally, all of the active plies were activated simultaneously. The results are plotted in Figure 19.

These diagrams can be used for controlling the response of the beam and the load distribution along it. It is observed that the actuators have significant controllability on M_3, but little control on F_1.

9. Conclusions

The structural analysis of geometrically nonlinear passive and active rotating composite beams was presented. The analysis included nonlinear dynamics of accelerating rotating beams and obtaining their transient and steady state responses.

The specific problem considered involved an accelerating rotating beam that starts from rest and at full speed converged to its steady state condition. The steady state behavior was obtained by solving the time-independent form of the governing nonlinear intrinsic differential equations of a beam. The

resulting boundary value problem was solved using the shooting method. The result compared very well with the solution obtained using the FDM.

The next step was the analysis of the effect of input perturbations on the response of rotating beams which are already in their steady state condition. The solution was performed using perturbations and the results were verified against those of the FDM.

Finally, the effect of inclusion of embedded anisotropic piezocomposite actuators in the beam structure was analyzed. In this way, the effect of inclusion of active materials at different orientations on the beam response and on the distributions of stress and stress resultants were illustrated.

Index of notation

A	cross-sectional area of the undeformed beam in x_2-x_3 plane	e_1	$[1\ 0\ 0]^T$
f	applied forces per unit length	F	internal forces
H	sectional angular momenta	g	determinant of metric tensor in curvilinear coordinates
i_2, i_3	cross-sectional mass moment	i_{23}	cross-sectional product of inertia
$\mathcal{H}$	kinetic energy function	$K = k + \bar{\kappa}$	deformed beam curvature vector
k	undeformed beam curvature vector	L	length of the beam
M	internal moments	m	applied moments per unit length
N	number of nodes	P	sectional linear momenta
S	stiffness matrix	t	time
V	velocity field	x_i	global system of coordinates
x_1	axis along the beam	x_2, x_3	cross-sectional axes
$\bar{x}_2, \bar{x}_3$	offsets from the reference line of the cross-sectional mass center	γ	$[\gamma_{11}\ 2\gamma_{12}\ 2\gamma_{13}]^T$
		Δ	identity matrix
κ_1	elastic twist	κ_i	elastic bending curvatures, $i = 2, 3$
μ	mass per unit length	ρ	mass density
Ω	angular velocity	$\check{\ }$	perturbations in space
$\hat{\ }$	perturbations in time	$'$	x_1-derivative
$\dot{\ }$	time derivative	$\tilde{\ }$	contraction with last index of $-e_{ijk}$
$\langle\langle u \rangle\rangle$	$\int_A u \sqrt{g}\, dx_2\, dx_3$	$\sqrt{g}$	$1 - x_2 k_3 - x_3 k_2$

Appendix: Vector J and matrices A, B from Section 4

Recall that a superscript + refers to the next time step. Entries not shown are equal to zero.

$$J_i(1) = \tfrac{1}{2}(F_{1,i} - F_{1,i+1})/\Delta x + \tfrac{1}{16}(\kappa_{3,i+1}F_{2,i+1} + \kappa_{3,i+1}F_{2,i} + \kappa_{3,i}F_{2,i+1} - 3\kappa_{3,i}F_{2,i})$$
$$- \tfrac{1}{16}(\kappa_{2,i+1}F_{3,i+1} + \kappa_{2,i+1}F_{3,i} + \kappa_{2,i}F_{3,i+1} - 3\kappa_{2,i}F_{3,i}) - \tfrac{1}{4}(f_{1,i+1} + f_{1,i} + f_{1,i+1}^+ + f_{1,i}^+)$$
$$- \tfrac{1}{2}(P_{1,i} + P_{1,i+1})/\Delta t - \tfrac{1}{16}(\Omega_{3,i+1}P_{2,i+1} + \Omega_{3,i+1}P_{2,i} + \Omega_{3,i}P_{2,i+1} - 3\Omega_{3,i}P_{2,i})$$
$$+ \tfrac{1}{16}(\Omega_{2,i+1}P_{3,i+1} + \Omega_{2,i+1}P_{3,i} + \Omega_{2,i}P_{3,i+1} - 3\Omega_{2,i}P_{3,i})$$

$$J_i(2) = \tfrac{1}{2}(F_{2,i} - F_{2,i+1})/\Delta x + \tfrac{1}{16}(\kappa_{1,i+1}F_{3,i+1} + \kappa_{1,i+1}F_{3,i} + \kappa_{1,i}F_{3,i+1} - 3\kappa_{1,i}F_{3,i})$$
$$- \tfrac{1}{16}(\kappa_{3,i+1}F_{1,i+1} + \kappa_{3,i+1}F_{1,i} + \kappa_{3,i}F_{1,i+1} - 3\kappa_{3,i}F_{1,i}) - \tfrac{1}{4}(f_{2,i+1} + f_{2,i} + f_{2,i+1}^+ + f_{2,i}^+)$$
$$- \tfrac{1}{2}(P_{2,i} + P_{2,i+1})/\Delta t - \tfrac{1}{16}(\Omega_{1,i+1}P_{3,i+1} + \Omega_{1,i+1}P_{3,i} + \Omega_{1,i}P_{3,i+1} - 3\Omega_{1,i}P_{3,i})$$
$$+ \tfrac{1}{16}(\Omega_{3,i+1}P_{1,i+1} + \Omega_{3,i+1}P_{1,i} + \Omega_{3,i}P_{1,i+1} - 3\Omega_{3,i}P_{1,i})$$

$$J_i(3) = \tfrac{1}{2}(F_{3,i} - F_{3,i+1})/\Delta x + \tfrac{1}{16}(\kappa_{2,i+1}F_{1,i+1} + \kappa_{2,i+1}F_{1,i} + \kappa_{2,i}F_{1,i+1} - 3\kappa_{2,i}F_{1,i})$$
$$- \tfrac{1}{16}(\kappa_{1,i+1}F_{2,i+1} + \kappa_{1,i+1}F_{2,i} + \kappa_{1,i}F_{2,i+1} - 3\kappa_{1,i}F_{2,i}) - \tfrac{1}{4}(f_{3,i+1} + f_{3,i} + f_{3,i+1}^+ + f_{3,i}^+)$$
$$- \tfrac{1}{2}(P_{3,i} + P_{3,i+1})/\Delta t - \tfrac{1}{16}(\Omega_{2,i+1}P_{1,i+1} + \Omega_{2,i+1}P_{1,i} + \Omega_{2,i}P_{1,i+1} - 3\Omega_{2,i}P_{1,i})$$
$$+ \tfrac{1}{16}(\Omega_{1,i+1}P_{2,i+1} + \Omega_{1,i+1}P_{2,i} + \Omega_{1,i}P_{2,i+1} - 3\Omega_{1,i}P_{2,i})$$

$$J_i(4) = \tfrac{1}{2}(M_{1,i} - M_{1,i+1})/\Delta x + \tfrac{1}{16}(\kappa_{3,i+1}M_{2,i+1} + \kappa_{3,i+1}M_{2,i} + \kappa_{3,i}M_{2,i+1} - 3\kappa_{3,i}M_{2,i})$$
$$- \tfrac{1}{16}(\kappa_{2,i+1}M_{3,i+1} + \kappa_{2,i+1}M_{3,i} + \kappa_{2,i}M_{3,i+1} - 3\kappa_{2,i}M_{3,i}) - \tfrac{1}{4}(m_{1,i+1} + m_{1,i} + m_{1,i+1}^+ + m_{1,i}^+)$$
$$- \tfrac{1}{2}(H_{1,i} + H_{1,i+1})/\Delta t - \tfrac{1}{16}(\Omega_{3,i+1}H_{2,i+1} + \Omega_{3,i+1}H_{2,i} + \Omega_{3,i}H_{2,i+1} - 3\Omega_{3,i}H_{2,i})$$
$$+ \tfrac{1}{16}(\Omega_{2,i+1}H_{3,i+1} + \Omega_{2,i+1}H_{3,i} + \Omega_{2,i}H_{3,i+1} - 3\Omega_{2,i}H_{3,i})$$
$$+ \tfrac{1}{8}(\gamma_{13,i+1}F_{2,i+1} + \gamma_{13,i+1}F_{2,i} + \gamma_{13,i}F_{2,i+1} - 3\gamma_{13,i}F_{2,i})$$
$$- \tfrac{1}{8}(\gamma_{12,i+1}F_{3,i+1} + \gamma_{12,i+1}F_{3,i} + \gamma_{12,i}F_{3,i+1} - 3\gamma_{12,i}F_{3,i})$$
$$- \tfrac{1}{16}(V_{3,i+1}P_{2,i+1} + V_{3,i+1}P_{2,i} + V_{3,i}P_{2,i+1} - 3V_{3,i}P_{2,i}) + \tfrac{1}{16}(V_{2,i+1}P_{3,i+1} + V_{2,i+1}P_{3,i} + V_{2,i}P_{3,i+1} - 3V_{2,i}P_{3,i})$$

$$J_i(5) = \tfrac{1}{2}(M_{2,i} - M_{2,i+1})/\Delta x + \tfrac{1}{16}(\kappa_{1,i+1}M_{3,i+1} + \kappa_{1,i+1}M_{3,i} + \kappa_{1,i}M_{3,i+1} - 3\kappa_{1,i}M_{3,i})$$
$$- \tfrac{1}{16}(\kappa_{3,i+1}M_{1,i+1} + \kappa_{3,i+1}M_{1,i} + \kappa_{3,i}M_{1,i+1} - 3\kappa_{3,i}M_{1,i}) - \tfrac{1}{4}(m_{2,i+1} + m_{2,i} + m_{2,i+1}^+ + m_{2,i}^+)$$
$$- \tfrac{1}{2}(H_{2,i} + H_{2,i+1})/\Delta t - \tfrac{1}{16}(\Omega_{1,i+1}H_{3,i+1} + \Omega_{1,i+1}H_{3,i} + \Omega_{1,i}H_{3,i+1} - 3\Omega_{1,i}H_{3,i})$$
$$+ \tfrac{1}{16}(\Omega_{3,i+1}H_{1,i+1} + \Omega_{3,i+1}H_{1,i} + \Omega_{3,i}H_{1,i+1} - 3\Omega_{3,i}H_{1,i}) + \tfrac{1}{4}(F_{3,i} + F_{3,i+1})$$
$$+ \tfrac{1}{16}(\gamma_{11,i+1}F_{3,i+1} + \gamma_{11,i+1}F_{3,i} + \gamma_{11,i}F_{3,i+1} - 3\gamma_{11,i}F_{3,i})$$
$$- \tfrac{1}{8}(\gamma_{13,i+1}F_{1,i+1} + \gamma_{13,i+1}F_{1,i} + \gamma_{13,i}F_{1,i+1} - 3\gamma_{13,i}F_{1,i})$$
$$- \tfrac{1}{16}(V_{1,i+1}P_{3,i+1} + V_{1,i+1}P_{3,i} + V_{1,i}P_{3,i+1} - 3V_{1,i}P_{3,i}) + \tfrac{1}{16}(V_{3,i+1}P_{1,i+1} + V_{3,i+1}P_{1,i} + V_{3,i}P_{1,i+1} - 3V_{3,i}P_{1,i})$$

$$J_i(6) = \tfrac{1}{2}(M_{3,i} - M_{3,i+1})/\Delta x + \tfrac{1}{16}(\kappa_{2,i+1}M_{1,i+1} + \kappa_{2,i+1}M_{1,i} + \kappa_{2,i}M_{1,i+1} - 3\kappa_{2,i}M_{1,i})$$
$$- \tfrac{1}{16}(\kappa_{1,i+1}M_{2,i+1} + \kappa_{1,i+1}M_{2,i} + \kappa_{1,i}M_{2,i+1} - 3\kappa_{1,i}M_{2,i}) - \tfrac{1}{4}(m_{3,i+1} + m_{3,i} + m_{3,i+1}^+ + m_{3,i}^+)$$
$$- \tfrac{1}{2}(H_{3,i} + H_{3,i+1})/\Delta t - \tfrac{1}{16}(\Omega_{2,i+1}H_{1,i+1} + \Omega_{2,i+1}H_{1,i} + \Omega_{2,i}H_{1,i+1} - 3\Omega_{2,i}H_{1,i})$$
$$+ \tfrac{1}{16}(\Omega_{1,i+1}H_{2,i+1} + \Omega_{1,i+1}H_{2,i} + \Omega_{1,i}H_{2,i+1} - 3\Omega_{1,i}H_{2,i}) - \tfrac{1}{4}(F_{2,i} + F_{2,i+1})$$
$$+ \tfrac{1}{16}(\gamma_{11,i+1}F_{2,i+1} + \gamma_{11,i+1}F_{2,i} + \gamma_{11,i}F_{2,i+1} - 3\gamma_{11,i}F_{2,i})$$
$$+ \tfrac{1}{8}(\gamma_{12,i+1}F_{1,i+1} + \gamma_{12,i+1}F_{1,i} + \gamma_{12,i}F_{1,i+1} - 3\gamma_{12,i}F_{1,i})$$
$$- \tfrac{1}{16}(V_{2,i+1}P_{1,i+1} + V_{2,i+1}P_{1,i} + V_{2,i}P_{1,i+1} - 3V_{2,i}P_{1,i}) + \tfrac{1}{16}(V_{1,i+1}P_{2,i+1} + V_{1,i+1}P_{2,i} + V_{1,i}P_{2,i+1} - 3V_{1,i}P_{2,i})$$

$$J_i(7) = \tfrac{1}{2}(V_{1,i} - V_{1,i+1})/\Delta x + \tfrac{1}{16}(\kappa_{3,i+1}V_{2,i+1} + \kappa_{3,i+1}V_{2,i} + \kappa_{3,i}V_{2,i+1} - 3\kappa_{3,i}V_{2,i})$$
$$- \tfrac{1}{16}(\kappa_{2,i+1}V_{3,i+1} + \kappa_{2,i+1}V_{3,i} + \kappa_{2,i}V_{3,i+1} - 3\kappa_{2,i}V_{3,i})$$
$$+ \tfrac{1}{8}(\gamma_{13,i+1}\Omega_{2,i+1} + \gamma_{13,i+1}\Omega_{2,i} + \gamma_{13,i}\Omega_{2,i+1} - 3\gamma_{13,i}\Omega_{2,i})$$
$$- \tfrac{1}{8}(\gamma_{12,i+1}\Omega_{3,i+1} + \gamma_{12,i+1}\Omega_{3,i} + \gamma_{12,i}\Omega_{3,i+1} - 3\gamma_{12,i}\Omega_{3,i}) - \tfrac{1}{2}(\gamma_{11,i} + \gamma_{11,i+1})/\Delta t$$

$$J_i(8) = \tfrac{1}{2}(V_{2,i} - V_{2,i+1})/\Delta x + \tfrac{1}{16}(\kappa_{1,i+1}V_{3,i+1} + \kappa_{1,i+1}V_{3,i} + \kappa_{1,i}V_{3,i+1} - 3\kappa_{1,i}V_{3,i})$$
$$- \tfrac{1}{16}(\kappa_{3,i+1}V_{1,i+1} + \kappa_{3,i+1}V_{1,i} + \kappa_{3,i}V_{1,i+1} - 3\kappa_{3,i}V_{1,i}) + \tfrac{1}{4}(\Omega_{3,i} + \Omega_{3,i+1})$$
$$+ \tfrac{1}{16}(\gamma_{11,i+1}\Omega_{3,i+1} + \gamma_{11,i+1}\Omega_{3,i} + \gamma_{11,i}\Omega_{3,i+1} - 3\gamma_{11,i}\Omega_{3,i})$$
$$- \tfrac{1}{8}(\gamma_{13,i+1}\Omega_{1,i+1} + \gamma_{13,i+1}\Omega_{1,i} + \gamma_{13,i}\Omega_{1,i+1} - 3\gamma_{13,i}\Omega_{1,i}) - (\gamma_{12,i} + \gamma_{12,i+1})/\Delta t$$

$$J_i(9) = \tfrac{1}{2}(V_{3,i} - V_{3,i+1})/\Delta x + \tfrac{1}{16}(\kappa_{2,i+1}V_{1,i+1} + \kappa_{2,i+1}V_{1,i} + \kappa_{2,i}V_{1,i+1} - 3\kappa_{2,i}V_{1,i})$$
$$- \tfrac{1}{16}(\kappa_{1,i+1}V_{2,i+1} + \kappa_{1,i+1}V_{2,i} + \kappa_{1,i}V_{2,i+1} - 3\kappa_{1,i}V_{2,i}) - \tfrac{1}{4}(\Omega_{2,i} + \Omega_{2,i+1})$$
$$- \tfrac{1}{16}(\gamma_{11,i+1}\Omega_{2,i+1} + \gamma_{11,i+1}\Omega_{2,i} + \gamma_{11,i}\Omega_{2,i+1} - 3\gamma_{11,i}\Omega_{2,i})$$
$$+ \tfrac{1}{8}(\gamma_{12,i+1}\Omega_{1,i+1} + \gamma_{12,i+1}\Omega_{1,i} + \gamma_{12,i}\Omega_{1,i+1} - 3\gamma_{12,i}\Omega_{1,i}) - (\gamma_{13,i} + \gamma_{13,i+1})/\Delta t$$

$$J_i(10) = \tfrac{1}{2}(\Omega_{1,i} - \Omega_{1,i+1})/\Delta x + \tfrac{1}{16}(\kappa_{3,i+1}\Omega_{2,i+1} + \kappa_{3,i+1}\Omega_{2,i} + \kappa_{3,i}\Omega_{2,i+1} - 3\kappa_{3,i}\Omega_{2,i})$$
$$- \tfrac{1}{16}(\kappa_{2,i+1}\Omega_{3,i+1} + \kappa_{2,i+1}\Omega_{3,i} + \kappa_{2,i}\Omega_{3,i+1} - 3\kappa_{2,i}\Omega_{3,i}) - \tfrac{1}{2}(\kappa_{1,i} + \kappa_{1,i+1})/\Delta t$$

$$J_i(11) = \tfrac{1}{2}(\Omega_{2,i} - \Omega_{2,i+1})/\Delta x + \tfrac{1}{16}(\kappa_{1,i+1}\Omega_{3,i+1} + \kappa_{1,i+1}\Omega_{3,i} + \kappa_{1,i}\Omega_{3,i+1} - 3\kappa_{1,i}\Omega_{3,i})$$
$$- \tfrac{1}{16}(\kappa_{3,i+1}\Omega_{1,i+1} + \kappa_{3,i+1}\Omega_{1,i} + \kappa_{3,i}\Omega_{1,i+1} - 3\kappa_{3,i}\Omega_{1,i}) - \tfrac{1}{2}(\kappa_{2,i} + \kappa_{2,i+1})/\Delta t$$

$$J_i(12) = \tfrac{1}{2}(\Omega_{3,i} - \Omega_{3,i+1})/\Delta x + \tfrac{1}{16}(\kappa_{2,i+1}\Omega_{1,i+1} + \kappa_{2,i+1}\Omega_{1,i} + \kappa_{2,i}\Omega_{1,i+1} - 3\kappa_{2,i}\Omega_{1,i})$$
$$- \tfrac{1}{16}(\kappa_{1,i+1}\Omega_{2,i+1} + \kappa_{1,i+1}\Omega_{2,i} + \kappa_{1,i}\Omega_{2,i+1} - 3\kappa_{1,i}\Omega_{2,i}) - \tfrac{1}{2}(\kappa_{3,i} + \kappa_{3,i+1})/\Delta t$$

$$J_i(13) = -\tfrac{1}{4}(P_{1,i} + P_{1,i+1}) + \tfrac{1}{4}\mu(V_{1,i} + V_{1,i+1}) + \tfrac{1}{4}\mu\bar{x}_3(\Omega_{2,i} + \Omega_{2,i+1}) - \tfrac{1}{4}\mu\bar{x}_2(\Omega_{3,i} + \Omega_{3,i+1})$$

$$J_i(14) = -\tfrac{1}{4}(P_{2,i} + P_{2,i+1}) + \tfrac{1}{4}\mu(V_{2,i} + V_{2,i+1}) - \tfrac{1}{4}\mu\bar{x}_3(\Omega_{1,i} + \Omega_{1,i+1})$$

$$J_i(15) = -\tfrac{1}{4}(P_{3,i} + P_{3,i+1}) + \tfrac{1}{4}\mu(V_{3,i} + V_{3,i+1}) + \tfrac{1}{4}\mu\bar{x}_2(\Omega_{1,i} + \Omega_{1,i+1})$$

$$J_i(16) = -\tfrac{1}{4}(H_{1,i} + H_{1,i+1}) - \tfrac{1}{4}\mu\bar{x}_3(V_{2,i} + V_{2,i+1}) + \tfrac{1}{4}\mu\bar{x}_2(V_{3,i} + V_{3,i+1})$$
$$+ \tfrac{1}{4}i(1,1)(\Omega_{1,i} + \Omega_{1,i+1}) + \tfrac{1}{4}i(1,2)(\Omega_{2,i} + \Omega_{2,i+1}) + \tfrac{1}{4}i(1,3)(\Omega_{3,i} + \Omega_{3,i+1})$$

$$J_i(17) = -\tfrac{1}{4}(H_{2,i} + H_{2,i+1}) + \tfrac{1}{4}\mu\bar{x}_3(V_{1,i} + V_{1,i+1}) + \tfrac{1}{4}i(2,1)(\Omega_{1,i} + \Omega_{1,i+1})$$
$$+ \tfrac{1}{4}i(2,2)(\Omega_{2,i} + \Omega_{2,i+1}) + \tfrac{1}{4}i(2,3)(\Omega_{3,i} + \Omega_{3,i+1})$$

$$J_i(18) = -\tfrac{1}{4}(H_{3,i} + H_{3,i+1}) - \tfrac{1}{4}\mu\bar{x}_2(V_{1,i} + V_{1,i+1}) + \tfrac{1}{4}i(3,1)(\Omega_{1,i} + \Omega_{1,i+1})$$
$$+ \tfrac{1}{4}i(3,2)(\Omega_{2,i} + \Omega_{2,i+1}) + \tfrac{1}{4}i(3,3)(\Omega_{3,i} + \Omega_{3,i+1})$$

$$J_i(19) = -\tfrac{1}{4}(\gamma_{11,i} + \gamma_{11,i+1}) + \tfrac{1}{4}R(1,1)(F_{1,i} + F_{1,i+1})$$
$$+ \tfrac{1}{4}R(1,2)(F_{2,i} + F_{2,i+1}) + \tfrac{1}{4}R(1,3)(F_{3,i} + F_{3,i+1}) + \tfrac{1}{4}Z(1,1)(M_{1,i} + M_{1,i+1})$$
$$+ \tfrac{1}{4}Z(1,2)(M_{2,i} + M_{2,i+1}) + \tfrac{1}{4}Z(1,3)(M_{3,i} + M_{3,i+1})$$

$$J_i(20) = -\tfrac{1}{2}(\gamma_{12,i} + \gamma_{12,i+1}) + \tfrac{1}{4}R(2,1)(F_{1,i} + F_{1,i+1})$$
$$+ \tfrac{1}{4}R(2,2)(F_{2,i} + F_{2,i+1}) + \tfrac{1}{4}R(2,3)(F_{3,i} + F_{3,i+1}) + \tfrac{1}{4}Z(2,1)(M_{1,i} + M_{1,i+1})$$
$$+ \tfrac{1}{4}Z(2,2)(M_{2,i} + M_{2,i+1}) + \tfrac{1}{4}Z(2,3)(M_{3,i} + M_{3,i+1})$$

$$J_i(21) = -\tfrac{1}{2}(\gamma_{13,i} + \gamma_{13,i+1}) + \tfrac{1}{4}R(3,1)(F_{1,i} + F_{1,i+1})$$
$$+ \tfrac{1}{4}R(3,2)(F_{2,i} + F_{2,i+1}) + \tfrac{1}{4}R(3,3)(F_{3,i} + F_{3,i+1}) + \tfrac{1}{4}Z(3,1)(M_{1,i} + M_{1,i+1})$$
$$+ \tfrac{1}{4}Z(3,2)(M_{2,i} + M_{2,i+1}) + \tfrac{1}{4}Z(3,3)(M_{3,i} + M_{3,i+1})$$

$$J_i(22) = -\tfrac{1}{4}(\kappa_{1,i}+\kappa_{1,i+1})+\tfrac{1}{4}Z(1,1)(F_{1,i}+F_{1,i+1})$$
$$+\tfrac{1}{4}Z(2,1)(F_{2,i}+F_{2,i+1})+\tfrac{1}{4}Z(3,1)(F_{3,i}+F_{3,i+1})+\tfrac{1}{4}T(1,1)(M_{1,i}+M_{1,i+1})$$
$$+\tfrac{1}{4}T(1,2)(M_{2,i}+M_{2,i+1})+\tfrac{1}{4}T(1,3)(M_{3,i}+M_{3,i+1})$$

$$J_i(23) = -\tfrac{1}{4}(\kappa_{2,i}+\kappa_{2,i+1})+\tfrac{1}{4}Z(1,2)(F_{1,i}+F_{1,i+1})$$
$$+\tfrac{1}{4}Z(2,2)(F_{2,i}+F_{2,i+1})+\tfrac{1}{4}Z(3,2)(F_{3,i}+F_{3,i+1})+\tfrac{1}{4}T(2,1)(M_{1,i}+M_{1,i+1})$$
$$+\tfrac{1}{4}T(2,2)(M_{2,i}+M_{2,i+1})+\tfrac{1}{4}T(2,3)(M_{3,i}+M_{3,i+1})$$

$$J_i(24) = -\tfrac{1}{4}(\kappa_{3,i}+\kappa_{3,i+1})+\tfrac{1}{4}Z(1,3)(F_{1,i}+F_{1,i+1})+\tfrac{1}{4}Z(2,3)(F_{2,i}+F_{2,i+1})$$
$$+\tfrac{1}{4}Z(3,3)(F_{3,i}+F_{3,i+1})+\tfrac{1}{4}T(3,1)(M_{1,i}+M_{1,i+1})$$
$$+\tfrac{1}{4}T(3,2)(M_{2,i}+M_{2,i+1})+\tfrac{1}{4}T(3,3)(M_{3,i}+M_{3,i+1})$$

A_i ($-$ sign) or B_i ($+$ sign) columns 1:3 rows 1:6

$$\begin{bmatrix} \pm 1/(2\Delta x) & -\tfrac{1}{16}(\kappa_{3,i+1}+3\kappa_{3,i}) & \tfrac{1}{16}(\kappa_{2,i+1}+3\kappa_{2,i}) \\ \tfrac{1}{16}(\kappa_{3,i+1}+3\kappa_{3,i}) & \pm 1/(2\Delta x) & -\tfrac{1}{16}(\kappa_{1,i+1}+3\kappa_{1,i}) \\ -\tfrac{1}{16}(\kappa_{2,i+1}+3\kappa_{2,i}) & \tfrac{1}{16}(\kappa_{1,i+1}+3\kappa_{1,i}) & \pm 1/(2\Delta x) \\ 0 & -\tfrac{1}{8}(\gamma_{13,i+1}+3\gamma_{13,i}) & \tfrac{1}{8}(\gamma_{12,i+1}+3\gamma_{12,i}) \\ \tfrac{1}{8}(\gamma_{13,i+1}+3\gamma_{13,i}) & 0 & -\tfrac{1}{4}-\tfrac{1}{16}(\gamma_{11,i+1}+3\gamma_{11,i}) \\ -\tfrac{1}{8}(\gamma_{12,i+1}+3\gamma_{12,i}) & \tfrac{1}{4}+\tfrac{1}{16}(\gamma_{11,i+1}+3\gamma_{11,i}) & 0 \end{bmatrix}$$

A_i or B_i columns 1:3 rows 19:24

$$\begin{bmatrix} -\tfrac{1}{4}R(1,1) & -\tfrac{1}{4}R(1,2) & -\tfrac{1}{4}R(1,3) \\ -\tfrac{1}{4}R(2,1) & -\tfrac{1}{4}R(2,2) & -\tfrac{1}{4}R(2,3) \\ -\tfrac{1}{4}R(3,1) & -\tfrac{1}{4}R(3,2) & -\tfrac{1}{4}R(3,3) \\ -\tfrac{1}{4}Z(1,1) & -\tfrac{1}{4}Z(2,1) & -\tfrac{1}{4}Z(3,1) \\ -\tfrac{1}{4}Z(1,2) & -\tfrac{1}{4}Z(2,2) & -\tfrac{1}{4}Z(3,2) \\ -\tfrac{1}{4}Z(1,3) & -\tfrac{1}{4}Z(2,3) & -\tfrac{1}{4}Z(3,3) \end{bmatrix}$$

A_i ($-$ sign) or B_i ($+$ sign) columns 4:6 rows 4:6

$$\begin{bmatrix} \pm 1/(2\Delta x) & -\tfrac{1}{16}(\kappa_{3,i+1}+3\kappa_{3,i}) & \tfrac{1}{16}(\kappa_{2,i+1}+3\kappa_{2,i}) \\ \tfrac{1}{16}(\kappa_{3,i+1}+3\kappa_{3,i}) & \pm 1/(2\Delta x) & -\tfrac{1}{16}(\kappa_{1,i+1}+3\kappa_{1,i}) \\ -\tfrac{1}{16}(\kappa_{2,i+1}+3\kappa_{2,i}) & \tfrac{1}{16}(\kappa_{1,i+1}+3\kappa_{1,i}) & \pm 1/(2\Delta x) \end{bmatrix}$$

A_i or B_i columns 4:6 rows 19:24

$$\begin{bmatrix} -\tfrac{1}{4}Z(1,1) & -\tfrac{1}{4}Z(1,2) & -\tfrac{1}{4}Z(1,3) \\ -\tfrac{1}{4}Z(2,1) & -\tfrac{1}{4}Z(2,2) & -\tfrac{1}{4}Z(2,3) \\ -\tfrac{1}{4}Z(3,1) & -\tfrac{1}{4}Z(3,2) & -\tfrac{1}{4}Z(3,3) \\ -\tfrac{1}{4}T(1,1) & -\tfrac{1}{4}T(1,2) & -\tfrac{1}{4}T(1,3) \\ -\tfrac{1}{4}T(2,1) & -\tfrac{1}{4}T(2,2) & -\tfrac{1}{4}T(2,3) \\ -\tfrac{1}{4}T(3,1) & -\tfrac{1}{4}T(3,2) & -\tfrac{1}{4}T(3,3) \end{bmatrix}$$

A_i ($-$ sign) or B_i ($+$ sign) columns 7:9 rows 4:9

$$\begin{bmatrix} 0 & -\tfrac{1}{16}(P_{3,i+1}+3P_{3,i}) & \tfrac{1}{16}(P_{2,i+1}+3P_{2,i}) \\ \tfrac{1}{16}(P_{3,i+1}+3P_{3,i}) & 0 & -\tfrac{1}{16}(P_{1,i+1}+3P_{1,i}) \\ -\tfrac{1}{16}(P_{2,i+1}+3P_{2,i}) & \tfrac{1}{16}(P_{1,i+1}+3P_{1,i}) & 0 \\ \pm 1/(2\Delta x) & -\tfrac{1}{16}(\kappa_{3,i+1}+3\kappa_{3,i}) & \tfrac{1}{16}(\kappa_{2,i+1}+3\kappa_{2,i}) \\ \tfrac{1}{16}(\kappa_{3,i+1}+3\kappa_{3,i}) & \pm 1/(2\Delta x) & -\tfrac{1}{16}(\kappa_{1,i+1}+3\kappa_{1,i}) \\ -\tfrac{1}{16}(\kappa_{2,i+1}+3\kappa_{2,i}) & \tfrac{1}{16}(\kappa_{1,i+1}+3\kappa_{1,i}) & \pm 1/(2\Delta x) \end{bmatrix}$$

A_i or B_i columns 7:9 rows 13:18

$$\begin{bmatrix} -\tfrac{1}{4}\mu & 0 & 0 \\ 0 & -\tfrac{1}{4}\mu & 0 \\ 0 & 0 & -\tfrac{1}{4}\mu \\ 0 & \tfrac{1}{4}\mu\bar{x}_3 & -\tfrac{1}{4}\mu\bar{x}_2 \\ -\tfrac{1}{4}\mu\bar{x}_3 & 0 & 0 \\ \tfrac{1}{4}\mu\bar{x}_2 & 0 & 0 \end{bmatrix}$$

A_i or B_i columns 10:12 rows 1:6

$$\begin{bmatrix} 0 & -\tfrac{1}{16}(P_{3,i+1}+3P_{3,i}) & \tfrac{1}{16}(P_{2,i+1}+3P_{2,i}) \\ \tfrac{1}{16}(P_{3,i+1}+3P_{3,i}) & 0 & -\tfrac{1}{16}(P_{1,i+1}+3P_{1,i}) \\ -\tfrac{1}{16}(P_{2,i+1}+3P_{2,i}) & \tfrac{1}{16}(P_{1,i+1}+3P_{1,i}) & 0 \\ 0 & -\tfrac{1}{16}(H_{3,i+1}+3H_{3,i}) & \tfrac{1}{16}(H_{2,i+1}+3H_{2,i}) \\ \tfrac{1}{16}(H_{3,i+1}+3H_{3,i}) & 0 & -\tfrac{1}{16}(H_{1,i+1}+3H_{1,i}) \\ -\tfrac{1}{16}(H_{2,i+1}+3H_{2,i}) & \tfrac{1}{16}(H_{1,i+1}+3H_{1,i}) & 0 \end{bmatrix}$$

A_i (− sign) or B_i (+ sign) columns 10:12 rows 7:12

$$
\begin{bmatrix}
0 & -\frac{1}{8}(\gamma_{13,i+1}+3\gamma_{13,i}) & \frac{1}{8}(\gamma_{12,i+1}+3\gamma_{12,i}) \\
\frac{1}{8}(\gamma_{13,i+1}+3\gamma_{13,i}) & 0 & -\frac{1}{4}-\frac{1}{16}(\gamma_{11,i+1}+3\gamma_{11,i}) \\
-\frac{1}{8}(\gamma_{12,i+1}+3\gamma_{12,i}) & \frac{1}{4}+\frac{1}{16}(\gamma_{11,i+1}+3\gamma_{11,i}) & 0 \\
\pm 1/(2\Delta x) & -\frac{1}{16}(\kappa_{3,i+1}+3\kappa_{3,i}) & \frac{1}{16}(\kappa_{2,i+1}+3\kappa_{2,i}) \\
\frac{1}{16}(\kappa_{3,i+1}+3\kappa_{3,i}) & \pm 1/(2\Delta x) & -\frac{1}{16}(\kappa_{1,i+1}+3\kappa_{1,i}) \\
-\frac{1}{16}(\kappa_{2,i+1}+3\kappa_{2,i}) & \frac{1}{16}(\kappa_{1,i+1}+3\kappa_{1,i}) & \pm 1/(2\Delta x)
\end{bmatrix}
$$

A_i or B_i columns 10:12 rows 13:18

$$
\begin{bmatrix}
0 & -\frac{1}{4}\mu\bar{x}_3 & \frac{1}{4}\mu\bar{x}_2 \\
\frac{1}{4}\mu\bar{x}_3 & 0 & 0 \\
-\frac{1}{4}\mu\bar{x}_2 & 0 & 0 \\
-\frac{1}{4}i(1,1) & -\frac{1}{4}i(1,2) & -\frac{1}{4}i(1,3) \\
-\frac{1}{4}i(2,1) & -\frac{1}{4}i(2,2) & -\frac{1}{4}i(2,3) \\
-\frac{1}{4}i(3,1) & -\frac{1}{4}i(3,2) & -\frac{1}{4}i(3,3)
\end{bmatrix}
$$

A_i or B_i columns 13:15 rows 1:6

$$
\begin{bmatrix}
-1/(2\Delta t) & \frac{1}{16}(\Omega_{3,i+1}+3\Omega_{3,i}) & -\frac{1}{16}(\Omega_{2,i+1}+3\Omega_{2,i}) \\
-\frac{1}{16}(\Omega_{3,i+1}+3\Omega_{3,i}) & -1/(2\Delta t) & \frac{1}{16}(\Omega_{1,i+1}+3\Omega_{1,i}) \\
\frac{1}{16}(\Omega_{2,i+1}+3\Omega_{2,i}) & -\frac{1}{16}(\Omega_{1,i+1}+3\Omega_{1,i}) & -1/(2\Delta t) \\
0 & \frac{1}{16}(V_{3,i+1}+3V_{3,i}) & -\frac{1}{16}(V_{2,i+1}+3V_{2,i}) \\
-\frac{1}{16}(V_{3,i+1}+3V_{3,i}) & 0 & \frac{1}{16}(V_{1,i+1}+3V_{1,i}) \\
\frac{1}{16}(V_{2,i+1}+3V_{2,i}) & -\frac{1}{16}(V_{1,i+1}+3V_{1,i}) & 0
\end{bmatrix}
$$

A_i or B_i columns 13:15 rows 13:15

$$
\begin{bmatrix}
\frac{1}{4} & 0 & 0 \\
0 & \frac{1}{4} & 0 \\
0 & 0 & \frac{1}{4}
\end{bmatrix}
$$

A_i or B_i columns 16:18 rows 4:6

$$
\begin{bmatrix}
-1/(2\Delta t) & \frac{1}{16}(\Omega_{3,i+1}+3\Omega_{3,i}) & -\frac{1}{16}(\Omega_{2,i+1}+3\Omega_{2,i}) \\
-\frac{1}{16}(\Omega_{3,i+1}+3\Omega_{3,i}) & -1/(2\Delta t) & \frac{1}{16}(\Omega_{1,i+1}+3\Omega_{1,i}) \\
\frac{1}{16}(\Omega_{2,i+1}+3\Omega_{2,i}) & -\frac{1}{16}(\Omega_{1,i+1}+3\Omega_{1,i}) & -1/(2\Delta t)
\end{bmatrix}
$$

A_i or B_i columns 16:18 rows 16:18

$$
\begin{bmatrix}
\frac{1}{4} & 0 & 0 \\
0 & \frac{1}{4} & 0 \\
0 & 0 & \frac{1}{4}
\end{bmatrix}
$$

A_i or B_i columns 19:21 rows 4:9

$$
\begin{bmatrix}
0 & \frac{1}{16}(F_{3,i+1}+3F_{3,i}) & -\frac{1}{16}(F_{2,i+1}+3F_{2,i}) \\
-\frac{1}{16}(F_{3,i+1}+3F_{3,i}) & 0 & \frac{1}{16}(F_{1,i+1}+3F_{1,i}) \\
\frac{1}{16}(F_{2,i+1}+3F_{2,i}) & -\frac{1}{16}(F_{1,i+1}+3F_{1,i}) & 0 \\
-1/(2\Delta t) & \frac{1}{16}(\Omega_{3,i+1}+3\Omega_{3,i}) & -\frac{1}{16}(\Omega_{2,i+1}+3\Omega_{2,i}) \\
-\frac{1}{16}(\Omega_{3,i+1}+3\Omega_{3,i}) & -1/(2\Delta t) & \frac{1}{16}(\Omega_{1,i+1}+3\Omega_{1,i}) \\
\frac{1}{16}(\Omega_{2,i+1}+3\Omega_{2,i}) & -\frac{1}{16}(\Omega_{1,i+1}+3\Omega_{1,i}) & -1/(2\Delta t)
\end{bmatrix}
$$

A_i or B_i columns 19:21 rows 19:21

$$
\begin{bmatrix}
\frac{1}{4} & 0 & 0 \\
0 & \frac{1}{4} & 0 \\
0 & 0 & \frac{1}{4}
\end{bmatrix}
$$

A_i or B_i columns 22:24 rows 1:6

$$
\begin{bmatrix}
0 & \frac{1}{16}(F_{3,i+1}+3F_{3,i}) & -\frac{1}{16}(F_{2,i+1}+3F_{2,i}) \\
-\frac{1}{16}(F_{3,i+1}+3F_{3,i}) & 0 & \frac{1}{16}(F_{1,i+1}+3F_{1,i}) \\
\frac{1}{16}(F_{2,i+1}+3F_{2,i}) & -\frac{1}{16}(F_{1,i+1}+3F_{1,i}) & 0 \\
0 & \frac{1}{16}(M_{3,i+1}+3M_{3,i}) & -\frac{1}{16}(M_{2,i+1}+3M_{2,i}) \\
-\frac{1}{16}(M_{3,i+1}+3M_{3,i}) & 0 & \frac{1}{16}(M_{1,i+1}+3M_{1,i}) \\
\frac{1}{16}(M_{2,i+1}+3M_{2,i}) & -\frac{1}{16}(M_{1,i+1}+3M_{1,i}) & 0
\end{bmatrix}
$$

A_i or B_i columns 22:24 rows 7:12

$$
\begin{bmatrix}
0 & \frac{1}{16}(V_{3,i+1}+3V_{3,i}) & -\frac{1}{16}(V_{2,i+1}+3V_{2,i}) \\
-\frac{1}{16}(V_{3,i+1}+3V_{3,i}) & 0 & \frac{1}{16}(V_{1,i+1}+3V_{1,i}) \\
\frac{1}{16}(V_{2,i+1}+3V_{2,i}) & -\frac{1}{16}(V_{1,i+1}+3V_{1,i}) & 0 \\
-1/(2\Delta t) & \frac{1}{16}(\Omega_{3,i+1}+3\Omega_{3,i}) & -\frac{1}{16}(\Omega_{2,i+1}+3\Omega_{2,i}) \\
-\frac{1}{16}(\Omega_{3,i+1}+3\Omega_{3,i}) & -1/(2\Delta t) & \frac{1}{16}(\Omega_{1,i+1}+3\Omega_{1,i}) \\
\frac{1}{16}(\Omega_{2,i+1}+3\Omega_{2,i}) & -\frac{1}{16}(\Omega_{1,i+1}+3\Omega_{1,i}) & -1/(2\Delta t)
\end{bmatrix}
$$

A_i or B_i columns 22:24 rows 22:24

$$
\begin{bmatrix}
\frac{1}{4} & 0 & 0 \\
0 & \frac{1}{4} & 0 \\
0 & 0 & \frac{1}{4}
\end{bmatrix}
$$

References

[Berdichevskii 1981] V. L. Berdichevskii, "On the energy of an elastic rod", *Prikl. Mat. Mekh.* **45**:4 (1981), 704–718. In Russian: translation in *J. Appl. Math. Mech.* **45**:4, (1981), 518–529.

[Cesnik and Palacios 2003] C. E. S. Cesnik and R. Palacios, "Modeling piezocomposite actuators embedded in slender structures", in *44th AIAA/ASME/ASCE/AHS/ASC Structures, Structural Dynamics, and Materials Conference* (Norfolk, VA, 2003), AIAA, Reston, VA, 2003. AIAA 2003-1803.

[Cesnik and Shin 1998] C. E. S. Cesnik and S. J. Shin, "Structural analysis for designing rotor blades with integral actuators", in *39th AIAA/ASME/ASCE/AHS/ASC Structures, Structural Dynamics, and Materials Conference* (Long Beach, CA, 1998), AIAA, Reston, VA, 1998. AIAA 1998-2107.

[Cesnik et al. 2001] C. E. S. Cesnik, S. J. Shin, and M. L. Wilbur, "Dynamic response of active twist rotor blades", *Smart Mater. Struct.* **10**:1 (2001), 62–76.

[Cesnik et al. 2003] C. E. S. Cesnik, R. S. Park, and R. Palacios, "Effective cross-section distribution of anisotropic piezocomposite actuators for wing twist", pp. 21–32 in *Smart structures and materials 2003: smart structures and integrated systems* (San Diego, CA), edited by A. M. Baz, Proceedings of SPIE **5056**, SPIE, Bellingham, WA, 2003.

[Esmailzadeh and Ghorashi 1997] E. Esmailzadeh and M. Ghorashi, "Vibration analysis of a Timoshenko beam subjected to a travelling mass", *J. Sound Vib.* **199**:4 (1997), 615–628.

[Esmailzadeh et al. 1995] E. Esmailzadeh, M. Ghorashi, and B. Mehri, "Periodic behavior of a nonlinear dynamical system", *Nonlinear Dynam.* **7**:3 (1995), 335–344.

[Ghorashi 1994] M. Ghorashi, *Dynamic and vibratory analysis of beams under dynamic loads induced by traveling masses and vehicles*, Ph.D. thesis, Mechanical Engineering Department, Sharif University of Technology, 1994.

[Ghorashi 2009] M. Ghorashi, *Dynamics of elastic nonlinear rotating composite beams with embedded actuators*, Ph.D. thesis, Mechanical and Aerospace Engineering Department, Carleton University, 2009.

[Ghorashi and Nitzsche 2008] M. Ghorashi and F. Nitzsche, "Steady state nonlinear dynamic response of a composite rotor blade using implicit integration of intrinsic equations of a beam", *Int. Rev. Aerospace Eng.* **1** (2008), 225–233.

[Hodges 2006] D. H. Hodges, *Nonlinear composite beam theory*, Progress in Astronautics and Aeronautics Series **213**, AIAA, Reston, VA, 2006.

[Hodges et al. 1992] D. H. Hodges, A. R. Atilgan, C. E. S. Cesnik, and M. V. Fulton, "On a simplified strain energy function for geometrically nonlinear behavior of anisotropic beams", *Compos. Eng.* **2**:5–7 (1992), 513–526.

[Palacios 2005] R. Palacios, *Asymptotic models of integrally-strained slender structures for high-fidelity nonlinear aeroelastic analysis*, Ph.D. thesis, University of Michigan, 2005.

[Shang and Hodges 1995] X. Shang and D. H. Hodges, "Aeroelastic stability of composite rotor blades in hover", pp. 2602–2610 in *36th AIAA/ASME/ASCE/AHS/ASC Structures, Structural Dynamics, and Materials Conference* (New Orleans, LA, 1995), AIAA, Reston, VA, 1995. AIAA 1995-1453.

[Yu and Hodges 2004] W. Yu and D. H. Hodges, "Elasticity solutions versus asymptotic sectional analysis of homogeneous, isotropic, prismatic beams", *J. Appl. Mech.* (*ASME*) **71**:1 (2004), 15–23.

[Yu et al. 2002a] W. Yu, D. H. Hodges, V. V. Volovoi, and C. E. S. Cesnik, "On Timoshenko-like modeling of initially curved and twisted composite beams", *Int. J. Solids Struct.* **39**:19 (2002), 5101–5121.

[Yu et al. 2002b] W. Yu, V. V. Volovoi, D. H. Hodges, and X. Hong, "Validation of the variational asymptotic beam sectional analysis", *AIAA J.* **40**:10 (2002), 2105–2112.

[Zwillinger 1998] D. Zwillinger, *Handbook of differential equations*, 3rd ed., Academic Press, San Diego, CA, 1998.

MEHRDAAD GHORASHI: mghoras2@connect.carleton.ca
Department of Mechanical and Aerospace Engineering, Carleton University, 1125 Colonel By Drive, Ottawa, ON K1S 5B6, Canada

FRED NITZSCHE: fred_nitzsche@carleton.ca
Department of Mechanical and Aerospace Engineering, Carleton University, 1125 Colonel By Drive, Ottawa, ON K1S 5B6, Canada

DYNAMIC FATIGUE OF CRACKED PIEZOELECTRIC CERAMICS UNDER ELECTROMECHANICAL LOADING: THREE-POINT BENDING TEST AND FINITE ELEMENT ANALYSIS

YASUHIDE SHINDO, FUMIO NARITA AND MITSURU HIRAMA

This paper studies the dynamic fatigue or slow crack growth in piezoelectric ceramics under electromechanical loading by a combined numerical-experimental approach. Constant load-rate testing was conducted in three-point flexure using the single-edge precracked-beam specimens under zero and positive electric fields, and the effects of electric field and loading-rate on the fracture load and crack propagation were examined. A finite element analysis was also employed to calculate the energy release rate for the permeable, impermeable and open crack models, and the effect of electric field on the energy release rate was discussed. Crack propagation velocity versus energy release rate curves at various loading-rate were then estimated based on the finite element analysis using measured data.

1. Introduction

Piezoelectric ceramics of the lead zirconate titanate (PZT) class have been used for a number of years as sensors and actuators. The high mechanical stresses and intense electric fields in PZT ceramics can induce cracking that can lead to premature failure of the piezoelectric devices. The properties of PZT ceramics are also susceptible to degradation under electromechanical loading. Therefore, an understanding of piezoelectric fracture [Shindo et al. 2003; 2005] and fatigue [Cao and Evans 1994; Lynch et al. 1995] is a key issue for the efficient and reliable design of the piezoelectric devices. Shindo et al. [2007] conducted an experimental and analytical study of the static fatigue behavior of PZT ceramics under electromechanical loading. Narita et al. [2007] also reported experimental and numerical examination of the fatigue crack growth in PZT ceramics under a cyclic mechanical load and a constant electric field.

Certain environments may affect formation and extension of cracks over time and at stress levels well below that which causes immediate failure to occur. This process is called dynamic fatigue or slow crack growth. Slow crack growth parameters have been estimated for only a few commercial ceramics and glass, and no one has investigated the resistance of piezoelectric ceramics to slow crack growth and the influence of electric field on the dynamic fatigue behavior.

In this study, we report numerical and experimental examination of the dynamic fatigue or slow crack growth in piezoelectric ceramics under electromechanical loading. A crack was created normal to the poling direction. Constant load-rate testing was conducted in three-point flexure under zero and positive electric fields using single-edge precracked-beam method. A finite element analysis was also used to evaluate the energy release rate for the permeable, impermeable and open crack models, and the effect

Elastic stiffnesses $(\times 10^{10}\,\text{N/m}^2)$					Piezoelectric coefficients (C/m^2)			Dielectric constants $(\times 10^{-10}\,\text{C/Vm})$	
c_{11}	c_{33}	c_{44}	c_{12}	c_{13}	e_{31}	e_{33}	e_{15}	ϵ_{11}	ϵ_{33}
17.0	16.5	3.05	10.6	11.5	−5.99	15.6	13.7	95.2	68.4

Table 1. Material properties of PCM-80.

of electric field on the energy release rate was discussed. The results were then examined in terms of the crack propagation velocity vs energy release rate curve.

2. Experimental procedure

Constant load-rate (dynamic fatigue) testing of commercially supplied hard PZT PCM-80 (Panasonic Electric Devices Co., Ltd., Japan) was carried out. The material properties are listed in Table 1. The specimens were 5 mm thick, 5 mm wide and 15 mm long. Poling was done along the axis of the 15 mm dimension. Through-thickness crack was introduced using the method described in [Narita et al. 2007]; the crack is about 0.5 mm long and has an initial gap of under 200 nm.

Figure 1 shows the testing set-up. A three-point flexure fixture with 13 mm span was used, and a load controlled mode was employed to apply for load rates from 0.05 to $1\,\text{Ns}^{-1}$ under 0 and $+0.1\,\text{MV/m}$. Crack growth was monitored during the test on the surface of the specimen with the aid of a digital microscope camera at 1000-fold magnification. The video camera records were also carefully observed to determine the crack length and the crack tip. From the detailed video photographs, the crack length can be easily measured. Because of the good resolution of the camera, the visual measurement of the crack length is not subject to large errors. This type of measurement procedure is used regularly. Due to cost and time constraints, the number of specimens was limited to two or three for each load-rate and electric field.
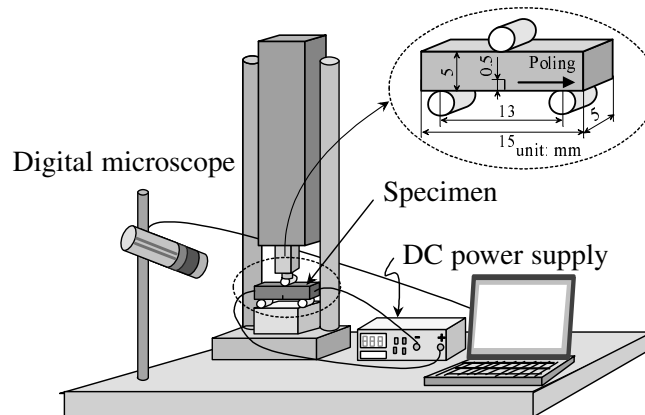
Figure 1. Testing set-up.
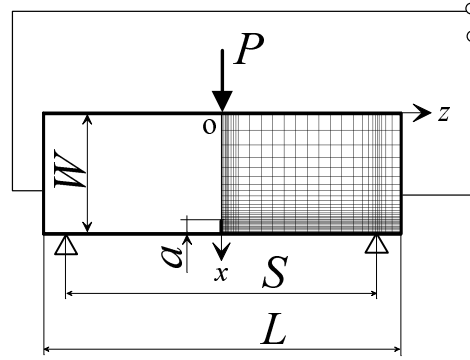
Figure 2. Schematic representation of finite element model.

3. Analysis

Consider a linear piezoelectric material with no body force and free charge. The basic equations for PZT ceramics, from [Tiersten 1969], are given in Appendix A.

Measured crack length a was recorded via video camera and then obtained as a function of the time t. In order to evaluate the energy release rate G of PZT, plane strain finite element analysis (ANSYS) was carried out for the cracked piezoelectric specimens. The specimen and loading geometries are shown in Figure 2. Let the coordinate axes $x = x_1$ and $z = x_3$ be chosen such that the $y = x_2$ axis coincides with the thickness direction. The z axis is oriented parallel to the poling direction. The three-point flexure specimen with a span S is a beam of width W and length L containing a crack of length a. Because of symmetry, only the right half of the model was used in the finite element analysis.

The crack is traction free and on its surface the normal component of the electric displacement and the tangential component of the electric field are continuous. Also, the geometry and the fields are symmetric. Thus

$$\sigma_{zx}(x, 0) = 0 \ (0 \leq x \leq W) \tag{1}$$

$$\begin{cases} u_z(x, 0) = 0 & (0 \leq x \leq W - a) \\ \sigma_{zz}(x, 0) = 0 & (W - a < x \leq W) \end{cases} \tag{2}$$

$$\begin{cases} \phi(x, 0) = 0 & (0 \leq x \leq W - a) \\ E_x(x, 0) = E_x^c(x, 0) & (W - a < x \leq W) \\ D_z(x, 0) = D_z^c(x, 0) & (W - a < x \leq W) \end{cases} \tag{3}$$

where the superscript c stands for the electric quantity in the void inside the crack. Equations (3) constitute the permeable crack boundary conditions [Parton 1976; Shindo et al. 1990]. The electric potential is all zero on the symmetry planes inside the crack and ahead of the crack, so the boundary conditions of (3) reduce to $\phi(x, 0) = 0$ $(0 \leq x \leq W)$. The electric field intensity $E_x^c(x, 0)$ is equal to zero, and the electric displacement $D_z^c(x, 0)$ is determined precisely by $(3)_3$ with the electric permittivity of the vacuum $\epsilon_0 = 8.85 \times 10^{-12}$ C/Vm. A mechanical load is produced by the application of a prescribed force

P at $x = 0$, $z = 0$ along the x-direction. For electrical loads, a negative or positive electric potential $\phi_0/2$ is applied at the edge $0 \leq x \leq W$, $z = L/2$. Other boundary conditions are summarized below.

At $x = 0$ (top surface)

$$\sigma_{xx}(0, z) = -P\delta(z) \tag{4}$$

$$\sigma_{xx}(0, z) = 0 \quad (0 < z \leq L/2) \tag{5}$$

$$\sigma_{xz}(0, z) = 0 \quad (0 \leq z \leq L/2) \tag{6}$$

$$D_x(0, z) = 0 \quad (0 \leq z \leq L/2) \tag{7}$$

At $z = L/2$ (side surface)

$$\sigma_{zz}(x, L/2) = 0 \quad (0 \leq x \leq W) \tag{8}$$

$$\sigma_{zx}(x, L/2) = 0 \quad (0 \leq x \leq W) \tag{9}$$

$$\phi(x, L/2) = \phi_0/2 \quad (0 \leq x \leq W) \tag{10}$$

At $x = W$ (bottom surface)

$$\sigma_{xx}(W, z) = 0 \quad (0 \leq z < S/2, S/2 < z \leq L/2) \tag{11}$$

$$u_x(W, S/2) = 0 \tag{12}$$

$$\sigma_{xz}(W, z) = 0 \quad (0 \leq z \leq L/2) \tag{13}$$

$$D_x(W, z) = 0 \quad (0 \leq z \leq L/2) \tag{14}$$

In Equation (4), $\delta(z)$ is the Dirac-delta function. The condition (10) gives the electric field $E_0 = -\phi_0/L$. In the finite element analysis, the energy release rate was computed using the path-independent integral approach. The energy release rate G is given by

$$G = \int_{\Gamma_0} \{Hn_x - (\sigma_{xx}u_{,x} + \sigma_{zx}u_{z,x})n_x - (\sigma_{zx}u_{,x} + \sigma_{zz}u_{z,x})n_z + D_xE_xn_x + D_zE_xn_z\}d\Gamma \tag{15}$$

where Γ_0 is a contour closing a crack tip and n_x, n_z are the components of the outer unit normal vector. The electrical enthalpy density H is expressed as

$$H = \tfrac{1}{2}\{c_{11}(u_{x,x})^2 + c_{33}(u_{z,z})^2 + 2c_{13}u_{x,x}u_{z,z} + c_{44}(u_{x,z} + u_{z,x})^2\} - \tfrac{1}{2}\{\epsilon_{11}(E_x)^2 + \epsilon_{33}(E_z)^2\}$$
$$- \{e_{15}(u_{x,z} + u_{z,x})E_x + (e_{31}u_{x,x} + e_{33}u_{z,z})E_z\}. \tag{16}$$

Equation (15) was implemented numerically in ANSYS using the J-integral approach, and the energy release rate was computed. For the calculation of J, three contours were defined in the finite element mesh. The values of J for each of these contours are practically identical and the variations with respect to the average value of J from three contours are less than 2%. Four-node element PLANE 13 was used in the model. The finite element mesh had 1900 elements and 1981 nodes. Our previous measurements of strain near electrode tip in piezoelectric devices [Yoshida et al. 2003; Shindo et al. 2004] and piezoelectric actuator tip deflection [Hayashi et al. 2003] verified the accuracy of the above scheme, and showed that the results obtained are of general applicability.
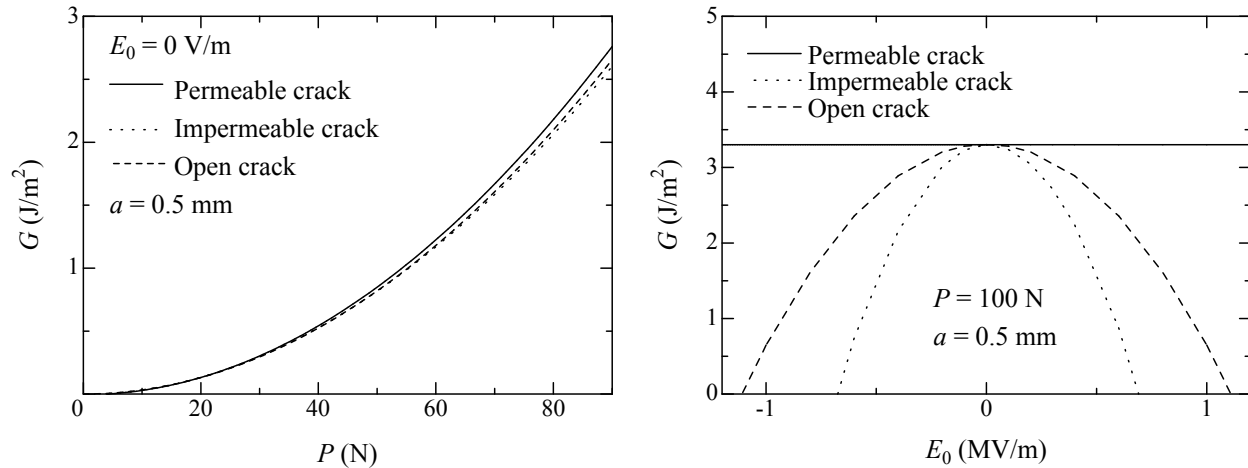
Figure 3. Left: Energy release rate versus applied load. Right: Energy release rate versus electric field.

McMeeking [2004] showed that due to a change of stored electrostatic energy within the crack, the energy release rate for an elliptical cavity of any shape is not equal to the energy release rate G for the slit-like crack as the material separates. Then he reported that if the initial crack gap is small, there is little difference between the energy release rate for the elliptical cavity and the G — see Equation (15) — for the slit-like crack. The energy release rates G for the impermeable [Deeg 1980; Pak 1990] and open [Hao and Shen 1994; McMeeking 1999] crack models are also discussed in Appendix B.

4. Results and discussion

Figure 3, left, presents the plot of the energy release rate G versus applied load P for the piezoelectric specimen (PZT PCM-80) with a crack of length $a = 0.5$ mm under electric field $E_0 = 0$ V/m. Little difference among three piezoelectric crack models is observed. Figure 3, right, shows the dependence of the energy release rate G for the permeable, impermeable and open crack models on the electric field E_0 under $P = 100$ N for $a = 0.5$ mm. The energy release rate for the permeable crack model is independent of the electric field. In the impermeable and open crack models, applying the electric field in either direction decreases the energy release rate. A negative energy release rate is also produced under large electric fields. According to the fracture mechanics interpretation, a negative energy release rate would correspond to a crack that could absorb energy due to crack extension. Since this would exclude the fracture in piezoelectric ceramics under electric fields, in contradiction with the experimental observations [Park and Sun 1995; Shindo et al. 2001, 2005], the parameters for the impermeable and open crack models have questionable physical significance. Therefore, the electrical boundary conditions (B.1) and (B.2) are not appropriate for a slit crack in piezoelectric ceramics, and the permeable crack model can be used to calculate the G of the specimens.

A summary of the results of constant load-rate testing for PZT PCM-80 under applied electric field $E_0 = 0$ and $+0.1$ MV/m is shown in Figure 4, where $\log P_c$ (fracture load) was plotted as a function of $\log (dP/dt)$ (load-rate). The error bars indicate maximum and minimum fracture loads at each load-rate
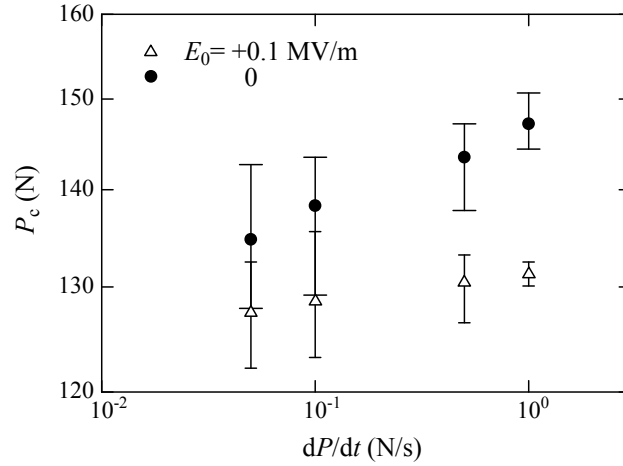
Figure 4. Fracture load as a function of load-rate.

and electric field, and triangle and dot are average values. The margin of error is larger at lower rates because of changes in microstructures near the crack tip at low load-rates. The PZT ceramics show an increase in fracture load as the load-rate increases, similar to behavior reported for dynamic fatigue in other non-piezoelectric ceramics [Pan et al. 1998; Choi and Salem 1998; Andrews et al. 2002]. The results also indicate that an overall decrease in fracture load occurs when testing under $E_0 = +0.1$ MV/m. Although experimental results show some scatter, the data are good enough to allow a relation between the fracture load and load-rate. The fracture load as a function of load-rate can be approximated by

$$P_c = K(\mathrm{d}P/\mathrm{d}t)^{1/(n+1)}, \tag{17}$$

where

$$
\begin{aligned}
K &= 147, \quad n = 34.6 \quad (E_0 = 0 \text{ V/m}), \\
K &= 131, \quad n = 99.5 \quad (E_0 = +0.1 \text{ MV/m}).
\end{aligned}
\tag{18}
$$

Figure 5, left, shows typical curves of crack propagation, Δa, measured as a function of loading time t, under an electric field $E_0 = 0$ and $+0.1$ MV/m at load-rate of 1.0 N/s. The crack can be seen to grow at progressively decreasing growth rates, with increasing size only after a certain delay time, 50 s. The rate of crack growth of the specimen under $E_0 = +0.1$ MV/m is substantially greater than that under $E_0 = 0$ V/m. The final failure occurred when the total crack growth distance on the side surface under $E_0 = 0$ and $+0.1$ MV/m is about 159 and 184 μm, respectively. Note that the rate of crack growth does not depend on the electric field before 50 s of delay time. Figure 5, right, shows similar results at a load-rate of 0.05 N/s. The stable crack growth velocity occurs after a delay time of about 1600 s. The final failure occurred when the crack growth increment of the specimen under $E_0 = 0$ and $+0.1$ MV/m is about 91 and 171 μm, respectively.

Figure 6, left, shows a comparison of crack propagation velocities $\mathrm{d}a/\mathrm{d}t$ under $E_0 = 0$ and $+0.1$ MV/m at 1.0 N/s, plotted as a function of the energy release rate G. The crack propagation velocity is obtained by the experiment, whereas the energy release rate is calculated by the finite element analysis for the
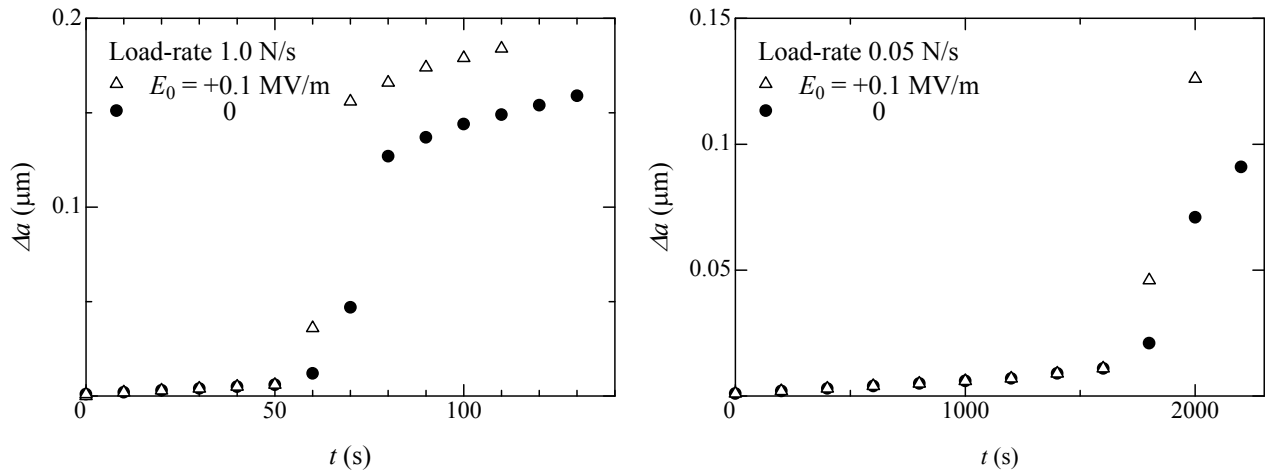
Figure 5. Variation of crack length as a function of time. Left: $dP/dt=1.0$ N/s. Right: $dP/dt=0.05$ N/s.
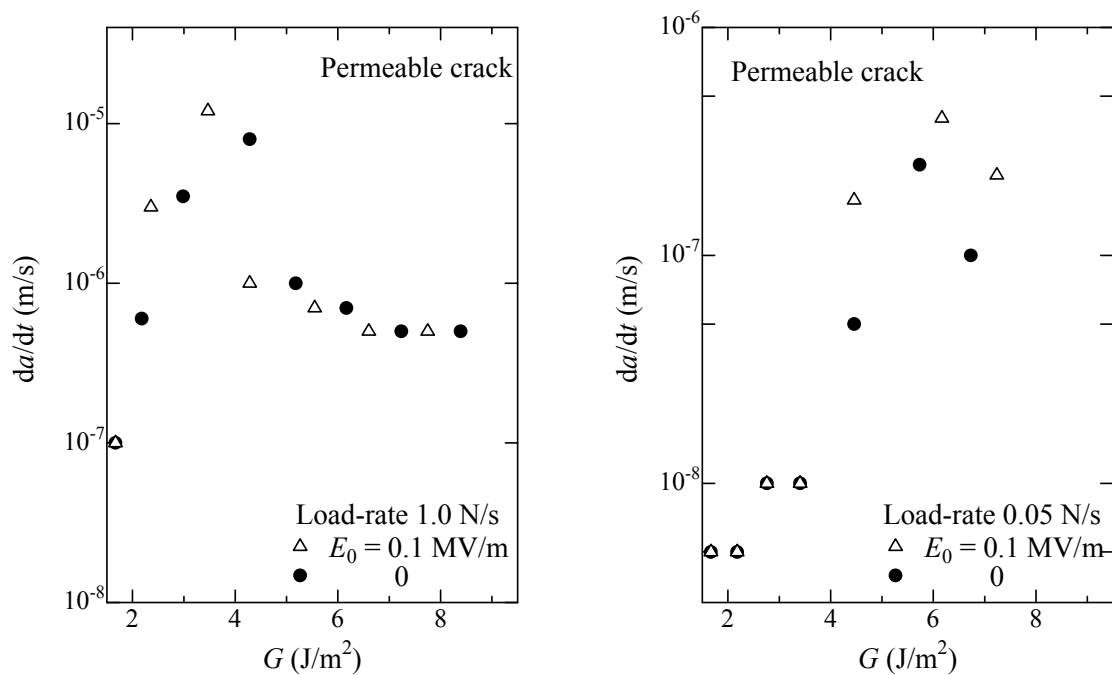

Figure 6. Crack propagation velocity as a function of energy release rate. Left: $dP/dt=1.0$ N/s. Right: $dP/dt=0.05$ N/s.

piezoelectric specimen with a permeable crack. The crack propagation velocity increases very quickly with the energy release rate, reaching a peak and then decreases before final failure. The decrease in the crack velocity is probably associated with microcrack nucleation and crack bridging [Lynch et al. 1995; Fang et al. 2004]. It can also been seen that positive electric field enhances crack propagation, whereas for $G > 5$ J/m^2, the crack velocity is not influenced by the electric field anymore. Figure 6, right, shows
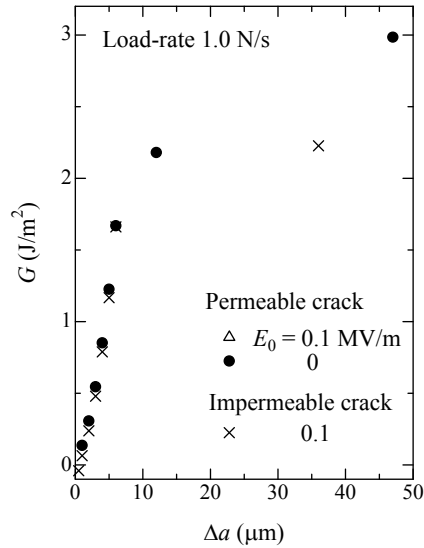
Figure 7. Energy release rate as a function of crack extension ($dP/dt = 1.0$ N/s).

similar results at load-rate of 0.05 N/s. The data suggest that there is a small influence of the electric field on the crack propagation for small G. At 0.05 N/s, the velocities are always lower than those at 1.0 N/s.

The energy release rate for the permeable crack model is calculated by the finite element analysis and plotted as a function of the measured crack extension under $E_0 = 0$ and $+0.1$ MV/m at 1.0 N/s in Figure 7. Also shown is the energy release rate for the impermeable crack model under $E_0 = +0.1$ MV/m. Comparing the energy release rates under $E_0 = 0$ MV/m for the permeable and impermeable crack models, little difference is observed (not shown). For the permeable crack model, the energy release rate increases with increasing the crack length and is independent of the electric field for small crack extensions. If we use the impermeable crack model to calculate the G, the energy release rate becomes negative (-0.04 J/m^2 for $\Delta a = 500$ nm) under $E_0 = +0.1$ MV/m and so, as mentioned earlier, we cannot use the impermeable crack model. Also, the energy release rate depends on the electric field for small crack extensions which is not in agreement with the experimental observations.

5. Conclusions

A combined numerical and experimental study is made to understand the influence of applied electric field on the crack behavior of piezoelectric ceramics. It is found that the piezoelectric ceramics under positive electric field has low dynamic fatigue or slow crack growth resistance, compared to those under no electric field. The crack propagation velocity increases at first with increasing the energy release rate, reaching a peak, and then tends to decrease at higher energy release rate before final failure. We expect the present study to encourage further research on the crack behavior of the piezoelectric ceramics under electromechanical loading.

Appendix A

The governing equations in Cartesian coordinates x_i $(i = 1, 2, 3)$ are

$$\sigma_{ji,j} = 0, \tag{A.1}$$

$$D_{i,i} = 0, \tag{A.2}$$

where σ_{ij} is the stress tensor, D_i is the electric displacement vector, $,i$ denotes partial differentiation with respect to the coordinate x_i, and the Einstein summation convention over repeated indices is used. The relation between the strain tensor ε_{ij} and the displacement vector u_i is

$$\varepsilon_{ij} = \tfrac{1}{2}(u_{j,i} + u_{i,j}). \tag{A.3}$$

The electric field intensity is

$$E_i = -\phi_{,i}, \tag{A.4}$$

where ϕ is the electric potential. The constitutive relations can be written as

$$\sigma_{ij} = c_{ijkl}\varepsilon_{kl} - e_{kij}E_k, \tag{A.5}$$

$$D_i = e_{ikl}\varepsilon_{kl} + \epsilon_{ik}E_k, \tag{A.6}$$

where c_{ijkl} and e_{ikl} are the elastic and piezoelectric constants, ϵ_{ik} is the dielectric permittivity, and

$$c_{ijkl} = c_{jikl} = c_{ijlk} = c_{klij}, \quad e_{kij} = e_{kji}, \quad \epsilon_{ik} = \epsilon_{ki}. \tag{A.7}$$

For piezoelectric ceramics which exhibit symmetry of a hexagonal crystal of class 6 mm with respect to the principal axes x_1, x_2, x_3, the constitutive relations can be written in the form

$$\begin{Bmatrix} \sigma_1 \\ \sigma_2 \\ \sigma_3 \\ \sigma_4 \\ \sigma_5 \\ \sigma_6 \end{Bmatrix} = \begin{bmatrix} c_{11} & c_{12} & c_{13} & 0 & 0 & 0 \\ c_{12} & c_{11} & c_{13} & 0 & 0 & 0 \\ c_{13} & c_{13} & c_{33} & 0 & 0 & 0 \\ 0 & 0 & 0 & c_{44} & 0 & 0 \\ 0 & 0 & 0 & 0 & c_{44} & 0 \\ 0 & 0 & 0 & 0 & 0 & c_{66} \end{bmatrix} \begin{Bmatrix} \varepsilon_1 \\ \varepsilon_2 \\ \varepsilon_3 \\ \varepsilon_4 \\ \varepsilon_5 \\ \varepsilon_6 \end{Bmatrix} - \begin{bmatrix} 0 & 0 & e_{31} \\ 0 & 0 & e_{31} \\ 0 & 0 & e_{33} \\ 0 & e_{15} & 0 \\ e_{15} & 0 & 0 \\ 0 & 0 & 0 \end{bmatrix} \begin{Bmatrix} E_1 \\ E_2 \\ E_3 \end{Bmatrix}, \tag{A.8}$$

$$\begin{Bmatrix} D_1 \\ D_2 \\ D_3 \end{Bmatrix} = \begin{bmatrix} 0 & 0 & 0 & 0 & e_{15} & 0 \\ 0 & 0 & 0 & e_{15} & 0 & 0 \\ e_{31} & e_{31} & e_{33} & 0 & 0 & 0 \end{bmatrix} \begin{Bmatrix} \varepsilon_1 \\ \varepsilon_2 \\ \varepsilon_3 \\ \varepsilon_4 \\ \varepsilon_5 \\ \varepsilon_6 \end{Bmatrix} + \begin{bmatrix} \epsilon_{11} & 0 & 0 \\ 0 & \epsilon_{11} & 0 \\ 0 & 0 & \epsilon_{33} \end{bmatrix} \begin{Bmatrix} E_1 \\ E_2 \\ E_3 \end{Bmatrix}, \tag{A.9}$$

where

$$\left. \begin{aligned} &\sigma_1 = \sigma_{11}, \ \sigma_2 = \sigma_{22}, \ \sigma_3 = \sigma_{33}, \\ &\sigma_4 = \sigma_{23} = \sigma_{32}, \ \sigma_5 = \sigma_{31} = \sigma_{13}, \ \sigma_6 = \sigma_{12} = \sigma_{21}, \end{aligned} \right\} \tag{A.10}$$

$$\left. \begin{aligned} &\varepsilon_1 = \varepsilon_{11}, \ \varepsilon_2 = \varepsilon_{22}, \ \varepsilon_3 = \varepsilon_{33}, \\ &\varepsilon_4 = 2\varepsilon_{23} = 2\varepsilon_{32}, \ \varepsilon_5 = 2\varepsilon_{31} = 2\varepsilon_{13}, \ \varepsilon_6 = 2\varepsilon_{12} = 2\varepsilon_{21}, \end{aligned} \right\} \tag{A.11}$$

$$c_{11} = c_{1111} = c_{2222}, \ c_{12} = c_{1122}, \ c_{13} = c_{1133} = c_{2233}, \ c_{33} = c_{3333}, \\ c_{44} = c_{2323} = c_{3131}, \ c_{66} = c_{1212} = \tfrac{1}{2}(c_{11} - c_{12}),$$
(A.12)

$$e_{15} = e_{131} = e_{223}, \quad e_{31} = e_{311} = e_{322}, \quad e_{33} = e_{333}.$$
(A.13)

Appendix B

A solution procedure for the impermeable and open crack models is outlined here. The impermeable boundary condition becomes

$$\phi(x,0) = 0 \quad (0 \le x \le W - a), \\ D_z(x,0) = 0 \quad (W - a < x \le W).$$
(B.1)

The energy release rate G for the impermeable crack model is given by Equation (15). The crack face electrical boundary condition for the open crack model is

$$\phi(x,0) = 0 \qquad\qquad (0 \le x \le W - a), \\ D_z^+ = D_z^- \qquad\qquad (W - a < x \le W), \\ D_z^+(u_z^+ - u_z^-) = \epsilon_0(\phi^- - \phi^+) \quad (W - a < x \le W),$$
(B.2)

where the superscripts $+$ and $-$ denote, respectively, the right and left sides of the cross-section where the crack is located (see Figure 2). The open crack model calculations start with $\phi = 0$ on the crack surface [McMeeking 1999]. The crack opening displacement and electric displacement on the crack surface are estimated, and the resulting potential difference is applied to the crack surface. The electroelastic fields are again solved leading to new crack opening displacement and electric displacement on the crack surface. If this is accomplished, then the potential difference is applied once more to the crack surface. The process is repeated until the solution converges. The energy release rate G for the open crack model is obtained by Equation (15).

Acknowledgements

References

[Andrews et al. 2002] M. J. Andrews, M. K. Ferber, and E. Lara-Curzio, "Mechanical properties of zirconia-based ceramics as functions of temperature", *J. Eur. Ceram. Soc.* **22**:14–15 (2002), 2633–2639.

[Cao and Evans 1994] H. C. Cao and A. G. Evans, "Electric-field-induced fatigue crack growth in piezoelectrics", *J. Am. Ceram. Soc.* **77**:7 (1994), 1783–1786.

[Choi and Salem 1998] S. R. Choi and J. A. Salem, "'Ultra'-fast fracture strength of advanced ceramics at elevated temperatures", *Mater. Sci. Eng. A* **242**:1–2 (1998), 129–136.

[Deeg 1980] W. F. J. Deeg, *The analysis of dislocation, crack, and inclusion problems in piezoelectric solids*, Ph.D. thesis, Stanford University, 1980.

[Fang et al. 2004] D. Fang, B. Liu, and C. T. Sun, "Fatigue crack growth in ferroelectric ceramics driven by alternating electric fields", *J. Am. Ceram. Soc.* **87**:5 (2004), 840–846.

[Hao and Shen 1994] T. H. Hao and Z. Y. Shen, "A new electric boundary condition of electric fracture mechanics and its applications", *Eng. Fract. Mech.* **47**:6 (1994), 793–802.

[Hayashi et al. 2003] K. Hayashi, Y. Shindo, and F. Narita, "Displacement and polarization switching properties of piezoelectric laminated actuators under bending", *J. Appl. Phys.* **94**:7 (2003), 4603–4607.

[Lynch et al. 1995] C. S. Lynch, W. Yang, L. Collier, Z. Suo, and R. M. McMeeking, "Electric field induced cracking in ferroelectric ceramics", *Ferroelectrics* **166**:1 (1995), 11–30.

[McMeeking 1999] R. M. McMeeking, "Crack tip energy release rate for a piezoelectric compact tension specimen", *Eng. Fract. Mech.* **64**:2 (1999), 217–244.

[McMeeking 2004] R. M. McMeeking, "The energy release rate for a Griffith crack in a piezoelectric material", *Eng. Fract. Mech.* **71**:7–8 (2004), 1149–1163.

[Narita et al. 2007] F. Narita, Y. Shindo, and F. Saito, "Cyclic fatigue crack growth in three-point bending PZT ceramics under electromechanical loading", *J. Am. Ceram. Soc.* **90**:8 (2007), 2517–2524.

[Pak 1990] Y. E. Pak, "Crack extension force in a piezoelectric material", *J. Appl. Mech.* (*ASME*) **57**:3 (1990), 647–653.

[Pan et al. 1998] L. S. Pan, M. Matsuzawa, and S. Horibe, "Stress rate dependence of fracture strength in pre-cracked zirconia ceramics", *Mater. Sci. Eng. A* **244**:2 (1998), 199–206.

[Park and Sun 1995] S. B. Park and C. T. Sun, "Fracture criteria for piezoelectric ceramics", *J. Am. Ceram. Soc.* **78**:6 (1995), 1475–1480.

[Parton 1976] V. Z. Parton, "Fracture mechanics of piezoelectric materials", *Acta Astronaut.* **3**:9–10 (1976), 671–683.

[Shindo et al. 1990] Y. Shindo, E. Ozawa, and J. P. Nowacki, "Singular stress and electric fields of a cracked piezoelectric strip", *Int. J. Appl. Electrom. Mater.* **1** (1990), 77–87.

[Shindo et al. 2001] Y. Shindo, M. Oka, and K. Horiguchi, "Analysis and testing of indentation fracture behavior of piezoelectric ceramics under an electric field", *J. Eng. Mater. Technol.* (*ASME*) **123**:3 (2001), 293–300.

[Shindo et al. 2003] Y. Shindo, F. Narita, K. Horiguchi, Y. Magara, and M. Yoshida, "Electric fracture and polarization switching properties of piezoelectric ceramic PZT studied by the modified small punch test", *Acta Mater.* **51**:16 (2003), 4773–4782.

[Shindo et al. 2004] Y. Shindo, M. Yoshida, F. Narita, and K. Horiguchi, "Electroelastic field concentrations ahead of electrodes in multilayer piezoelectric actuators: experiment and finite element simulation", *J. Mech. Phys. Solids* **52**:5 (2004), 1109–1124.

[Shindo et al. 2005] Y. Shindo, F. Narita, and M. Mikami, "Double torsion testing and finite element analysis for determining the electric fracture properties of piezoelectric ceramics", *J. Appl. Phys.* **97** (2005), 114109.

[Shindo et al. 2007] Y. Shindo, F. Narita, and F. Saito, "Static fatigue behavior of cracked piezoelectric ceramics in three-point bending under electric fields", *J. Eur. Ceram. Soc.* **27**:10 (2007), 3135–3140.

[Tiersten 1969] H. F. Tiersten, *Linear piezoelectric plate vibrations*, Plenum, New York, 1969.

[Yoshida et al. 2003] M. Yoshida, F. Narita, Y. Shindo, M. Karaiwa, and K. Horiguchi, "Electroelastic field concentration by circular electrodes in piezoelectric ceramics", *Smart Mater. Struct.* **12**:6 (2003), 972–978.

YASUHIDE SHINDO: shindo@material.tohoku.ac.jp
Department of Materials Processing, Graduate School of Engineering, Tohoku University, Sendai 980-8579, Japan

FUMIO NARITA: narita@material.tohoku.ac.jp
Department of Materials Processing, Graduate School of Engineering, Tohoku University, Sendai 980-8579, Japan

MITSURU HIRAMA: *Department of Materials Processing, Graduate School of Engineering, Tohoku University, Sendai 980-8579, Japan*

ON INHOMOGENEITY, GROWTH, AGEING
AND THE DYNAMICS OF MATERIALS

GERARD A. MAUGIN

The explicit dependence of material properties on the basic space-time parametrization of continuum mechanics is a most interesting departure from standard behavior. The best framework to formally place these effects in evidence is the so-called material mechanics of materials advocated by the late G.Herrmann. Among the manifestations of these dependencies, material inhomogeneity is the most obvious and frequent one, but others such as volumetric growth or ageing also occur naturally, not to speak of artificial situations where one tries to build dynamic materials whose parts purposefully react differently in space and time at the will of the designer. These different cases are briefly sketched out first on the basis of a Lagrangian formulation and then in the general framework of thermomechanics.

1. Introduction

Long before the works of Kuhn [1962], the French epistemologist Bachelard [1940] wrote a marvelous little book introducing the notion of epistemological fracture (the equivalent of the change of scientific paradigm of Kuhn). Bachelard introduced the notion that many marked scientific progresses are made through the *negation* of previous theories; at least this is what appears in the language used and also in the definition of the object of study. He wrote of the historical introduction of non-Euclidean geometry and of non-Newtonian physics. We could as well speak of non-Riemannian geometry (used in generalizations of Einstein's general relativity theory and the theory of crystal defects which have been of interest to us) and maybe of the more popularized nonlinear sciences. This is more to the point because nonlinearity can only be defined mathematically by a negation of linearity [Maugin et al. 1992, Ch. 1]. The negation or deprivation of a property in science is marked by different prefixes, depending mostly on the predominant influence of Greek or Latin: thus "*non*linear", "*an*isotropic", "*in*homogeneous", "*hetero*geneous", to cite only examples from the mechanics of materials. Sometimes more sophisticated expressions had to be found.

Most of the nineteenth century's phenomenological physics (heat conduction, electromagnetics, early continuum mechanics) is based on the consideration of linear, isotropic, homogeneous, time-independent properties. It is that relative simplicity which allowed for rapid developments thanks to the allied relative mathematical simplicity of associated problems. The success of some mathematical techniques (such as Fourier series and integral transforms) is directly associated to their adequacy in treating these problems. But some "non" properties were soon to appear especially in optics and crystallography where anisotropy plays a fundamental role. With such considerations new mathematical tools had to be developed such as tensor algebra (W. Voigt in crystallography) and then analysis (such as in general relativity), while nonlinearity largely forced the development of perturbation theory and other techniques. In modern

continuum thermomechanics which is our current interest, canons of a somewhat standardized mathematically formal presentation were fixed in the second part of the twentieth century. This resulted in the blossoming of treatises on continuum mechanics, a phenomenon best illustrated by the justified success met by the treatises of [Truesdell and Toupin 1960; Truesdell and Noll 1965], the textbooks of Eringen [1962; 1967], and many more, often influenced by the books of these pioneers. Many of the material properties and accompanying "non" properties were defined more precisely in these treatises, and these definitions have been duly accepted and copied by the whole profession. However, even in these very inclusive treatises the "non" properties are only paid lip-service except for nonlinearity (necessary in the framework of finite strains) and anisotropy (in order to consider the mechanics of crystals or of some fiber-reinforced materials). But the three phenomena heralded in the title of this contribution have taken a much greater importance in recent years with the necessary consideration of different types of material inhomogeneity (as in polycrystals, layered composites, and graded materials), of materials newly examined from the mechanical viewpoint (biological materials), and of an interest in new properties (as in ageing). Remarkably enough, all these properties are related to the space-time parametrization of the mechanical (and more generally physical) properties of materials. In a nutshell, most properties were considered independent of this parametrization until very recently, while now we are forced to look into this dependency. This, of course, is a matter of scale of observation (in space and time), but the space and time scales of interest have evolved rendering this matter of foremost interest.

The mathematical apparatus that deals directly with the invariance or lack of invariance with respect to changes of the space-time parametrization is the celebrated theorem of Noether [1918] in field theory. Accordingly, we consider below as a constructive example a simple variational formulation for elastic-like materials in finite strains. This has recently been exploited in a rather new field of research in continuum mechanics, called Eshelbian mechanics or configurational mechanics or mechanics on the material manifold [Noether 1918; Maugin 1993; 1995]. This approach, together with Noether's theorem, yields a canonical thermomechanics of materials where so-called canonical momentum and energy are treated in parallel, corresponding, respectively, to the changes of material coordinates and time. When dissipation is present and a standard variational formulation is no longer feasible, we shall then see how to reformulate a consistent theory. Finally, a glimpse at the future is reported.

The late George Herrmann was much interested in wave propagation in inhomogeneous (layered) structures. He also devoted much of his last research work to material and configurational forces with applications to the strength of materials; see, for example, [Kienzler and Herrmann 2000]. Thus it is natural that the present paper be dedicated to his memory.[1]

2. A sufficiently general variational formulation

We are concerned with simple general features of field theories in a continuum with space-time parametrization $\{X, t\}$, where X stands for material coordinates of classical continuum mechanics [Truesdell and Toupin 1960], and t for a timelike scalar variable (Newton's absolute time). We consider first Hamiltonian

---

[1]In fact, the material herein was presented as the Introductory Lecture at the *International Symposium on Defect Mechanics in Materials*, ISDMM, Aussois, France, March 2007, also dedicated to G. Herrmann. But the paper was not ready in time for the proceedings of that conference, edited by C. Dascalu and the author, to appear in 2008 as a special issue of the *International Journal of Fracture*.

actions of the type

$$A(\phi; V) = \int_{V \times I} L(\phi^\alpha, \partial_\mu \phi^\alpha; X^\mu) d^4 X, \tag{2-1}$$

where ϕ^α, $\alpha = 1, 2, \ldots, N$, denotes the ordered array of fields, say the independent components of a certain geometric object, and $d^4 X = dV\, dt$. This is a Cartesian-Newtonian notation, with

$$\{\partial_\mu = \partial/\partial X^\mu; \quad \mu = 1, 2, 3, 4\} = \{\partial/\partial X^K, \quad K = 1, 2, 3; \ \partial/\partial X^4 \equiv \partial/\partial t\}, \tag{2-2}$$

since

$$\{X^\mu, \quad \mu = 1, 2, 3, 4\} = \{X = (X^K, \quad K = 1, 2, 3), \quad X^4 = t\}.$$

The summation over dummy indices (Einstein convention) is enforced. We do not pay attention to boundary and initial conditions and impose no external sources. From expression (2-1) two types of equations can be derived: There are those relating to each one of the fields ϕ^α — these are the field equations — and those which express a general conservation law of the system governing all fields simultaneously. The first group is none other than the set of Euler-Lagrange variational equations

$$E_\alpha \equiv \frac{\delta L}{\delta \phi^\alpha} := \frac{\partial L}{\partial \phi^\alpha} - \frac{\partial}{\partial t}\left(\frac{\partial L}{\partial(\partial \dot{\phi}^\alpha)}\right) - \frac{\partial}{\partial X^K}\left(\frac{\partial L}{\partial(\partial \phi^\alpha/\partial X^K)}\right) = 0, \tag{2-3}$$

for each $\alpha = 1, 2, \ldots, N$, at any regular material point X and for any time t.

The second group of equations are the result of the variation of the parametrization, and these results, on account of the former group, express the invariance or lack of invariance of the whole system under changes of this parametrization. The resulting equations are nothing but the expression of the celebrated Noether's theorem [1918], which states that to any symmetry of the system there corresponds the conservation (or lack of strict conservation) of a current [Soper 1976]. Here, with respect to time and space-like parametrization we have the following two equations, a scalar conservation law in the explicit form

$$\frac{\partial H}{\partial t}\bigg|_X - \nabla_R \cdot \mathbf{Q} = h, \tag{2-4}$$

and a co-vectorial conservation (material) law

$$\frac{\partial \mathbf{P}}{\partial t}\bigg|_X - \operatorname{div}_R \mathbf{b} = \mathbf{f}^{\text{inh}}, \tag{2-5}$$

where we defined the following canonical quantities:

- Energy (Hamiltonian density)

$$H := \sum_\alpha \dot{\phi}^\alpha (\partial L/\partial \dot{\phi}^\alpha) - L, \qquad \dot{\phi}^\alpha \equiv \partial \phi^\alpha/\partial t; \tag{2-6}$$

- Energy flux vector

$$\mathbf{Q} = \left\{ Q^K := -\sum_\alpha \dot{\phi}^\alpha \frac{\partial L}{\partial(\partial_K \phi^\alpha)} \right\}; \tag{2-7}$$

- Canonical (material) momentum

$$\mathbf{P} = \left\{ P_K := -\sum_\alpha \frac{\partial \phi^\alpha}{\partial X^K} \frac{\partial L}{\partial(\partial \phi^\alpha/\partial t)} \right\}; \tag{2-8}$$

- Canonical stress tensor

$$b = \left\{ b_{.L}^K := -\left(L\delta_{.L}^K - \sum_\alpha \frac{\partial \phi^\alpha}{\partial X^L} \frac{\partial L}{\partial(\partial \phi^\alpha/\partial X^K)} \right) \right\}, \qquad (2\text{-}9)$$

with source terms

$$h := -\left.\frac{\partial L}{\partial t}\right|_{\text{expl}}, \qquad f^{\text{inh}} := \left.\frac{\partial L}{\partial X}\right|_{\text{expl}}, \qquad (2\text{-}10)$$

where the notation expl means that the derivatives are taken at fixed fields ϕ^α.

Definitions of various systems. Physical systems in which h does not vanish are said to be rheonomic (after Boltzmann cited by [Lanczos 1962, p.32]). Systems in which the material force f^{inh} does not vanish are said to be materially inhomogeneous. This is best illustrated by the case of hyperelasticity.

Other symmetries, and thus other consequences of Noether's theorem can be applied — such as for rotations [Maugin 1993, Section 5.2–5.5] — but these are not discussed further here as they will not be exploited. More is to be found on Noether's theorem and its relationship to the theory of Lie groups in [Olver 1986]. The above is quite sufficient for our purpose.

The case of hyperelasticity. This corresponds to a trivial and isomorphic application of the above given formulae with a special choice of the fields ϕ^α. They are the physical components (components in physical space at time t) of the placement of the material particle X; that is

$$x = \bar{x}(X, t). \qquad (2\text{-}11)$$

The physical velocity of X and the deformation gradient are defined by

$$v := \left.\frac{\partial \bar{x}}{\partial t}\right|_X, \qquad F := \left.\frac{\partial \bar{x}}{\partial X}\right|_t \equiv \nabla_R \bar{x}. \qquad (2\text{-}12)$$

For a first-order gradient theory of elasticity, the Lagrangian density L per unit volume in the reference configuration of the continuous body reads

$$L = \bar{L}(v, F; X, t) = K(v; X, t) - W(F; X, t), \qquad (2\text{-}13)$$

where W is the elasticity potential and K is the kinetic energy given in a general manner by

$$K = \tfrac{1}{2}\rho_0(X, t)v^2. \qquad (2\text{-}14)$$

Accordingly, Equations (2-3) through (2-5) render the balance of linear physical momentum (three components of the field x in physical space) as

$$\left.\frac{\partial p}{\partial t}\right|_X - \text{div}_R\, T = 0, \qquad (2\text{-}15)$$

and the balance of energy (a scalar equation), and the balance of material momentum (a covectorial equation on the material manifold) in the form of Equations (2-4) and (2-5), with the following expressions

for the quantities involved:

$$p := \rho_0 v, \qquad\qquad T := \frac{\partial W}{\partial F}, \tag{2-16}$$

$$H = K + W, \qquad\qquad Q = T \cdot v, \tag{2-17}$$

$$P := -\rho_0 v \cdot F, \qquad\qquad b = -(L\mathbf{1}_R + T \cdot F), \tag{2-18}$$

$$h := -(K/\rho_0)\frac{\partial \rho_0}{\partial t}\Big|_X + \frac{\partial W}{\partial t}\Big|_{\text{expl}}, \tag{2-19}$$

$$f^{\text{inh}} := (K/\rho_0)\frac{\partial \rho_0}{\partial X}\Big|_t - \frac{\partial W}{\partial X}\Big|_{\text{expl}}. \tag{2-20}$$

These are, respectively, the physical linear momentum p, the first Piola-Kirchhoff stress T, the Hamiltonian (energy) density H, the energy flux or Poynting vector Q, the material momentum P, the Eshelby material stress b (see [Maugin and Trimarco 1992], who gave this name to what Eshelby himself used to refer to as the energy-momentum tensor or Maxwell stress), the energy source h in a rheonomic system, and the material inhomogeneity force f^{inh} [Maugin 1993; 1995]. Rheonomic systems are rarely studied but in such systems energy is not conserved. (2-4) becomes a strict conservation law (no source), only when the system considered is scleronomic (that is, with no explicit time dependence of the Lagrangan density, according to the classification of Boltzmann and Lanczos). The possible explicit time dependency comes through the matter density in the kinetic energy and through the elasticity potential. This is seldom envisioned. But the possibility that the reference material density be an explicit function of time is nonetheless the basic working hypothesis in the theory of material growth (as in biological tissues [Epstein and Maugin 2000]), according to which

$$\frac{\partial \rho_0}{\partial t}\Big|_X \neq 0. \tag{2-21}$$

The selection of the word "growth" and the sign of the right-hand side in (2-21) are arbitrary since the inverse phenomenon, resorption, with the opposite sign is not forbidden.

The possibility that the elasticity potential W might depend explicitly on time,

$$\frac{\partial W}{\partial t}\Big|_{\text{expl}} \neq 0, \tag{2-22}$$

would refer to the phenomenon of ageing (evolution in time of material elasticity coefficients), a domain of research that remains practically unexplored probably due to the difficulty to measure experimentally the time evolution of interest. Note that the selection of the word ageing indicates an arrow of time since the opposite phenomenon, rejuvenation, is certainly forbidden by the second law of thermodynamics.

Together with the two conditions

$$\frac{\partial \rho_O}{\partial X}\Big|_t \neq 0, \qquad \frac{\partial W}{\partial X}\Big|_{\text{expl}} \neq 0, \tag{2-23}$$

relating to the two forms of material inhomogeneities, inertial ones — these appear only while dealing with problems of dynamics — and (here) elastic ones, Equations (2-21) and (2-22) define the "non" properties in which we are interested. However, in contrast to conditions (2-23), which bear no relationship

to irreversible thermodynamics, conditions (2-21) and (2-22) are related to it since they result in a non-conservation of energy. As a result, the nonspecified right-hand sides in these conditions are subjected the second law while those in Equations (2-23) are data in a specific problem.

Of course, the vast majority of elastic materials considered until now correspond to scleronomic systems. However, the frequent dependency of both ρ_0 and W on the material point X in materially inhomogeneous solids is an evidence, and its manifestation as a source term in (2-5) provides the basis for the theory of all types of material forces in solids. As a conclusion of this point, we note that hyperelasticity clearly is a paradigmatic theory of fields.

Now, the dynamic elasticity encapsulated in a Lagrangian such as (2-13) may be fully nonlinear as regards deformation processes, but it does not contain any characteristic length, except for inhomogeneous materials where the material spatial variation of the material properties (density, elasticity coefficients) may provide such a length. Homogeneous elasticity exhibiting a characteristic intrinsic length of necessity involves gradients of higher order than the first, e.g, the second material gradient of the placement or, just the same, the material gradient of the deformation gradient. That is, we may have to consider a generalization of (2-13) of the type

$$L = \bar{L}(v, F, \nabla_R F; X, t) = K(v; X, t) - W(F, \nabla_R F; X, t), \tag{2-24}$$

where the inertial contribution is left unchanged. In this case more lengthy representations than (2-7) and (2-9) have to be used.

3. Dissipation: elementary approach

The variational approach in Section 2, paradigmatic as it is, is not equipped to deal with true dissipative processes. However a simple argument shows the way for remedying this. We would have energy conservation if the right-hand side of (2-4) would vanish. Without introducing any thermal processes, this could be accomplished by adding from the outside a term that makes this right-hand side vanish. This will be a dissipation rate Φ. Thus we would have

$$\Phi = -\left(-\frac{\partial L}{\partial t}\Big|_{\text{expl}}\right) = \Phi_{\text{growth}} + \Phi_{\text{age}}, \tag{3-1}$$

with (2-19)

$$\Phi_{\text{growth}} = K\Pi_0/\rho_0, \qquad \Phi_{\text{age}} = -\frac{\partial W}{\partial t}\Big|_{\text{expl}}, \tag{3-2}$$

where Π_0 is the right-hand side of (2-21). This right-hand side will typically be of the form

$$\Pi_0 = R_0 + \nabla_R \cdot M \tag{3-3}$$

(see [Epstein and Maugin 2000]), where R_0 is an external supply — of, say, nutrients, via some biophysical process — and M is an influx of mass. Since K and ρ_0 are obviously positive, so must be Π_0 in order to guarantee a positive Φ_{growth}. As to Φ_{age} a simplistic case exemplifies the situation. We may assume that the explicit time dependence of W is only through material functions (with certain tensorial properties, a set of scalars being the simplest case) $\alpha(t)$. Then using a notation intentionally akin to that of the thermodynamics of irreversible processes with internal variables [Maugin 1999], we will set and

have

$$A := -\frac{\partial W}{\partial \alpha}, \qquad \Phi_{\text{age}} = A\dot{\alpha}, \tag{3-4}$$

where the appropriate inner product must be used in the last expression which is classically written as a bilinear form, the product of a thermodynamical force, A, and a time rate. The total expression must be non-negative according to the second law of thermodynamics. Consider a one-dimensional homogeneous elasticity in small strains ε such that $W(\varepsilon; t) = \frac{1}{2}\mu(t)\varepsilon^2$. Here α is a positive shear modulus, which may decrease exponentially with time: $\mu(t) = \mu_0[1 - \exp((t - t_0)/\tau)]$, with μ_0 and τ positive. Then $\Phi_{\text{age}} = \frac{1}{2}\mu(t_0)\varepsilon^2/\tau$, as shown by an elementary calculation. Of course, Φ_{age} (otherwise always positive) goes to zero for finite elastic energies as the characteristic ageing time τ increases indefinitely. This is but a rather naïve description of the phenomenon of creep. We shall return to this in further works.

4. Full irreversible thermodynamics

In that general case, like in the rest of continuum mechanics, we must start with a statement of global balance laws for a continuous simply connected material region B of the body, bounded by a sufficiently regular boundary ∂B equipped with unit outward normal N. We can thus state (omitting the balance of angular momentum):

- Balance of mass

$$\frac{d}{dt}\int_B \rho_0 \, dV = \int_B R_0 \, dV + \int_{\partial B} N \cdot M \, dA; \tag{4-1}$$

- Balance of linear (physical) momentum (in the absence of body forces)

$$\frac{d}{dt}\int_B p \, dV = \int_{\partial B} N \cdot T \, dV; \tag{4-2}$$

- First law of thermodynamics (E is the internal energy per unit reference volume; Q is the material heat flux; h_0 is a possible body heat source)

$$\frac{d}{dt}\int_B (K + E) \, dV = \int_B (h_0 - \tfrac{1}{2}v^2 R_0) \, dV + \int_{\partial B} (N \cdot T \cdot v - N \cdot Q - (\tfrac{1}{2}v^2)N \cdot M) \, dA; \tag{4-3}$$

- Second law of thermodynamics (S is the entropy per unit reference volume and θ is the non-negative thermodynamical temperature)

$$\frac{d}{dt}\int_B S \, dV \geq \int_B \theta^{-1}(h_0 - \tfrac{1}{2}v^2 R_0) \, dV - \int_{\partial B} \theta^{-1}N \cdot (Q + \tfrac{1}{2}v^2 M) \, dA. \tag{4-4}$$

In making these statements we have (i) implicitly assumed the necessity to include sources and fluxes of energy and entropy via energy mass source and transfer, and (ii) consistently written the sources of energy and entropy with the integrating factor θ^{-1}.

On account of the usual argument of continuity of the involved quantities, we immediately have the local form of Equations (4-1) through (4-4) at any regular material point X in B:

- Equation governing the mass density

$$\frac{\partial \rho_0}{\partial t}\bigg|_X = R_0 + \nabla_R \cdot M; \tag{4-5}$$

- Balance of linear (physical) momentum

$$\left.\frac{\partial \boldsymbol{p}}{\partial t}\right|_X - \operatorname{div}_R \boldsymbol{T} = \boldsymbol{0}; \tag{4-6}$$

- First law of thermodynamics

$$\left.\frac{\partial}{\partial t}(K+E)\right|_X - \nabla_R \cdot (\boldsymbol{T} \cdot \boldsymbol{v} - \boldsymbol{Q} - \tfrac{1}{2}v^2 \boldsymbol{M}) = h_0 - \tfrac{1}{2}v^2 R_0; \tag{4-7}$$

- Second law of thermodynamics

$$\left.\theta \frac{\partial S}{\partial t}\right|_X \geq h_0 - \tfrac{1}{2}v^2 R_0 - \nabla_R \cdot (\boldsymbol{Q} + \tfrac{1}{2}v^2 \boldsymbol{M}) + \boldsymbol{S} \cdot \nabla_R \theta, \tag{4-8}$$

where

$$\boldsymbol{S} := \theta^{-1}(\boldsymbol{Q} + \tfrac{1}{2}v^2 \boldsymbol{M}). \tag{4-9}$$

From (4-6) we obtain the kinetic-energy theorem by scalar product by $\boldsymbol{v}$. Accounting for the fact that a simple calculation allows one to show that

$$\left(\frac{\partial}{\partial t}\rho_0 \boldsymbol{v}\right) \cdot \boldsymbol{v} = \left.\frac{\partial K}{\partial t}\right|_X + \tfrac{1}{2}v^2 \left.\frac{\partial \rho_0}{\partial t}\right|_X, \tag{4-10}$$

we obtain

$$\left.\frac{\partial K}{\partial t}\right|_X + \tfrac{1}{2}v^2 \left.\frac{\partial \rho_0}{\partial t}\right|_X - \nabla_R \cdot (\boldsymbol{T} \cdot \boldsymbol{v}) + \boldsymbol{T} {:} (\nabla_R \boldsymbol{v})^T = 0. \tag{4-11}$$

Substituting into (4-7) we have the internal energy equation

$$\left.\frac{\partial E}{\partial t}\right|_X + \nabla_R \cdot \boldsymbol{Q} - \boldsymbol{T} {:} \dot{\boldsymbol{F}} + \boldsymbol{M} \cdot \nabla_R(\tfrac{1}{2}v^2) = h_0, \tag{4-12}$$

since

$$(\nabla_R \boldsymbol{v})^T = \dot{\boldsymbol{F}} := \left.\frac{\partial}{\partial t}(\boldsymbol{F}(\boldsymbol{X}, t))\right|_X. \tag{4-13}$$

We now introduce the Helmholtz free energy W by

$$W = E - S\theta. \tag{4-14}$$

and note that since E, W, and S are constitutive functions, if the physical system is rheonomic, we must isolate the implicit partial time derivatives. Thus we shall write as an example

$$\left.\frac{\partial W}{\partial t}\right|_X = \left.\frac{\partial W}{\partial t}\right|_{\text{impl}} + \left.\frac{\partial W}{\partial t}\right|_{\text{expl}}, \tag{4-15}$$

with a similar decomposition for E and S. On taking the partial time derivative of (4-14) we have thus

$$\left.\frac{\partial E}{\partial t}\right|_X = \left.\frac{\partial W}{\partial t}\right|_{\text{impl}} + \left.\frac{\partial W}{\partial t}\right|_{\text{expl}} - S \left.\frac{\partial \theta}{\partial t}\right|_X - \theta \left.\frac{\partial S}{\partial t}\right|_X. \tag{4-16}$$

Combining (4-8), (4-1) and (4-16) we arrive at an expression of the second law of thermodynamics known as the Clausius-Duhem inequality, here in the remarkable form

$$-\left(\left.\frac{\partial W}{\partial t}\right|_{\text{impl}} + S \left.\frac{\partial \theta}{\partial t}\right|_X\right) + \boldsymbol{T} {:} \dot{\boldsymbol{F}} + \Phi_{\text{age}} + \Phi_{\text{growth}} - \boldsymbol{S} \cdot \nabla_R \theta \geq 0, \tag{4-17}$$

where the dissipation rates due to ageing and growth are defined just as in Equations (3-2)–(3-3). Note that neither anisotropy nor material inhomogeneity play any role in the above derivation. Herein above no constitutive equations have been assumed, even for the Piola-Kirchhoff stress $\boldsymbol{T}$. The example closest to the consideration of Sections 2 and 3 is that dealing with a materially inhomogeneous, rheonomic thermoelastic conductor of heat for which the free energy W may be considered a function

$$W = \bar{W}(\boldsymbol{F}, \theta; \boldsymbol{X}, t). \tag{4-18}$$

The usual argument to exploit (4-17) is not altered by the presence of the last two arguments in (4-18). Accordingly, we have the constitutive equations

$$\boldsymbol{T} = \frac{\partial \bar{W}}{\partial \boldsymbol{F}}, \qquad S = -\frac{\partial \bar{W}}{\partial \theta}, \tag{4-19}$$

while there remains the dissipation inequality

$$\Phi_{\text{age}} + \Phi_{\text{growth}} - \boldsymbol{S} \cdot \nabla_R \theta \geq 0. \tag{4-20}$$

It remains to establish the expression of the balance of material momentum in this case to compare to the developments of Section 2.

5. Balance of material momentum

In the presence of dissipation we know that this can be obtained only by parodying the Noether's identity of variational field theory [Maugin 2006a]. This is mainly achieved by taking the inner product of (4-6) by $\boldsymbol{F}$ to the right. We can try to go as far as possible without specifying the functional dependence of the energy density [Maugin 2006b], or work out the special case (4-18) for which we already know that thermal effects introduce a pseudoforce of material inhomogeneity as a contribution in the right-hand side of the canonical (4-5) [Epstein and Maugin 1995]. What about growth and ageing [Chudnovsky and Preston 1996]? Do they create such material pseudoforces? Although we could follow the general approach of [Maugin 2006b], we simply consider the case of the known form (4-18). Since the operations involved in this manipulation concern only space derivatives (material gradients) and no time derivatives, we can state that ageing will not modify the balance of material momentum, and we could state more generally that nothing would a priori be modified in quasi-statics. But inertia (and hence matter density) is involved in the full dynamics so that this is the only point to be examined more carefully. As a matter of fact, following a now-traditional computation we clearly have

$$\left(\frac{\partial}{\partial t}\rho_0\boldsymbol{v}\right) \cdot \boldsymbol{F} = -\frac{\partial \boldsymbol{P}}{\partial t}\bigg|_X - \nabla_R\left(\rho_0\frac{\boldsymbol{v}^2}{2}\right) + \left(\frac{\boldsymbol{v}^2}{2}\right)\nabla_R\rho_0, \quad \boldsymbol{P} := -\rho_0\boldsymbol{v} \cdot \boldsymbol{F}. \tag{5-1}$$

This shows that there is no alteration brought to the classical derivation of the equation of balance of material momentum from the balance of physical momentum due to growth processes since the first term in the right-hand side of (5-1) is the classical term. Accordingly, in the case where (4-18) holds true, we would obtain in that manner the same formal expression as in classical (scleronomic) materially inhomogeneous thermoelasticity

$$\frac{\partial \boldsymbol{P}}{\partial t}\bigg|_X - \operatorname{div}_R \boldsymbol{b} = \boldsymbol{f}^{\text{inh}} + \boldsymbol{f}^{\text{th}}, \tag{5-2}$$

wherein

$$\boldsymbol{b} = -(L^{\text{th}}\mathbf{1}_R + \mathbf{TF}), \qquad \boldsymbol{f}^{\text{inh}} := \left.\frac{\partial L^{\text{th}}}{\partial \boldsymbol{X}}\right|_{\text{expl}}, \qquad \boldsymbol{f}^{\text{th}} := S\nabla_R\theta, \qquad L^{\text{th}} = K - \bar{W}(\boldsymbol{F}, \theta; \boldsymbol{X}, t).$$

So much for a short exploration of the works on ageing to be expanded later on.

6. A glimpse at the future of adaptive structures

So far, only natural objects have been envisaged in our considerations. But in these times of man-designed new materials and more particularly smart materials and adaptive structures, we may think of designing structures made of materials that are artificially rendered materially inhomogeneous and rheonomic and this at a scale that may suit certain exploitation at the microscopic and nanoscopic levels. Imagine, for instance that we have a material of which the material property such as elasticity may vary in time according to a certain time scale while, the mass distribution may vary in space in the way that we like. Because of the good choice of material coordinates and Newtonian time as space-time coordinates, an equation of motion such as (2-15), expressed componentwise as

$$\left.\frac{\partial}{\partial t}\rho_0(\boldsymbol{X})v_i\right|_X - \left.\frac{\partial}{\partial X^K}T_{.i}^K\right|_t = 0, \tag{6-1}$$

will yield an equation where the space-dependent density comes out of the time derivative in the first term and the purely time-dependent material property will come out of the material divergence in the second term. In the case of linear elasticity in small strains this will give in one-dimension a wave equation of the type

$$u_{tt} - c^2(x, t)u_{xx} = 0, \tag{6-2}$$

with a space-time dependent acoustic velocity. This can be realized in several ways in an essentially one-dimensional structure such as a rod with more or less smoothly varying cross section and local elasticity controlled in time by an external field such as an electromagnetic one. An equation such as (6-2) is mathematically linear (in the elastic displacement u), but the dynamical overall behavior of the resulting structure may be akin to some nonlinear structure as regards certain signals carried by the structure. The latter becomes thus a dynamical structure in the sense of [Lurie 2007], and from here we can dream of several interesting possibilities that we let the reader discover by himself. An allied problem appears in the form of homogenization in both space and time.

References

[Bachelard 1940] G. Bachelard, *La philosophie du non: essai d'une philosophie du nouvel esprit scientifique*, Presses Universitaires de France, Paris, 1940.

[Chudnovsky and Preston 1996] A. Chudnovsky and S. Preston, "Geometrical modeling of material aging", *Extracta Mathematicae* **11**:1 (1996), 22–36. Spain.

[Epstein and Maugin 1995] M. Epstein and G. A. Maugin, "Thermoelastic material forces: definition and geometric aspects", *C. R. Acad. Sci. II B Mec.* **320** (1995), 63–68.

[Epstein and Maugin 2000] M. Epstein and G. A. Maugin, "Thermomechanics of volumetric growth in uniform bodies", *Int. J. Plast.* **16**:7-8 (2000), 951–978.

[Eringen 1962] A. C. Eringen, *Nonlinear theory of continuous media*, McGraw Hill, New York, 1962.

[Eringen 1967] A. C. Eringen, *Mechanics of continua*, Wiley, New York, 1967. Reprinted 1980 by Krieger, Malabar, FL.

[Kienzler and Herrmann 2000] R. Kienzler and G. Herrmann, *Mechanics in material space: with applications to defect and fracture mechanics*, Springer, Berlin, 2000.

[Kuhn 1962] T. S. Kuhn, *The structure of scientific revolutions*, vol. 2, International encyclopedia of unified science. Foundations of the unity of science **2**, Univ. Chicago Press, Chicago, 1962.

[Lanczos 1962] C. Lanczos, *The variational principles of mechanics*, Mathematical expositions **4**, University of Toronto Press, Toronto, 1962.

[Lurie 2007] K. A. Lurie, *An introduction to the mathematical theory of dynamic materials*, Advances in mechanics and mathematics **15**, Springer, New York, 2007.

[Maugin 1993] G. A. Maugin, *Material inhomogeneities in elasticity*, Applied mathematics and mathematical computation **3**, Chapman and Hall, London, 1993.

[Maugin 1995] G. A. Maugin, "Material forces: concepts and applications", *Appl. Mech. Rev.* (*ASME*) **48** (1995), 213–245.

[Maugin 1999] G. A. Maugin, *The thermodynamics of nonlinear irreversible behaviors*, World Scientific, Singapore, 1999.

[Maugin 2006a] G. A. Maugin, "On canonical equations of continuum thermomechanics", *Mech. Res. Commun.* **33**:5 (2006), 705–710.

[Maugin 2006b] G. A. Maugin, "On the thermomechanics of continuous media with diffusion and /or weak nonlocality", *Arch. Appl. Mech.* **75**:10-12 (2006), 723–738.

[Maugin and Trimarco 1992] G. A. Maugin and C. Trimarco, "Pseudomomentum and material forces in nonlinear elasticity: variational formulations and application to brittle fracture", *Acta Mech.* **94**:1-2 (1992), 1–28.

[Maugin et al. 1992] G. A. Maugin, J. Pouget, R. Drouot, and B. Collet, *Nonlinear electromechanical couplings*, Wiley, New York, 1992.

[Noether 1918] E. Noether, "Invariante Variationsprobleme", *Nachr. Gesellschaft. Wiss. Göttingen* (1918), 235–257. English translation in *Transport Th. Stat. Mech.* **1**:3 (1971), 183–207.

[Olver 1986] P. J. Olver, *Applications of Lie groups to differential equations*, Springer, Berlin, 1986.

[Soper 1976] D. E. Soper, *Classical field theory*, Wiley, New York, 1976.

[Truesdell and Noll 1965] C. Truesdell and W. Noll, *The non-linear field theories of mechanics*, edited by S. Flügge, Handbuch der Physik **III-3**, Springer, Berlin, 1965.

[Truesdell and Toupin 1960] C. A. Truesdell and R. A. Toupin, *The classical field theories*, edited by S. Flügge, Handbuch der Physik **III-1**, Springer, Berlin, 1960.

GERARD A. MAUGIN: gerard.maugin@upmc.fr
Université Pierre et Marie Curie (Paris 6), Institut Jean Le Rond d'Alembert, Case 162, 4 place Jussieu,, 75252 Paris Cedex 05, France

BRITTLE FRACTURE BEYOND THE STRESS INTENSITY FACTOR

C. T. SUN AND HAIYANG QIAN

It is commonly believed that the fracture toughness of a brittle material can be characterized by a single parameter such as the stress intensity factor. In this study, it was demonstrated that when the crack is highly constrained, the first nonsingular opening stress term at the crack tip, in addition to the K-field (the singular stress term), is necessary to predict fracture. Fracture experiments were conducted using plexiglass specimens with a center crack. Relatively rigid metallic end tabs were used to generate boundary constraints on the specimen. The level of constraint was varied by varying the gage length between the end tabs. For a given crack length, the fracture load increases as the gage length decreases. If the stress intensity factor is used to determine the corresponding fracture toughness of plexiglass, the experimental data would indicate that the fracture toughness decreases as the gage length decreases. This is equivalent to saying that the fracture toughness of a brittle material can be affected by boundary conditions. It was shown that this behavior is the result of a diminishing size of the K-dominance zone and that the stress intensity factor alone cannot fully capture the fracture force. A new constant parameter was introduced to account for the effect of the near-tip nonsingular stress field on fracture.

1. Introduction

It is a common notion that, for brittle materials, fracture can be characterized by a stress intensity factor alone and that the nonsingular part of the near-tip stress field may be ignored. However, it has been found in many situations that the use of stress intensity (or energy release rate) alone may lead to variable fracture toughness, resulting from constraining conditions on the crack. One of the notable examples is in adhesively bonded structural joints. Gardon [1963] performed an adhesive peeling test and found that the peeling force decreased as the adhesive layer became thinner. Bascom et al. [1975] and Bascom and Cottington [1976] discovered from the tapered double cantilever beam test that the strength of rubber-modified epoxy-bonded specimens increased with the decrease of the adhesive thickness. This behavior was subsequently confirmed by many researchers [Kin Loch and Shaw 1981; Daghyani et al. 1995a; 1995b; Ikeda et al. 2000; Yan et al. 2001; 2002; Lee et al. 2003; 2004] using the same adhesive material and similar specimens. Attempts were made to use plastic zone size and its shape ahead of the crack tip to qualitatively explain the adhesive thickness-dependent fracture toughness [Kin Loch and Shaw 1981].

Similar to adhesive joints, there are cracked elastic bodies in which the singular stress field (the K-field) is very small and may not be sufficient to describe the state of stress in the fracture process zone, and thus a constant stress intensity factor is not sufficient to characterize the fracture toughness of brittle materials. On the other hand, for elastic-plastic materials, Larsson and Carlson [1973] and Rice [1974] recognized the influence of T-stress (the first nonsingular normal stress parallel to the crack plane) on the

crack tip plastic zone size and on the fracture behavior. Since then, there have been numerous publications addressing different aspects of T-stress. For instance, Leevers and Radon [1982] introduced a biaxiality ratio to account for the effect of the nonsingular stress terms, and Kardomateas et al. [1993] used the biaxiality ratio to explain the difference between the fatigue crack growth rates of short cracks and long cracks.

The purpose of this research is to employ the concept of the K-dominance zone near the crack tip to gauge the importance of the nonsingular stress terms. We focus on relatively brittle materials so that the first nonsingular term in the near-tip opening stress, rather than the T-stress, is considered in characterizing the fracture condition. A center cracked plexiglass specimen clamped on both loading sides was used to conduct the fracture experiment. To vary the contribution of the nonsingular stress to the total opening stress near the crack tip, the distance between the clamps was varied. It is demonstrated that the near-tip stress field, especially the size of the region dominated by the singular stress field (the K-dominance zone), can be significantly altered by the boundary constraints resulting from the clamps. Consequently, the fracture load cannot be predicted using the stress intensity factor alone. A two-parameter fracture model is proposed to characterize a nonconstant apparent fracture toughness of plexiglass.

2. Specimens and fracture experiment

Center cracked plexiglass specimens as shown in Figure 1 were used in the fracture test. The thickness was 4.76 mm (0.1875 inch) for all specimens. The specimen width (W) was 76.2 mm (3 inch) and a crack of length ($2a$) 25.4 mm (1 inch) was created using a water jet cutting machine. The crack created in this manner was not sharp enough and was extended further for about a millimeter using a razor blade (see Figure 2). The height (T) of the end tabs was 38.1 mm (1.5 inch). Five different values of gage length ($2h$) were considered to vary the constraining effect of the boundary on the crack. The gage length was selected to yield six different ratios to the initial crack length: $h/a = 10, 4, 2, 1, 0.5$ and 0.25. The constraining effect on the crack is characterized by the h/a ratio.

Aluminum end tabs (3.9 mm thick) were bonded on the specimens. Fracture tests were performed on an MTS 22 kip machine under a constant displacement rate loading at 0.001 mm/sec.
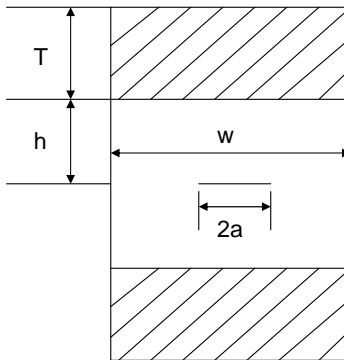
Figure 1. Specimen configuration.
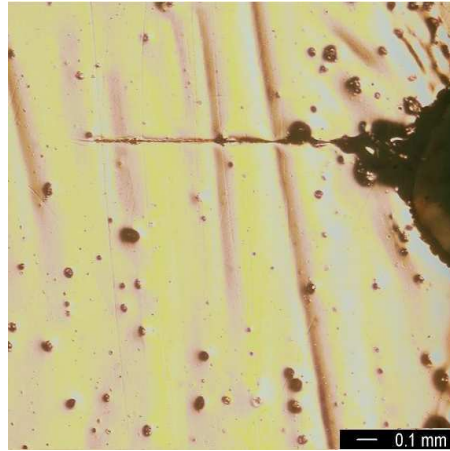
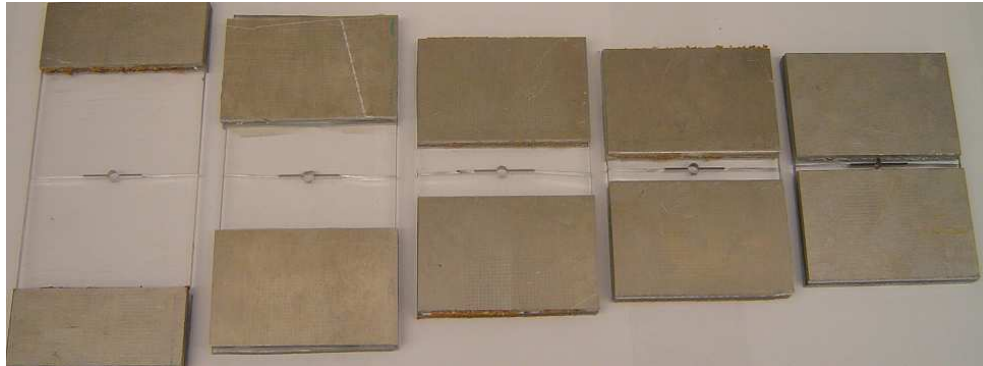**Figure 2.** Sharp crack tip created by a razor blade.

Figure 3. Specimens after fracture.

Figure 3 shows sample specimens with different gage lengths after the fracture test. The failure appears to be a typical brittle fracture failure and no stable crack growth was observed. For each gage length (h/a ratio), at least three specimens were tested. Figure 4 shows the failure loads for specimens with the six gage lengths. The data clearly show that for h/a smaller than 2, the average strength of the specimens increases with decreasing h/a value. For h/a ratios larger than 2, the failure load appears to approach a constant. In other words, the strength of the specimen is not affected by the gage length when the constraining effect diminishes. On the other hand, the strength of the specimen seems to keep increasing as the gage length decreases.

3. Analysis of fracture data

3.1. *Finite element model.* The elastic stress analysis is performed using the commercial finite element code ABAQUS 6.6. In view of the symmetric configuration of the specimen, a quadrant of the specimen is modeled. Symmetric boundary conditions are applied along the corresponding edges of symmetry. Because aluminum has a much greater elastic modulus than plexiglass, the clamped boundary can be
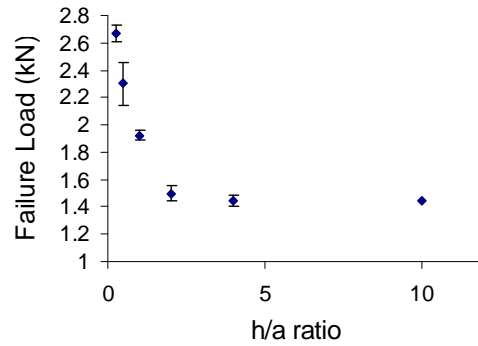
Figure 4. Experimental failure loads for different h/a ratios.
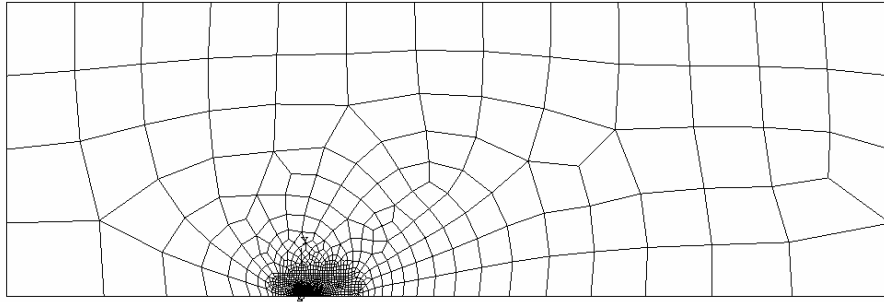
Figure 5. Finite element mesh for specimen with $h/a = 1$.

regarded as a rigid boundary so that a uniform displacement loading is assumed. In the numerical analysis, the crack length is the initial crack length created by the water jet plus the small extension produced by the razor blade.

Figure 5 shows the typical configuration and mesh of one of the models for $h/a = 1$. A 4-node plane strain element (CPE4) is used. In order to capture the high stress gradient field near the crack tip for small gage length cases, relatively fine mesh sizes are adopted around the crack tip. The smallest element size is less than 0.0001 of the half crack length which ensures converged solutions. The mesh around the crack tip is also made uniform in order to facilitate the computation of the energy release rate using the modified crack closure method [Rybicki and Kanninen 1977]. The stress intensity factor is then obtained from its relation with the energy release rate. An elastic Young's modulus for the plexiglass of 2.8 GPa (reported by the manufacturer) and a Poisson's ratio of 0.3 are used in the calculation.

3.2. *Conventional LEFM fracture prediction.* In linear elastic fracture mechanics (LEFM), the stress intensity factor is used to characterize the fracture toughness (K_c) of a brittle material. For a given specimen thickness the value of K_c is assumed to be a constant. To check the validity of the this assumption regarding the specimen configuration, the stress intensity factors for different h/a ratios are calculated for an applied load of 2 kN, with the result given in Figure 6. It is seen that the stress intensity factor is greatly influenced by the h/a ratio in the range of h/a smaller than 4. In LEFM, fracture toughness is considered as a material constant and is used as the single parameter to predict fracture failure. If this assumption is valid, then the value of K_c can be determined using the specimen with $h/a = 4$ and then
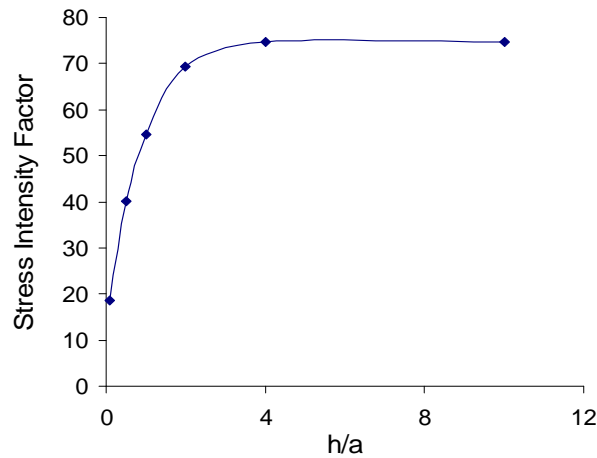
Figure 6. Effect of h/a ratio on stress intensity factor.
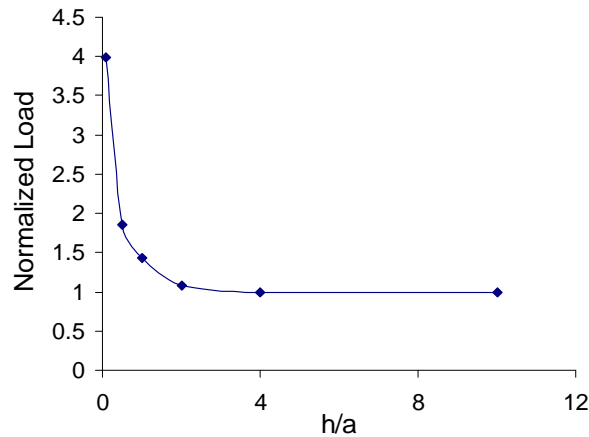

Figure 7. Failure loads (for the same critical stress intensity factor) normalized by the failure load corresponding to $h/a = 4$.

used to predict the failure loads for other specimens with smaller h/a ratios, as shown in Figure 7. (All failure loads in that figure are normalized with respect to the failure load for $h/a = 4$.)

3.3. *Comparison with experimental result.* From the results presented in Figures 6 and 7, the fracture toughness approaches a constant value K_c^∞ for $h/a \geq 4$. If this K_c^∞ value is used to predict the failure loads for all specimens with different h/a ratios, then the predicted failure loads for h/a smaller than 4 deviate significantly from the experimental results, as shown in Figure 8. Note that in Figure 8, the experimental failure load is normalized with respect to the failure load of the specimen with $h/a = 4$. It is evident that the LEFM prediction appears to be valid only for h/a ratios larger than 4, for which the boundary constraining effect diminishes and the stress intensity factor is a constant value for a given applied load (see Figure 6). If a single K_c parameter is to be adopted to characterize the fracture toughness of plexiglass, then the value of K_c must be a function of h/a (see Figure 9). The asymptotic value K_c^∞ as the fracture toughness is only valid for large values of h/a ratios.
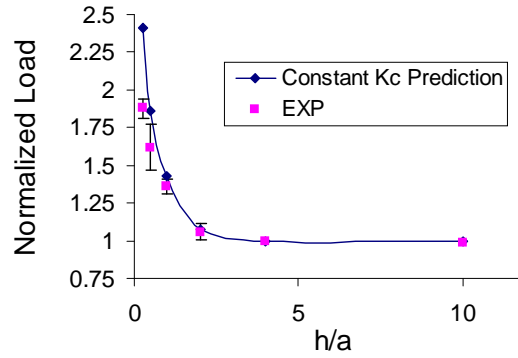
Figure 8. Comparison of LEFM prediction and experimental data.
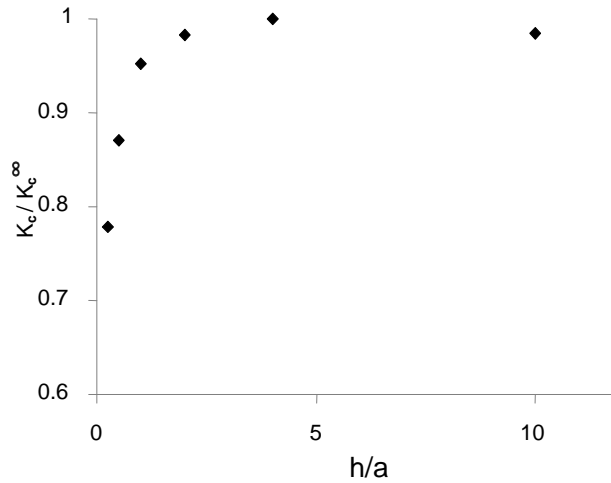
Figure 9. Apparent K_c based on LEFM and experimental failure load.

4. K-dominance zone analysis

The reason that a single parameter K_c is sufficient to characterize fracture toughness in brittle materials is based on the assumption that the singular stress field (the K field) is the dominant stress field near the crack tip and that the "fracture process" zone is totally contained inside the K-dominance zone. If this assumption is not valid then the fracture process may be influenced by the nonsingular part of the near tip stress. Thus, to explain the discrepancy displayed in Figure 8, the size of the K-dominance zone must be investigated.

The total opening stress ahead of the crack tip can be expressed in a general form as

$$\sigma_{yy} = \frac{K}{\sqrt{2\pi x}} + \text{ nonsingular stress},\tag{1}$$
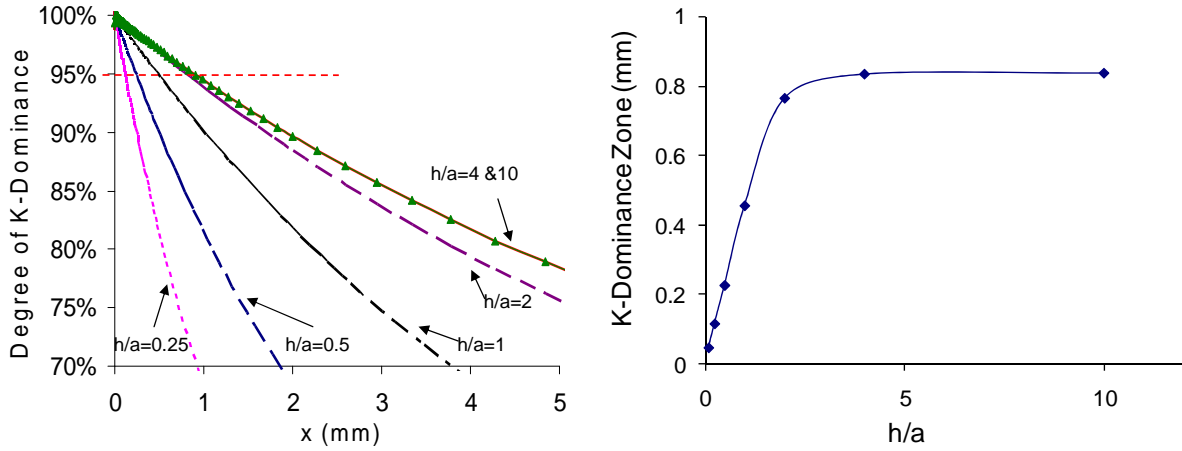
Figure 10. Left: K-dominance as a function of x. Right: Size of the K-dominance zone (region where $\Lambda \geq 95\%$).

where K is the stress intensity factor and x is the distance from the crack tip. At a given location x, the weight of the singular term can be quantified by the degree of K-dominance defined as

$$\Lambda = \frac{\sigma_{yy}^{\text{Singular}}}{\sigma_{yy}^{\text{Singular}} + \left|\sigma_{yy}^{\text{Nonsingular}}\right|}, \tag{2}$$

where

$$\sigma_{yy}^{\text{Singular}} = \frac{K}{\sqrt{2\pi x}}, \qquad \sigma_{yy}^{\text{Nonsingular}} = \sigma_{yy} - \sigma_{yy}^{\text{Singular}}.$$

The value of Λ represents the percentage of the singular stress in the total opening stress at a given location. Figure 10, left, shows the degree of K-dominance as a function of the distance from the crack tip. As expected, for all the curves, the value of Λ starts from 100% at the crack tip and then decreases as the distance from the crack tip increases. Note that Λ drops much faster in specimens with smaller gage lengths (h/a ratio) than those with larger gage lengths; for h/a ratios larger than 4, the Λ curves approach a limiting curve.

Define the K-dominance zone as the region in which $\Lambda \geq 95\%$; this region can be determined from the plot of Λ, and its dependence on h/a is shown in Figure 10, right. Clearly, the size of the K-dominance zone becomes a constant for $h/a \geq 4$. Below this ratio, the zone shrinks significantly as the h/a ratio decreases.

We conclude from these results that, as the gage length (or h/a) decreases, the nonsingular stress may not be negligible compared to the singular term in the near-tip region. In other words, the stress intensity factor cannot fully represent the stress field except for a region extremely close to the crack tip. This is why the stress intensity factor alone cannot adequately serve as the fracture failure criterion.

5. Two-parameter model

As we saw in Figure 10, the K-dominance zone decreases as the h/a ratio decreases. This indicates that the stress intensity factor is no longer sufficient to represent the full stress effect ahead of the crack tip
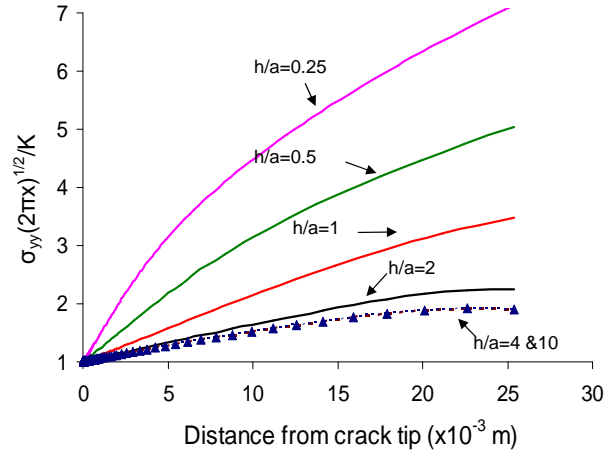
Figure 11. Distribution of opening stress ahead of the crack tip.

and that the nonsingular stress may be needed to predict the fracture load. From William's expansion of the near-tip opening stress we have

$$\sigma_{yy}\sqrt{2\pi x} = K + C_0\sqrt{2\pi}x + C_1\sqrt{2\pi}x^{3/2} + \cdots. \tag{3}$$

The $\sigma_{yy}\sqrt{2\pi x}$ vs. x curves for various h/a ratios are calculated and plotted in Figure 11. Note that in Figure 11, loads are selected so that the same stress intensity factor is produced for all cases of h/a ratios. As shown in Figure 11, the magnitude of the nonsingular stress may become comparable to the singular stress at a small distance from the crack tip, especially for those associated with smaller h/a ratios. It is also found that the near tip opening stress distributions for $h/a = 4$ and $h/a = 10$ are almost identical. This shows that the boundary constraining effect vanishes when the h/a ratio reaches a certain value ($h/a = 4$ in this case).

It is seen from Figure 11 that $\sigma_{yy}\sqrt{2\pi x}$ increases almost linearly with respect to x near the crack tip and can be closely approximated as

$$\sigma_{yy}\sqrt{2\pi x} = K + Ax. \tag{4}$$

Rearranging (4), we have

$$\sigma_{yy}\sqrt{2\pi x}/K = 1 + Cx \quad (C = A/K). \tag{5}$$

The value of the coefficient C depends on the value of h/a and can be obtained from the result of Figure 11:

$$C = \left(65(h/a)^{-1.3} + 61.37\right)\text{m}^{-1}. \tag{6}$$

Note that the value of C approaches a constant $C_0 = 61.37\text{m}^{-1}$ as h/a increases beyond 4.

Define the effective stress intensity factor based on the expression of (4) as

$$K^{\text{eff}} = \sigma_{yy}\sqrt{2\pi x_0} = K + Ax_0, \tag{7}$$

where x_0 is a critical distance to be determined from the experimental result. If, in addition, we set

$K^{\text{eff}} = K_c^\infty$ for $h/a \geq 4$, then (7) becomes

$$K_c^\infty = K_c + Ax_0 = K_c(1 + Mx_0), \tag{8}$$

where

$$M = C - 61.37 = 65(h/a)^{-1.3}\text{m}^{-1}. \tag{9}$$

From (8), the apparent fracture toughness for any given h/a ratio is given by

$$K_c = K_c^\infty/(1 + Mx_0). \tag{10}$$

Finally, the critical distance x_0 is determined by least square fitting of the experimental data for six different h/a ratios, shown in Figure 9. We obtain $x_0 = 0.75$ mm. Thus the apparent fracture toughness K_c can be explicitly expressed as

$$K_c = \frac{K_c^\infty}{1 + Mx_0} = \frac{K_c^\infty}{1 + 0.49(h/a)^{-1.3}}. \tag{11}$$

The above equation indicates that the decrease of the K-dominance zone size with the h/a ratio reduces the apparent fracture toughness. Figure 12 shows the experimental K_c together with the result obtained from (11).

   To predict the failure load for a given h/a ratio, the apparent fracture toughness K_c calculated according to (11) is used. In (11), effective fracture toughness K^{eff} and critical distance x_0 are regarded as material constants and coefficient A is obtained from the near-tip opening stress calculated by the FEA. Figure 13 shows the comparison of the failure loads obtained using the constant $K_c = K_c^\infty$ and the two-parameter model, respectively. It can be seen that the two parameter model is more adequate in predicting the failure load. It is of interest to note that the two-parameter model predicts that the failure load would begin to decrease rapidly at the h/a ratio around 0.1. In fact, based on (11), the failure load would diminish as the h/a ratio approaches zero. The validity of this result needs further experimental verification.
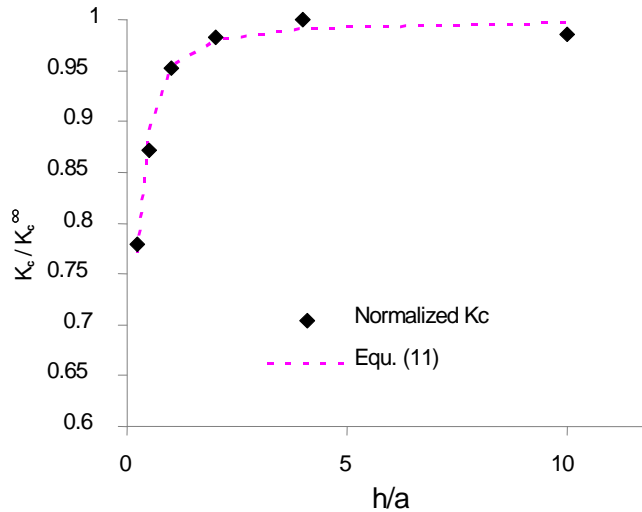

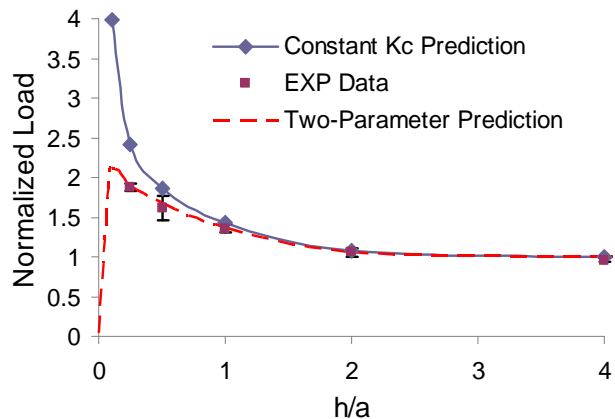**Figure 12.** Apparent fracture toughness K_c predicted by Equation (11).

Figure 13. Failure load according to the two-parameter model.

6. Conclusion

It has been demonstrated that even for materials commonly considered as brittle, the LEFM may not always be adequate for characterizing their toughness properties. The main reason lies in the fact that, under some boundary conditions, the crack tip region in which the singular stress represented by the stress intensity factor (the K-field) becomes very small and cannot adequately describe the fracture force. Consequently, the nonsingular part of the opening stress field in addition to the K-field is needed to predict fracture. The two-parameter model that includes the stress intensity factor and the first dominant nonsingular stress term seems to be capable of predicting fracture loads for plexiglass under general crack tip stress conditions.

Acknowledgement

References

[Bascom and Cottington 1976] W. D. Bascom and R. L. Cottington, "Effect of temperature on the adhesive fracture behavior of an elastomer-epoxy resin", *J. Adhesion* **7**:4 (1976), 333–346.

[Bascom et al. 1975] W. D. Bascom, R. L. Cottington, R. L. Jones, and P. Peyser, "The fracture of epoxy- and elastomer-modified epoxy polymers in bulk and as adhesives", *J. Appl. Polym. Sci.* **19**:9 (1975), 2545–2562.

[Daghyani et al. 1995a] H. R. Daghyani, L. Ye, and Y. W. Mai, "Mode-I fracture behaviour of adhesive joints, I: Relationship between fracture energy and bond thickness", *J. Adhesion* **53**:3–4 (1995), 149–162.

[Daghyani et al. 1995b] H. R. Daghyani, L. Ye, and Y. W. Mai, "Mode-I fracture behaviour of adhesive joints, II: Stress analysis and constraint parameters", *J. Adhesion* **53**:3–4 (1995), 163–172.

[Gardon 1963] J. L. Gardon, "Peel adhesion, I: Some phenomenological aspects of the test", *J. Appl. Polym. Sci.* **7**:2 (1963), 625–641.

[Ikeda et al. 2000] T. Ikeda, A. Yamashita, D. Lee, and N. Miyazaki, "Failure of a ductile adhesive layer constrained by hard adherends", *J. Eng. Mater. Technol.* (*ASME*) **122**:1 (2000), 80–85.

[Kardomateas et al. 1993] G. A. Kardomateas, R. L. Carlson, A. H. Soediono, and D. P. Schrage, "Near tip stress and strain fields for short elastic cracks", *Int. J. Fract.* **62**:3 (1993), 219–232.

[Kin Loch and Shaw 1981] A. J. Kin Loch and S. J. Shaw, "The fracture resistance of a toughened epoxy adhesive", *J. Adhesion* **12**:1 (1981), 59–77.

[Larsson and Carlson 1973] S. G. Larsson and A. J. Carlson, "Influence of non-singular stress terms and specimen geometry on small-scale yielding at crack tips in elastic-plastic materials", *J. Mech. Phys. Solids* **21**:4 (1973), 263–277.

[Lee et al. 2003] D. B. Lee, T. Ikeda, N. Miyazaki, and N. Choi, "Fracture behavior around a crack tip in rubber-modified epoxy adhesive joint with various bond thicknesses", *J. Mater. Sci. Lett.* **22**:3 (2003), 229–233.

[Lee et al. 2004] D. B. Lee, T. Ikeda, N. Miyazaki, and N. Choi, "Effect of bond thickness on the fracture toughness of adhesive joints", *J. Eng. Mater. Technol.* (*ASME*) **126**:1 (2004), 14–18.

[Leevers and Radon 1982] P. S. Leevers and J. C. Radon, "Inherent stress biaxiality in various fracture specimen geomtries", *Int. J. Fract.* **19**:4 (1982), 311–325.

[Rice 1974] J. R. Rice, "Limitations to the small scale yielding approximation for crack tip plasticity", *J. Mech. Phys. Solids* **22**:1 (1974), 17–26.

[Rybicki and Kanninen 1977] E. F. Rybicki and M. F. Kanninen, "A finite element calculation of stress intensity factors by a modified crack closure integral", *Eng. Fract. Mech.* **9**:4 (1977), 931–938.

[Yan et al. 2001] C. Yan, Y. W. Mai, Q. Yuan, L. Ye, and J. Sun, "Effects of substrate materials on fracture toughness measurement in adhesive joints", *Int. J. Mech. Sci.* **43**:9 (2001), 2091–2102.

[Yan et al. 2002] C. Yan, K. Xiao, L. Ye, and Y. W. Mai, "Numerical and experimental studies on the fracture behavior of rubber-toughened epoxy in bulk specimen and laminated composites", *J. Mater. Sci.* **37**:5 (2002), 921–927.

C. T. SUN: sun@purdue.edu
Purdue University, School of Aeronautics and Astronautics, 701 W. Stadium Ave, W. Lafayette, IN 47907, United States

HAIYANG QIAN: hqian@purdue.edu
Purdue University, School of Aeronautics and Astronautics, 701 W. Stadium Ave, W. Lafayette, IN 47907, United States

A MULTISCALE MODEL OF THE ORGAN OF CORTI

CHARLES R. STEELE, JACQUES BOUTET DE MONVEL AND SUNIL PURIA

The organ of Corti is the sensory epithelium in the cochlea of the inner ear. It is modeled as a shell-of-revolution structure with continuous and discrete components. Our recent work has been on the inclusion of the viscous fluid. Measurements from various laboratories provide the opportunity to refocus on the elastic properties. The current detailed model for the organ of Corti is reasonably consistent with diverse measurements. Most components have little stiffness in the propagation direction. However, the isotropic stiffness of the pillar heads is found to offer an explanation for the difference in point load and pressure measurements. The individual rows of inner hair cell stereocilia with tip links and the Hensen stripe are included, since these details are important for the determination of the neural excitation. The results for low frequency show a phase of tip link tension similar to auditory nerve measurements. The nonlinearity of fluid in the small gaps is considered. A result is that as amplitude increases, because of the near contact with the Hensen stripe, the excitation changes polarity, similar to the peak-splitting neural behavior sometimes observed.

1. Introduction

The cochlea of the inner ear is a transducer, as described in many sources, such as [Geisler 1998].[1] The input is the sound, which causes air pressure to act on the tympanic membrane after propagating through the outer ear. Generally, the middle ear alleviates the impedance mismatch between the external air and the fluid of the cochlea. With a change in area from the eardrum to the stapes, which is the last bone of the middle ear, the amplitude of input pressure is increased without significantly affecting the time pattern. The output of the cochlea is electrical, consisting of the firings of the 30,000 individual nerve fibers that comprise the auditory nerve in humans. These signals are conducted along the auditory pathway in the brain, ending in the auditory cortex, where perception takes place.

The remarkable feature is that the nerve fibers from the cochlea are sharply tuned to frequency, so the cochlea can be considered as providing an on-line Fourier analysis of the input time signal. The cochlea establishes many basic features of hearing, such as frequency discrimination and the interaction of multiple input tones. The accuracy and ranges of frequency and amplitude of this transducer are better than man-made devices by orders of magnitude. Therefore there are both the interesting scientific question of how such a device works and the related medical question of what can be done about malfunction.

The cochlea is frequently approximated by a *box model*, in which the coiling is neglected and the geometry of the input region, containing the input piston (the stapes) and a relief window (the round window), is grossly simplified. The box is long (diameter around 1 mm and length 30 mm in humans)

[1]Many web pages deal with the cochlea. For the purposes of this article one of the most helpful is the page maintained by F. Mammano and R. Nobili of the Venetian Institute of Molecular Medicine, http://147.162.36.50/cochlea/index.htm.
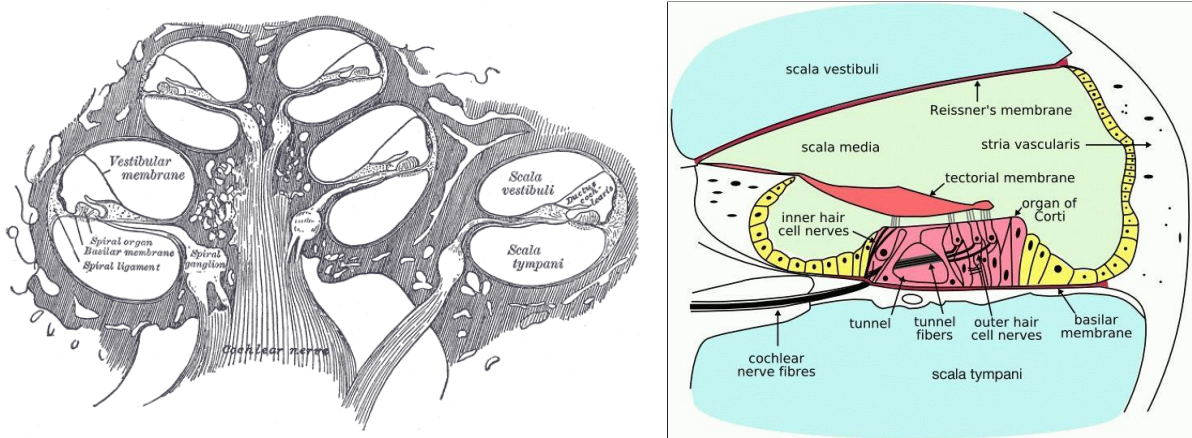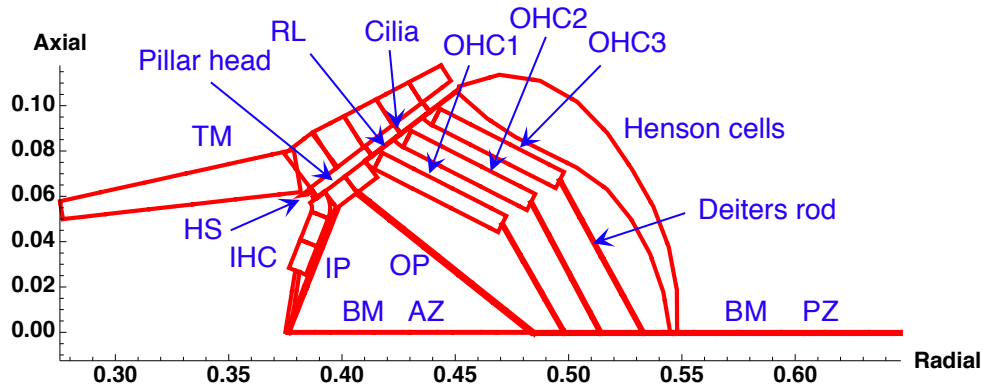
Figure 1. The cochlea is a long tapering tube that spirals around a bundle of nerve fibers. These fibers connect all along the tube to sensor cells located in a wall that partitions the tube lengthwise into two regions, the scala vestibuli and the scala tympani. (As seen on the right there is a third chamber, the scala media, but for our purposes it and the scala vestibuli can be regarded as one.) From [Gray 1918, Fig. 928] and [Wikipedia 2004].

and is filled with fluid with mechanical properties close to water. A partition divides the box along the length into two regions: the scala vestibuli (SV) connected to the input stapes, and the scala tympani (ST) connected to the round window. The partition is similar to a rigid plate with an elastic strip in the middle, the basilar membrane (BM). The stiffness of the elastic region is relatively high near the stapes (the base) and low at the far end (the apex of the coiled cochlea). The magnitude of stiffness is such that for frequencies in the auditory range, there is a significant interaction between the fluid and the elasticity of the basilar membrane. The result is a traveling, fluid-elastic wave that reaches maximum amplitude at a particular distance from the stapes and then decreases rapidly. The decrease is caused by the dissipation due to fluid viscosity when the wavelength is short. Because of the gradient in stiffness of the basilar membrane, there is a correspondence between the location of the maximum and frequency of excitation. High frequency creates a maximum near the base and low frequency a maximum near the apex.

Along the elastic portion of the partition is a sensory epithelium called the organ of Corti (OC), shown schematically in Figures 2 and 3. This is an elaborate elastic structure containing receptor cells, consisting of one row of inner hair cells (IHC) and three rows of outer hair cells (OHC). In the present work, we focus on the elastic and fluid-elastic aspects of this organ. The basic question is how the motion of the basilar membrane, indicated by the simple box model, is transmitted to the inner hair cells, into which the majority of the neural fibers project.

The auditory nerve threshold is close to the basilar membrane response, as shown in the chinchilla cochlea [Narayan et al. 1998]. However the complex arrangement of the OC makes it likely that the actual excitation of the stereocilia of the inner hair cells does not merely follow the motion of the basilar membrane. Hence there is interest in developing more detailed simulations of this organ [Steele and Puria 2005; Cai and Chadwick 2002; Andoh and Wada 2003].

BM = basilar membrane	Flexible portion of the partition separating the two chambers of the cochlea (scala vestibuli and scala tympani).
IHC = inner hair cell	Primary receptors, since connected to the majority of the neural fibers.
OHC = outer hair cell	Three rows, designated OHC1, OHC2, and OHC3. Much less innervation than the inner hair cells. Walls are piezoelectric, which enable them to play significant role in feedback enhancement of the vibration.
IP = inner pillar	Stiffening rod near the IHC, consisting of a bundle of microtubules.
OP = outer pillar	Stiffening rod near OHC1. Together the IP and OP are called the arches of Corti.
cilia (or stereocilia)	The "hairs" on each hair cell. Tip links connect the rows of stereocilia. When in tension, ion channels open and the hair cell depolarizes. This provides the basic transduction of mechanical force to neural discharge.
AZ = arcuate zone	Thin portion of the BM, between the IP and OP. The AZ, IP and OP form a stiff triangular structure.
PZ = pectinate zone	Thick portion of the basilar membrane between the OP and the support on the right. Consists of a double layer of radial collagen fibers, with little longitudinal elastic stiffness.
TM = tectorial membrane	Thick membrane overlying the organ of Corti. Gelatinous with low elastic modulus and somewhat orthotropic.
HS = Hensen's stripe	Strip of material that is attached to the TM, and seems to form a pocket for the tips of the stereocilia of the IHC.
RL = recticular lamina	Thin conical shell containing heads of all hair cells, through which stereocilia protrude.
Hensen cells	Soft cells attached to the RL and BM, forming the boundary of the organ of Corti on the right.
Deiters rod	Bundle of microtubules connecting base of each OHC to the BM.

Figure 2. Elastic elements in shell of revolution model for the organ of Corti in the apical region of the guinea pig cochlea. The radial and axial distances are in mm.
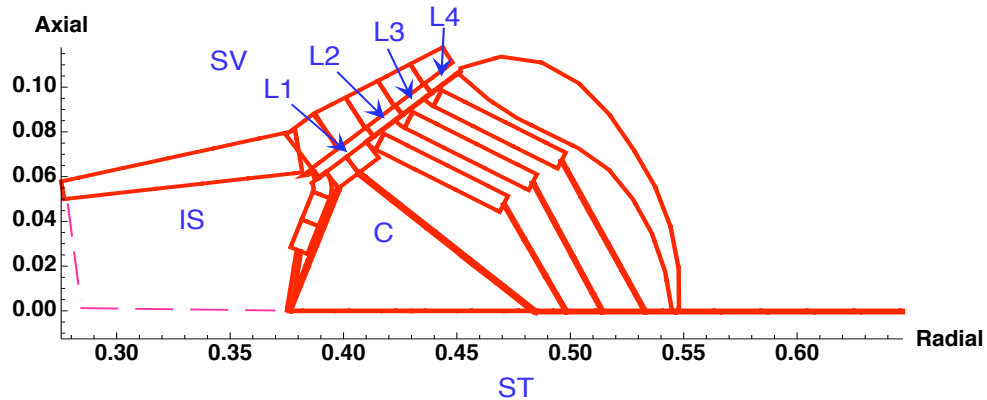
SV = scala vestibuli	Fluid region on which input sound pressure acts through the stapes. (In our model, the scala media and scala vestibuli are merged.)
ST = scala tympani	Fluid region to which relief window (round window) is connected.
IS = inner sulcus	Fluid region, bounded by the TM above and the IHC to the right, with stiff walls on the partition below and to the left (not shown).
C = cortilymph	Fluid filling the organ of Corti, surrounding the OHC, OP, and Deiters rods.
L1 = layer 1	Fluid beneath the TM and between the stereocilia of the IHC and the OHC1. The successive subtectorial membrane fluid regions are designated as L2, L3, and L4.

Figure 3. Fluid regions in model for the apical region of the guinea pig cochlea.

Our earlier investigation [Steele and Puria 2005] was motivated by the measurements of the inner hair cell response by Cheatham and Dallos [1999] in the upper turns of the guinea pig cochlea and the auditory nerve and basilar membrane responses in the base of the chinchilla [Ruggero et al. 2000]. The inner hair cells at the apex behave as might be expected, with a maximum excitation when the BM is between maximum displacement and velocity toward scala vestibuli. However, the neural recordings at the base indicate excitation with velocity toward scala tympani. It was found in [Steele and Puria 2005] that the phase of inner hair cell excitation, related to the tension in the tip link of the tallest stereocilium of the inner hair cell, can be anything, particularly depending on the elastic properties of the overlying tectorial membrane. However, at the guinea pig base, with tectorial membrane elastic properties given by the measurements in [Shoelson et al. 2004; Freeman et al. 2003], the excitation occurs for basilar membrane displacement and velocity toward scala tympani, consistent with measurements in [Ruggero et al. 2000], while at the apex, the excitation is for basilar membrane displacement and velocity toward scala vestibuli, consistent with measurements in that region [Cheatham and Dallos 1999].

The present effort continues [Steele and Puria 2005] with a focus on a thorough reevaluation of the recent experimental results on geometry and stiffness to improve the model. Secondly, the nonlinear solution for the full OC model is developed. The nonlinearities considered are: (1) the buckling of supporting structures (the inner and outer pillar cells and the Deiters rods); (2) the nonlinear flow of fluid in the confined region under the overlying tectorial membrane.

2. Box model without organ of Corti

It is remarkable that the OC may be stripped off, leaving only the BM as an orthotropic, sandwich plate dividing the two fluid regions, for a model that does rather well for describing the fluid-elastic waves [Yoon et al. 2006]. There is actually a third fluid region containing endolymph on the side of the OC. However, this is merged with the scala vestibuli for the usual two-chambered box model. Even with such simplifications, the computation including the three-dimensional viscous fluid by direct methods is daunting, requiring 5–20 hours on a high-speed parallel computer for the time integration of a few cycles of response [Givelberg and Bunn 2003]. Instead we advocate the use of the WKB asymptotic wave analysis method in the frequency domain, with which the computation time is around one second per frequency on a desktop computer. Our application of this method to the three-dimensional analysis of the cochlea is an extension of previous work in two dimensions [Ranke 1950]. The WKB method is well known for treatment of ordinary differential equations [Olver 1974] when solutions vary "rapidly" while the coefficients vary "slowly". Carlini [1817] apparently used this approximation for the first time. The extension to the cochlea is possible because the wavelength of the traveling wave is generally small in comparison with the distance over which the stiffness of the BM varies significantly. Thus the local wave number can be calculated from the three-dimensional fluid equations coupled with the plate equations at a given cross section, assuming that the properties are constant.

Validation. The calculated results [Steele and Taber 1979] compare well with experimental measurements in a 6-times life-sized box model of the human cochlea [Helle 1974]. This experimental model is important because Helle measured all the properties, including the BM viscoelastic property and the viscosity of the fluid, as well as all the geometry. The objection to the use of Helle's physical model as a "gold standard" for confirming a basic cochlear calculation is the size. To correspond to the human cochlea, scaling of the properties of stiffness and viscosity must be done, and it is difficult to have all parameters scaled properly. Several laboratories are developing life-sized models. In our effort [Wittbrodt et al. 2006] there is reasonably good agreement between the three-dimensional WKB solution and the direct measurements for the amplitude and phase of the traveling wave on the BM. Further validation comes from the excellent agreement between the calculations from the box model with three-dimensional viscous fluid, without adjustment of parameters, [Yoon et al. 2006] and the *in vivo* measurements of pressure in the fluid [Olson 1998]. Therefore the use of asymptotic methods seems justified for extension to a more detailed model with OC included.

3. Extension to detailed organ of Corti

Despite the success of the simple box model, the OC has an important role that has yet to be explained properly. We saw in Figure 2 the significant elastic elements of the OC, while Figure 3 highlighted the fluid regions. Both figures represent a radial cross section of a nearly axisymmetric configuration, with the axis running vertically on the left. Therefore we consider the OC as a shell-of-revolution structure consisting of discrete and orthotropic elastic elements. There are no air pockets in the cochlea, so the regions not taken by elastic tissue are filled with fluid that has the mechanical properties of water.

3.1. *Analysis.* In the finite element approach [Cai and Chadwick 2002; Andoh and Wada 2003], a fine mesh is used for the entire cross section including the fluid and tissue. Our approach [Steele 1999] is

to extend the WKB approach for the simple box model by considering a limited number of degrees of freedom for each fluid region. The simplest is to consider the one-dimensional approximation for each of the interior regions. With this the pressure is assumed to be constant in the cross section of each fluid region. Thus for the fluid regions in Figures 2 and 3, the problem reduces to just eight degrees of freedom, one for the volume displacement in the circumferential direction of each fluid region. Since the present results are obtained as a continuation of [Steele and Puria 2005], the details of the equations will not be repeated here.

The basic relations are as follows. The change in cross-sectional area for the fluid regions is given by the vector $\boldsymbol{D}_w$ that is related to the vector of pressures acting on the walls of the regions $\boldsymbol{F}_w$ by an elastic compliance matrix $\boldsymbol{E}$:

$$\boldsymbol{D}_w = \boldsymbol{E} \cdot \boldsymbol{F}_w. \tag{1}$$

The compliance matrix is symmetric with positive diagonal terms. The individual term E_{ij} is the cross-sectional area change of region i due to a unit pressure on region j. The fluid flow between the regions in the cross section is described by the relation of the vector of fluid area changes $\boldsymbol{D}_f$ and the pressures with a permeability matrix $\boldsymbol{C}$:

$$\dot{\boldsymbol{D}}_f = -\boldsymbol{C} \cdot \boldsymbol{F}_w, \tag{2}$$

in which the dot represents the time derivative. The permeability matrix is also symmetric with positive diagonal terms. The longitudinal (circumferential) displacement of fluid in the regions is given by the vector $\boldsymbol{Q}$. The continuity condition provides the relation

$$\dot{\boldsymbol{Q}}_{,X} = \dot{\boldsymbol{D}}_f - \dot{\boldsymbol{D}}_w = -(\boldsymbol{C} \cdot \boldsymbol{F}_w + \boldsymbol{E} \cdot \dot{\boldsymbol{F}}_w), \tag{3}$$

in which x is the longitudinal arc length (the distance along the cochlea from the stapes). Finally the equation for motion of the fluid in the longitudinal direction is:

$$(\boldsymbol{A} \cdot \boldsymbol{F})_{,X} = -(\rho \ddot{\boldsymbol{Q}} + \boldsymbol{B} \cdot \dot{\boldsymbol{Q}}), \tag{4}$$

in which $\boldsymbol{F}$ is the vector of averaged pressures, $\boldsymbol{A}$ is the diagonal matrix of areas, $\boldsymbol{B}$ is the diagonal matrix of viscous resistance, and ρ is the density of the fluid. Equations (3) and (4) are just an extension of the familiar one-dimensional model, if the averaged pressure is assumed to be the same as the pressure on the wall:

$$\boldsymbol{F} \approx \boldsymbol{F}_w. \tag{5}$$

Generally, this is a poor approximation, particularly in the region of maximum amplitude, so the three-dimensional fluid behavior must be considered to relate the averaged and wall pressures, as described in the preceding section. In the present work, however, the focus is on the low frequency response for which the wavelength is long, (5) is valid, and the longitudinal displacement of fluid is small, that is, $\boldsymbol{Q} = 0$. Therefore (3) reduces to

$$\boldsymbol{C} \cdot \boldsymbol{F} + \boldsymbol{E} \cdot \dot{\boldsymbol{F}} = 0 \tag{6}$$

which describes the low frequency, viscous motion of the cochlear cross section in Figures 2 and 3.

4. Static response of organ of Corti

The static elastic response (1) is crucial. Our approach, continued from [Steele 1999; Steele and Puria 2005], is to use the computer program Fast4, which is specifically developed for the efficient treatment of structures consisting of shells of revolution [Steele and Shad 1995].
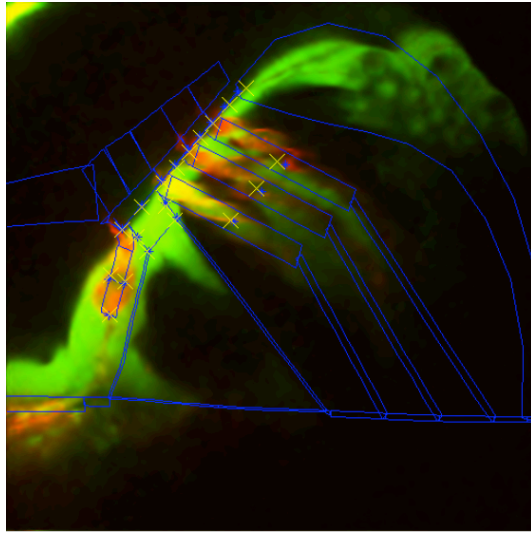
With this program, adjacent components may have elastic moduli and/or dimensions differing by orders of magnitude. The cochlea is just such a multiscale problem, with the bone of the partition having dimensions on the millimeter scale, the hair cells and supporting cells on the micrometer scale, and the tip links connecting stereocilia having thickness on the nanometer scale. The elastic moduli of the components vary from the gelatinous TM around 10 kPa to the bone of the partition and walls at 20 GPa. The table for input [Steele 1999] has some 80 geometric and material properties. Much of the geometry can be obtained from a high quality micrograph of the cross section. With a knowledge of the protein fibers, an estimate can be made for the effective stretching and bending stiffness of a particular element. However, uncertainty remains, for example, in the volume fraction of protein in a particular element and in the stiffness of ground substance. Following are the current considerations for refinement and verification.

4.1. *Consistency with the anatomy.* Much detail for the anatomy at the guinea pig apex is available, including average values and standard deviations of the dimensions of elements from 35 cochleas [Kelly 1989]. Ulfendahl and colleagues provide good cross sections for different distances from the stapes. The lengths and densities of microtubules in pillar cells, Deiters rod and the phalangeal process in guinea pigs at different distances from the base are also available [Zetes et al. 2004]. We assume that the distribution of the BM collagen fibers in cat [Cabezudo 1978] holds for guinea pig.

A substantial advance is provided by a new confocal microscopic technique [Fridberger et al. 2002]. The preparation is an excised guinea pig cochlea. However, the observation is through a hole in the bone at the apex, so no damage is done to the OC and the support structure on both edges of the BM. A penetration through the fluid and tissue provides good detail of the stereocilia, hair cells and pillars, but only a small portion of the BM.

A difficulty in interpreting the optical results is that the image plane is not the radial section, but at some angle of rotation about a radial line and an angle about the cochlear axis. Therefore an optimization program was developed [Boutet 2007] that we briefly outline. The first step is to determine the unknown optical angles with the knowledge of the geometry [Kelly 1989]. Figure 4 shows the Fast4 representation in blue lines added to the optical section. The elements are rectangular in the radial plane, but appear trapezoidal in the optical section. So the shell model agrees reasonably well with the actual geometry. The next step is to obtain the proper stiffness for the elastic components to obtain a best fit with the measured displacements. The starting point is component stiffness from the consideration of various other measurements.

4.2. *Consistency with stiffness measurements.* Information on the static stiffness of the components of the OC in guinea pig is available. This includes the static point load stiffness at points across the BM in the guinea pig base [Miller 1985] and the stiffness of microtubules and cross bridging in the pillar cells [Tolomeo and Holley 1997]. With an advance in atomic force microscopy, the impedance at points across the RL, with BM constrained and TM removed, for the frequency range 0.5 to 40 kHz has been

Figure 4. Optical image of OC at the apex of the guinea pig cochlea [Fridberger et al. 2002] with Fast4 shell model superposed (blue lines). This shows the configuration with the maximum downward pressure, which causes a buckling of the IP. In the animation (which can be found at http://pjm.math.berkeley.edu/jomms/2009/4-4/jomms-v4-n4-x10-corti.avi) the blue and yellow X symbols represent fixed points that initially coincide, so the maximum discrepancy can be seen in OHC3. The animation shows both the upward and downward displacement due to steps in the static pressure.

obtained [Scherer and Gummer 2004]. The impedance provides the static stiffness and the effective thickness of the RL [Steele et al. 2005]. The isolated TM has been measured in guinea pigs [Abnet and Freeman 2000; Shoelson et al. 2004], and apparently has an effective Young's modulus of 10–30 kPa. A most thorough measurement of the stiffness of stereocilia is also available [Langer et al. 2001]. The OHC attract considerable attention because they have the unusual property of *electromotility*, that is, the wall has piezoelectric properties. Thus a change in the intracellular electrical potential, in addition to causing excitation of neurons connected to the base, cause a change in the length of the cell. This most likely pumps energy into the motion of the BM in the normal function of the cochlea. The elastic and piezoelectric coefficients are determined from a summary of isolated cell measurements [Spector et al. 1999]. With the usual composite structure analysis, the properties of the components of the OC are found that generally satisfy the condition of consistency with the microstructure, the geometry, and the static stiffness measurement.

4.3. *Consistency with the quasistatic motion of the OC.* An example of the calculation for the deformation due to a static pressure load acting on the BM is shown in Figure 5. Note the opening of the fluid region L1 near the stereocilia of the IHC. This does not occur in previous simplified models of the OC. The close view of the stereocilia is in Figure 6. It appears that the tips of the tall stereocilia are close to the HS, as shown by the dashed lines for the undeformed configuration. The fluid flow in this restricted region is of considerable importance in the dynamic response.
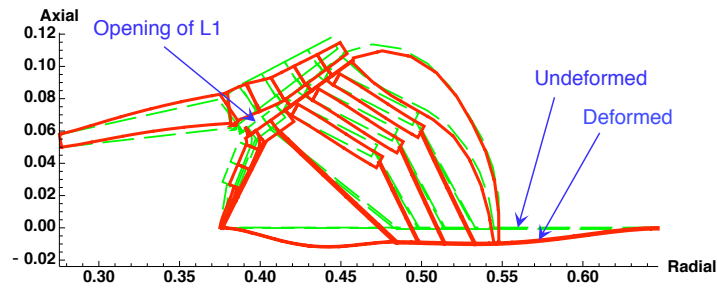
Figure 5. Deformation due to static pressure loading of the BM toward the ST. The dashed and solid lines show the undeformed and deformed configurations, respectively. Note the opening of the fluid region L1.
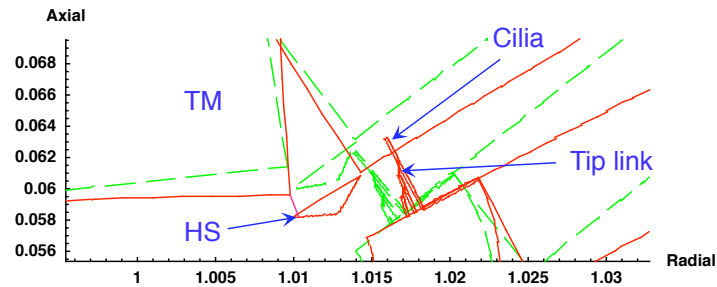

Figure 6. Close view of the stereocilia on the inner hair cell. The Hensen stripe (HS) is the triangle attached to the TM above. The green dashed lines show the undeformed configuration, with the tip of the tallest stereocilium near the HS. The red solid lines show the deformed configuration, greatly amplified. The radial and axial distances are in mm. Tip links connect the three rows of stereocilia.

Much more detail is provided by Fridberger et al. [2002], who subject the OC to quasistatic steps in pressure difference between SV and ST. The values at every pixel are recorded. One example is in Figure 7, which shows the displacement of a point at the middle of OHC3 for the steps in loading. There is a pronounced difference in the displacement magnitude and direction for loading in the two directions. This strong nonlinearity we attribute to a buckling of the IP. The model calculations indicate that the IP is
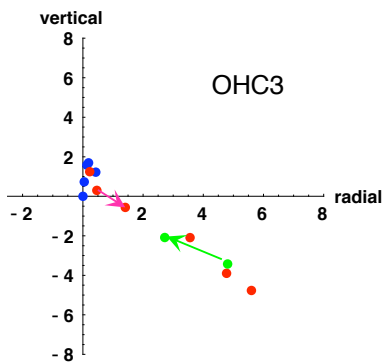
Figure 7. Measurement of displacement at the center of OHC3 for the guinea pig apex with steps in static pressure [Fridberger et al. 2002]. Dimensions are in μm. The blue points are for the initial loading steps in the upward direction. The red points show first unloading and then steps in downward loading. Finally the green points are for unloading. We attribute the severe nonlinearity to a buckling of the IP for downward loading.

subjected to compressive loading for the downward pressure loading large enough to cause buckling. The amplitude of displacement is several μm, which is much larger than the normal range for hearing. Thus from the current estimates, it appears unlikely that this effect is of physiological significance. However, this nonlinear behavior provides some confirmation that standard elastic structural analysis is applicable for such tissue.

The nearly linear behavior in Figure 7 for downward loading indicates that the buckling transition occurs in the first 1 μm of displacement. Consequently, a reduced elastic modulus for the IP provides a simulation of the postbuckled behavior of the structure.

4.4. *Tuning stiffness values with optimization.* A complete optimization program has been developed for adjusting the stiffness values for the individual components of the OC, to achieve a best fit to the measured displacement at a number of points [Boutet 2007]. Figure 4 shows the agreement between the calculation and the measurements at the maximum downward displacement. A subset of points is marked by the blue and yellow X's. For the initial configuration of zero pressure, these coincide. The maximum discrepancy at this maximum downward displacement can be seen to be at OHC3. The animation of Figure 4 for the steps of loading in both directions shows that the calculation and measurement nearly coincide.

An important point is that the beginning values of stiffness are those from the estimates for the microstructure and the various static measurements, discussed in the preceding section. The final values from the optimization are generally within an order of magnitude of the original values, which is considered to be reasonable.

4.5. *Consistency between point and pressure loading.* Additional information on the elastic structure of the OC is revealed from the displacement at points under a probe, as first measured by von Békésy [1960]. Furthermore, Cooper [2000] observes that the radial profile of displacement of the BM is ubiquitous for frequencies below, at, and above that producing maximum displacement in several animals, including gerbil and guinea pig. Certainly for the low frequencies, the loading of the BM should be just pressure. So we consider a simple beam model for the BM as shown in Figure 8 with point loading and pressure loading. The beam consists of the thinner AZ and the thicker PZ. In addition, the possible support of the outer pillar in Figures 2 and 3 is represented by the spring with spring constant k.

Homer et al. [2004] optimize such a beam model, without the spring ($k = 0$), to produce Cooper's radial profile of displacement under a pressure loading. They find that clamping of the right edge and hinging of the left edge produces the best results.
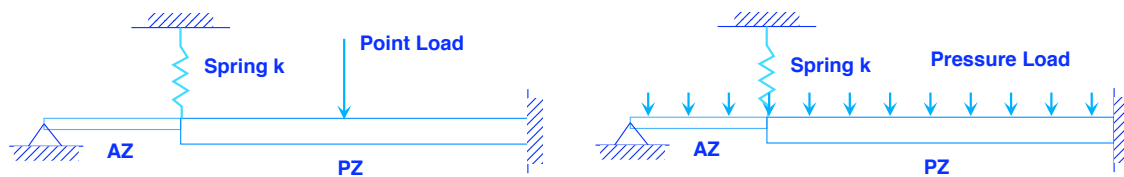

Figure 8. Simple beam model for BM. As in [Homer et al. 2004] the beam is clamped on the right end and simply-supported on the left end. However, we add a spring attachment to simulate the outer pillar and include the different thicknesses in the AZ and PZ. The experimental results are for point load (left) and pressure loading (right).
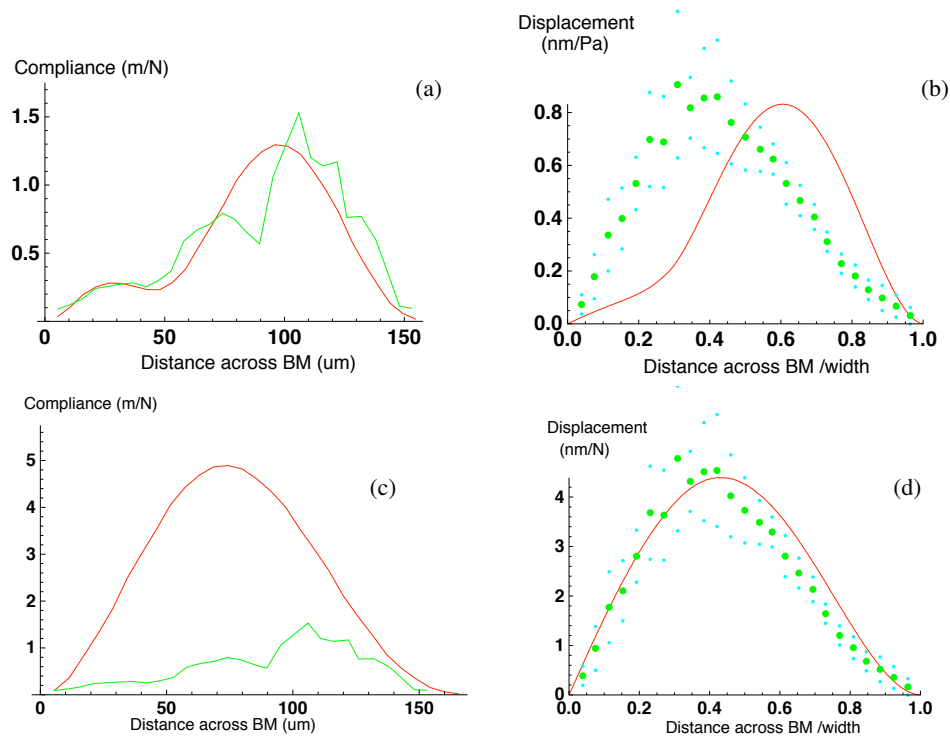
Figure 9. Beam model for fit with experimental measurements of BM in guinea pig. In (a) and (c) are the point load compliance results from specimen K1 by [Miller 1985] (green). In (b) and (d) is the BM displacement profile from [Cooper 2000] shown by the green dotted curve. The small green dots show the bounds. The calculations (red) are for the beam model with hinged support on the inner pillar and clamped support on spiral ligament. The thickness in AZ $= 5\,\mu$m, thickness in PZ $= 7.4\,\mu$m, width $=$ 160 μm. The elastic properties are: $E_{AZ} = 0.09\,$GPa, $E_{PZ} = 0.021\,$GPa, outer pillar spring $k = 0.4\,$MPa. In (a) the model is fit to the point load measurements, (b) the same model displacement with pressure, showing a lack of fit with the Cooper profile. (c) Setting $k = 0$ in model yields a poor fit with measurements for the point loading, but (d) provides a reasonable agreement with Cooper for pressure loading.

Figure 9(a) shows the compliance at points across the basilar membrane as measured by a 10-micron probe in guinea pig K1 [Miller 1985]. Note the tendency for an increase in compliance at around 30 μm, which is in the AZ. It appears to be difficult to produce such behavior without a significant spring constant k corresponding to the OP. The result for the beam model (Figure 8) with the parameters chosen for a best fit is shown by the red curve in Figure 9(a). However, with the same elastic values, the response for pressure loading is compared to Cooper's profile in Figure 9(b). A reasonable fit for both the point load and the pressure load for one beam model does not appear possible. The conclusion is that the effective spring constant k is not the same in the two loading cases. The consequence of keeping the beam properties the same, but setting $k = 0$, is a poor fit with the point load compliance (Figure 9(c)), but a good fit with Cooper's profile in Figure 9(d).
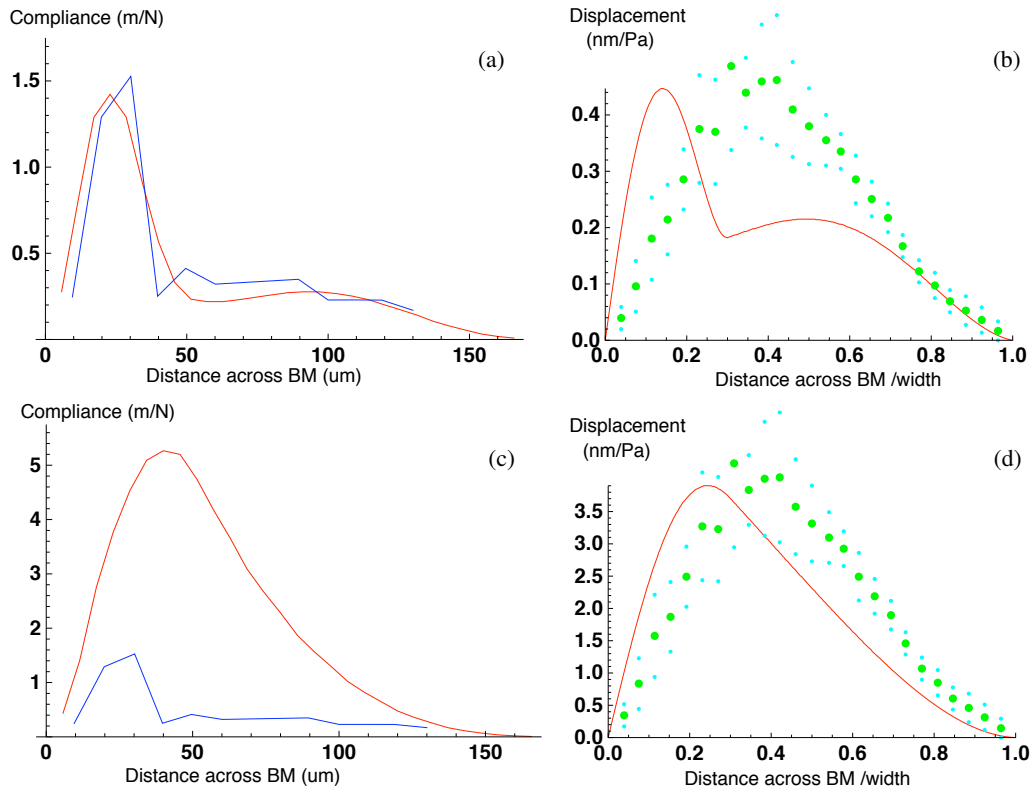
Figure 10. Beam model for fit with experimental measurements of BM in gerbil. In (a) and (c) are the point load compliance results in one gerbil by [Olson and Mountain 1994] (blue). In (b) and (d) is the BM displacement profile from [Cooper 2000] shown by the green dotted curve. The calculations (red) are for a solid beam model with hinged support on the inner pillar and clamped support on spiral ligament. The thickness in $AZ = 2.2\,\mu$m, thickness in $PZ = 19\,\mu$m, width $= 160\,\mu$m. The elastic properties are: $E_{AZ} = 0.09$ GPa, $E_{PZ} = 0.011$ GPa, outer pillar spring $k = 0.4$ MPa. (a) The model is fit to point load measurements, (b) The same model displacement with pressure, showing a lack of fit with Cooper. (c) Setting $k = 0$ in model yields a poor fit for the point loading, but (d) a similarity to the Cooper profile for pressure loading.

The effect is more pronounced in gerbil. Figure 10(a) shows the compliance at points across the basilar membrane as measured in one gerbil by [Olson and Mountain 1994]. The red curve shows the beam model with parameters for a best fit. The response for pressure load is, however, quite unlike Cooper's profile, as shown in Figure 10(b). If the spring constant is set to zero ($k = 0$), the compliance under a point load is much too large (Figure 10(c)). However, the displacement under pressure is not far from Cooper's profile (Figure 10(d)). This is only a general indication, since in the gerbil BM the lower layer of collagen fibers are in the form of a large arc, rather than the flat plate in Figure 8.

The possible explanation for the inconsistency of the point and pressure loading lies in the orthotropic structure of the OC (Figures 2 and 3). Most elements are soft, such as the TM and the Hensen cells
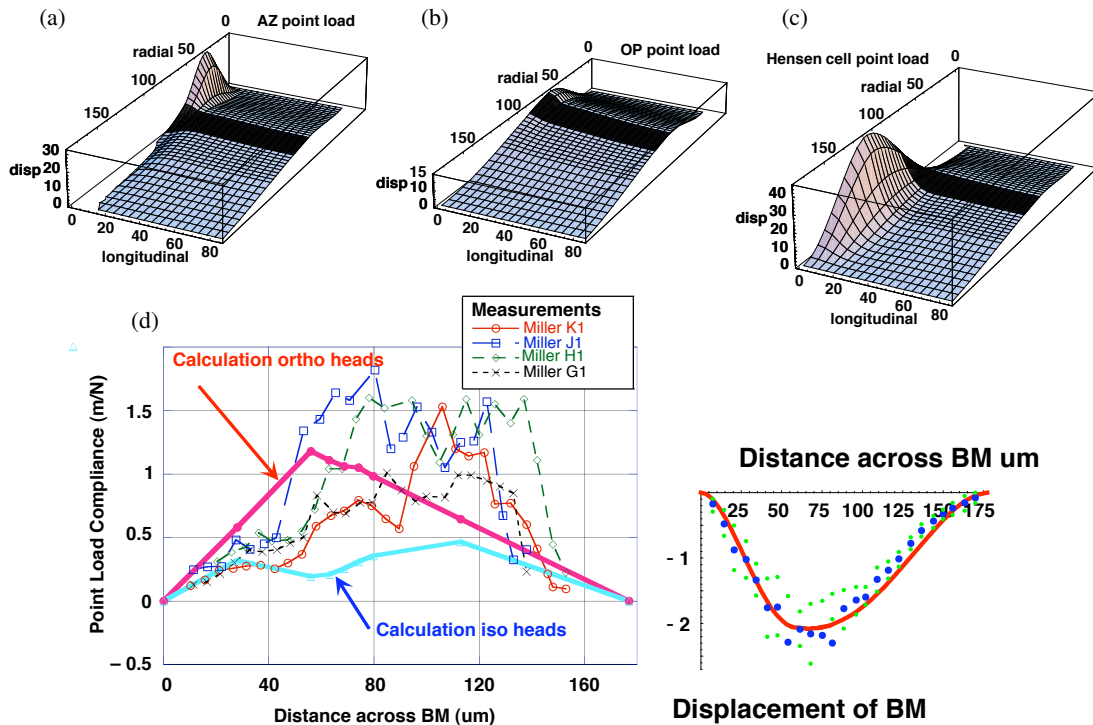
Figure 11. Fast4 full OC model with isotropic pillar heads for static pressure loading of the BM in the guinea pig base. Parts (a)–(c) show the displacement of a rectangular region of the BM consisting of the full width in the radial direction and $80\,\mu$m in the longitudinal direction, on one side of the $10\,\mu$m probe load. The displacement in the longitudinal direction decreases: (a) rapidly for load in the center of AZ, (b) slowly for load at the outer pillar, and (c) rapidly for load at the Hensen cells. (d) Magnitude of compliance under probe load from measurements and computation with isotropic and orthotropic heads. (e) Comparison with Cooper's profile for pressure with isotropic heads.

on the right side, or discrete, such as the hair cells and the pillar cells. However, the heads of the pillars, just under the fluid region L1, consist of microtubules with high stiffness coupling in the direction perpendicular to the plane of Figures 2 and 3. Thus the array of pillars and heads will have an effective torsional stiffness. This could provide a significant stiffness k for the localized point load, but negligible effect for the pressure loading, when the neighboring pillars are moving together.

With the full model, Figures 2 and 3, the complete three-dimensional deformation due to a static point load can be computed as in Figure 11. So far as we are aware this is the first model calculation for this effect. The elastic and geometric properties are the same as in all the previous calculations, except for the longitudinal stiffness of the pillar heads. If the pillar head is isotropic, there is a substantial effect. Figure 11(a) shows the displacement of the BM when the point load is centered in the AZ. The decay of displacement in the radial direction is fairly gradual, due to the stiff radial fibers in the BM. In the longitudinal direction there are no fibers, only ground substance, and the decay is very rapid. For the load at the outer pillar, however, the pattern is quite different (Figure 11(b)). The total displacement

at the point load is smaller, and the decay in the longitudinal direction is much slower. This is clearly due to the torsional stiffness of the heads, that is, a resistance of one head from rotating with respect to its neighbors. Finally in Figure 11(c) the load is located at the Hensen cells in the PZ. For this, the displacement under the point load is large, and the decay in the longitudinal direction is rapid. Figure 11(d) shows the plot of the displacement under the point load for the load at different locations in the radial direction, as in Figure 9(a). Miller's measurements for four guinea pig cochleas are included. The continuous lines show the results from the calculations for the isotropic and orthotropic pillar heads. For the orthotropic values, that is, low torsional stiffness of the heads, the maximum displacement occurs for the load at the outer pillar. For the isotropic heads, however, the displacement for the load at the pillars has a minimum, giving a shape of the response similar to Miller's measurements. The amplitude is low by a factor of roughly 2, so a small modification of all the elastic properties is needed. Figure 11(e) shows the shape of the BM displacement under pressure compared with Cooper's profile with the isotropic heads. The tentative conclusion is that the full three-dimensional model (Figures 2 and 3) with isotropic pillar heads, unlike the simple beam model Figure 8 with fixed k, can explain both the point load measurements and the pressure deformation of the BM.

5. Dynamic response of organ of Corti

The next step is to consider the dynamic response of the OC for low frequency, for which in each fluid region the longitudinal motion of the fluid is negligible and the pressure is constant. Therefore the
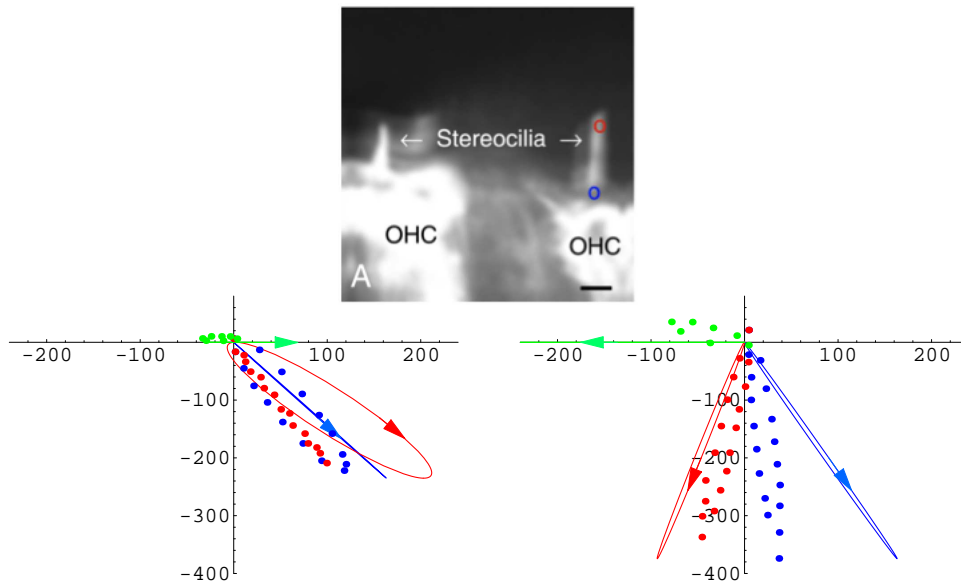

Figure 12. Displacement of tip and base of stereocilia at 200 Hz for around 85 dB SPL during one cycle of motion. Top: optical section. Bottom: dots show measurements [Fridberger et al. 2006] while curves show computed values. The horizontal and vertical axes show the displacement components tangent and perpendicular to the RL in nm. The curves are shifted so the maximum excursion during the cycle is the point at the origin.

problem is governed by Equation (6), containing only the elastic and viscous flow terms. Since no internal longitudinal flow occurs, the volume of fluid in the cross section is constant. The region of Cortilymph (C), surrounding the discrete OP and the OHC, is completely enclosed and so has no area change. Fluid flows between the regions IS, L1, L2, L3, and SV. This flow is governed by the permeability of viscous flow through and around the stereocilia. The pressures in the ducts SV and ST are prescribed to be equal in magnitude and opposite in sign. Thus the quantities in (6) are split into independent and dependent components [Steele and Puria 2005]. Following are new results.

5.1. *Displacement of stereocilia.* New capability is available for the optical imaging focused on the IHC and OHC stereocilia for motion at the frequency of 200 Hz [Fridberger et al. 2006]. Figure 12 (top) shows the image of the stereocilia of the IHC and OHC1. Details are obtained for the trajectory of the motion of the base and tip at 200 Hz. In Figure 12 (bottom) the measured values are shown by the dots and the Fast4 computation by the continuous lines. Of interest is that the tip motion is rather sensitive to the stiffness of TM and stereocilia, while the base motion is not. Note that the amplitude of displacement in Figure 12 (bottom) has a maximum of 400 nm, in comparison with the maximum amplitude of 12 μm for the static load steps in Figure 7. Measurements at lower sound intensity levels indicate that the response in Figure 12 is quite linear [Fridberger et al. 2006], so the buckling does not occur.

5.2. *Phase of tip link tension.* The linear solution of (6) with the IHC stereocilia and tip links included yields interesting results for the response for various initial gaps between the head of the tall stereocilium and the overlying TM and the adjacent HS [Steele and Puria 2005]. The phases of the different components for a soft TM and stiff OHC stereocilia at the guinea pig apex are shown in Figure 13. The
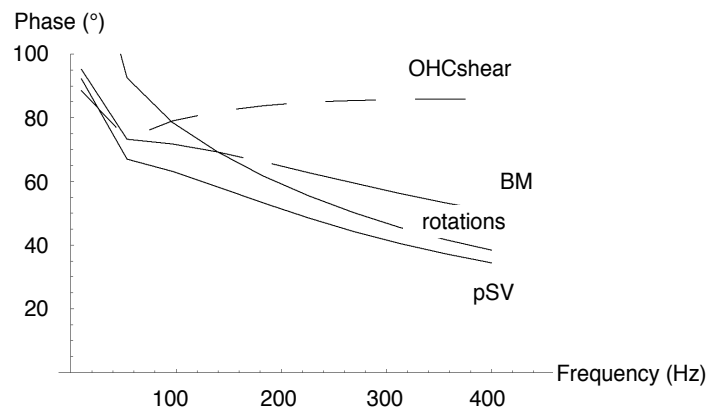

Figure 13. Phase of IHC tip link tension with respect to different components of the OC as computed from the model for the guinea pig apex for soft TM and stiff OHC stereocilia. The phases of the shear on the OHC, the BM displacement, the rotations of the stereocilia and the pressure in SV are not the same, as commonly assumed. The phase of tip link tension with respect to OHC shear is nearly 90°, similar to the measurements [Cheatham and Dallos 1999]. The phase difference between the relative rotation of the tall stereocilia of IHC and OHC1 is close to that measured [Fridberger et al. 2004].
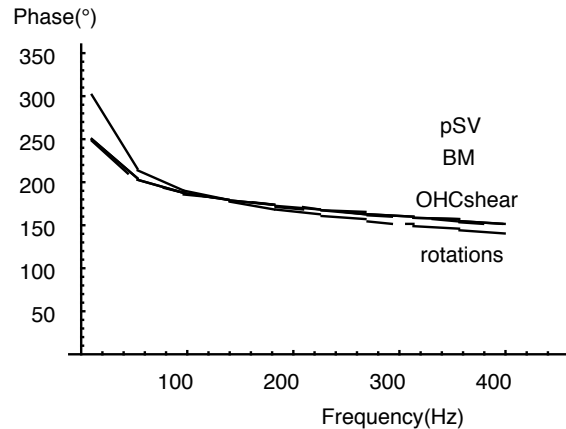
Figure 14. Phases for the guinea pig base calculated for OC with viscous fluid, with normal (stiff) TM and OHC stereocilia. Unlike the apex with the soft TM in Figure 13, the phase of the various quantities is essentially the same, as is usually assumed.

various quantities of OHC shear, BM displacement, pressure in SV, and relative rotation of IHC and OHC stereocilia, which are normally thought to be exactly in phase, are at somewhat different phases. At the base, however, with *stiff* TM and *stiff* OHC stereocilia, the phases of all the quantities are the same, as shown in Figure 14. The phase corresponds to excitation for displacement of the BM toward SV, qualitatively similar to the auditory nerve excitation reported [Ruggero et al. 2000]. However, this does not offer an explanation of the measurements [Fridberger et al. 2004], where a difference is found in BM displacement and electrical potential in the Cortilymph, similar to what we find in the apex in Figure 13, if the potential is related to the shear force on the OHC stereocilia.

To show that the phase depends on the stiffness of the overlying TM, the results for several orders of magnitude of the Young's modulus are shown in Figure 15. The indication is [von Békésy 1960; Abnet and Freeman 2000] a value around 10–30 kPa, which gives the phase near 180°, that is, for excitation with BM displacement towards ST. The softer TM, accommodates to the fluid in L1 and the phase is
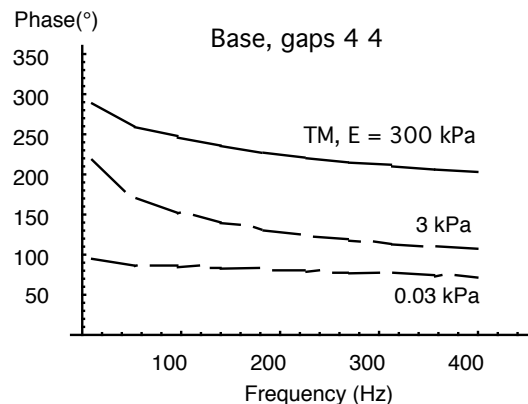

Figure 15. Dependency of phase of tip link tension on Young's modulus of TM in the guinea pig base. This is the linear solution for initial gaps between the tall stereocilium tip and the TM and the HS both 4% of the tip radius.

case	cause	mechanism	effect on IHC neurons	phase
1	Small gap with HS (or high frequency). Tips of the tallest stereocilia of the IHC nearly stick to the HS.	Tip lags the base, causing decrease in tip link tension in phase with BM displacement.	inhibition	0°
2	Large gap with HS and TM (or lower frequency). Stereocilia are pulled through fluid.	Tip lags the base, causing decrease in tip link tension in phase with BM velocity.	inhibition	90°
3	Small gap with TM. Area of region L1 increases, and tips of the tallest stereocilia nearly stick to the TM, so L1 has negative pressure.	Outward pressure on stereocilium, causing increase in tip link tension in phase with BM displacement.	excitation	180°
4	Large gap with TM. The area of region L1 increases, so fluid flows from IS into L1.	Outward pressure on stereocilium, causing increase in tip link tension in phase with BM velocity.	excitation	270°

Table 1. Effects on phase of IHC tip link tension for BM motion toward ST, for which the base of the stereocilia moves in the positive radial direction. Cases 1 and 2 prevail for a relatively soft TM, while Cases 3 and 4 prevail for a relatively stiff TM.

near 90°, that is, for BM velocity toward SV. This range of TM modulus values seems extreme, but the lower value of 0.03 kPa may be near that for the bird TM, while the TM for the mustache bat is nearly pure collagen, with a modulus probably around 3 GPa.

Thus the phase can be anything, depending on the initial gaps and the stiffness. We attempt to sort out the main features in Table 1. Case 1 indicates the behavior if there is a small gap between the tip of the IHC stereocilium and the HS. For a thin fluid layer, high force is required to move the layers apart, so the tip of the stereocilium is nearly stuck to the HS. Displacement of the BM toward ST (downward in Figures 2 and 3) causes a bending of the stereocilium that reduces the tip link tension, which causes hyperpolarization of the cell and generally an inhibition of neural firing. If the gap is larger, Case 2, the stereocilium is pulled through the fluid which also reduces the tip link tension, but in phase with the BM velocity, which is a phase of 90° with respect to Case 1. Since the effect of the viscosity increases with frequency, there is a shift from Case 2 to Case 1 with increasing frequency, as seen in Figure 13 for the phase of tip link tension with respect to the BM displacement (curve labeled BM). This is generally the behavior expected with the phase somewhere between 0 and 90° [Cheatham and Dallos 1999]. The new feature [Steele and Puria 2005] is due to the geometry of the shell structure Figure 2, and 3, which shows the static deformation due to the pressure toward ST. Particularly note that the region L1 opens with this displacement of the BM. This behavior is confirmed by recent measurements in [Nowotny and Gummer 2006]. So this creates the possibility of Case 3 and Case 4 in Table 1 with phase of excitation of 180° and 270°. In Figure 14 for the guinea pig base the transition from Case 4 to Case 3 with increasing frequency is clear. In Figure 15 the transition from Cases 1–2 to Cases 3–4 with stiffening of the TM can be seen. For the soft TM, the opening of L1 has little effect, since the TM adapts to the fluid with minimum pressure.

5.3. *Nonlinear response.* For large displacements, buckling of the elastic structure is possible, as previously discussed. For acoustic excitation in the normal range, this does not seem to be significant. However, an obvious source of strong nonlinearity is the fluid gap between the tip of the IHC stereocilia and the HS and TM. In the previous work [Steele and Puria 2005] various results from lubrication theory are used, such as the formula for the force required to move a cylindrical surface with the radius R apart from a flat surface with the velocity $\dot{g}_{\mathrm{HS}}$

$$F_{\mathrm{fluid}} = -3\sqrt{2}\pi/\mu\dot{g}_{\mathrm{HS}}\left(\frac{R}{g_{\mathrm{HS}}}\right)^{3/2} \tag{7}$$

in which μ is the viscosity of the fluid and g_{HS} is the minimum distance between the two surfaces. For the linear solution, g_{HS} is fixed as the initial gap. For the nonlinear solution, however, g_{HS} is taken as the current gap. This nonlinearity affects only a few terms in the permeability matrix C in (6). The nonlinear tenth-order system is solved using the forward integration function NDSolve in Mathematica. This requires around one minute for a given problem to compute several cycles of response.

The results for the force in the tip link of the IHC stereocilia for the guinea pig base at different intensities are in Figure 16. The input is a pressure difference between ST and SV, which varies sinusoidally, as shown by the blue curve in each plot. The positive maximum corresponds to maximum pressure toward SV, which causes shear on the OHC stereocilia in the excitatory direction. The solution is for the initial condition of zero displacement of all elements at time zero. It can be seen that what appears to be a nearly steady-state response is achieved in these few cycles. An expanded view for very small time shows that all displacements do start with zero as prescribed; there exist very short time response modes.

For low pressure, the response agrees closely with the linear steady-state solution. The maximum tension in the tip link for this frequency is nearly 180° out of phase with the pressure, that is, for pressure toward SV. For pressure of 30 Pa (corresponding to a sound pressure level, or SPL, of 124 dB), a small nonlinear effect appears as a distortion of the response curve consisting of a small plateau; see Figure 16(a). For a slight increase in pressure to 35 Pa (b), the plateau becomes a small secondary peak. For another step in pressure to 40 Pa (c), the secondary peak becomes positive. Thus there are two peaks of maximum tip link tension in each cycle. For another step to 50 Pa (d), the secondary peak becomes dominant. This secondary peak is almost in phase with the driving pressure. So, for a change in pressure corresponding to about 5 dB, there is a shift in the phase of the excitation of 180°. For a middle ear pressure gain from the ear canal to SV of 30 dB, this shift in phase would correspond to about 95 dB-SPL, close to the transition level reported [Ruggero et al. 2000]. What we do not see is the second shift back in phase occurring at about 30 dB higher pressure, as seen in the auditory nerve. The calculations show only an increase in the relative size of the secondary peak. Note that the out-of-phase peak stays about constant in (a–e), while the in-phase peak grows in amplitude. The theory uses resultant forces per unit length in the circumferential direction. However, this may be reduced to the effective force per tip link, which is the amplitude shown in Figure 16(a–d). These amplitudes appear to be consistent with the experiments on stereociliary bundles which yield the estimate that a Ca^{2+}-bound channel requires approximately 3 pN more force to open [Cheung and Corey 2006].

The change in the gap between the tip of the IHC tall stereocilium and the Hensen stripe is shown in Figure 16(f) for high pressure. The initial gap for these calculations is about 20 nm. So the gap is nearly

shut with the value of -20 nm, for almost half of the cycle in (f). Of course, the gap is never totally closed, since infinite force would be required.
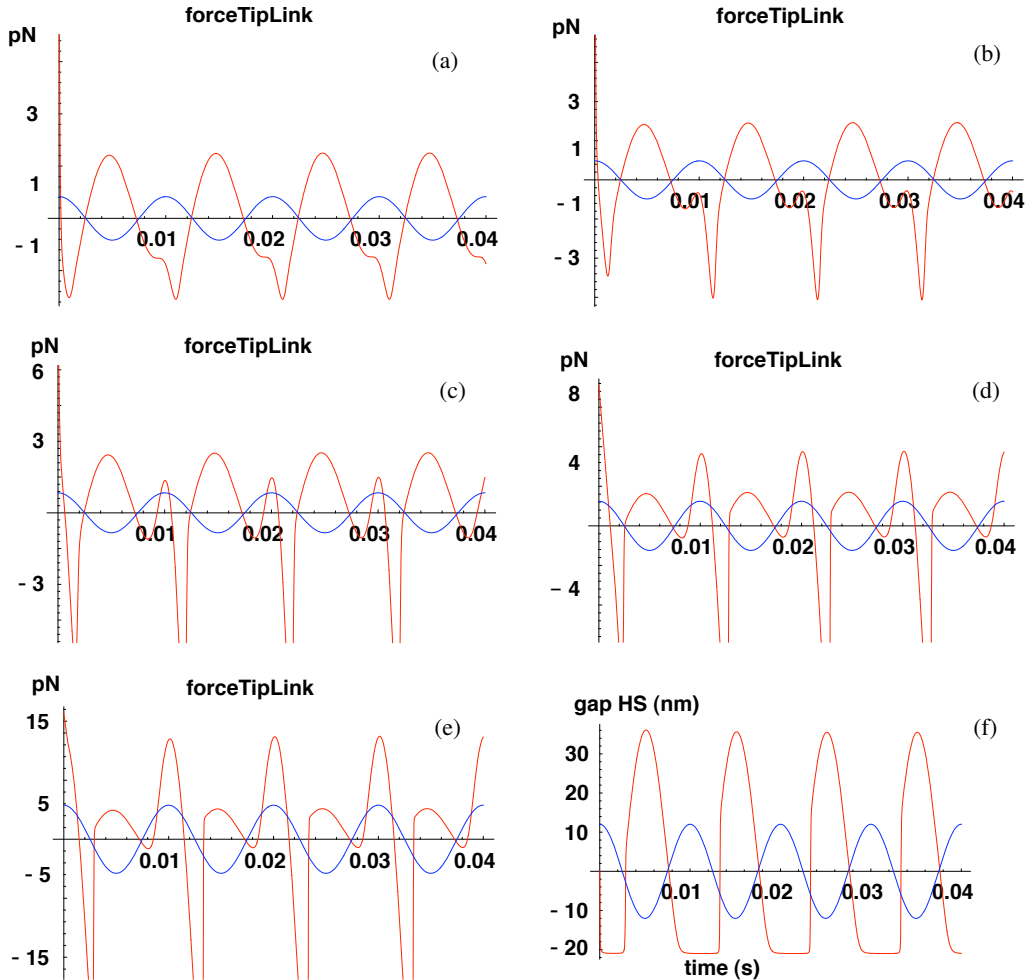

Figure 16. Nonlinear solution for the guinea pig base with initial gaps between the tip of IHC stereocilium and HS and TM of 7% (20 nm) at 100 Hz. (a) At the pressure difference ST-SV of 30 Pa the excitatory force in the tip link is out-of-phase with the pressure, but the negative portion acquires a secondary step that is in-phase. (b) At 35 Pa, the negative step becomes a small peak. (c) At 40 Pa, the secondary peak becomes positive. (d) At 50 Pa, the secondary peak becomes the dominant excitatory force. (e) At 60 Pa, the secondary peak becomes larger. (f) The gap between the Hensen stripe and the stereocilium tip shows that the secondary peak occurs when the tip comes into close contact. This offers an explanation for the 180° change in phase measured in auditory nerve fibers at 80 dB-SPL (in the ear canal) by [Ruggero et al. 2000]. Also the presence of the two excitatory peaks within the cycle (c)–(e) suggests a reason for the "peak splitting" sometimes observed in auditory nerve fibers.

6. Summary and discussion

The response of the organ of Corti shown in Figures 2–4 is a multidimensional problem, with the dimensions of the elastic elements ranging from millimeters to nanometers and the elastic moduli ranging from GPa to kPa. These components act together to transfer the input sound pressure into the proper neural excitation, so the separation of the process into uncoupled stages is not advantageous. All components are together in the shell-of-revolution simulation with the program Fast4. The recent advances in measurement are used to improve the elastic properties of components. With these one obtains the deformation shown in Figure 5 due to static pressure loading toward ST. This reveals a feature that is overlooked in simplified models. The subtectorial fluid region L1 opens in the vicinity of the inner hair cells. This opening of the fluid layer actually occurs, as shown by recent measurements in the guinea pig cochlea with electrical stimulation [Nowotny and Gummer 2006].

A good indication that the model components are put together properly comes from the superposition of the shell model and the optical image of the intact cross section [Fridberger et al. 2002], shown in Figure 4. The animation of the deformation due to steps in the static pressure load toward SV shows similar behavior of the model and actual organ of Corti. For loading in the opposite direction, [Fridberger et al. 2002] find a much larger response. The explanation is that a buckling of the outer pillars occurs, which can be seen in some of the images. This confirms that the IP and OP have an important role in maintaining the mechanical integrity of the OC. The optical signal does not have sufficient strength when passing deep into the tissue so the basilar membrane does not appear in the optical image.

The next paradox is the discrepancy between the measurements of the BM with point load and pressure. It seems that a simple beam model (Figure 8) cannot represent both. A possible explanation comes from the longitudinal stiffness of the pillar heads. This produces a significant torsional stiffness, which resists the deformation of the BM under a localized point load, but has much less effect for pressure. With isotropic pillar heads, in the three-dimensional model (Figures 2 and 3), both the point load and pressure conditions can be reasonably satisfied (Figure 11). The present analysis does not take into consideration the inclination of the hair cells and the phalangeal processes that connect the end of the hair cells to the RL. These will most likely provide additional longitudinal elastic coupling.

At this time the computational procedure for the full traveling wave solutions for all frequencies is not completed. However, there is interest in the low frequencies for which the longitudinal motion is not so significant, so the present three-dimensional model can be used. For these frequencies there is phase locking of the auditory nerve fibers. We assume that the neural excitation is proportional to the tension in the tip links (Figure 6). The results show excitation generally between BM displacement and velocity toward SV at the guinea pig apex. This is consistent with the intracellular recordings [Cheatham and Dallos 1999] and measurements of the relative rotation of IHC and OHC stereocilia [Fridberger et al. 2006] (Figure 12). At the guinea pig base, the phase of excitation is for BM motion toward ST, which is consistent with the direct measurements [Ruggero et al. 2000]. The key reason for this phase difference is that the fluid region under the TM and between the IHC and OHC stereocilia tends to open for BM motion toward ST. This causes fluid to flow in from the inner sulcus, bending the IHC stereocilia in the excitatory direction. In the apex, this is not so significant since the TM adapts more readily. The summary of the phase possibilities is in Table 1.

An important mechanical nonlinearity is caused by the small gap between the stereocilia of the IHC and the HS and TM. The actual initial gap will probably never be determined. Consequently in [Steele and Puria 2005], various values for this were assumed and some effect was found on the phase and amplitude of IHC excitation in the linear calculation of response. The present nonlinear calculation shows the effect of the amplitude of pressure on phase (Figure 16). For high pressure, corresponding to about 90 dB-SPL, the phase of the IHC excitation switches 180°. This is quite similar to the auditory nerve behavior sometimes observed [Ruggero et al. 2000]. Furthermore the intensity levels at which peak splitting develops, given in 1 dB steps in [Kiang 1990], look similar to the development of the two positive peaks in Figure 16. The negative peaks are most likely not realistic, since such sharp negative peaks are not seen in the IHC recordings [Cody and Mountain 1989]. This may be because the resting tension in the tip links is not included in these calculations. The neural behavior is variable [Cai and Geisler 1996], and the peak splitting and change in phase are not found in the guinea pig base [Wada et al. 2002]. However, it seems that the present calculations, based on the observation of the HS near the IHC stereocilia [Edge et al. 1998; Fridberger et al. 2006], support completely the notion that the Hensen stripe plays a crucial role in the excitation of the IHC. The suggestion is made [Zwislocki 1986] that there must be some mechanical nonlinear coupling between the TM and the OC. [Cody and Mountain 1989] provide further evidence for this. The present results appear to offer strong indication that the nonlinearity is simply due to the restricted fluid flow between the tip of the IHC stereocilia and the HS.

7. Conclusion

The cochlea of the inner ear offers significant challenges. The present consideration of passive static and low frequency response permits a focus on purely mechanical, that is, elastic-fluid aspects. The first task is the proper description of tissue components ranging over six orders of magnitude in size and elastic modulus. The assumption is that all of these behave elastically. Generally, we find consistency between the stiffness estimated from the microstructure and that computed from the available static measurements. The full three-dimensional shell model for the organ of Corti is necessary. This is evident from the consideration of the basilar membrane displacement under a point load and under pressure that cannot be described by a simple beam model.

The full model is certainly necessary to obtain the neural excitation, which is caused by fluid forces against the stereocilia of the inner hair cells. The full model shows effects missing from previous simplified models, in particular that a displacement of the basilar membrane causes an opening of the fluid region under the tectorial membrane. That opening and the proximity of the tips of the stereocilia to the Hensen stripe are critical for the phase of the excitation. Thus we offer an answer to long-standing questions on the phase of neural excitation. When the nonlinearity in the fluid layer is included, using lubrication theory, a change in the response is found with a small change in the amplitude of excitation, that offers an explanation for the long-standing question of neural peak splitting.

We have made some progress toward a satisfactory description of the tissue. An indication that all scales are represented properly is the agreement with experiments on the millimeter scale for BM point load response and on the nanometer scale for tip link forces. With this we have answered some basic questions. The challenge ahead is to obtain the high frequency response with the full model.

References

[Abnet and Freeman 2000] C. C. Abnet and D. M. Freeman, "Deformations of the isolated mouse tectorial membrane produced by oscillatory forces", *Hearing Res.* **144**:1–2 (2000), 29–46.

[Andoh and Wada 2003] M. Andoh and H. Wada, "Dynamic characteristics of the force generated by the outer hair cell motility in the organ of Corti (theoretical consideration)", *Trans. Jpn. Soc. Mech. Eng. C* **46**:4 (2003), 1256–1265.

[von Békésy 1960] G. von Békésy, *Experiments in hearing*, edited by E. G. Wever, McGraw-Hill, New York, 1960.

[Boutet 2007] J. Boutet de Monvel, M. Alessandro, J. Stefan, I. Tomo, M. von Tiedemann, A. Fridberger, M. Ulfendahl, and C. R. Steele, "From cochlear kinematics to cochlear mechanics: matching model to experiments", *Otol.* (*Japan*) **17**:2 (2007), 76–84.

[Cabezudo 1978] L. M. Cabezudo, "The ultrastructure of the basilar membrane in the cat", *Acta Otolaryngol.* **86**:3 (1978), 160–175.

[Cai and Chadwick 2002] H. Cai and R. Chadwick, "Radial structure of traveling waves in the inner ear", *SIAM J. Appl. Math.* **63**:4 (2002), 1105–1120.

[Cai and Geisler 1996] Y. Cai and C. D. Geisler, "Temporal patterns of the responses of auditory-nerve fibers to low-frequency tones", *Hearing Res.* **96**:1–2 (1996), 83–93.

[Carlini 1817] F. Carlini, "Ricerche sulla convergenza della serie che serve alla soluzione del problema di Keplero", *Effem. Astron.* (*Milano*) **44**:1818 (1817), 3–48 (Appendice).

[Cheatham and Dallos 1999] M. A. Cheatham and P. Dallos, "Response phase: a view from the inner hair cell", *J. Acoust. Soc. Am.* **105**:2 (1999), 799–810.

[Cheung and Corey 2006] E. L. M. Cheung and D. P. Corey, "Ca^{2+} changes the force sensitivity of the hair-cell transduction channel", *Biophys. J.* **90**:1 (2006), 124–139.

[Cody and Mountain 1989] A. R. Cody and D. C. Mountain, "Low-frequency responses of inner hair cells: evidence for a mechanical origin of peak splitting", *Hearing Res.* **41**:2–3 (1989), 89–99.

[Cooper 2000] N. P. Cooper, "Radial variation in the vibrations of the cochlear partition", pp. 109–115 in *Proceedings of the International Symposium on Recent Developments in Auditory Mechanics* (Sendai, 1999), edited by H. Wada et al., World Scientific, Singapore, 2000.

[Edge et al. 1998] R. M. Edge, B. N. Evans, M. Pearce, C.-P. Richter, X. Hu, and P. Dallos, "Morphology of the unfixed cochlea", *Hearing Res.* **124**:1–2 (1998), 1–16.

[Freeman et al. 2003] D. M. Freeman, C. C. Abnet, W. Hemmert, B. S. Tsai, and T. F. Weiss, "Dynamic material properties of the tectorial membrane: a summary", *Hearing Res.* **180**:1–2 (2003), 1–10.

[Fridberger et al. 2002] A. Fridberger, J. Boutet de Monvel, and M. Ulfendahl, "Internal shearing within the hearing organ evoked by basilar membrane motion", *J. Neurosci.* **22**:22 (2002), 9850–9857.

[Fridberger et al. 2004] A. Fridberger, J. Boutet de Monvel, J. Zheng, N. Hu, Y. Zou, T. Ren, and A. Nuttall, "Organ of Corti potentials and the motion of the basilar membrane", *J. Neurosci.* **24**:45 (2004), 10057–10063.

[Fridberger et al. 2006] A. Fridberger, I. Tomo, M. Ulfendahl, and J. Boutet de Monvel, "Imaging hair cell transduction at the speed of sound: dynamic behavior of mammalian stereocilia", *Proc. Nat. Acad. Sci. U.S.A.* **103**:6 (2006), 1918–1923.

[Geisler 1998] C. D. Geisler, *From sound to synapse: physiology of the mammalian ear*, Oxford University Press, New York, 1998.

[Givelberg and Bunn 2003] E. Givelberg and J. Bunn, "A comprehensive three-dimensional model of the cochlea", *J. Comput. Phys.* **191**:2 (2003), 377–391.

[Gray 1918] H. Gray (revised by W. H. Lewis), *Anatomy of the human body*, 20th ed., Lea & Febiger, Philadelphia, 1918. Reproduced in http://www.bartleby.com/107.

[Helle 1974] R. Helle, *Beobachtungen an hydromechanischen Modellen des Innenohres mit Nachbildung von Basilarmembran, Corti-Organ und Deckmembran*, Ph.D. Thesis, Technical University of Munich, 1974.

[Homer et al. 2004] M. Homer, A. Champneys, G. Hunt, and N. P. Cooper, "Mathematical modeling of the radial profile of basilar membrane vibrations in the inner ear", *J. Acoust. Soc. Am.* **116**:2 (2004), 1025–1034.

[Kelly 1989] J. P. Kelly, "Cellular organization of the guinea pig's cochlea", *Acta Otolaryngol.* Suppl. 467 (1989), 97–112.

[Kiang 1990] N. Y. Kiang, "Curious oddments of auditory-nerve studies", *Hearing Res.* **49**:1–3 (1990), 1–16.

[Langer et al. 2001] M. G. Langer, S. Fink, A. Koitschev, U. Rexhausen, J. K. H. Hörber, and J. P. Ruppersberg, "Lateral mechanical coupling of stereocilia in cochlear hair bundles", *Biophys. J.* **80**:6 (2001), 2608–2621.

[Miller 1985] C. E. Miller, "Structural implications of basilar membrane compliance measurements", *J. Acoust. Soc. Am.* **77**:4 (1985), 1465–1474.

[Narayan et al. 1998] S. S. Narayan, A. N. Temchin, A. Recio, and M. A. Ruggero, "Frequency tuning of basilar membrane and auditory nerve fibers in the same cochleae", *Science* **282**:5395 (1998), 1882–1884.

[Nowotny and Gummer 2006] M. Nowotny and A. W. Gummer, "Nanomechanics of the subtectorial space caused by electromechanics of cochlear outer hair cells", *Proc. Nat. Acad. Sci. U.S.A.* **103**:7 (2006), 2120–2125.

[Olson 1998] E. S. Olson, "Observing middle and inner ear mechanics with novel intracochlear pressure sensors", *J. Acoust. Soc. Am.* **103**:6 (1998), 3445–3463.

[Olson and Mountain 1994] E. S. Olson and D. C. Mountain, "Mapping the cochlear partition's stiffness to its cellular architecture", *J. Acoust. Soc. Am.* **95**:1 (1994), 395–400.

[Olver 1974] F. J. W. Olver, *Asymptotics and special functions*, Academic Press, New York, 1974.

[Ranke 1950] O. F. Ranke, "Theory of operation of the cochlea: a contribution to the hydrodynamics of the cochlea", *J. Acoust. Soc. Am.* **22**:6 (1950), 772–777.

[Ruggero et al. 2000] M. A. Ruggero, S. S. Narayan, A. N. Temchin, and A. Recio, "Mechanical bases of frequency tuning and neural excitation at the base of the cochlea: comparison of basilar-membrane vibrations and auditory-nerve-fiber responses in chinchilla", *Proc. Nat. Acad. Sci. U.S.A.* **97**:22 (2000), 11744–11750.

[Scherer and Gummer 2004] M. P. Scherer and A. W. Gummer, "Impedance analysis of the organ of Corti with magnetically actuated probes", *Biophys. J.* **87**:2 (2004), 1378–1391.

[Shoelson et al. 2004] B. Shoelson, E. K. Dimitriadis, H. Cai, B. Kachar, and R. S. Chadwick, "Evidence and implications of inhomogeneity in tectorial membrane elasticity", *Biophys. J.* **87**:4 (2004), 2768–2777.

[Spector et al. 1999] A. A. Spector, W. E. Brownell, and A. S. Popel, "Mechanical and electromotile characteristics of auditory outer hair cells", *Med. Biol. Eng. Comput.* **37**:1 (1999), 247–251.

[Steele 1999] C. R. Steele, "Toward three-dimensional analysis of cochlear structure", *ORL J. Oto-Rhino-Lary.* **61**:5 (1999), 238–251.

[Steele and Puria 2005] C. R. Steele and S. Puria, "Force on inner hair cell cilia", *Int. J. Solids Struct.* **42**:21–22 (2005), 5887–5904.

[Steele and Shad 1995] C. R. Steele and K. u.-R. Shad, "Asymptotic-numeric solution for shells of revolution", *Appl. Mech. Rev.* (*ASME*) **48**:11, part 2 (1995), S44.

[Steele and Taber 1979] C. R. Steele and L. A. Taber, "Comparison of WKB calculations and experimental results for three-dimensional cochlear models", *J. Acoust. Soc. Am.* **65**:4 (1979), 1007–1018.

[Steele et al. 2005] C. R. Steele, M. P. Scherer, C. Chandrasekaran, and A. W. Gummer, "An analytic model for the mechanical point impedance of the organ of Corti", poster session of the 28th annual midwinter research meeting of the Association for Research in Otolaryngology, 2005.

[Tolomeo and Holley 1997] J. A. Tolomeo and M. C. Holley, "Mechanics of microtubule bundles in pillar cells from the inner ear", *Biophys. J.* **73**:4 (1997), 2241–2247.

[Wada et al. 2002] H. Wada, A. Takeda, and T. Kawase, "Timing of neural excitation in relation to basilar membrane motion in the basal region of the guinea pig cochlea during the presentation of low-frequency acoustic stimulation", *Hearing Res.* **165**:1–2 (2002), 165–176.

[Wikipedia 2004] Illustration in Wikipedia entries relating to the inner ear, 2004, Available at http://commons.wikimedia.org/wiki/File:Cochlea-crosssection.png. Attributed to Oarih Ropschkow.

[Wittbrodt et al. 2006] M. J. Wittbrodt, C. R. Steele, and S. Puria, "Developing a physical model of the human cochlea using microfabrication methods", *Audiol. Neurotol.* **11**:2 (2006), 104–112.

[Yoon et al. 2006] Y.-J. Yoon, S. Puria, and C. R. Steele, "Intracochlear pressure and organ of Corti impedance from a linear active three-dimensional model", *ORL J. Oto-Rhino-Lary.* **68**:6 (2006), 365–372.

[Zetes et al. 2004] D. E. Zetes, J. A. Tolomeo, and M. C. Holley, "Mapping the mechanical properties of cytoskeletal structures in the mammalian inner ear", 2004. Manuscript.

[Zwislocki 1986] J. J. Zwislocki, "Are nonlinearities observed in firing rates of auditory-nerve afferents reflections of a nonlinear coupling between the tectorial membrane and the organ of Corti?", *Hearing Res.* **22**:1–3 (1986), 217–221.

CHARLES R. STEELE: chasst@stanford.edu
Stanford University, Mechanical Engineering, Durand Building, Room 262, Stanford, CA 94305-4035, United States

JACQUES BOUTET DE MONVEL: jmonvel@pasteur.fr
Unité de Génétique et Physiologie de L'Audition, Inserm UMRS 587, Institut Pasteur, 25 Rue du Dr. Roux, 75724 Paris, cedex 15, France

SUNIL PURIA: puria@stanford.edu
Stanford University, Mechanical Engineering, Durand Building, Room 262, Stanford, CA, 94305-4035, United States
and
Stanford University, Otolaryngology — Head and Neck Surgery, Stanford, CA 94305, United States

SUBMISSION GUIDELINES

ORIGINALITY

Authors may submit manuscripts in PDF format on-line. Submission of a manuscript acknowledges that the manuscript is *original and has neither previously, nor simultaneously, in whole or in part, been submitted elsewhere.* Information regarding the preparation of manuscripts is provided below. Correspondence by email is requested for convenience and speed. For further information, consult the Web site at http://www.jomms.org or write to

jomms.steele@stanford.edu

LANGUAGE

Manuscripts must be in English. A brief abstract of about 150 words or less must be included. The abstract should be self-contained and not make any reference to the bibliography. Also required are keywords and subject classification for the article, and, for each author, postal address, affiliation (if appropriate), and email address if available. A home-page URL is optional.

FORMAT

Authors are encouraged to use LaTeX and the standard article class, but submissions in other varieties of TeX, and, exceptionally in other formats, are acceptable. Electronic submissions are strongly encouraged in PDF format only; after the refereeing process we will ask you to submit all source material.

REFERENCES

Bibliographical references should be listed alphabetically at the end of the paper and include the title of the article. All references in the bibliography should be cited in the text. The use of BibTeX is preferred but not required. Tags will be converted to the house format (see a current issue for examples), however, in the manuscript, the citation should be by first author's last name and year of publication, e.g. "as shown by Kramer, et al. (1994)". Links will be provided to all literature with known web locations and authors are encoraged to provide their own links on top of the ones provided by the editorial process.

FIGURES

Figures prepared electronically should be submitted in Encapsulated PostScript (EPS) or in a form that can be converted to EPS, such as GnuPlot, Maple, or Mathematica. Many drawing tools such as Adobe Illustrator and Aldus FreeHand can produce EPS output. Figures containing bitmaps should be generated at the highest possible resolution. If there is doubt whether a particular figure is in an acceptable format, the authors should check with production by sending an email to:

production@mathscipub.org

Each figure should be captioned and numbered so that it can float. Small figures occupying no more than three lines of vertical space can be kept in the text ("the curve looks like this:"). It is acceptable to submit a manuscript with all figures at the end, if their placement is specified in the text by means of comments such as "Place Figure 1 here". The same considerations apply to tables.

WHITE SPACE

Forced line breaks or page breaks should not be inserted in the document. There is no point in your trying to optimize line and page breaks in the original manuscript. The manuscript will be reformatted to use the journal's preferred fonts and layout.

PROOFS

Page proofs will be made available to authors (or to the designated corresponding author) at a web site in PDF format. Failure to acknowledge the receipt of proofs or to return corrections within the requested deadline may cause publication to be postponed.

In memoriam
George Herrmann